The Oxidation Damage of Ni-based Superalloy, RR1000, with Different Surface Modifications and the Role of Oxidation in Fatigue Crack Initiation

UNIVERSITY OF BIRMINGHAM

by

SAM CRUCHLEY

A thesis submitted to
The University of Birmingham
For the degree of
DOCTOR OF PHILOSOPHY

Department of Metallurgy and Materials
College of Engineering and Physical Sciences
The University of Birmingham

Abstract

Nickel-based superalloys have been optimised, compositionally and microstructurally, to operate in the highly stressed conditions occurring in the hot sections of gas turbine engines. Under such conditions degradation by oxidation occurs and plays a key role in determining the lifetimes of the components. For this reason it is important to understand the oxidation processes occurring and the mechanisms involved. Most oxidation studies, especially those on Ni-based superalloys used in rotor discs are performed in the ground or polished condition rather than the actual condition in which the component would enter service and it is important to quantify the effect that different surface modifications have on it. Additionally studies have primarily focussed on the study of oxidation without the application of an external load. This is an important omission since in the real life operating conditions, these materials, and the components they will be used for, often experience significant external stresses.

The oxidation behaviour of RR1000 with different surface modifications has been well studied using detailed metallographic and mass gain measurements. The oxide comprises of an external chromia scale with isolated grains of TiO_2 on the outer surface. Sub-surface internal alumina is present, beneath which the presence of TiN occurs (at higher temperatures >800^{o}C), all contained within a γ' denuded zone. The chromia external scale growth rate is significantly greater than pure chromia on chromium and the enhancement is attributed to the increased ionic transport caused by doping of the chromia layer with Ti. This effect is still seen regardless of surface condition prior to oxidation. All the different surface conditions, regardless of the amount of residual stress/cold work induced, produced the same oxide composition, but did significantly change the internal alumina precipitate morphology. The presence of cold work causes the γ' denuded zone to recrystallise reducing the grain size in this area dramatically.

The positive identification of voids and oxides by focussed ion beam (FIB) imaging can be complex and prone to misinterpretation and thus the use of several imaging conditions and tilt angles must be used, along with conventional preparation methods, to confirm or refute the presence of 'voids' underneath oxides.

Oxides, especially internal intergranular oxides have been shown to crack under room temperature fatigue conditions, causing a significant fatigue life deficit at a maximum applied stress of 800 MPa and 1000 MPa. Between 825-900 MPa, plastic yielding of the γ' denuded zone occurred leading to a substantial increase in fatigue life, through either blunting the crack by deforming to accommodate the stress concentration at the crack tip or by preventing cracking of the oxides.

Acknowledgements

I am extremely grateful to my supervisors Professor Hugh Evans and Professor Paul Bowen for all their encouragement, guidance and support without which this work would not have been possible. In addition I would like to thank Dr Hangyue Li for her valuable advice throughout. Dr Mary Taylor was a constant source of valuable contributions throughout my study, without her guidance much of this work would have been much more time consuming and difficult. Her contributions were greatly appreciated.

At Rolls-Royce plc thanks are owed to Dr Mark Hardy, Dr Svjetlana Stekovic and Dr Dan Child for providing me with not only the samples required but also for many helpful discussions and guidance as well as continually pushing me.

At the University of Birmingham, I would like to thank Dr Jifeng Sun for his exceedingly valuable contribution to my thesis by helping me perform focussed ion beam microscopy. Thanks are required for the expertise Dr Rengen Ding provided with the TEM. I would also like to thank Mr Paul Stanley, Mr Jas Singh, Mr Mick Cunningham, Mr Dave Price and Dr Tim Doel for their technical support, which allowed my experimental work to run a lot more smoothly and enjoyably. I would also like to acknowledge the help that Dr Brian Connolly has given me throughout my time here. Dr Allan Walton and the hydrogen group are owed thanks for allowing me use of their confocal microscope as does Professor Hanshan Dong and Mr Dennis Formosa for the provision of nano-indentation.

I would also like to thank everyone in the office, in particular to Danial Khoshkhou, Chris Simpson, Jonny Boukhobza, Matthew Dear, Craig Knaggs and Andy Du Plessis for their friendship, support and valuable discussions on relevant and irrelevant topics.

The work conducted in this thesis was funded jointly by Rolls-Royce plc and the Engineering and Physical Sciences Research Council (EPSRC). Their contribution is gratefully acknowledged.

Publications

The following peer-reviewed papers were produced from parts of this doctoral research:

1. **S. Cruchley**, M.P. Taylor, H.E. Evans, P. Bowen, M.C. Hardy, and S. Stekovic, *Microstructural Characterisation of High Temperature Oxidation of Nickel Base Superalloy RR1000 and the Effect of Shot-Peening*, in *Superalloys 2012: 12th International Symposium on Superalloys*, 2012, TMS: Seven Springs, PA. p. 751-758.

2. **S. Cruchley**, M.P. Taylor, H.E. Evans, P. Bowen, M.C. Hardy, and S. Stekovic, *Chromia layer growth on a Ni-based superalloy: Sub-parabolic kinetics and the role of titanium*, Corrosion Science, 2013. **75***:* p. 58-66.

3. **S. Cruchley**, M.P. Taylor, H.E. Evans, P. Bowen, J. Sumner, J.R. Nicholls, N.J. Simms, R.J. Chater, B. A. Shollock, B. Foss, M. C. Hardy and S. Stekovic, *A Cautionary Note on the use of Focused Ion Beam (FIB) Sectioning as a Technique for Characterising Oxidation Damage in Ni-based Superalloys*, Materials at High Temperatures, 2014. **31**(1): p. 27-33.

4. **S. Cruchley**, M.P. Taylor, H.E. Evans, M.C. Hardy and D.J. Child, *Characterisation of the sub-surface oxidation damage in Ni-based superalloy, RR1000*, Materials Science and Technology, 2014. **30**(15): p. 1884-1889.

5. **S. Cruchley**, M.P. Taylor, H.Y. Li, H.E. Evans, P. Bowen, M.C. Hardy and D.J. Child, *Effect of prior oxidation on high cycle fatigue performance of RR1000 and the role of oxidation in fatigue crack initiation*, Materials at High Temperature, **32**(1-2): p. 68-73.

6. **S. Cruchley**, M.P. Taylor, R.G. Ding, H.E. Evans, M.C. Hardy and D.J. Child, *Comparison of chromia growth kinetics in a Ni-based superalloy, with and without shot-peening*, submitted to Corrosion Science.

7. **S. Cruchley**, M.P. Taylor, H.Y. Li, H.E. Evans, P. Bowen, M.C. Hardy and D.J. Child, *The role of oxidation damage in fatigue crack initiation of an advanced Ni-based superalloy*, submitted to International Journal of Fatigue.

Table of Contents

Chapter 1 - Literature Review

1.1 Gas Turbine Engines

1.1.1 How do they work?

Newton's third law of motion states that

"For every force acting on a body there is an equal and opposite reaction"

The jet engine applies this principle by forcing a fluid in one direction so creating an equal reaction, thrust, that moves the engine in the opposite direction.

The action of a gas turbine jet engine can be divided into three stages: the fan and compressor stage, combustor stage and the turbine stage. The fan serves to draw air into the engine core and in turbofan designs additionally through a bypass duct (which provides much of the thrust). The air drawn into the engine core is then compressed through several rotating stages delivering a high temperature, high pressure flow of air to the combustor. This highly compressed air is mixed with vaporised fuel and ignited, where combustion temperatures can reach up to ~2000ºC.

This hot gas stream then enters the turbine and is expanded to a lower pressure and temperature. This expansion drives the rotating turbine blade and disc assembly which drives the compressor and fan via a series of centrally rotating shafts. The turbine as with the compressor may consist of several stages, typically a low pressure (LP), an intermediate pressure (IP) and a high pressure (HP) stage, in modern high pressure turbofans. Each of these stages drive the corresponding stage of the fan and compressor. The hot gases then exit through a choked nozzle designed to minimise engine noise, with any spare pressure and temperature in the gas stream being used to cause a change in momentum of the air behind the engine. This causes a corresponding momentum change in the engine, resulting in the aircraft moving forwards. The architecture of a modern three-stage high bypass turbofan can be seen in Figure 1-1.

There are several types of gas turbine engines currently used: turbofan (high and low bypass), turbojet and turboprop. Each of these designs has their own strengths and as such is designed for different applications, balancing the need for operational speed with engine efficiency. The propulsive efficiency of several different types of gas turbine engine at different operating speeds is shown in Figure 1-2, and clearly shows that a high bypass turbofan is designed for efficiency whereas a turbojet for pure speed.

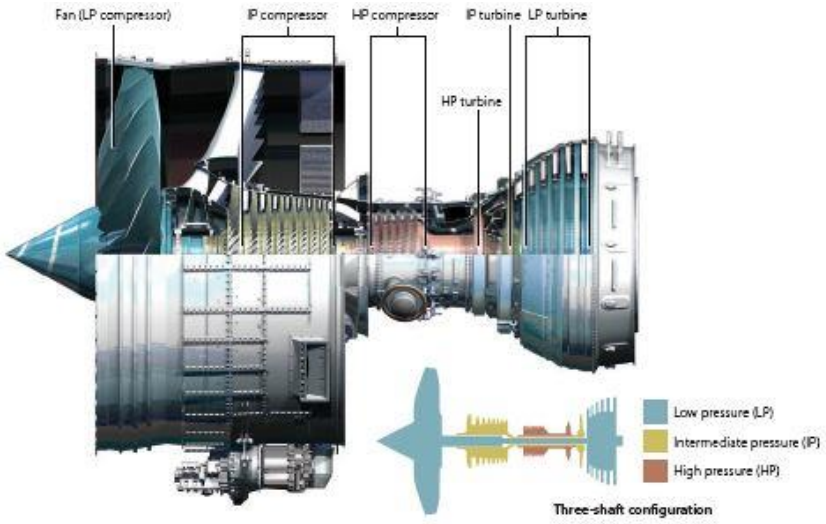

Figure 1-1: Civil three-shaft gas turbine engine [1].

Propulsive efficiency compares the power supplied to the aircraft with the increase in kinetic energy of the air through the engine. If the jet velocity is nearly equal to the forward speed, the kinetic energy of the jet is used very efficiently and propulsive efficiency tends to unity. Unfortunately this is opposite to net thrust and as jet velocity nears the speed of the aircraft the net thrust reduces to zero. Modern civil gas turbine engines are optimised for fuel efficiency and so typically have a high bypass ratio turbofan architecture, whereas military aircraft are optimised for speed and so have a turbojet architecture often with afterburner capabilities.

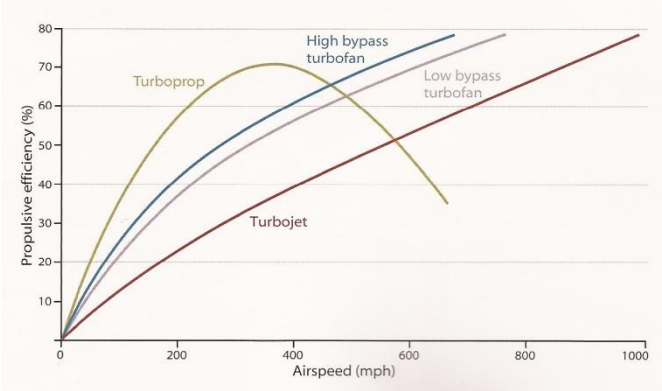

Figure 1-2: The change in propulsive efficiency of several types of gas turbine engine against airspeed [1].

Thermodynamically the gas turbine engine can be considered as a heat engine, with the output power being dependent on the increase in temperature and pressure of the working fluid. It can therefore be simplistically modelled by Brayton's cycle in which air is compressed isentropically (in an adiabatic process). Combustion occurs at a constant pressure and the expansion of gases through the turbine stage occurs isentropically in order to return to the starting pressure [2].

Specific fuel consumption of a modern gas turbine engine can be considered to have two components: thermal efficiency and propulsive efficiency. It can simplistically be improved in several ways: Incorporating a larger bypass ratio, by increasing the turbine entry temperature (TET) or by increasing the overall pressure ratio (OPR) (Figure 1-3). The overall pressure ratio is the ratio of the stagnation pressure at the start and end of the compressor. The latter two (TET & OPR) increase the thermal and mechanical demand placed on the compressor and turbine materials.

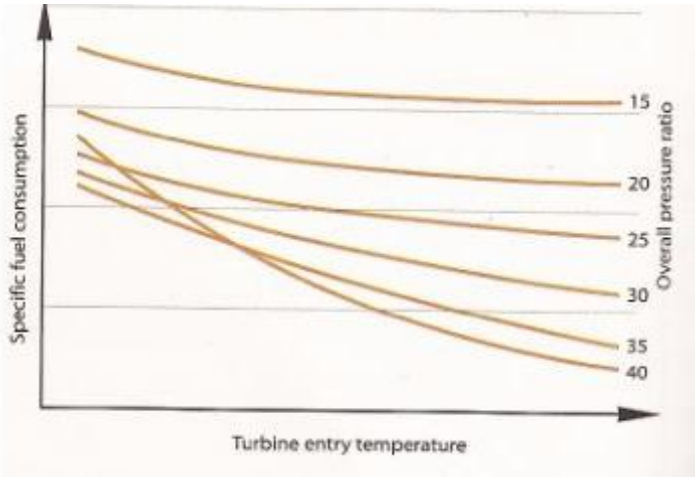

Figure 1-3: The effect of turbine entry temperature and overall pressure ratio on specific fuel consumption of a gas turbine engine [1].

1.1.2 Environment and regulation

The emissions from a gas turbine engine are a result of the combustion process. ACARE 2020 is a set of demanding international regulations on both the reduction of noise and emissions from a baseline date of 2000 [3]. These are described below:

- Reduce CO_2 emissions by 50% per passenger kilometre.
- Reduce NO_x emissions by 80%.
- Reduce perceived aircraft noise by 50%.

Each of these targets presents significant engineering challenges, with the reduction in fuel burn and CO_2 requiring contributions from the engines (15-20%), the airframes (20-25%) as well as improved air traffic management and operational efficiency (5-10%) [3]. Modern aircraft are already significantly quieter than earlier designs, with aircraft noise coming from a combination of both airframe and engine noise. To reduce engine noise a reduction in the jet velocity and a lowering of the speed of the rotating components is required since the noise generated by the jet engine is approximately proportional to the eighth power of the jet velocity. To achieve this reduction in jet velocity (and therefore noise) an increase in the bypass ratio is required, which has the added benefit of increasing propulsive efficiency.

These regulations provide the driving force for engine manufacturers to improve the efficiency of future engines. This driving force puts increasing pressure on the development of materials used so that higher temperatures and stresses can be sustained.

1.1.3 Turbine section

The turbine produces a rotation power output along a shaft, which is used to provide drive to the fan and compressor (as well as accessories i.e. electrical power) and in a three shaft design consists of three stages: low pressure, intermediate pressure and high pressure (Figure 1-4).
It is made from several components:

- Casings
- Discs
- Shafts
- Nozzle guide vanes
- Blades

The emphasis here is on the turbine disc components and is considered in more detail below:

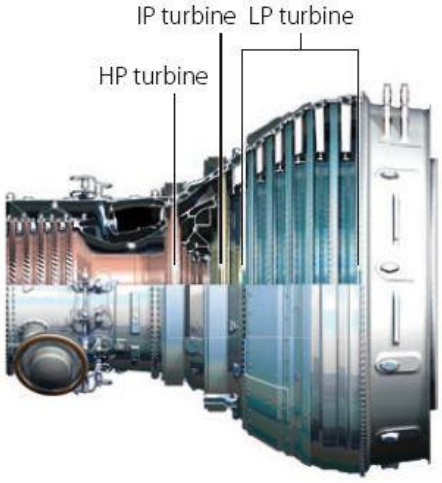

Figure 1-4: Turbine section of a gas turbine engine, illustrating the three different stages; high pressure (HP), intermediate pressure (IP) and low pressure (LP) [1].

1.1.3.1 Turbine discs

The main function of the turbine discs is to locate and retain the rotating blades enabling the circumferential force produced by them to be transmitted to the compressor through the central shafts. Each row of blades is retained in the rim of a disc, via a root fixing, designed to withstand the enormous centrifugal loads exerted on the disc by the mass of rotating blades. The discs have drive arms connected to a corresponding stage of the compressor via a shaft. The high pressure sections represent the most demanding conditions in terms of stress and temperature in which these

components operate, with temperatures at the discs rim approaching 700°C and stresses nearing 1000 MPa in the bore [4, 5]. The discs are considered a safety critical component of the engine and aircraft assembly. This means it is a part whose single failure can hazard the operational capability of the aircraft [6]. This is generally because the high energy fragments from a burst disc cannot be contained within the engine casing and therefore potentially have drastic effects on the ability of the engine and aeroplane to continue to operate safely. These components must therefore maintain a high level of integrity throughout their service life and therefore must be manufactured using materials with excellent high temperature mechanical properties these include: high yield stress and tensile stress in order to prevent yield and fracture, ductility and fracture toughness to impart tolerance to defects, resistance to fatigue crack initiation, low fatigue crack propagation rates and high creep and dwell crack growth resistance [7]. The choice of material and microstructure used is therefore of utmost importance.

1.2 Nickel-Based Superalloys

The choice of materials for high temperature aerospace alloy applications is limited, due in part to their need for high strength in a high temperature working environment: this temperature is also set to rise further due to the need to maximise efficiency. While Ti alloys can comfortably meet the required mechanical properties for the fan and intermediate compressor stages their performance deteriorates as the temperature exceeds 550°C and is not suitable in the high pressure compressor or turbine sections of a jet engine. A superalloy is a material that retains its mechanical properties at elevated temperatures and is therefore ideally suited for this role [8]. They are among the most compositionally complex metallic alloys developed and are usually Ni, Co or Fe/Ni based. Nickel has a number of significant properties which lends itself to selection as the base material for superalloys used in disc rotor applications:

- Abundant material and hence acceptable bulk costs
- Relatively high melting point - 1455°C
- Reasonable density – 8907 $kg.m^{-3}$
- FCC structure capable of being highly alloyed
- No phase changes up to the melting point
- Acceptable environmental resistance when alloyed with Cr and Al

Nickel has therefore become the choice base material for use in this environment [7] with Ni-based superalloys having the best blend of high temperature environmental resistance and mechanical properties (Figure 1-5). Development of Ni-based superalloys has primarily been based on improving the mechanical properties although recent trends are now focussing on improving the oxidation resistance since operational temperatures continue to rise in response to the need for reducing emissions and improving fuel consumption. This produces a significant challenge since the addition of alloying elements required for oxidation resistance generally has a detrimental effect on high temperature mechanical properties.

1.2.1 Metallurgy of Ni-based superalloys

The chemical composition of Ni-based superalloys is complex and often contains 10 or more alloying additions. Nickel-based superalloys are typified by a two-phase microstructure: a continuous matrix material of gamma phase (γ) and an ordered intermetallic gamma prime (γ') (Ni_3Al) precipitate. Other phases such as Topological close packed (TCP) phases (e.g. σ = CrCo , μ = Co_7Mo_6 and laves = Fe_2Nb) and orthorhombic delta phase (δ = Ni_3Nb) are possible but are often not desirable or common [7, 9]. The full composition of some Ni-based superalloys used in turbine discs is shown in Table 1-I, and illustrates the large number of alloying elements used. Each of these alloying elements has a particular function, often more than one, and these can be seen in Table 1-II and Figure 1-6. Figure

1-6 also shows that some trace and minor elements such as nitrogen, oxygen and sulphur are detrimental to the performance of Ni-based superalloys. These elements are not intentionally added but can often be included accidently as impurities during the manufacturing process. Nitrogen has been shown to cause micro-porosity during solidification [10, 11], as well as the ability to dissolve in MC and M_6C to form carbonitrides which embrittle the grain boundaries reducing ductility. Oxygen above 50 parts per million (ppm) can significantly reduce the stress rupture life [10-12], while sulphur segregates to the grain boundaries because of its low solubility in nickel and has the propensity to form sulfocarbides (M_2SC) which can act as crack initiation sites at small plastic strains and reduce creep rupture life and ductility [10, 12]. Sulphur also reduces the adhesion of oxide scales reducing environmental resistance [7]. Other minor elements like carbon and boron are purposefully added to provide grain boundary strength by the formation of carbides and borides, which is discussed in more detail in section 1.2.1.4

The behaviour of each alloying element and its influence of phase stability depends strongly upon its position within the periodic table, with these elements being largely taken from the D-block transition metals [13]. The phase the element partitions to is largely dependent on the percentage difference in the atomic diameter of the alloying element to Ni. Elements with similar atomic radii tend to partition to the γ phase stabilising it, whereas elements with larger atomic radii promote the formation of γ′. Elements such as carbon and boron, which have drastically smaller atomic radii, tend to segregate to the grain boundaries [7].

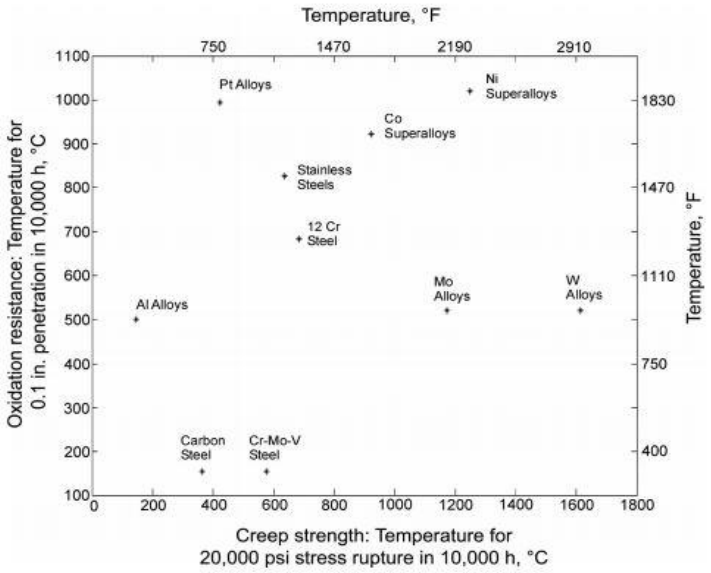

Figure 1-5: High temperature environmental resistance against creep strength for various metallic alloys [14].

Table 1-I: Composition of several Ni-based superalloys for rotor disc applications [7, 15-17].

Composition (% wt)	Ni	Co	Cr	Mo	Ti	Al	Ta	Hf	Zr	C	B	W	Nb	Fe	Density ($kg.m^{-3}$)
Udimet 720 Li	Bal	15.0	16	3	5	2.5	-	-	0.05	0.025	0.018	1.25	-	-	8420
Astroloy	Bal	17	15	5.3	3.5	4	-	-	-	0.06	0.03	-	-	-	8310
Waspaloy	Bal	13.6	19.3	4.2	3.6	1.3	-	-	0.05	0.01	0.04	-	-	-	8380
ME3	Bal	18.2	13.1	3.8	3.5	3.5	2.7	-	0.05	0.03	0.03	1.9	1.4	-	8750
IN718	Bal	-	19	3	0.9	0.5	-	-	-	0.04	-	-	5.1	18.5	8330
Rene 95	Bal	8.0	14.0	3.5	2.5	3.5	-	-	0.05	0.03	0.01	3.5	3.5	-	8730
RR1000	Bal	18.5	15	5	3.6	3	2	0.5	0.06	0.03	0.02	-	-	-	8540
IN718 plus	Bal	9.1	18	2.7	0.75	1.45	-	-	-	0.02	0.005	1.0	5.4	9.5	8448

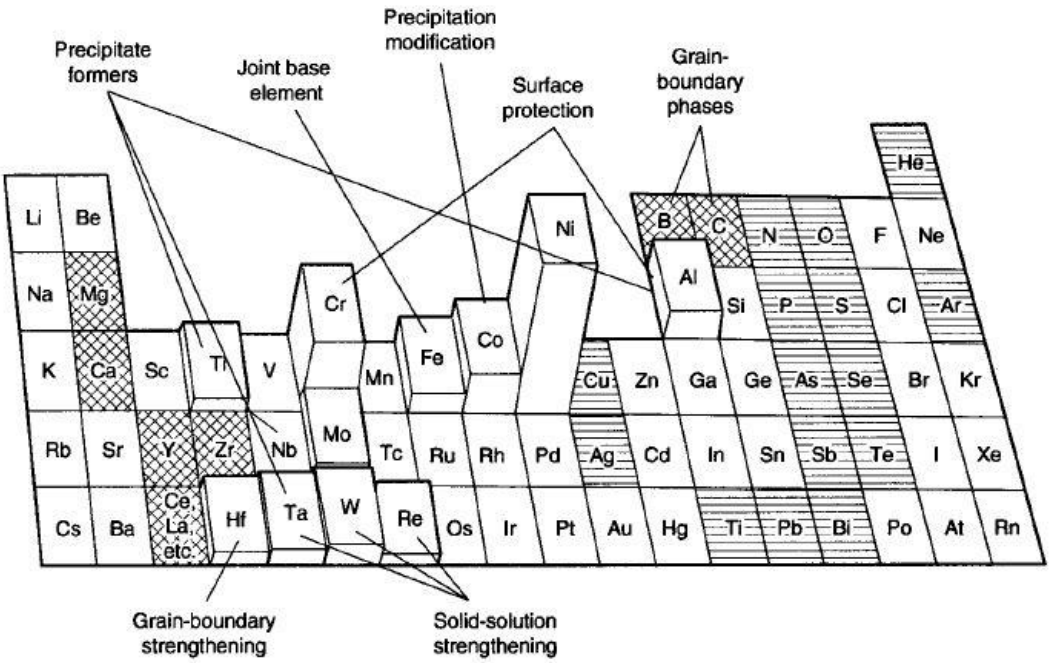

Figure 1-6: Alloying elements commonly used in Ni-based superalloys, with the role they play in strengthening the alloy. Beneficial minor elements are marked with cross-hatch, while detrimental elements are marked with horizontal line hatch [18].

Table 1-II: The role of alloying additions in Nickel-based superalloys.

Alloy additions	Solid solution strengtheners	γ′ formers	Carbide formers	Grain boundary strengtheners	Oxidation Resistance
Cr	x		x		x
Al		x			x
Ti		x	x		
Mo	x		x		
W	x		x		
B				x	
Zr				x	
C				x	
Ni		x	x		
Hf			x	x	
Ta		x	x	x	

Typical phases present in a nickel-based superalloy are discussed below, with the two main constituents γ and γ′ discussed in detail.

1.2.1.1 Gamma matrix (γ)

The gamma matrix is the continuous base phase on which the alloy is built around. It is a nickel base austenitic phase, and is in general the main constituent phase in a Ni-based superalloy. It has a face centre cubic (fcc) crystal structure which accommodates significant amounts of various alloying elements such as Cr, Mo and Co in solution.

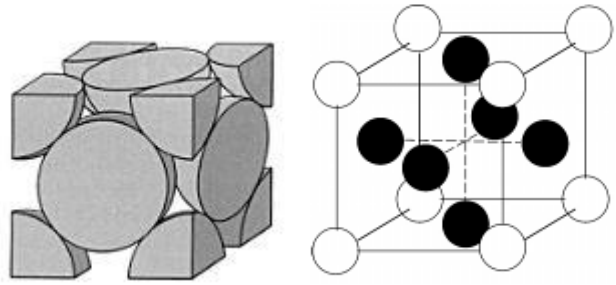

Figure 1-7: (a) FCC crystal structure. (b) FCC crystal structure of a γ′ phase with the shaded dots on the faces corresponding to nickel and the clear dots corresponding to Ti or Al which are always situated on the corners in an ordered crystal of γ′[7].

1.2.1.2 Gamma prime (γ′)

Gamma prime (γ′) is the main strengthening phase or precipitate phase present in nickel-based superalloys. It is rich in elements Al, Ti and Ta; although Ni_3Al is the dominant compound which displays an ordered $L1_2$ primitive lattice crystal structure with a site preference. Ni atoms occupy the face centred positions and Al (Ti/Ta) the corner atoms (Figure 1-7). The strength of the phase is associated with extensive directional covalent bonds and preferential Ni-Al bonding resulting in a strong chemically ordered structure [7]. This $L1_2$ crystal structure has a very similar lattice parameter to that of γ, leading to a stable alloying system [7, 19]. The morphology of the precipitates depends on the γ/γ′ mismatch, if the mismatch is small (± 0 – 0.2%) small spherical particles are formed but if the mismatch is larger (± 0.5 - 1%) cuboidal particles are formed [18, 19]. The morphology changes from a spherical particle to a cuboidal one as the γ/γ′ mismatch increases and the driving force changes from a need to minimise surface energy to one in which the elastic energy is minimised [20].

There are three types of γ′ in a typical alloy microstructure: primary, secondary and tertiary. Primary γ′ resides on the γ phase boundaries and the particles are in the region of 2-5 μm in size. It is formed from the remaining γ′ particles that do not enter solution during a sub-solvus heat treatment. Upon cooling the γ′ particles prevent grain growth by exerting a pinning pressure which counteracts the driving force for grain growth controlling the grain size [21]. With a super-solvus heat treatment all γ′ particles enter solution and therefore no primary γ′ forms and no pinning of the grain boundaries occurs allowing a larger grain size. Secondary γ′ forms during cooling within the γ grains from the Al (Ti, Ta) that comes out of solution to combine with Ni and can be formed from both sub and super-solvus heat treatments. The cooling rate determines the secondary γ′ size which has a typical diameter

of 70 – 120 nm. Tertiary γ′ precipitates form within the γ grains and are around 5 – 10 nm in size but can coarsen with aging or extended service [7]. The volume fraction of γ′ is extremely important in deciding the mechanical properties of the Ni-based superalloy and is determined by the alloying elements (and amount of) and the processing conditions, i.e. heat treatments. Typically the γ′ volume fraction lies in the range of 40-50% in polycrystalline rotor disc alloys [7].

While gamma and gamma prime are the main two phases in the majority of Ni-based superalloys, other phases can often occur in limited amounts.

1.2.1.3 Gamma double prime and TCP phases

Gamma double prime (γ′′) exhibits a body centred tetragonal (BCT) ordered crystal structure and is generally formed in superalloys rich in both Fe and Nb of which RR1000 has neither, so minimal if any is found in the alloy. It usually displays a DO_{22} crystalline ordered Ni-Nb intermetallic compound with the composition of Ni_3Nb. It has a disc morphology (~10 nm thick and 50 nm in diameter) and its high strength is associated with its coherence with the γ matrix and the coherence strains it develops as well as the limited number of slip systems available in this phase [7].

Alloys containing γ′′ are susceptible to the formation of orthorhombic delta (δ) phase in the overaged condition [18]. It is an orthorhombic Ni_3Nb intermetallic compound and is incoherent with the γ matrix. Significant amounts of δ should be avoided as it leads to a severe degradation of the mechanical properties of the alloy.

Topological close-packed (TCP) phases are detrimental phases. They form when super-saturation of the γ matrix with excessive quantities of Cr, Mo, W and Re occurs. They promote the precipitation of intermetallic phases which are rich in these elements and deplete the γ matrix of solid solution strengtheners. There are several types of TCP phases: sigma, mu and laves each with different morphologies [9, 22]. Both sigma (σ) and laves phase occur after extended high temperature exposure in Fe-Ni based and Co-based superalloys. These both exhibit an irregular elongated globular shape. Sigma phase has a tetragonal crystal structure with a range of possible compositions (FeCr, CrCo and Cr_2Ru), whereas laves phase has a hexagonal crystals structure with a range of Co and Fe rich compositions (Fe_2Nb, Fe_2Ti and Co_2Ti). Mu (μ) phase forms after a high temperature exposure in superalloys containing high amounts of molybdenum and tungsten. It exhibits Widmanstätten plate morphologies and has a rhombohedral crystal structure. A range of Co and Mo rich compositions (Co_2W_6 and Mo_6Co_7) can occur. Careful control of alloying elements is required to avoid nucleation of these phases.

1.2.1.4 Carbides and borides

Various carbides and borides form in Ni-based superalloys, the type depends upon the exact alloy composition and the processing conditions employed. In many superalloys the MC carbide precipitates at high temperature from the liquid phase. This is because superalloys are usually rich in Ti, Ta and Hf which are all elements that strongly encourage carbide formation. There are several different types of carbides and borides formed, with the important types being MC, M_6C, $M_{23}C_6$, M_7C_3 and M_3B_2, which precipitate in many forms: globular, blocky or script [18]. MC carbides decompose over time to other carbides such as M_6C, $M_{23}C_6$ which prefer to reside on the grain boundaries. The role of carbides and borides has proven controversial, but it is now accepted that the high temperature creep properties of the superalloy are improved in many circumstances if carbon and boron are present. This is largely due to the carbides and borides being positioned on grain boundaries and acting as grain boundary strengtheners by inhibiting grain boundary sliding and therefore improving rupture and creep strength [7, 23].

1.2.2 Strengthening mechanisms

Nickel-based superalloys have outstanding strength at high temperature. They derive their strength from a number of mechanisms: solid-solution strengthening, precipitate hardening and carbide strengthening. The mechanical properties of Ni-based superalloys depends strongly upon the state of the microstructure which is controlled by chemical composition and processing conditions. These will be discussed subsequently briefly as a detailed appraisal is outside the scope of this thesis. However a more detailed analysis is provided by standard texts [7, 24, 25].

1.2.2.1 Solid solution strengthening

Solid solution strengthening is the increase in matrix strength through the substitution of solute atoms in the matrix [23]. This occurs by hindering dislocation motion therefore increasing the stress needed for dislocation motion to occur thereby strengthening the material. There are two types of solid solutions: Substitutional and interstitial. Interstitial solid solution occurs when solute atoms are much smaller than the solvent atoms and occupy interstitial sites within the crystal structure. Substitutional solid solution occurs when solute atoms replace solvent atoms at lattice sites in the crystal structure. They are more likely to form between atoms with similar radii ($< \pm 15\%$), valence, electronegativity and chemical bonding [26]. Solute atoms can interact with dislocations in several ways: Elastic, Modulus, Stacking fault, Short and Long range order [27].

The first two methods are considered to be the most effective strengtheners. Elastic interaction occurs due to the difference in size of the solute atoms from the parent atoms, imposing local elastic lattice strains. Smaller solute atoms produce tensile lattice strains and larger solutes induce compressive

lattice strains. These stretch the lattice uniformly producing a symmetrical strain field around the solute. These are relatively weak compared with the asymmetric strain field produced around interstitial atoms. This is due to the symmetrical strain field not having a shear stress component and therefore not able to interact with screw dislocations [26]. Large substitutional solutes tend to segregate to the regions of tensile strain situated below an edge dislocation core whereas small substitutional solutes segregate to the region of compressive strain above the edge dislocation core. This puts the dislocation into a lower energy state reducing the overall elastic strain energy of the lattice. In order for further dislocation motion to occur an increase in stress is needed to move the dislocation to a less favourable position therefore increasing the yield stress of the material [26, 27]. The larger the atomic size difference the greater the strengthening effect, although above a size difference of ~ 15% the solubility of the solute is low and the strengthening effect is significantly reduced.

Modulus interactions are similar to elastic ones and occur when the solute atoms have different shear moduli to the parent atoms, changing the local modulus of the crystal. This imposes additional strain fields on the lattice and because of a change in shear modulus both edge and screw dislocations are hindered. The lowering of the stacking fault energy means that dislocation mobility is reduced and cross-slip onto a new plane is difficult. Thus when a dislocation meets an obstacle, there is more resistance to the dislocation movement onto a new plane to avoid the obstacle [23]. Short range order arises from the tendency for solute atoms to arrange themselves so that they have more than the equilibrium number of dissimilar neighbours. The opposite can also occur and is where solute atoms group together in the region of the lattice and is called clustering. Strengthening occurs because the movement of a dislocation through a region of short range order or clustering reduces the degree of local order. This causes an increase in the energy of the alloy and therefore additional stress must be applied to sustain the dislocation motion. Long range order interactions arise from the formation of a superlattice, which is a long range periodic arrangement of dissimilar atoms. The movement of a dislocation through a superlattice creates a region of disorder called anti-phase boundary (APB) because the atoms across the slip plane have become out of phase, there is an energy penalty associated with it [27].

1.2.2.2 Precipitation hardening

It is the precipitate γ' which provides the principal strengthening effect in these alloys. Critically the strength of γ' (Nominally $Ni_3(Al, Ti, Ta)$) increases with increasing temperature (up to ~750ºC) [28-30] and is the dominant strengthening mechanism for the alloys outstanding high temperature strength. The Ni_3Al precipitates are coherent intermetallic compounds which inhibit the dislocation motion. Movement of dislocations in a matrix containing precipitates can only take place by cutting

through or by bypassing the precipitates. There are several factors that control the effectiveness of this strengthening mechanism. These include: the volume fraction and size of the precipitate, the coherency strains between the matrix and the precipitate (due to the difference in their lattice parameters) and the anti-phase boundary (APB) energy in the presence of an ordered precipitated.

The optimal situation is for the matrix and precipitate to have the same crystal structure and very similar crystal lattices. This allows more precipitates to be packed into the matrix. The introduction of preferred positions for individual atoms increases the amount of energy required to pass dislocations through a precipitate. The movement of a planar defect through an ordered precipitate must disorder the precipitate creating an APB, since this is associated with an energy barrier a strengthening effect occurs.

The strengthening achieved increases with particle size, because it requires that dislocations cut through the precipitate. However this increase in strength with increasing particle size is limited by Orowan looping, where dislocations will bypass the particle if it is too large. The strengthening in this case is provided by the extra work needed for the dislocation to alter its path. When precipitate size is too small dislocations may pass through the crystal too easily, and the strength will be lower than optimal. Therefore precipitate size is very important. Dislocation climb is another method by which dislocations can bypass the particle. It is a high temperature diffusion controlled process whereby dislocations move out of their slip plane onto a parallel slip plane directly above or below the original slip plane. This usually occurs by diffusion of vacancies to the site of the dislocation.

At elevated temperatures cross-slipping is activated. Here the dislocation slips onto another plane to avoid the precipitate causing the formation of Kear-Wilsdorf locks. This requires greater energy input and therefore the yield stress increases and is the reason for the increase in yield stress with increasing temperature.

1.2.3 Rotor disc manufacture

High pressure rotor discs are machined from Ni-based superalloy forgings. Two methods of manufacture are historically used to create these forgings, the first and cheapest method is a cast and wrought process and the second is a more time consuming and costly powder metallurgy route.

1.2.3.1 Ingot metallurgy

The conventional cast and wrought process of manufacturing turbine disc components is typically applied in the fabrication of alloys with relatively low levels of alloying elements. This involves vacuum induction melting (VIM) to produce a cast followed by electro-slag refining and vacuum arc

re-melting in a triple-melt process. This is needed because the level of segregation is high and there is a large population of refractory particles present after VIM, so additional melts are needed to remove these impurities. The ingot then undergoes thermal-mechanical working to improve the compositional homogeneity, before undergoing a series of forging operations to produce a component close to the final desired shape [31].

1.2.3.2 Powder metallurgy

The new generation of disc alloys, of which RR1000 is one, are produced using powder metallurgy (PM). This method involves several steps, Figure 1-8, the first of which is inert gas atomisation from master melts produced by vacuum induction melting (VIM) processing. This is followed by re-melting and atomisation of the alloy. The cleanliness of this process is important as any contamination will be incorporated in the powder. This is done by pouring molten metal into a tundish with a ceramic nozzle surrounded by several gas jets. These gas jets, force a high pressured stream of inert gas, usually argon, into the molten metal which causes the formation of small spherical particles. The particles then pass through a sieve, which is used to remove any large particles or refractory material from the powder, into a can and then degased before being sealed. The can then undergoes hot isostatic pressing (HIP) before isothermal forging into shape occurs [31, 32].

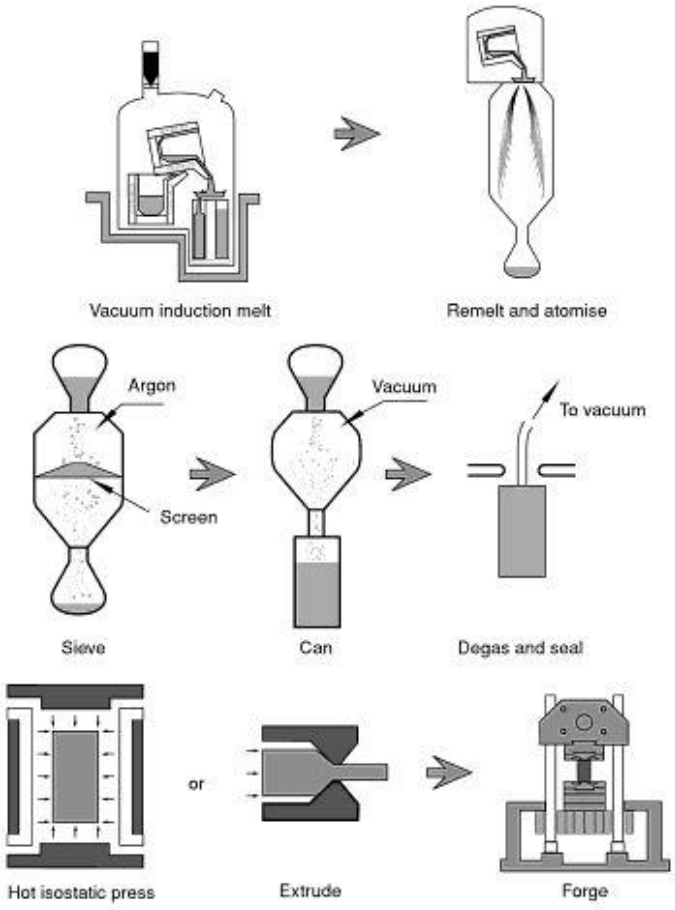

Figure 1-8: The main stages in the powder metallurgy processing route [7].

This is in contrast to the old (but more cost effective) method of cast and wrought. Powder metallurgy is needed because high levels of refractory elements can segregate during melt processing. Powder metallurgy therefore gets improved property uniformity due to the elimination of segregation and the development of a fine grain size. It also reduces the concentration of inclusions and porosity defects, although this is achieved at a greater cost and through a more complex and time consuming processing route.

1.2.3.3 Post-processing

Neither of these processing routes leaves the part completely finished. Some further processing is necessary. There are several post-process treatments either a sub or super-solvus heat-treatment usually followed by an aging treatment, which allows the microstructure (grain size, γ' volume fraction) to be controlled, through heat treatment temperatures and cooling rates.

In both processing methods, machining is necessary with the forging first being machined to a pre-specified geometry for non-destructive examination (NDE) before undergoing subsequent machining (turning and milling) until the desired shape is achieved. This leads to the mass of the final part being considerably smaller than the original forging. Powder processing produces less wastage since the geometry of the forgings can be made closer to the dimensions of the final part needed for NDE than ingot metallurgy.

Finally surface treatments like, shot-peening are often used on components before they are entered into service. It is a cold working process used to produce a compressive residual stress layer and to modify the near surface mechanical properties. Shot-peening has previously been shown to retard the development and propagation of fatigue cracks from surface regions, therefore extending component lives [33]. It entails impacting a surface with shot (round metallic, glass, or ceramic particles) with force sufficient to create surface plastic deformation. Shot-peening uses three main criteria to control the process: description of the shot used, an Almen intensity value and a percentage coverage. The Almen intensity is related to the strain energy transferred during peening and is defined by the arc height deflection of a thin metal strip, called an Almen strip (3″ x 0.75″ x 0.03-0.1″), when peened on one side. It is affected by shot size, hardness and velocity. The percentage coverage is simply the percentage of the surface that is impacted with shot. 100% coverage means the entire surface has been impacted at least once by a shot and can mean that some locations may have been impacted multiple times.

1.3 High Temperature Oxidation

Oxidation occurs when metals are exposed to elevated temperatures in the presence of oxygen. It is often defined as the loss of electrons and gain of ions which results in the formation of an oxide scale on the surface of the material. This has the potential consequence of causing a load-bearing section loss and changing the composition of the alloy. At room temperature oxidation is not a significant issue as the kinetics are so low that the effect on the component is negligible. This is not the case at elevated temperatures, where oxidation can be significant [34]. Crystal defects, surface preparative condition (stress and surface roughness), crystal orientation and impurity content are all controlling factors in the formation of oxides [35, 36]. There is no practical strategy for preventing high temperature oxidation; therefore the best long term strategy is to design alloys which minimise the rate of oxidation through the formation of a dense protective oxide layer. Thus a high temperature material needs to be able to maintain a protective layer during exposure in order to be oxidation resistant [36, 37].

1.3.1 Thermodynamics of oxidation

The thermodynamics of oxidation are an important consideration and help determine whether it is possible for an oxide to form and in an alloy which element will oxidise. A possible oxidation reaction follows the simple equation 1.1, which shows that a metal atom (M) will combine with an oxygen molecule (O) to form an oxide (MO_2) [36].

$$M + O_2 = MO_2 \quad (1.1)$$

This reaction will only take place if the Gibbs free energy change, $\Delta G°$, is negative. The more negative the Gibbs free energy change the more thermodynamically stable the oxide and the greater affinity of that element for oxygen. The oxygen dissociation pressure of oxide formation can be described by:

$$\Delta G^o = RT \ ln \ Po_2 \quad (1.2)$$

where: T is the absolute temperature, R is the molar gas constant and Po_2 is the partial pressure of oxygen. This governs the oxygen partial pressure which must be exceeded for the reaction to occur. This occurs at very small partial pressures, which are often exceeded in most basic vacuums and therefore of little consequence to the materials used in industrial and aerospace applications.

The Gibbs free energy change (ΔG°) is given by equation 1.3 [36, 38].

$$\Delta G^\circ = \Delta H^\circ - T\Delta S^\circ \quad (1.3)$$

Where ΔH° is the enthalpy change under standard conditions and ΔS° is the entropy change under standard conditions. Almost all metals oxidise because the Gibbs free energy is, in the vast majority of cases, negative (one exception is gold). The lower the ΔG°, the more stable the oxide and the lower the dissociation partial pressure. This can be seen in the Ellingham diagram, Figure 1-9, which shows the thermodynamic stability of the oxides. Neither enthalpy nor entropy vary significantly with temperature and therefore each reaction is generally a linear relationship, unless a phase change occurs and then the slope of the line will change. The oxidation reactions tend to have a positive slope, meaning that the thermodynamic stability of the oxide reduces with increasing temperature and at a high enough temperature where, ΔG° = 0, the oxide layer dissociates or does not form [36, 38]. It is important to note that the dominant oxide forming is not always the most stable oxide and depends largely on the kinetics of oxide growth.

1.3.2 Mechanisms of oxidation

High temperature oxidation of many materials results in the formation and growth of a continuous external oxide scale and often the internal oxidation of the less noble constituents of the oxidised material. It is therefore important to investigate the mechanisms to determine the reaction pathway for continued oxidation.

1.3.2.1 Adsorption

The initial stage of oxidation is the adsorption of atmospheric gas to form a monolayer on the surface of the substrate. This process occurs by both physical and chemical adsorption, requiring the attraction of oxygen molecules to the substrate via van der Waals forces and the chemical bonding of the gas to the metal surface [39]. A continuous layer is formed by lateral growth from discrete oxide nuclei. Since a growing external oxide scale separates its own substrate from the oxidising environment, once an oxide has formed, in order for it to grow, one of two conditions must be satisfied. Either oxygen ions must diffuse inward or metal ions outward through the oxide scale [36, 37, 39].

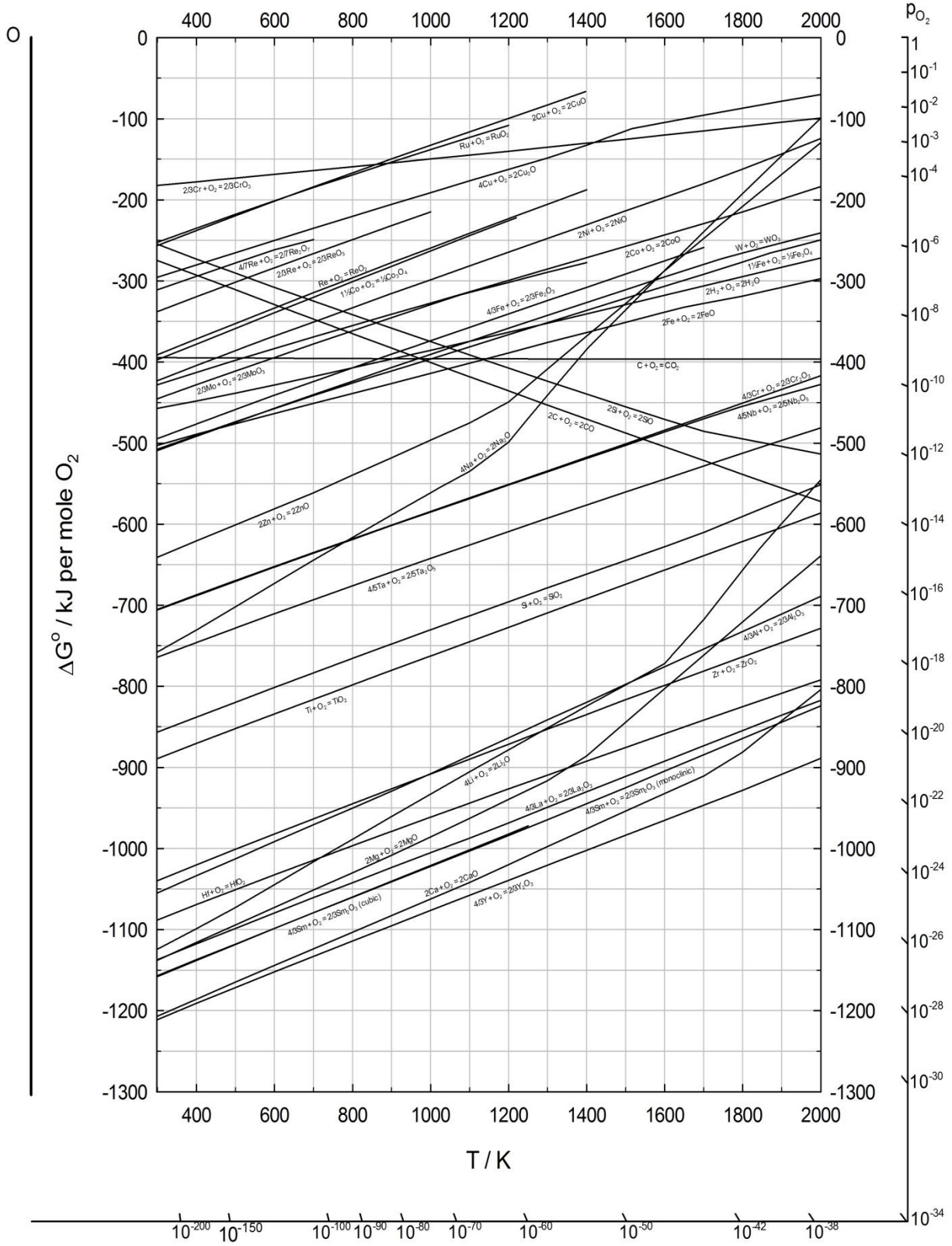

Figure 1-9: An Ellingham diagram showing the thermodynamic driving force for a number of common oxides (Courtesy of W. M. Pragnell). A change in the slope of the line indicates a phase change in the oxide.

1.3.2.2 Diffusion in metal oxides

Natural species such as metal atoms or oxygen gas cannot be transported through oxides by diffusion because they are ionic. Instead ionic species and electrons must simultaneously be transported across the oxide scale (Figure 1-10). If cation migration is dominant, the oxide will form at the oxide surface, whereas if anion migration is dominant, then the oxide will grow at the metal/oxide interface. Oxidation of a metal may proceed by diffusion of both cations and anions and the overall rate of oxidation is determined by the rate of diffusion of the ion that diffuses faster.

The migration of ions and electrons across the oxide film is controlled by the defect structure of the oxide. Several mechanisms are available to explain the transport of ions through ionic solids and these can be divided into mechanisms belonging to stoichiometric crystals and non-stoichiometric crystals. Oxides are seldom precisely stoichiometric and almost always contain an excess or deficiency in metal ions and/or a corresponding deficiency or excess in oxygen ions and in order to maintain charge neutrality a corresponding excess of electrons and/or electron holes is present. Imperfections in solids may be divided into two main groups; point defects or lattice defects, and line and surface defects. Point defects include vacancies, interstitial atoms and misplaced atoms. The line and surface defects include dislocations and grain boundaries [35, 39, 40].

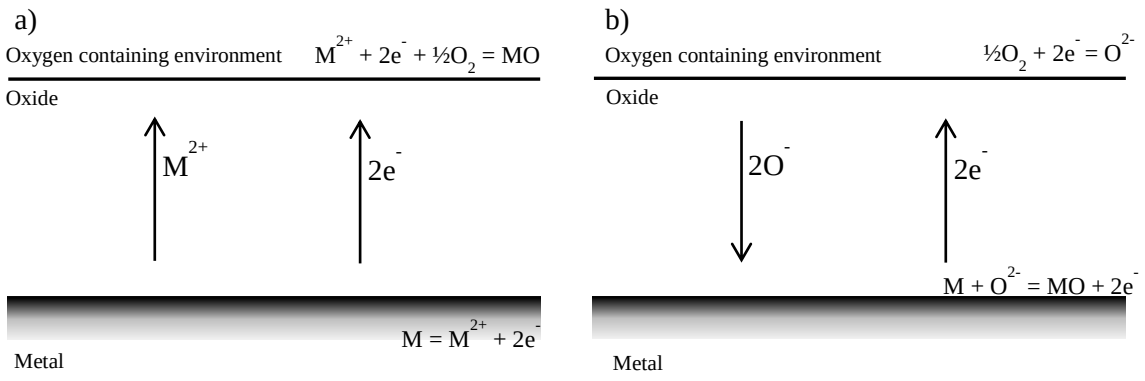

Figure 1-10: Schematic diagram of the a) cations and b) anion diffusion processes which occur during high temperature oxidation.

Point defects

There are two common types of point defects found in oxides, either oxygen (anion) defects or metal (cation) defects. Anion defects are oxides with either a deficit or excess of oxygen relative to stoichiometric condition and involve either oxygen ion vacancies or oxygen interstitials. Cation defects are oxides with either a deficit or excess of metal and occur with either metal vacancies or metal interstitials (Figure 1-11).

Oxides can be categorised as either p-type or n-type semi-conductors depending on the dominate defect structure and transport mechanism. A p-type semi-conductor is an oxide deficient in metal and either contains metal cation vacancies (V_m^{n-}) or oxygen interstitials (O^{2-}) and a n-type semi-conductor is an excess metal oxide containing either oxygen vacancies (V_o^{2+}) or interstitial cations (M^{n+}). Electro-neutrality of the system is achieved with the inclusion of an electron hole or an excess electron respectively. Metal cations and oxygen anions diffuse through the lattice by exchange with these cation or anion vacancies. The process is thermally activated as an energy barrier is associated with each exchange [36, 39, 40].

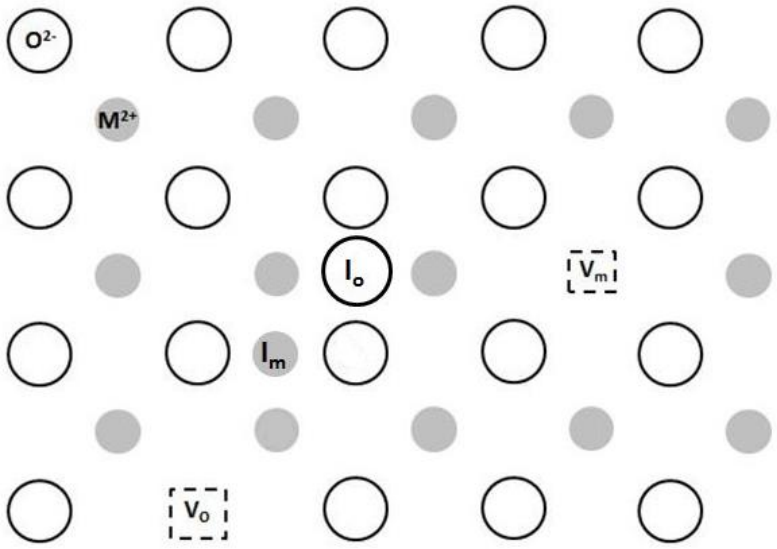

Figure 1-11: Intrinsic point defects of a MO oxide. V_m = cation vacancy, I_m = cation interstitial, V_O = anion vacancy, I_o = anion interstitial, M^{2+} = self-interstitial cation and O^{2-} = self-interstitial anion.

Dissolved impurity and dopant atoms are also considered as point defects. If the dopant ions have a valency different from those of the base ions of the oxide and are present in sufficient concentrations their primary effect on the defect structure and defect concentrations is to influence the charge neutrality of the system. Dopant elements with a higher charge than that of the dominant cation create a positive charge imbalance which is countered by the production of cation vacancies that have an effective negative charged associated with them. Dopants with a lower charge replace cation vacancies and pair electron holes in order to maintain charge neutrality [40]. This is the case with Ti in chromia, and has been reported that Ti is incorporated as a Ti^{4+} ion, which while having minimal effect on the chromia lattice spacing even at higher dopant levels [41], increases the concentration of chromium vacancies [42, 43] leading to a corresponding increase in the oxidation rate through enhanced diffusion rates of chromium ions across the oxide layer [44].

Line and surface defects

Line and surface defects such as dislocations and grain boundaries can provide faster short circuit diffusion pathways. As temperature decreases short circuit diffusion dominates because the activation energy required for lattice diffusion is higher, because lattice diffusion can only occur via vacancy exchange. In the case of grain boundaries it is the local lattice mismatch between grains which gives rise to increased diffusion rates [35, 40], as there is a lower energy barrier due to a more favourable diffusion path. This occurs because of the increased space and disorder in between the grain boundaries. As the grain boundary misfit increases, the space and disorder in between the boundaries increases and therefore the more favourable the diffusion pathway becomes. One consequence of the presence of these short circuit diffusion pathways is that the mobility of both anions and cations can be increased leading to higher rates of diffusion and therefore a quicker oxidation rate.

1.3.3 Kinetics of oxidation

Most oxides are more thermodynamically stable than their metal in oxidising environments (Figure 1-9); the issue is not whether oxidation will occur but rather the kinetics of the reaction. As the temperature increases so does the rate of ion transport resulting in increased oxidation kinetics [36]. The reaction product from an oxidation reaction will generally act as a barrier between the metal surface and the environment which often slows the rate of the reaction. In general the kinetics of high temperature oxidation can be described by one of three regimes: Linear, Parabolic, Cubic (Figure 1-12). In reality oxidation on a clean metal surface occurs initially according to a linear law [37]. Once the surface is covered by an oxide layer one of the other laws dominates depending on the properties of the formed oxide layer. A protective oxide layer is dense and slow growing thus controlling the transport of oxidants across the barrier. Examples of elements which form such oxides are Si, Al, Cr [36, 37]. The kinetics of oxidation can be reasonably described by the following equation:

$$\left(\frac{\Delta m}{A}\right)^n = k_n\, t \tag{1.4}$$

Or

$$\xi^n = k_n{}'\, t \tag{1.5}$$

where $\left(\frac{\Delta m}{A}\right)$ is the mass change/surface area (mg.cm^{-2}), ξ is oxide thickness (μm), t is exposure time (seconds) and k_n is the rate constant for mass gain data and k_n' is the rate constant for thickness data.

The value of n can be determined by plotting log $\left(\frac{\Delta m}{A}\right)$ (or log ξ) against log t and describes the oxide growth regime with the majority of cases it being approximated to 2, assuming parabolic growth kinetics according to Wagner's theory of parabolic oxidation [45]. In reality many systems do not follow Wagner's theory exactly because one or more assumptions are not met. This is particularly true during the initial stages of oxidation where a transient period of faster kinetics can occur leading a modification to Wagner's model [46].

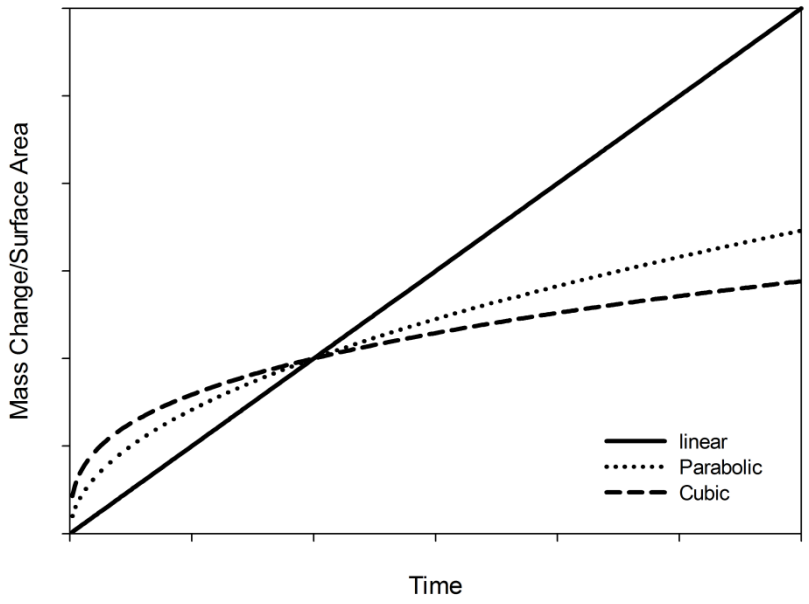

Figure 1-12: Relationship between different oxide growth regimes for oxidation kinetics.

An Arrhenius Equation (Equation 1.6) can be used to calculate the activation energy for the formation of the oxide.

$$k_n = k_o \exp\left(\frac{-Q}{RT}\right) \quad (1.6)$$

where Q is the activation energy for oxide growth (J.mol^{-1}), k_o is the pre-exponential constant, R is the gas constant, T is the exposure temperature (K).

1.3.4 Oxidation of alloys

The mechanism of oxidation of alloys is more complex than for pure metals as alloys generally contain two or more oxidising elements. As a result the oxide scales on alloys will not contain the same relative amounts of the alloy constituents as the alloy does, as this depends on the thermodynamic stabilities of the oxides and the relative diffusion rates of reacting atoms through the oxides and within the alloy. Therefore both the thermodynamics and kinetics affect the oxides formed. Throughout the oxidation process the composition and structure of oxide scales on alloys will often

change. As pure metals are rarely used in the manufacture of structural components, an understanding of the oxidation of alloys and particularly the methods to achieve oxidation resistance is of great importance. There are several main types of oxide formation in alloys: selective oxidation, mixed or complex oxide scales and internal oxidation (covered in more detail in 1.3.5).

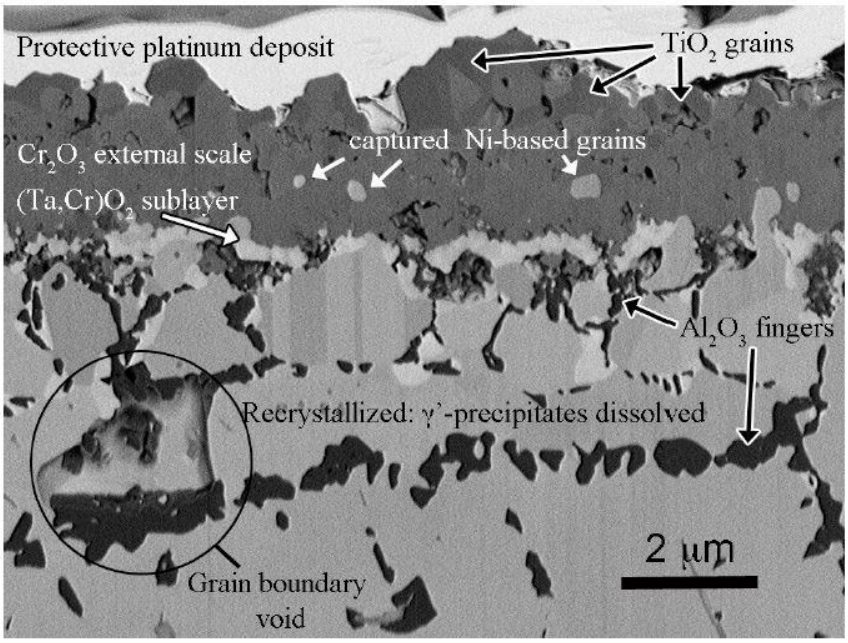

Figure 1-13: Selective oxidation of Ni-based superalloy, ME3, oxidised in air at 815°C for 2020 hours, showing selective oxidation of Cr_2O_3 externally with internal oxidation of Al_2O_3 [47].

Selective oxidation occurs in alloys, in which a solute oxidises preferentially to the parent element of the alloy, as is often the case in Ni-based superalloys (Figure 1-13), where chromium or aluminium can oxidise to form a semi-protective scale of Cr_2O_3 or Al_2O_3. This can have the effect of allowing protective oxide scales to form on alloys that would otherwise produce a non-protective oxide scale, although selective oxidation to form a protective layer will only occur above a critical concentration of the active alloying elements. Much work is directed towards finding alloys which have the required mechanical properties while also forming one of the common protective scales. Mixed oxide scales are similar in that selective oxidation occurs of two or more alloy constituents leading to a composite or layered oxide scale. Furthermore complex oxides can occur when oxides of the alloying components react with each other to form a more stable oxide (double oxides or spinels). In multi-component alloys a mixture of selective oxidation, mixed or complex oxides and internal oxidation can occur.

1.3.4.1 Formation of protective oxides

Oxidation-resistant alloys are those in which the ions diffuse slowly through the oxide scale. If the diffusion is slow, then the oxide scale will grow slowly and providing it remains intact, will act as a

protective layer. The oxides that have the lowest diffusion rates, and hence most likely to form the best protective layers are chromia (Cr_2O_3), alumina (Al_2O_3) and silica (SiO_2). Figure 1-14 shows the temperature dependence of the parabolic rate constants for chromia, alumina and silica amongst other non-protective oxides, illustrating that these are the slowest growing oxides. In order for a scale to remain protective, in addition to ion/oxygen transport through the scale, the diffusion of the oxidising element within the alloy towards the oxide/alloy interface is required to occur at a quick enough rate to avoid the oxide becoming thermodynamically unstable and dissociating. In general, for prolonged service under isothermal conditions Cr_2O_3 scales provide protection up to a maximum of 900^{o}C, Al_2O_3 to 1400^{o}C and SiO_2 to around 1700^{o}C [48].

Chromia (Cr_2O_3)

Chromia is very important as a protective passive oxide scale and is the oxide of choice for Ni-based superalloys used in rotor disc applications. Chromia is thermodynamically stable and has a minimal deviation from perfect stoichiometry. This causes the rates of metal and oxygen diffusion across the oxide scale to be sufficiently low that the oxide grows at an acceptably slow rate, leading to a protective oxide scale. Figure 1-14 shows the large improvement in oxide growth rate that chromia has over Ni and Co oxides. Although above 900°C Cr_2O_3 reacts further with oxygen to form a volatile species (CrO_3) leading to the loss of the protective scale [36, 49]. Chromia is also the oxide of choice for providing protection against type II hot corrosion [36]. The overall development of a chromia scale on alloys is dependent on the thermodynamics and kinetics of the possible oxides formed. Often transient oxides can form initially (e.g. NiO in Ni-Cr alloys) before a healing layer of chromia is formed underneath. The alloy chromium concentration largely determines whether chromia forms as an internal precipitate or as an external scale [50], with typically >12 wt.% required to form a protective surface layer in most Ni-Cr and Ni-Cr-Al alloys [51]. The larger the concentration of chromium the quicker a continuous chromia layer will be established externally [51]. Once a continuous external surface chromia layer has been established, oxidation of chromium is considered to occur by the reaction [52]:

$$2Cr^{3+} + 6e^{-} + \frac{3}{2}\,O_2\,(g) \leftrightharpoons Cr_2O_3 \qquad (1.7)$$

Transport of Cr^{3+} ions to the scale-gas interface occurs and a reaction with oxygen take place leading to new oxide being formed on the outer surface of the chromia layer. While growth is dominated by the transport of chromium ions across the growing oxide scale the contribution from inward transport of oxygen cannot be neglected [53]. The oxidation rates of chromia on a number of alloying systems have been extensively studied and have been found to vary considerably [54]. This has been attributed to numerous factors [52]: formation of volatile chromium rich oxides, short-circuit diffusion paths in

the alloy and scale, the purity of the metal, impurity doping of the scale [55] and differences in exposure techniques.

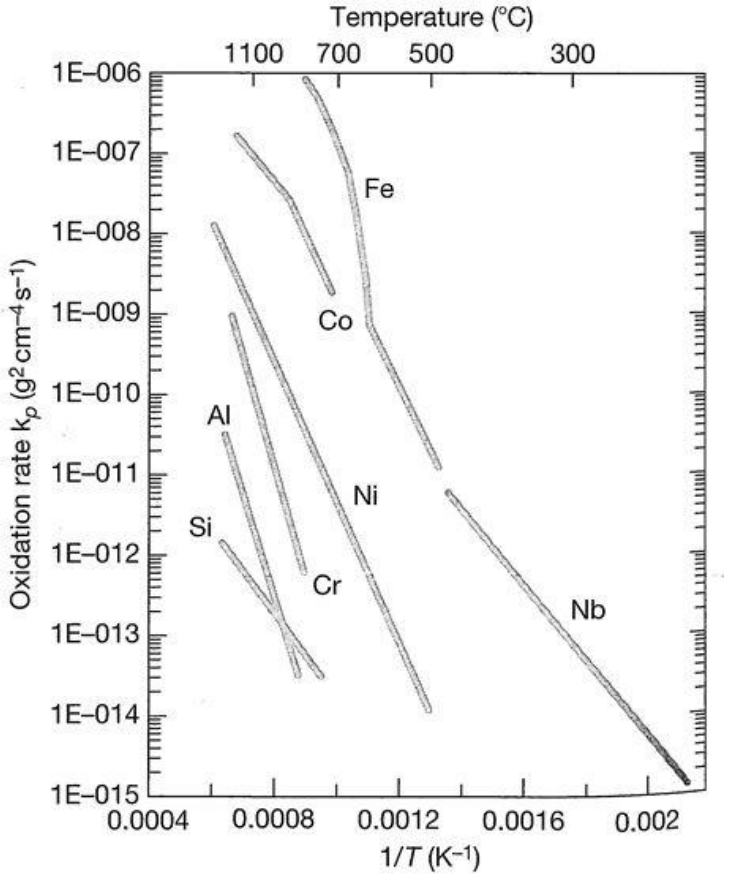

Figure 1-14: The temperature dependence of the parabolic rate constant of the oxides formed on several metals, with more than one oxide forming on Co, Nb and Fe and a single oxide on the rest, Cr_2O_3, NiO, Al_2O_3 and SiO_2 taken from [56].

Alumina (Al_2O_3)

Alumina is the oxide of choice for high temperature environments (>900°C), as the transport processes are significantly slower than in a Cr_2O_3 scale. This can be seen in Figure 1-14. Alumina is such an attractive oxide that not only does it form on alloys with sufficient aluminium to form a continuous scale but is induced in other alloys by applying an aluminium rich coating. The stoichiometric phase α–Al_2O_3 is the most stable form of aluminium oxide and it exhibits very low concentrations of both ionic and electronic defects. The other two thermodynamically stable forms are γ–Al_2O_3 and θ-Al_2O_3. These tend to be metastable transient oxide phases which transition to stable α–Al_2O_3, leading to a reduction in oxidation rate. α–Al_2O_3 grows predominately by inward oxygen transport although a small amount of outward transport of Al^{3+} ions occurs. The oxide scale is then formed on the oxide/alloy interface [57]. The addition of chromium (15%) to the alloy has been shown to facilitate the establishment of an Al_2O_3 scale on alloys with low aluminium concentrations (<10%) [58]. In the case where there is insufficient aluminium for a protective external oxide scale to

develop then internal precipitates can form underneath a non-protective or protective chromia oxide scale.

Silica (SiO_2)

Silica is an attractive choice for high temperature oxide regimes since it again exhibits a minimal deviation from stoichiometry and therefore forms a very effective diffusion barrier. SiO_2 tends to grow more slowly than both Al_2O_3 and Cr_2O_3 due to its extremely low growth rates and near perfect stoichiometry (Figure 1-14). Small additions of Si to chromia forming austenitic stainless steels have been shown to improve oxidation performance via the formation of a thin interlayer between the substrate alloy and the chromia scale [59, 60]. In Cr containing alloys, silica takes much longer to develop a continuous healing layer than Al_2O_3 via the coalescence of internal oxides [61]. This leads to considerably more transient oxide, Cr_2O_3, forming initially [61]. Stott et al. (1995) suggested this was because the relative Gibbs free energies for both Cr_2O_3 and SiO_2 are closer together than Cr_2O_3 and Al_2O_3, leading to a reduction in internal silica formation [61]. The addition of Si to Fe-, Co- and Ni-based alloys tend to have a detrimental effect on the mechanical properties of the alloy and so SiO_2 is not utilised to its full potential [56].

1.3.4.2 Phase dissolution

It is often preferable to promote the selective oxidation of a single element from an alloy in order to produce a slow growing protective oxide scale. However selective oxidation of one element necessarily depletes the near surface region of the alloy of that element, leading to the production of a solute depletion profile. If the depletion profile produces a concentration below that needed to maintain the formation of a precipitate then a precipitate denuded zone can form in the region immediately below the surface oxide (Figure 1-15). This is the case in a number of alloying systems with Ni-based superalloys and steels being two of them. The extent of depletion of an element being selectively oxidised depends on a number of factors, it's concentration, rate of scale growth, the precipitate dissolution speed and alloy inter-diffusion coefficient. If the alloy is depleted below the concentration that will allow diffusion in the alloy to provide a sufficient amount of the oxidising element to the alloy interface to maintain the protective oxide, then failure of the protective oxide can occur in a process called chemical failure (discussed in section 1.3.6).

Chromium carbide dissolution has been shown to occur in both chromia forming steels and superalloys. It occurs due to the selective oxidation of chromium and the dissolution of the chromium carbides in order to replenish the chromium loss leaving a particle free zone in the near surface region [62-65]. The carbide dissolution increases the carbon content in the matrix and the chromia scale prevents the carbon from leaving. Therefore carbon diffuses into the centre of the alloy due to a

concentration gradient and an increase in volume fraction of carbides occurs there [62, 64-66]. Phase dissolution of γ′ is commonly found in Ni-based superalloys used for both turbine blades [67] and rotor discs [47]. In the both cases it is due to aluminium depletion causing the dissociation of γ′ particles (Ni_3Al). In the former instance this is due to the formation of a protective external scale of alumina and in the latter through the formation of significant internal alumina precipitates.

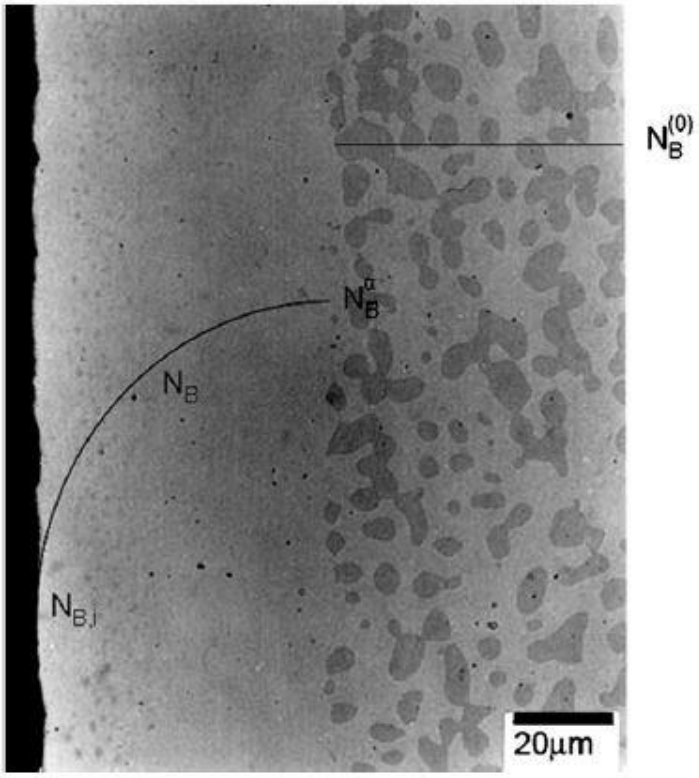

Figure 1-15: Phase dissolution of B in a two phase alloy AB exhibiting selective oxidation of a Ni-Si alloy [68].

1.3.4.3 Protrusions into oxide scale

Protrusions are seen in a number of alloying systems: Ag-In, Ag-Pd-Sn-In, Steels, and a range of Ni-based alloys [60, 68-74]. These result in the formation of a non-planar metal/oxide interface (Figure 1-16) and are normally comprised of matrix phases that have been depleted of the oxidised elements.

There are several proposed mechanisms by which this process can occur. This morphology may have developed as a result of undercutting by oxide formation where selective oxidation of a γ′ particle occurs leaving the γ channels unaffected and therefore leaving the matrix encapsulated or protruding into the oxide [75]. Furthermore a model for the formation of protrusions in chromium containing steels was produced and stated that these undulations were produced by the heterogeneous internal oxide growth [60, 76].

Alternatively actual protuberances may have developed with matrix metal being pushed up into the oxide scale, since the processes of internal oxidation result in significant compressive stresses being developed in the near surface metal matrix. These stresses develop from the increased volume of the oxide compared with the metal matrix. In relieving these compressive stresses the formation of these protrusions can occur. Several mechanisms have been proposed for their formation and revolve around outward alloy creep to accommodate the increase in volume resulting from internal particle formation and the associated compressive stresses [70, 73, 75, 77]. Similar mechanisms have been proposed for internal nitridation [72, 78] and carburisation [71].

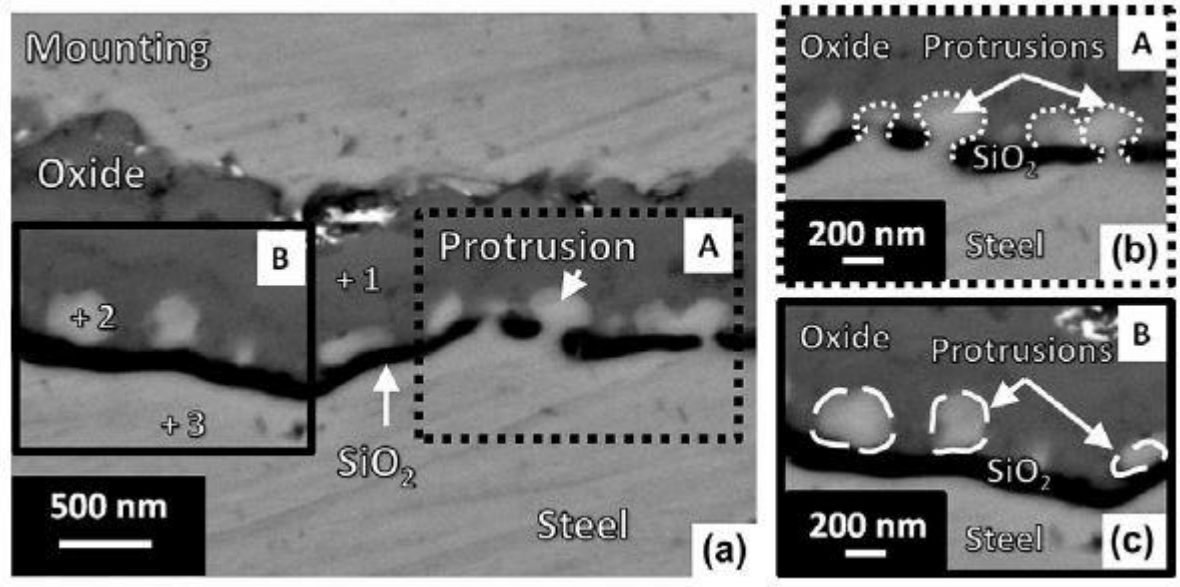

Figure 1-16: BSE image of a cross-section through 441 ferritic steel oxidised at 1060°C for 60 seconds, illustrating protrusion formation [60].

Mackert et al. [74] reported that in Ag-Pd-Sn-In alloys the outward material transport of silver and palladium to form protrusions was caused by the volume increase of internal oxides and proposed that this occurred due to Nabarro-Herring creep. This was backed up by a study performed in Ni-Al and Ni-Al-Si in which outward transport of Ni occurred at >900°C [79]. Alternatively grain boundary sliding acted as the stress relief mechanism with extrusion of the matrix occurring adjacent to the grain boundaries forming protrusions at the surface in similar Ni-Al alloys [80]. Protrusions have even been attributed to external scale failure [77].

1.3.5 Internal oxidation

Internal oxidation is the process in which oxygen diffuses into an alloy and causes sub-surface precipitation of an oxide of one or more elements in the alloy. It can occur in the absence of or underneath an external oxide layer. Internal oxidation is not desired because it changes the optimised

mechanical properties of the alloy, which can result in internal stresses, elemental depleted zones and compositional changes. The presence of brittle ceramic oxide phases, sub-surface, can also be detrimental to the mechanical properties of the component and can act as crack initiation sites. The following conditions must be met in order for internal oxidation to occur [36]:

- The free energy (ΔG^o) of formation (per mole of oxygen) for the solute metal oxide in the bulk alloy must be more negative than the ΔG^o of formation (per mole of oxygen) of the lowest oxide of the base metal.
- The ΔG^o of formation for the reaction of dissolved oxygen and solute element must be negative and the base metal must have a solubility and diffusivity for oxygen which is sufficient to achieve the required activity of dissolved oxygen at the reaction front.
- The solute concentration of the bulk alloy must be lower than that required for the transition from internal to external oxidation.
- No surface layer must prevent the dissolution of oxygen into the alloy.

If these last two conditions are not met then internal oxidation cannot occur [55]. It requires the rate of diffusion of oxygen in the alloy to be appreciably faster than that of the alloying element, in this case where no surface oxide layer is present. If this condition is satisfied then an oxygen gradient is established in the alloy and the dissolved oxygen will react to form oxide of the less noble alloying element in a zone beneath the alloy surface. The internally oxidised zone extends to a depth at which the concentration of dissolved oxygen becomes too small for the formation of the oxide. The rate of internal oxidation is generally found to be diffusion controlled and the depth of the internal oxidised zone can be described by [36]:

$$\xi_I = \left(\frac{2\, N_o^{(s)} D_O}{v\, N_m^{(o)}}\, t \right)^{\frac{1}{2}} \tag{1.8}$$

where ξ_I is the internal oxidised zone depth, t is time, D_o is the self-diffusion coefficient of oxygen in the alloy, $N_o^{(s)}$ is the oxygen solubility in the substrate, $N_m^{(o)}$ is the mole fraction of oxidising element (M) in the un-oxidised alloy and v is the number of oxygen atoms per M atom in the precipitated oxide and depends on the stoichiometry of the oxide formed. This give the depth of internal oxidation as a function of time, it is also worth noting:

- The penetration depth has a parabolic time dependence, ξ proportional $t^{½}$
- The penetration depth for a fixed time is inversely proportional to the square root of the atom fraction of solute in the bulk alloy

- Careful measurement of the front penetration as a function of time for an alloy of known solute concentration can yield a value for the solubility-diffusivity product, for oxygen in the matrix metal.

Additionally there are several limitations with this approach in that it is not valid where an external oxide scale is present nor when significant counter diffusion of the oxidising element is occurring. Finally it is assumed that the internal oxide precipitates do not affect the inward diffusion of oxygen, whereas in most practical cases they act as diffusion barriers. In most practical applications of high temperature alloys, internal oxides form beneath an external oxide scale. Rhines et al. [81] and Maak [82] calculated an expression for internal oxide growth in combination with a parabolically growing external scale. Assuming that the shift in the metal/oxide interface is given by:

$$X^2 = 2\,k_p'\,.\,t \tag{1.9}$$

where X is the position of the metal/oxide interface at time t, k_p' is the parabolic rate constant for the external oxide. The product N_oD_o can be calculated:

$$N_oD_o = N_m^o\,v\,\frac{\xi\,(\xi - X)}{2\,t}.\frac{1}{F\left[\xi/2(D_m\,t)^{1/2}\right]} \tag{1.10}$$

where N_m is atomic fraction of the oxidising element, D_m is diffusivity of oxidising element (M) and F (auxiliary function) is described by:

$$F(u) = \pi^{1/2}\,u\exp(u^2)\,\mathrm{erf}\,C\,u \tag{1.11}$$

in which u:

$$u = \left(\frac{k_p}{2\,D_m}\right)^{1/2} \tag{1.12}$$

Again while more complex that equation 1.8, there are still limitations with this approach, with it specifically requiring a parabolically growing external oxide scale, assuming that half this scale equates to an inward shift of the metal/oxide interface, as well as again assuming the internal oxide precipitates do not affect the inward diffusion of oxygen. Internal oxidations influence on the mechanical properties of the alloy is related to the morphology of the internal oxide precipitates. The oxide precipitate size is determined principally by a competition at the reaction front for solute atoms between the rate of nucleation of new precipitates and the subsequent growth of existing precipitates.

The size of internal oxide precipitates can be determined by a number of factors: deeper penetration fronts, higher solute concentrations, lower oxygen solubility, higher temperature, higher particle-matrix interfacial free energy and less stable oxides will favour larger precipitates forming [36, 83]. There are two types of precipitates, intragranular and intergranular. Intergranular penetrations form along the grain boundaries or other similar microstructural features, whereas intragranular form at the reaction front in a uniform manner [84]. There are several phenomena which deviate from the assumptions made in Wagner's theory for internal oxidation [36, 85]. These include:

- Preferential formation of internal oxides on alloy grain boundaries, often with precipitate denuded zones adjacent as grain boundaries act as short-circuit diffusion pathways.
- Extrusion of parent metal from the internal oxidation zone to form pure metal nodules on the surface.
- Alternating bands of internal oxide particles running parallel to the specimen surface.

The shape of internal oxide precipitates has been shown to vary over a wide variety of possible morphologies (spherical, sheets, rods) depending on the interfacial energies, strain energy and the velocity of the advancing reaction front [85]. A more comprehensive review of internal oxidation is provided by Rapp (1965) [83].

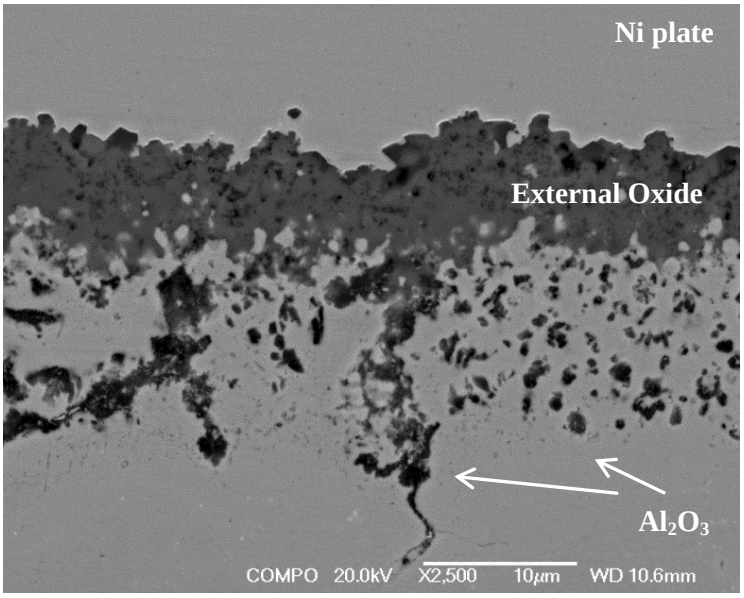

Figure 1-17 : BSE image showing extensive internal formation of Al_2O_3 in a Ni-based superalloy oxidised in laboratory air at 800°C for 2000 hours.

1.3.5.1 Transition from internal to external oxidation

Transition from internal to external oxidation occurs when the concentration of the less noble alloying element is increased above a critical value. This leads to the alloy no longer being oxidised internally but results in the formation of an external oxide scale of the less noble element. Wagner proposed that the transition occurred when the internal oxide particles reached a critical volume, which blocks further reaction between the oxygen atoms and the solute atoms by reducing the cross-section available for oxygen diffusion towards the reaction front [45]. A couple of additional factors can affect the transition by increasing the outward flux of the less noble element and include cold work (by increasing short circuit diffusion pathways) and the presence of a second solute whose oxide has a stability between the main alloying element and the less noble internally oxidised element. Giggins and Pettit (1971) [86] used the Ni-Al-Cr alloying system to experimentally produce ternary oxidation diagrams for oxide formation at 1000^{o}C-1200^{o}C.

Figure 1-18 shows the different oxides formed on these ternary alloys, which are the same as most Ni-based superalloys, in that they form a non-protective NiO external scale with subsurface Al and Cr rich oxide at low concentrations of Al and Cr (Figure 1-19(a)), a Cr_2O_3 external scale with subsurface Al_2O_3 at moderate concentrations of Cr (>12%) and low Al contents (<5%) (Figure 1-19(b)) and a continuous layer of Al_2O_3 at higher Al contents (Figure 1-19(c)). These are shown in Figure 1-18 as region I, II and III respectively. Figure 1-19(d) also shows the compositional space of Ni-based superalloys and includes chromia forming Ni-based superalloys, RR1000, ME3 and Udimet 720 [87].

It must be acknowledged that chromia forming rotor disc alloys are not designed for these high temperatures, with operational limits of <800^{o}C but it shows in principle that these alloys have borderline amounts of Cr and Al to form protective oxide scales. The external formation of the less noble element at lower concentrations can occur if the partial pressure of oxygen (PO_2) is great enough to form the oxide of the second solute thus decreasing the inward flux of oxygen. This is useful in the design of high temperature alloys as the elements which provide protection by selective oxidation (Cr, Al, Si) often have detrimental effects on the mechanical properties of the alloys and therefore this process known as secondary gettering allows these elements to be kept as low as possible [36, 39, 83]. In these Ni-Al-Cr alloys, the oxide formed was determined by the alloy composition and the volume fractions of Cr_2O_3 and Al_2O_3 precipitated internally within the alloy. Transition from a non-protective NiO oxide occurs when the volume fraction of internal Al_2O_3 and Cr_2O_3 reached a level that was sufficient to inhibit the diffusion of oxygen into the alloy but permitted enough to oxidise Al or Cr [86].

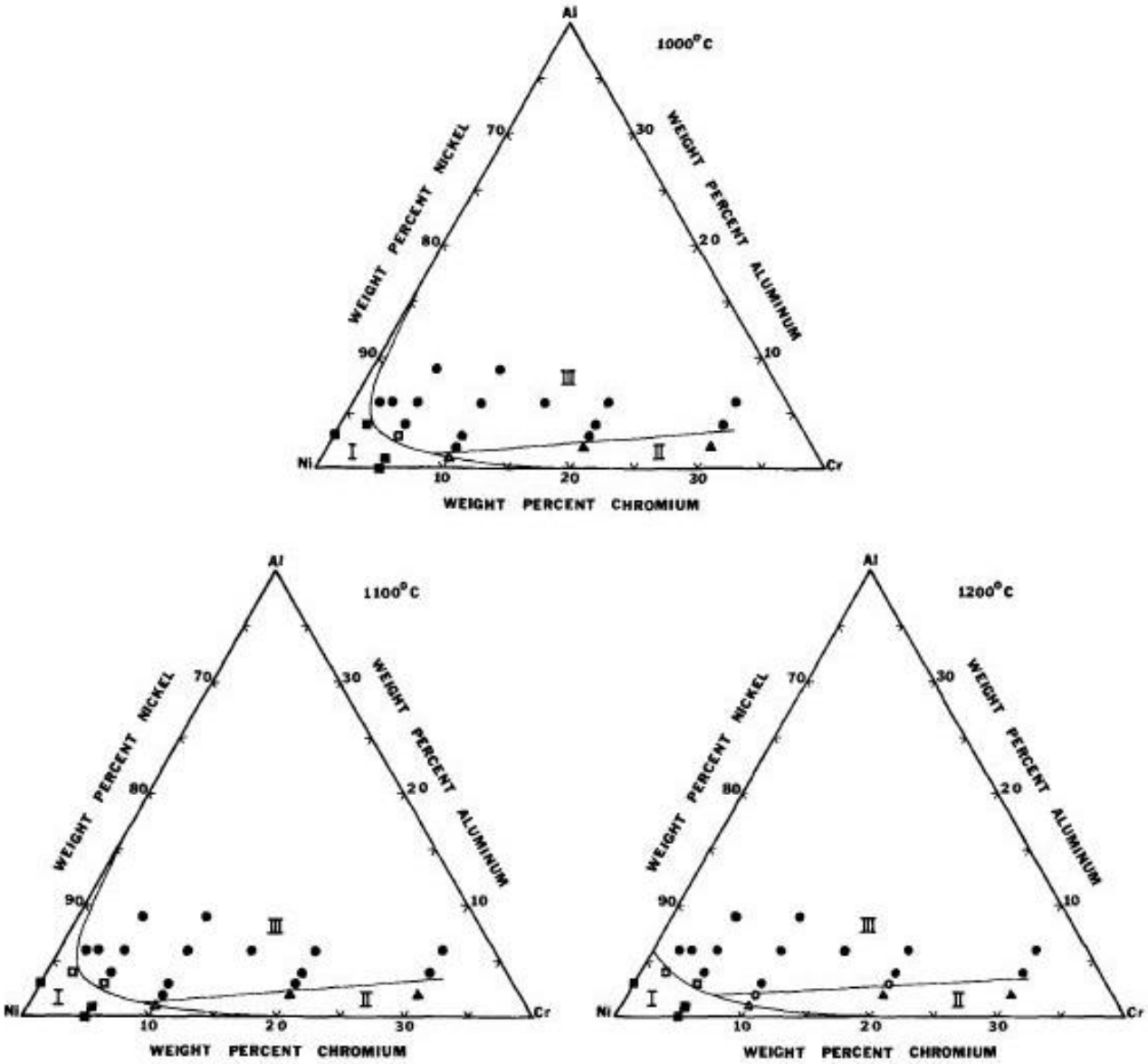

Figure 1-18: Ternary diagrams showing the composition limits for the three oxidation mechanisms of Ni-Cr-Al alloys in 0.1 atm of oxygen and at 1000-1200°C [86]. Region I is NiO external scale and subsurface Cr or Al rich oxide, region II is Cr_20_3 with subsurface Al_2O_3 and region III is a continuous external Al_2O_3 layer.

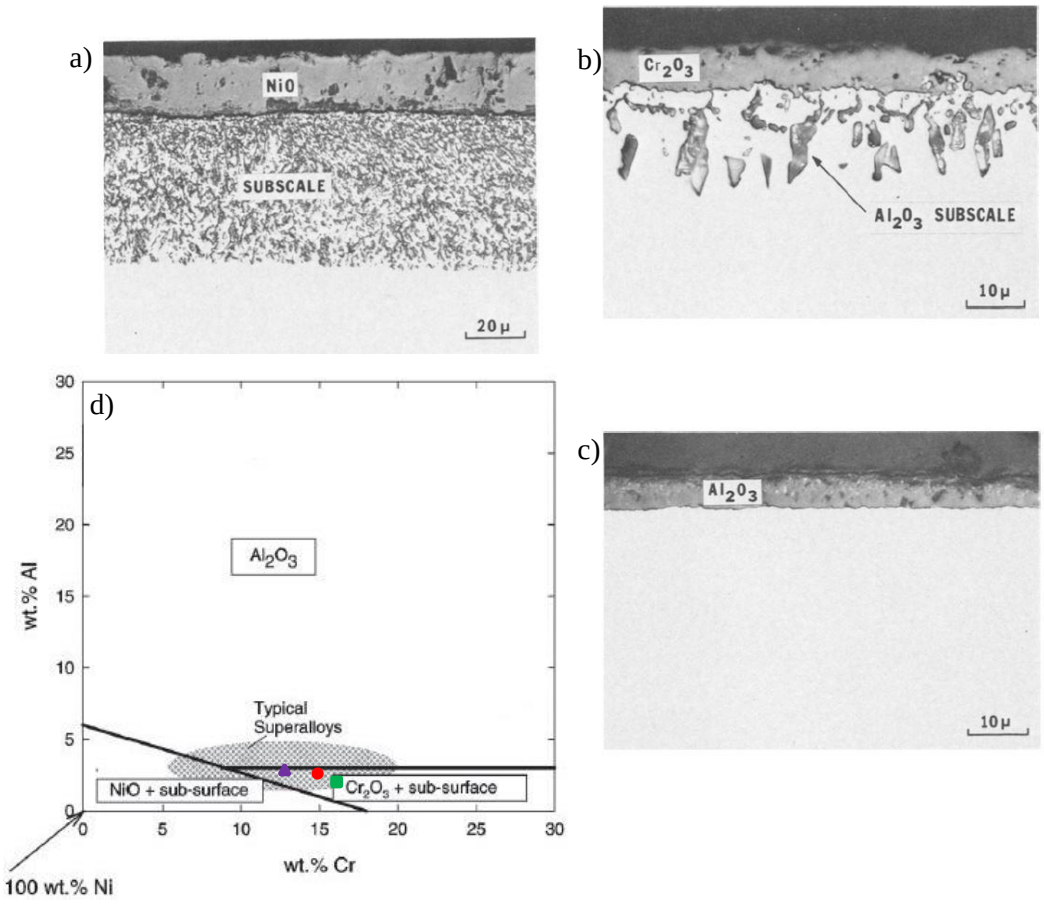

Figure 1-19: a) Region I showing an external scale of NiO and subsurface Cr or Al rich oxide, b) Region II showing an external Cr_2O_3 scale with Al_2O_3 subsurface, c) Region III showing a continuous Al_2O_3 scale. d)A schematic map, based on experimental data from Giggins and Pettit (1971), showing the type of oxide formed, adapted from [87] to include chromia forming Ni-based superalloys, RR1000 (red dot), ME3 (purple triangle) and Udimet 720 (green square).

1.3.6 Chemical failure/breakaway oxidation

Chemical failure was originally seen in chromia forming austenitic steel (20Cr- 25Ni) and can arise where the long term protection of alloys during high temperature exposure relies on the formation of a dense oxide layer produced by selective oxidation [88]. Chemical failure occurs when the oxide layer can no longer be replenished due to a lack of the protective oxide forming element diffusing upwards towards the surface. This is due to either a diffusion barrier stopping the oxidising element diffusion to the surface or a depleted zone of the oxidising element. There are two types of chemical failure: mechanically induced chemical failure (MICF) and intrinsic chemical failure (InCF). Mechanically induced chemical failure occurs if the protective oxide layer was to spall or crack and the solute concentration of the oxidising element is too low to re-form the protective layer, leading to the formation of a non-protective oxide scale. The other method, intrinsic chemical failure, occurs when the oxide layer is adherent and the oxidising element (often a minority constituent of the alloy) that

forms a protective layer becomes progressively depleted as the oxide scale increases in thickness. Once the alloy is sufficiently depleted of the oxidising element, the oxide layer becomes thermodynamically unstable and can be reduced by other elements to form less protective oxide scales. Once chemical failure occurs it then leads to potential failure through breakaway oxidation, where a non-protective oxide layer forms rapidly and leads to rapid section loss of the component [88].

Breakaway oxidation can occur in two ways, depending on the oxidant depletion profile. If the depletion profile is localised, this attack will be halted by the formation of another protective oxide layer underneath. The process will then be repeated and breakaway oxidation occurs again. The other is when the depletion profile is across the entire section thickness of the component and is depleted below the concentration needed to re-form the protective oxide layer. If this occurs the component will quickly undergo rapid section loss leading to potential failure, a depleted profile of a single element can also cause a phase change in the alloy therefore affecting the mechanical properties of the component. Section thickness of the component is therefore important in both types of chemical failure, in that it determines the amount of the oxidising element in reserve. The thicker the section the larger the reservoir of the oxidising element and, due to the parabolic nature of oxidation, the longer the exposure time before significant elemental depletion occurs. Another important factor is the oxidising element's diffusion kinetics as fast diffusing element will ensure that the protective layer is maintained until the section becomes entirely depleted. This has been recorded in an alumina forming Ni-based superalloy, with a CoNiCrAlY bond coat and thermal barrier coating (TBC) system, where depletion of aluminium occurs leading to intrinsic chemical failure and breakaway oxidation of the component at the bond coat/TBC interface. The increase in volume due to breakaway oxidation leads to failure of the coating [89].

1.3.7 Stresses in oxide scales

At high temperatures most alloys rely on a protective oxide scale, in which failure through cracking or spallation would be detrimental and enhance degradation of the component. Under most service conditions components experience significant stresses which can originate from a number of sources: through external loads, oxide growth stress, large temperature changes and gradients or through geometric constraint. All these stresses have to be accommodated by elastic or plastic deformation or through creep of either the metal or oxide. Once a critical value of stress or strain is reached and exceeded, mechanical failure of the scale can ensue. This is also a stress relief mechanism but can however have the effect of removing adherent protective scales, which can be lost unless restored by a scale healing mechanism [35].

1.3.7.1 Growth stresses

The growth stresses arising from external oxide growth are beyond the scope of this project and are covered in detail in the following texts/reviews [90-92]. Significant stresses can be generated internally from the formation of internal oxides where the increase in volume when one mole of alloy is internally oxidised can be estimated [93]:

$$V = V_{alloy}\,(1 - N_m^o) + N_{ox}^o \tag{1.13}$$

where V is the total volume when one mole of alloy is internally oxidised, V_{alloy} is the molar volume of the alloy, N_{ox}^{o} is the volume of oxide formed from one mole of solute atoms, N_m^{o} is the molar fraction of metal solute atoms in the alloy. Hence the increase in volume ratio (V_{ratio}) is:

$$V_{ratio} = \frac{V - V_{alloy}}{V_{alloy}} \tag{1.14}$$

It would be expected that an increase in volume due to internal oxide would result in significant compressive stresses being generated within this internally oxidised region. As described previously one mechanism of accommodating this stress is the outward extrusion of matrix metal leading to protrusion formation on the surface.

1.3.7.2 Thermal stresses

The change in temperature during cooling (or heating) of an oxide and substrate can lead to the development of considerable mechanical stresses. This occurs because of the mismatch in the thermal coefficient of expansion between the parent alloy and oxide scale, this is especially the case when there is a mixed oxide scale. The thermal coefficients of expansion for the oxide are in most cases lower than those of the substrate metal and therefore compressive stresses will develop in the oxide upon cooling. When the stress can no longer be accommodated within the scale, cracking or spallation of the oxide scale will occur. This generally makes the presence of thermally cycled exposures much more damaging than isothermal exposures, as well as being a more realistic representation of in-service conditions. In most cases the in-plane stress can be calculated for thin oxides on a thick substrate [90, 91]:

$$\sigma_{ox} = \frac{-E_{ox}\;\Delta T\;(\alpha_{met} - \alpha_{ox})}{1 - v_{ox}} \tag{1.15}$$

where, σ_{ox} is the in-plane stress in the oxide layer, E_{ox} is the Young's modulus of the oxide, α_{met} and α_{ox} are the thermal coefficient of expansion of the metal and oxide respectively, ΔT is the temperature change (initial temperature minus final temperature) and ν_{ox} is the Poisson's ratio of the oxide. Clearly the magnitude of the stress will be dependent on the size of the temperature change and the difference in thermal coefficients of expansion. Typical coefficients of thermal expansion of Cr_2O_3, Al_2O_3 and Ni/Fe-based alloy 800, Ni-based alloy Nimonic 75 and Ni-based superalloy CMSX 6 are shown in Table 1-III. Using equation 1.15, the in-plane stress in the oxide can be calculated upon cooling, using the following parameters (along with those in Table 1-III): E_{ox} for alumina (365 GPa) and chromia (275 GPa) can be taken from an experimentally determined graph from Saeki et al. (2011) [94], ν_{ox} of 0.29 (Cr_2O_3) and 0.24 (Al_2O_3) [95] and using a temperature drop of 680 and 880 K from a component cooling down from a realistic in service temperature of 973 K to RT (293 K) and 1173 K to RT for a typical chromia forming rotor disc alloy and alumina forming blade alloy respectively. This will give in-plane compressive stresses of 1.8 GPa and 3.3 GPa for rotor disc and blade alloy respectively, when cooling from typical in-service conditions. It indicates that failure of the oxide scale under thermally cyclic conditions is more likely in alumina forming alloys than chromia forming due to the former having a much larger temperature drop.

Table 1-III: Coefficients of thermal expansion [90, 92, 95, 96].

Material	Coefficient of thermal expansion (10^6 K^{-1})	T (^{o}C)
Cr_2O_3	7.3	100-1000
Cr_2O_3	8.5	400-800
Al_2O_3	8.1	400-800
Alloy 800	16.2-19.2	20-1000
Nimonic 75	15.4	20-700
CMSX 6	15.8	-

1.3.7.3 External stresses

The effect of external stresses on the integrity of oxides is of extreme importance for high temperature in service components since the protective effect of a dense oxide scale is dependent on its ability to remain intact. Knowing the stress/strain at which this external scale will fail is extremely useful when considering the corrosion resistance of a component [91, 97].

1.3.7.4 Stress response

All stresses must be accommodated within either the underlying substrate or within the oxide scale. There are several methods of accommodating the stresses: cracking or spallation of the oxide, plastic or elastic deformation of the substrate and/or oxide or creep of either the substrate and/or oxide. Cracking and spallation of the oxide scale have the most severe consequences, since they have the effect of removing the oxide scale and exposing the clean surface to an oxidising environment. Oxide cracking generally only occurs when the oxide is put under tension, whereas under compressive stresses oxide spallation is more likely. Decohesion of the metal/oxide interface or inter-oxide interface is required for spallation to occur, this is easier to achieve under compression than under tension. In tension the shear stress component needs to be larger than the interfacial stress, after through-thickness cracking, which is rarely found [91, 98]. The fracture toughness of the typical oxides found in Ni-based superalloys are listed in Table 1-IV. Once these values are exceeded cracking of the scale occurs, these values are typically much less than those expected of most metallic alloys.

Experimental data on the critical tensile strains to crack the oxide shows that they are often only a few tenths of 1% [92, 97]. Such strains are encountered in many practical applications, which means that through-scale cracking has to be expected during in-service exposures.

Table 1-IV: Fracture toughnesses of typical oxides found in Ni-based superalloys and the temperature at and substrate they were recorded on.

Oxide	Substrate	K_{1c} (MPa.m$^{-1/2}$)	Temperature (^{o}C)	Reference
Cr_2O_3	Nimonic 75	2.0 (±0.4)	700	[97]
Cr_2O_3	Alloy 800H	0.4-2.1	775	[99]
Al_2O_3	Fe-18Cr-Al-Ce steel	0.4-1.0	800	[99]

Tensile failure

It can be realistically considered that the oxide layer deforms elastically until fracture, since the tensile fracture strains of oxides tend to be less than 1%. As oxide scales are brittle phases even at high temperatures, scale failure can be described using a fracture mechanics approach. This assumes any cracking of the external oxide scale will develop from surface or sub-surface defects present in the oxide scale. Oxides contain defects and clusters of these defects can be found in the same plane [97]. The critical stress for scale failure to occur with a known defect size can be calculated using equation 1.16 [91]. It is assumed that the principal stresses within the oxide are tensile and in the plane of the oxide layer:

$$\sigma_c = \frac{K_{1c}}{f(\pi a)^{0.5}} \tag{1.16}$$

where σ_c is the critical stress to failure, K_{1c} is the critical stress intensity factor, f is a defect geometry factor (1.12 for a surface notch, 1.0 for an embedded defect and 0.64 for a semi-circular defect of radius c) and a is the defect size (half the length of a defect or radius if circular). The failure strain of the oxide scale can also be modelled using a similar approach [92]:

$$\varepsilon_c = \frac{K_{1c}}{f\, E_{ox}\sqrt{\pi\, a}} \tag{1.17}$$

where E_{ox} is the Young's modulus of the oxide, and ε_c is the critical strain to failure. Furthermore, a number of small defects can interact with each other in a mechanical sense if they are lying close to each other. This has the effect of creating a much larger effective defect size, which then determines the failure behaviour of the scale. This is discussed in more detail in Hancock and Nicholls (1988) along with a numerical evaluation [97] .

Compressive failure

Commonly, there are two routes to spallation, buckling and wedging (Figure 1-20).

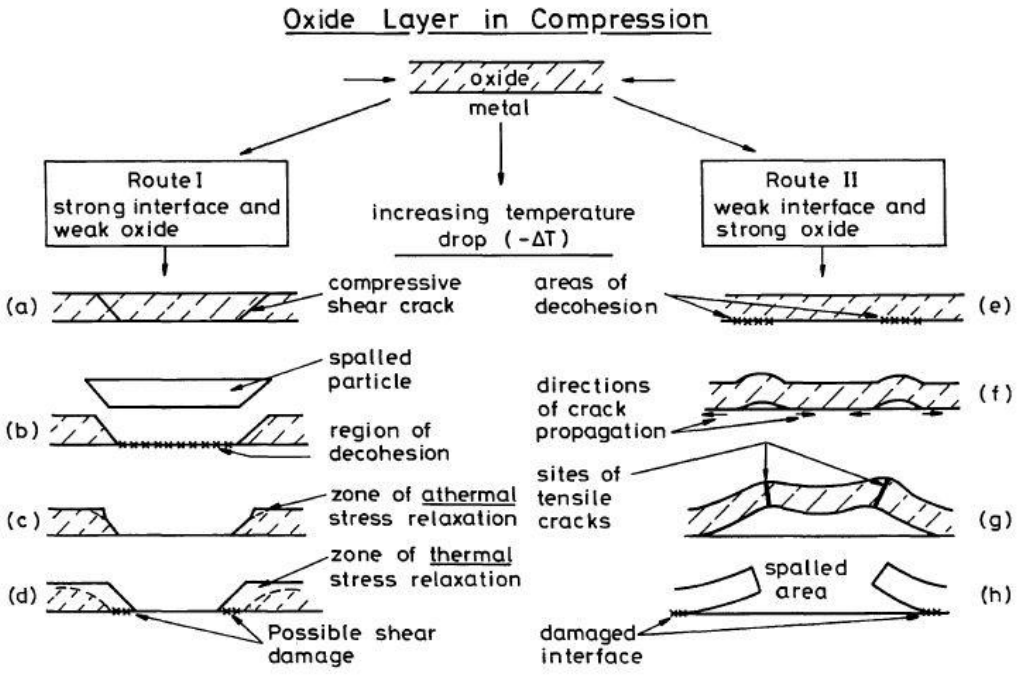

Figure 1-20: Cracking and spallation caused by compressive oxide stresses, showing two routes to failure (route I – wedging and route II – buckling) [91].

The mechanism of failure is determined by the relative strengths of the metal/oxide interface and the oxide scale. Route I spallation occurs when the oxide-metal interface is intrinsically stronger than the

compressive fracture strength of the oxide. It assumes that the interface is not weakened by voids or segregation of trace elements and therefore initial failure occurs by shear cracking of the oxide scale, presumably at a defect within the scale. Interfacial decohesion then transpires by wedging leading to the spallation and local failure of the oxide scale [92, 100, 101]. In route II a weak oxide-metal interface is assumed and spallation is a result of decohesion at the interface leading to buckling of the external oxide layer. The buckle then leads to through-thickness cracking and subsequent spallation of the oxide scale [92, 101].

Crack healing

Fortunately oxides on most structural alloys have the ability to heal any cracks that develop, given enough time, by reforming the protective oxide scale. The exposure of the underlying alloy surface to an oxidising environment will lead to the local oxide growth rates in the vicinity of the crack being significantly higher than that of the rest of the scale and result in the rapid reformation of the oxide scale. The time taken for an oxide to self-heal a crack can be calculated simply from [91]:

$$t_h = \frac{\xi_c \, w}{2 \, k_p'} \tag{1.18}$$

where t_h is the time to scale healing, ξ_c is the crack thickness, w is the crack width and k_p' is the parabolic rate constant. The critical strain at which crack healing can no longer occur can be calculated using the following equation [91]:

$$\dot{\epsilon}_c = \left(\frac{2 \, k_p' \, \dot{\varepsilon}_1^m}{\xi_c \, \lambda_1} \right)^{1/(m+1)} \tag{1.19}$$

where $\dot{\varepsilon}_c$ is the critical strain rate for crack healing, λ_1 is the spacing between the cracks measured at a strain rate $\dot{\varepsilon}_1$ and m the exponent describing the dependence of λ on $\dot{\varepsilon}$. Under a tensile strain a competition ensues between the rate of crack healing and the rate of crack opening. At low strain rates the rate at which the oxide crack faces move apart is lower than the oxide growth rate within the through-thickness crack, thus allowing crack healing to occur [102]. At larger strain rates crack healing cannot occur as further deformation occurs at a rate quicker than oxide formation can occur [99]. This is also the case if elemental depletion has occurred within the near surface region of the substrate due to earlier selective oxidation. The reformation of a protective oxide scale may not occur instead a non-protective oxide of a major alloying element will be formed. This can lead to unacceptably large oxidation rates. Crack healing of protective Cr_2O_3 scale has been reported at 800^{o}C on Ni-based alloy 800 and high chromium steels [98, 103].

1.3.8 Oxidation of nickel-based superalloys

The oxidation behaviour of several nominally chromia-forming nickel-based superalloys has been studied extensively, e.g. IN718, RR1000, Udimet720, ME3 etc. [104-114]. This was performed using both isothermal and cyclic oxidation tests and since the oxide scale is affected by the composition of the alloy and that Ni-based superalloys are heavily alloyed, duplex oxides are often seen. These oxides are dependent on the temperature of exposure as well as the time of exposure, with short exposures and extreme temperatures (>900ºC) producing drastically different oxides. That said, in general the oxide scale is reported as being duplex consisting of a dense Cr_2O_3 layer and an outer layer of TiO_2 but, in addition, a sub-surface internal oxide of Al_2O_3 forms, often as an acicular intergranular penetration [104, 105]. The internal oxide is associated with a γ′ denuded zone that extends further into the alloy, caused by Al depletion. Other oxides are often seen, e.g. NiO and CoO, and are often associated with transient oxidation. Observations on the chromia forming Ni-based superalloy, RR1000, obtained through the use of focused ion beam (FIB) sample preparation and imaging, have reported the presence of subsurface voids after oxidation which is in disagreement with previous observations in this alloy and similar Ni-based superalloys and so is currently in dispute [107]. Most studies tended to assess the reaction kinetics using weight change measurements and have shown that the rate of oxidation is higher than would be expected for the formation of a protective layer of pure chromia. This is of course not unexpected since other alloy constituents are being oxidised.

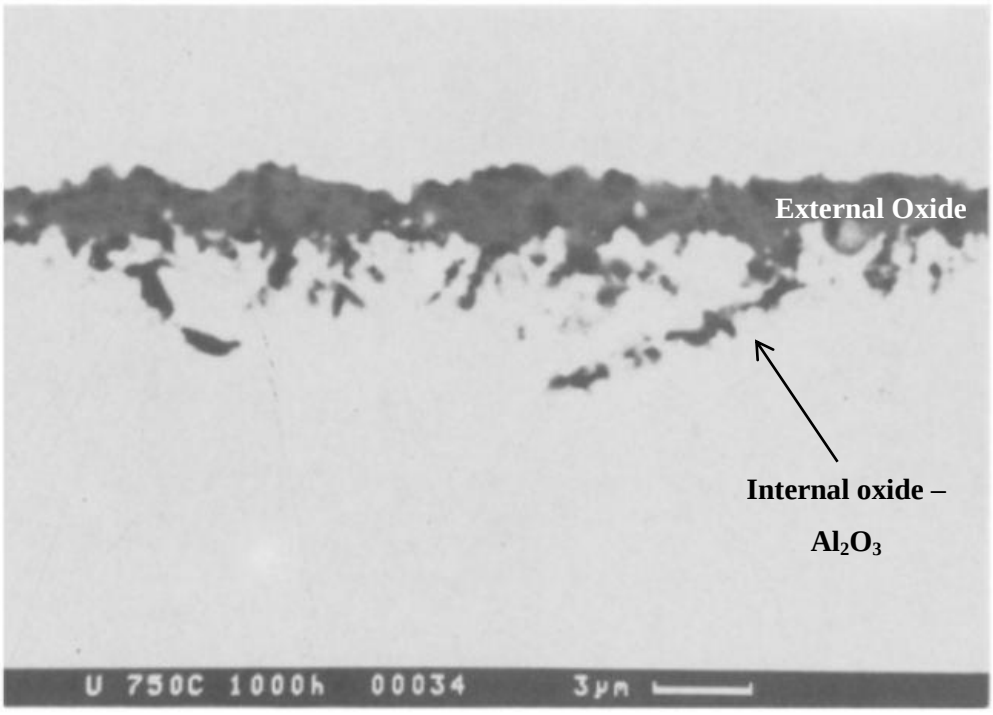

Figure 1-21: Oxidation damage on Udimet 720, oxidised at 750°C for 1000 hours [104].

1.3.9 Effect of surface modification on oxidation

Surface finish and residual stress underneath the surface are controlled and modified to improve the mechanical properties of in-service components. The oxidation performance of an alloy is not always investigated in this way. A number of studies have established that the oxidation behaviour of stainless steels, Ni alloys and Fe-Cr alloys are dependent on the surface finish prior to oxidation. Additionally, little work has subsequently been conducted on the effect of surface condition on the oxidation of Ni-based superalloys, with most studies looking at the ideal highly polished or as-received machined condition [47, 107, 115].

1.3.9.1 Shot-peening

Shot-peening has been widely employed to improve the fatigue resistance by inducing significant surface compressive residual stresses [116, 117]. The effect of shot-peening has been investigated in both chromia forming steels and Ni-Fe based alloys in both air and water vapour. The effect of shot-peening on pre-oxidised pure zirconium with the oxide scale removed; found that when oxidised in 200 mbar of O_2 at 650^{o}C for 30 minutes, a slower oxidation rate was found in the shot-peened condition. It was also recorded that the longer the shot-peening time the greater the reduction in the oxidation rate and therefore the greater the oxidation resistance. This has been attributed to the significant compressive residual stresses introduced and thus the negative residual stress gradient in the thin surface region acting as a reverse driving force for diffusion [118].

Shot-peening of the surface of steels prior to oxidation can have a beneficial effect. Several studies have been performed on austenitic 18% chromium and martensitic with 12% chromium steel oxidised between 700^{o}C – 800^{o}C. In steels of relatively low chromium contents (<12%) the beneficial effect was only found at 750^{o}C and 800^{o}C. This beneficial effect was found at all temperatures in 18% chromium steel after 72 to 75 hours of high temperature exposure. This has been attributed to increased supply of chromium through dislocations acting as diffusion pathways (short circuit) leading to a change in the kinetics of oxidation through earlier formation of a protective oxide scale but this effect depends on the amount of chromium in the base alloy [119]. Another study using similar 18% and 12% chromium austenitic and martensitic steels at 750^{o}C for 92 (12%) – 120 hours (18%) found a similar effect, with the 18% chromium containing steel having a more pronounced effect. Shot-peening introduces a localised plastic zone in the near surface with an increased dislocation density which therefore acts as diffusion pathways for chromium promoting the formation of protective chromium rich oxides [120]. In super 304H steel, a 18% Cr containing alloy, shot-peening again improved the oxidation resistance, in both steam and air at 600-700^{o}C, through the promotion of a chromium rich oxide scale over a duplex iron rich outer oxide and inner Fe, Cr, Ni and Mn rich spinel [121]. This was again attributed to enhanced diffusion due to an increased dislocation

density. Finally in high chromium containing steels (TP304H and HR3C) a similar effect was seen, when the specimens were oxidised in water vapour at 650^{o}C, with the shot-peened alloys having improved oxidation kinetics. This improvement was driven by a change in oxide composition from Fe-rich to a thinner Cr-rich oxide. A similar mechanism to previous studies was proposed in that shot-peening caused an ultra-fine surface microstructure and plenty of slip bands which resulted in enhanced chromium diffusivity to form more protective chromium- rich oxides [122].

While most of the work has been conducted in steels one study on a Fe-Ni alloy 800H has been conducted and found similar results, with the shot-peening condition producing a simpler and thinner oxide through improved chromium diffusivity promoting the formation of chromium rich oxides. This was tested in both cyclic oxidation (42 cycles of 24 hours) conditions, in air at 850^{o}C and in the presence of supercritical water at 500^{o}C with a dissolved oxygen content of 25 ppb [123].

1.3.9.2 Cold work

The oxidation behaviour of several materials (iron, stainless steels and Ni-alloys) has been investigated in the presence of surface cold work. It has been demonstrated that the effect of cold work has a similar effect (as expected) to shot-peening, in that during high temperature oxidation chromia layers form more readily on surfaces containing cold work. In a 2.25Cr -1Mo steel oxidised in pure oxygen between 400-950^{o}C it was found that while cold work had a negligible effect on the oxidation kinetics below 700^{o}C a marked decrease was seen above this temperature. This was attributed to the faster diffusion of chromium in the cold worked material leading to a chromium rich spinel [124]. This was backed up by a study investigating the effect of oxidation in water/steam on AISI 304 and 410 steels between 400^{o}C-600^{o}C for prolonged periods of time (up to 2000 hours). A reduction in oxidation rate was found in the cold worked samples and was again attributed to the same mechanism, enhanced chromium diffusion due to a high dislocation density producing a protective chromium scale [125]. Further studies have found similar effects with steels exposed at 527-727^{o}C in air and recorded that cold work caused a martensitic structure in 304 and 321 steels that caused the earlier formation of protective Cr_2O_3 scale leading to a reduction in oxidation kinetics. In Incoloy 800H a small increase in oxidation kinetics was found and credited to increased diffusion pathways [126]. Similarly the effect of cold work is not always positive and can have an negative effect by increasing the oxidation kinetics of iron [127-129]. This has been attributed to cold work providing sinks for the cation vacancies arriving at the iron/oxide interface thus preventing the formation of pores underneath the oxide scale. These pores are thought to reduce the oxidation rate.

1.3.9.3 Surface roughness

Several studies have looked at the effect of surface roughness on the oxidation behaviour of nickel, iron and a number of alloys, and have shown it to play a role in the oxidation behaviour. A faster oxidation rate was seen with greater surface roughness on pure nickel [130], when oxidised at 800^{o}C in 1 atmosphere of oxygen for up to 24 hours. Three different surface roughnesses were used: R_a = 575 nm, 30.2 nm and 16.5 nm with the smoothest surface having the slowest NiO growth rate. In contrast in iron a slower oxidation rate was achieved with a rougher surface or with a surface with square or v shaped grooves [131]. Specimens were grit blasted or grooved to increase the surface roughness before being oxidised in air at 800^{o}C for up to 3 hours. They attributed the reduction in oxidation rate to the formation of voids within the oxide sale, which act as diffusion barriers for iron ions. For Fe-Cr-Al alloys with different surface roughnesses were oxidised at 1100^{o}C for 30 minutes and 900^{o}C for 2 hours. The composition of the oxide scale and the scale thickness differed depending on the surface finish illustrating that the surface roughness influenced the composition and growth rate [132]. The oxide changed from a Fe rich to Al rich as the roughness decreased and the oxide thickness generally decreased as the roughness decreased. The exception was the smoothest 1 μm condition which showed the thickest oxide, although thickness was measured using a reflection technique rather than metallographic sectioning and there is some doubt over the accuracy of this technique.

This has also been investigated on similar Fe-Cr-Al alloys during a 5 hour high temperature exposure (1000^{o}C). Two different finishes 1200 grit and 1.5 micron diamond finish were used and found that the rougher surface had faster oxidation kinetics. The rougher surface also induced a change in oxide composition to produce iron-rich nodules as well as Al_2O_3. Greater surface roughness provided enhanced cold work which in turn increased the diffusion rate of Fe during the initial stages of oxidation. The effect was also seen for chromia forming alloys where the increased surface roughness enhanced chromia formation by increasing the diffusion rate of Cr [133]. This is supported by the studies discussed previously looking at both the effect of shot-peening and cold work. Further evidence for increased surface roughness being detrimental to oxidation resistance is provided by a study investigating the oxidation of 304L steel in dry static oxygen at 600^{o}C for 24, 168 and 672 hours, with either a 1000 grit or a 1 μm surface finish [134]. Again a change in oxides occurs with an increased amount of spinel oxide on the rougher specimens leading to an enhanced mass gain. The enhancement of oxidation growth rate is not just the case in air or oxygen atmospheres, it is also found in other atmospheres (H_2-H_2O, N_2- H_2-H_2O and N_2-O_2) in chromium rich steels (up to 20%). Several chromium rich steels, with chromium contents ranging from 9-20%, were oxidised at 600^{o}C for 1, 10 and 100 hours in a range of atmospheres. Five different surface conditions were used with the rougher surfaces producing significant initial increases in mass gains in all the atmospheres tested.

This was attributed to the creation of fast diffusion pathways to the surface caused by surface roughening or working but does have the advantage of, in high chromium steel, helping the formation of a protective chromium rich scale.

The effect of surface roughness in Ni-based superalloys has been investigated by one study [108] and shown that a rougher surface has an adverse effect on the oxidation kinetics at 704°C. Several surface finishes were tested 220 grit (R_a=231 μm), 600 girt (R_a =160 μm) and 1200 grit (R_a = 48 μm) with the roughest surface (220 grit surface finish) producing the largest mass gain. The composition of the oxide is chromia and does not change between the different surface conditions. So a potential reason for the increased oxidation kinetics may be that, like shot-peening, a rougher surface enhances chromium diffusion to the surface, leading to enhanced nucleation of oxide particles over smoother surfaces [108]. The surface roughness of the bond coat of Ni-based alloy Haynes 230 has been shown to affect the oxidation resistance and thermal barrier coating life, when oxidised in laboratory air for 1000 hours at 1000 or 1100^{o}C. Localised asperities created due to the rough bond coat surface undergo oxidation to form a protective alumina scale, at 1100^{o}C the asperity can become depleted of aluminium leading to chemical failure and breakaway oxidation (Figure 1-22). This can have the secondary effect of causing failure of the thermal barrier coating due to the volume increase associated with the non-protective breakaway oxides formed at the asperity [135].

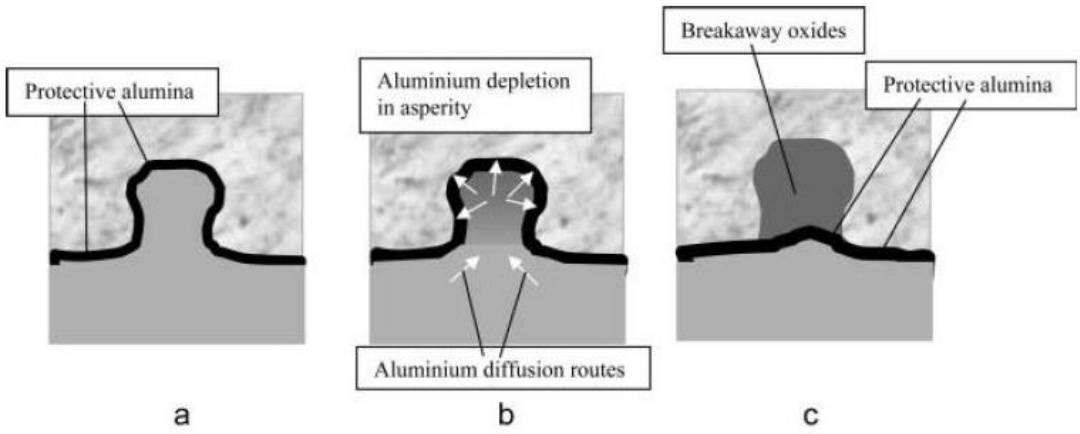

Figure 1-22: Schematic diagram describing chemical failure and breakaway oxidation due to a high surface roughness on a bond coat below a thermal barrier coating. a) shows the formation of a protective alumina layer, b) shows rapid depletion and restricted replenishment of aluminium and c) shows breakaway oxidation of the apreity and a re-healing alumina layer underneath. Taken from Taylor et al. (2008) [135].

In summary shot-peening clearly enhances chromium diffusion through an increase in dislocation density in the near surface region. Changes in oxide composition and the quicker formation of protective oxide scales are the main reason for the improved oxidation resistance but can also cause increased oxidation rates where protective scales are normally formed. In relative terms, the chromium content of RR1000 is also low at 15% wt. (16.5% at.) and shot-peening could be expected to have a similar effect in RR1000. The effect of cold work is similar to shot-peening in that an

increased dislocation density leads to early formation of protective oxides although it has also been shown to enhance non-protective oxides and its role depends on the chemistry of the alloy. Similarly the enhancement of oxidation rates due to a rougher surface finish has been recorded in a number of alloys and has largely been attributed to an increase in diffusion of elements to the surface and often a change in oxide composition, normally forming a less protective oxide. The increase in surface roughness also has the potential to cause localised chemical failure and breakaway oxidation in asperities that make up the rough surface. Most of the studies investigating the effect of surface roughness [130-132, 134] used oxide thickness measurements, while three used mass gain measurements to evaluate the oxidation kinetics [108, 131, 133]. Only one of these studies accounted for the increased surface area by calculating a "true" surface area instead of a geometric area [131], this is an important distinction as it allows a more accurate determination of the effect surface roughness has on the oxidation kinetics and not just the effect of the increased surface area.

1.3.10 Application of an external load on oxidation

High temperature oxidation of metals has focussed primarily on the study of oxidation without the application of an external load. This is an important omission since in the real life operating conditions these materials, and the components they will be used for, often experience significant external stresses. Therefore the extent of the oxidation damage under the application of an external load will more accurately describe their behaviour in service. While the literature on the subject is quite sparse, compared to oxidation in the unstressed condition, several studies have investigated the application of an external load, either compressive or tensile, on a number of alloy systems.

Studies in this area have often focussed on nickel and simple nickel-based alloys as this is the base metal/system used in most superalloys. A tensile stress has been consistently shown to increase the oxidation damage on Ni, with Zhou et al (2010) finding a critical tensile stress (6 MPa) at which this effect occurred at 700°C [136, 137]. A critical stress of 10 MPa is needed in order for cracking of the external scale to occur in the Ni/NiO system [136], which could indicate why under lower stresses no oxidation damage enhancement was recorded. Moulin et al (1996) investigated the effect of oxygen diffusion in Ni and Ni oxide under creep, creep-fatigue and fatigue conditions and found the oxide scale was thicker under fatigue conditions than in the unstrained alloy and significant spallation and cracking was found in the creep and creep-fatigue conditions [138]. The stressed alloys also exhibited significant internal oxidation. Oxidation under a tensile creep stress of 13-25 MPa at 800^{o}C in a reduced partial pressure of oxygen was investigated on a Fe-1Si alloy. This caused an increase in the oxide scale growth, with the oxide scale thicker by a factor of 2, while also inducing more internal oxidation, with intergranular and intragranular penetrations now present. A change in oxide composition was also recorded [139, 140]. Ni-20Cr alloys were oxidised between 500 and 900°C

under a tensile creep load, with the creep strains ranging from 0.5 – 19.6%. In one study the specimens were interrupted at set times and another taken to failure and both studies found the internal and external oxide layers to be much thicker than those formed without an applied load but only at strains above 1% [141, 142]. The nature of the oxide layer, however, did not change but increased oxygen diffusion via short circuit diffusion paths generated by the applied strain caused an increase in oxidation rate. On Ni-Cr-Al alloys oxidised at 1000°C for 1 hour, it was found that the minimum mass change and oxide thickness occurred at a stress of 7.4 MPa (<1% strain) above which a dramatic increase in oxidation kinetics and oxide thickness was observed. It was postulated that up until 7.4 MPa the tensile load was relieving the stress in the oxide film stopping any cracking or spallation and it enhanced the diffusion of Al leading to the formation of a protective aluminium rich oxide. In all other conditions, unstressed and highly stressed (9.8-14.7 MPa or 3-5% strain) significant internal alumina and voids were formed underneath a chromium rich outer scale [143].

The application of a compressive stress on both pure Ni and Fe-20Cr caused an increase in the oxidation rates during short term exposures in air at 700 and 900°C respectively [136, 137, 144]. The effect of a compressive load on pure Ni was found to be more pronounced than that of a tensile load [136]. A couple of studies have looked at the more complex Cr-Mo steels at 610°C and 700°C. The first study investigated the effect of fatigue loading (total strain range of 0.74% in a triangular waveform) and found an enhancement of the oxidation kinetics [145]. The second study investigated the integrity of the oxide scale when oxidised under an external tensile load. Interestingly the scale became more adherent and the temperature drop needed to cause spallation increased when oxidised under an external stress. It appears that the application of external stress had a relieving effect on the growth stresses within the oxide and therefore reduced spallation [64]. Like similar Ni binary and ternary alloys the effect of a tensile load has been investigated on a complex Fe-Ni based superalloy oxidised at 827-1027°C for relatively short periods of time (5-370 hours). While the tensile loads applied were relatively low (29.4 MPa maximum stress) the results again found no compositional change of the oxide scale, either internally or externally. It did however record a small enhancement of oxide thickness and sub-surface intragranular oxide depth as well as finding a large increase in the depth of intergranular penetrations [146].

Little work has been performed in this area on Ni-based superalloys but one such study has investigated the effect of a cyclic tensile stress (670 MPa max) on the oxidation damage of RR1000 [147]. The maximum applied stress equated to 65% of the 0.2% proof stress of RR1000 and was performed using a frequency of 0.25 Hz. It was found that the application of a cyclic tensile stress did not alter the composition or morphology of the oxidation damage, with the oxides being chromia and rutile based. The nature of internal damage in this case was postulated to be different to other similar

Ni-based superalloys indicating the presence of sub-surface micro-voids. It is now understood, however, that this is a misinterpretation and these are in fact internal alumina particles, consistent with other Ni-based superalloys [47, 104, 115, 148]. The study did however find an enhancement of the oxide scale thickness and an increase in the depth of internal damage with a large applied stress (670 MPa) when compared to a lower (100 MPa) or unstressed area. The effect was only seen at 750ºC and 800ºC, with a doubling of the overall oxide depth being recorded at 800°C, whereas at 700°C little if any effect was found [147]. In contrast, on the Ni-based alloys Haynes 75 and 230, the application of a uniform tensile stress (133 MPa max) produced both lower mass gain and thinner oxide scales than on unstressed samples. This was attributed to increased chromium diffusion and a shorter transient oxide period, leading to an early formation of a protective chromia scale [149]. At much higher temperatures (1000°C) IN100 superalloy was oxidised under fatigue loading [150]. This led to an enhancement of the external oxide scale thickness, it seems that this occurred because of cracking of the external oxide scale leading to direct access of oxygen to the metal and therefore it can be expected that the oxidation kinetics will be enhanced [150]. Enhancements were also recorded in the internal alumina depth of Udimet 720 when a minimum dwell loading cycle was applied with a maximum applied strain of 0.7%, with an increase from, 0.86 μm to 1.06 μm. A 100% increase in external layer, alumina penetration and γ′ denuded zone was recorded in ME3 when the same dwell was applied [151].

In summary it seems that the literature is mixed but seems to show that there may be a threshold stress/strain needed to induce an enhancement in the oxidation damage. It could be justified that there is a critical strain to failure or cracking of the scale and therefore oxidation through the cracks enhances the rate. Schütze (1986) proposed a critical strain rate threshold for crack healing, below which rapid repair of the scale occurs, above which is prevented and enhanced oxidation is observed [103]. At strain rates above the threshold value crack healing cannot occur as further deformation occurs at a rate quicker than oxide formation can occur. In addition it could be argued that a moderate external load could improve oxidation performance if spallation of the oxide is expected or it promotes the faster formation of a protective oxide. On the whole there is a lack of oxide composition change with both simple single/binary alloys and similarly complex alloys exhibiting the same oxide scale.

1.3.11 Effect of oxidation damage on mechanical properties

The role of environmental degradation on the mechanical performance of a component is important, since the formation of internal oxides is undesirable and may have a significant detrimental effect on the alloy [84, 152]. It has been postulated that internal oxides that form at the alloy grain boundaries have the potential to act as preferential crack initiation sites and therefore reduce component lives.

This is especially the case when strengthening elements are removed during the formation of internal oxides [84]. The effect of a large portion of the typical in-service environmental damage can be investigated using extensive prior high temperature exposures, since it has been shown in the previous section that while an applied load can increase the oxidation kinetics it does not affect the composition of the scale [147].

The tests on the Ni-based superalloy, ME3, have shown that prior high temperature exposure in an oxidative environment (>700^{o}C) for prolonged periods of time (100-2020 hours) have a detrimental effect on the high temperature (704^{o}C) notched fatigue life [47]. The thicker the external scale and the deeper the internal damage the more pronounced the reduction in life [47]. The reduction in life in this case was driven by $M_{23}C_6$ carbide dissolution. Removal of the internally oxidised region did not lead to a complete recovery in high temperature fatigue life but the removal of the carbide dissolution zone did. This indicated that grain boundary strengthening from the $M_{23}C_6$ carbides is important to crack initiation for these tests. The dissolution of chromium carbides in Inconel 617 improved the high temperature creep strength. This occurred because while an extensive carbide free zone was recorded at the specimen surface, due to selective oxidation of chromium, the carbon released from the carbide dissolution in the surface region, migrated to the centre and enhanced carbide formation there. This enhanced carbide precipitation more than compensated for the lack of carbides at the surface [62].

Another study using extensive prior exposures on the Ni-based superalloy, ME3 (704^{o}C for 439 hours) and Udimet 720 (650^{o}C and 704^{o}C for 100 or 1029 hours) found that the mean lives of pre-oxidised specimens had up to a 70% reduction in LCF life. A change of crack initiation was also seen from sub-surface (as-received) to surface (pre-oxidised). Performing the prior exposures in vacuum led to no reduction in fatigue life, illustrating that oxidation damage is driving the reduction in life [151]. Pre-oxidation under an applied stress (97 MPa) has been shown to cause a further reduction in LCF life of the Ni-based superalloy, Rene 80, over both as-treated and unstressed prior oxidised (100 hours at 982^{o}C) specimens. This is in addition to the reduction in life the unstressed prior oxidised specimens recorded over the as-treated specimens [153]. Fatigue testing of the Ni-based superalloy, IN100, at 1000^{o}C in an oxidative environment has been shown to drastically reduce the life to crack initiation compared with tests performed in vacuum. The crack initiation life was similar to the total number of cycles it took to fracture the oxide [150].

Extensive evidence exists in the literature describing the role oxidising environments have on high temperature (>500^{o}C) dwell fatigue performance. The substantial acceleration in crack growth rates in the presence of oxygen is associated with an intergranular crack path, in contrast to the transgranular crack path seen in low oxygen environments (Vacuum/Argon) [154-157]. Understanding the mechanisms of this phenomenon has been the subject of considerable research and has resulted in two

main theories. The first of these theories is called dynamic embrittlement and envisages the diffusion of oxygen into the grain boundary at or ahead of the crack tip, thus lowering the cohesion of the grain boundary permitting enhanced crack growth (Figure 1-23) [154, 158, 159]. It is sometimes implied that oxygen penetration along the grain boundary, ahead of a crack tip, can extend to distance of 100 μm or more, forming a damaged zone [160], although this has been disputed [161].

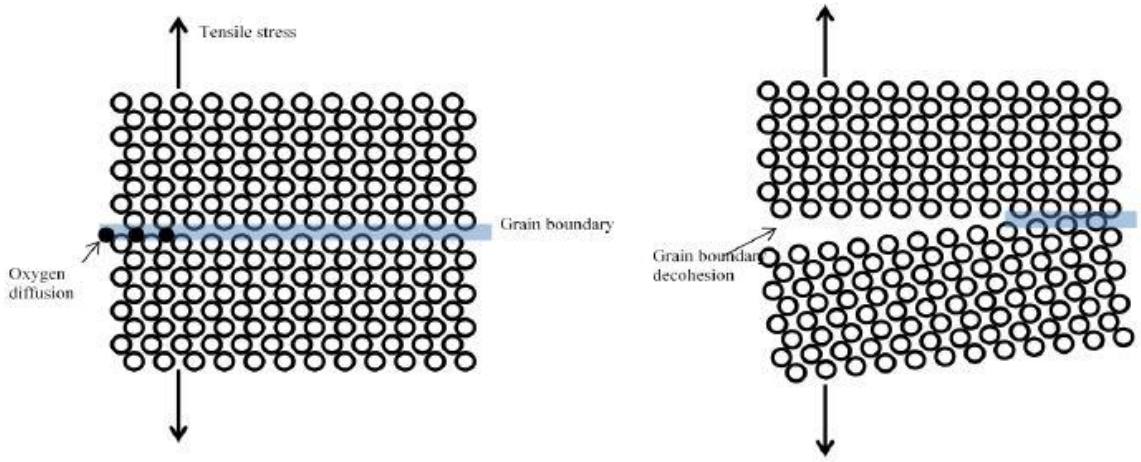

Figure 1-23: Schematic diagram showing the dynamic embrittlement mechanism [162].

The second theory is called stress assisted grain boundary oxidation (sagbo) and proposed the formation of brittle oxides at or ahead of the crack tip (Figure 1-24). Crack advancement occurs via the subsequent repeated cracking and reforming of these brittle oxide intrusions [163, 164]. Recent evidence illustrates that the formation of oxides at or ahead of the crack tip is more credible than the creation of a huge damaged zone. Evans et al [165] state that it is more likely that oxides such as NiO, Cr_2O_3, TiO_2 and Al_2O_3 will form rather than oxygen penetrating along the grain boundary reducing cohesion. This is because the free energy change of oxide formation is significantly more negative than binding energies for the grain boundary. Furthermore strong experimental evidence shows the formation of such oxides ahead of the crack tip during high temperature sustained load and dwell crack growth in the Ni-based superalloy, RR1000 providing strong evidence to the premise that fracturing of these oxides causes crack advancement [166]. Further evidence of oxides ahead of the crack tip on Ni-based superalloys is provided by Viskari et al [167].

The presence of oxidative environments and particularly oxidation has been shown to have a significant effect on mechanical performance, be it surface and internal oxidation damage leading to early crack initiation or oxidation at the crack tip. It has been demonstrated that these oxides can crack under mechanical loading leading to an impairment of mechanical properties.

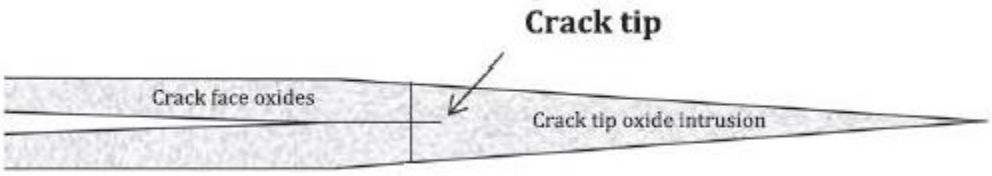

Figure 1-24: Schematic diagram showing oxides at and ahead of the crack tip [166].

Chapter 2 - Aims

The aims for this doctoral research are as follows:

- Characterise the oxidation damage on coarse-grained RR1000 at exposure temperatures of 650-800°C for prolonged periods of time (~8000 hours).

- Characterise the extent of the sub-surface elemental depletion and γ′ denuded zone in respect of time and temperature.

- Investigate the effect different surface treatments (polished [R_a =0.3 μm], shot-peened, vibro-peened, turned and swaged) have on the oxidation kinetics and sub-surface damage on RR1000.

- Evaluate the influence of prior oxidation on the fatigue performance of RR1000 and the role of oxidation in fatigue crack initiation.

Chapter 3 - Material

RR1000 is a 3rd generation Ni-based superalloy used for high temperature rotor disc applications which is produced via a powder metallurgy route. The nominal composition is stated in Table 3-I. Material was provided by Rolls-Royce plc. in two grain sizes and several surface conditions:

3.1 Coarse-Grained (CG) RR1000

The material had undergone a super-solvus solution heat treatment at 1170°C for 2 hours before being still air cooled. An ageing treatment was then applied at 760°C for 16 hours before being air cooled. This produced a coarse-grained variant with a grain size of 30-50 μm, with secondary and tertiary γ′ 200-400 nm and 10-20 nm in size respectively.

3.2 Fine-Grained (FG) RR1000

The material had undergone a sub-solvus solution heat treatment at 1120ºC for 4 hours before being fan assisted air cooled. An ageing treatment was applied at 760ºC for 16 hours before being air cooled. This produced a fine-grained variant with a grain size of 4-6 μm, with primary, secondary and tertiary γ′ 1-5 μm, 200-400 nm and 10-20 nm in size respectively.

3.3 Surface Conditions

Several surface conditions were used during experimental testing, with only those used during the oxidation testing described below, with the surface conditions used during mechanical testing being included separately:

3.3.1 Polished (PO) CG RR1000 and FG RR1000

Samples were prepared for isothermal oxidation tests by being cut from a large piece of CG RR1000 into small samples (~10-15 mm x 5-10 mm x 1-2 mm) using a Struers Ltd. Accutom-5 precision cutting machine at a low speed (<0.05 mm/min) to limit surface damage. The edges and corners were chamfered at approximately 45° and all surfaces ground to remove any residual surface damage using wet SiC papers before being polished using progressively finer diamond solutions to a 6 μm surface finish (Ra ≈ 0.3 μm).

3.3.2 Shot-peened (SP) CG RR1000

Specimens of CG RR1000 were machined to 20 mm x 10 mm x 3 mm, using a Struers Ltd. Accutom-5 precision cutting machine at a low speed (<0.05 mm/min) to limit surface damage. The surfaces were ground and the edges chamfered to a 1200 grit finish using wet SiC papers to remove any

residual surface damage. These were shot-peened (SP) by Rolls-Royce plc. using the following conditions: 110H steel shot, intensity of 6-8 Almen and with 200% coverage.

3.3.3 Vibro-peened (VP) CG RR1000

Specimens of CG RR1000 were machined to 50 mm x 20 mm x 3 mm, the surfaces were ground and edges chamfered to a 1200 grit finish to remove any residual surface damage. These were vibro-peened (VP) on one side by Rolls-Royce plc. Following this these were cut into 20 mm x 10 mm x 3 mm samples using a Struers Ltd. Accutom-5 precision cutting machine at a low speed (<0.05 mm/min) to limit surface damage. The edges and corners were chamfered using 1200 grit wet SiC papers.

3.3.4 Turned (TU) CG RR1000

Wedged pieces of CG RR1000 **(**Figure 3-1), left over from the production of washer rings, which had been turned into shape on two sides were machined into 20 mm x 10 mm x 3 mm specimens using a Struers Ltd. Accutom-5 cutting machine at a low speed (<0.05 mm/min) to limit surface damage. The corners and edges were chamfered using 1200 grit wet SiC paper but due to the thick nature of the wedged pieces of CG RR1000 once machined into smaller specimens only one side of the specimen had a turned surface.

3.3.5 Swaged (SW) FG RR1000

A cylinder of FG RR1000 was swaged causing an area reduction of 31.3 % reducing the cross-sectional area from 27 mm^2 to 22.4 mm^2. Specimens of FG RR1000 were cut using a Struers Ltd. Accutom-5 precision cutting machine into semi-circular pieces with a radius of 11 mm and thickness of 2-3 mm. The top and bottom surfaces were ground to remove any residual surface damage using wet SiC papers before being polished using progressively finer diamond solutions to a 6 μm surface finish (Ra ≈ 0.3 μm).

Table 3-I: Nominal composition of RR1000 in both atomic and weight %.

	Ni	Co	Cr	Mo	Ti	Al	Ta	Hf	Zr	C	B
Weight %	Bal	18.5	15.0	5.0	3.6	3.0	2.0	0.5	0.06	0.015	0.027
Atomic %	Bal	17.9	16.5	3.0	4.3	6.4	0.6	0.2	0.04	0.13	0.08

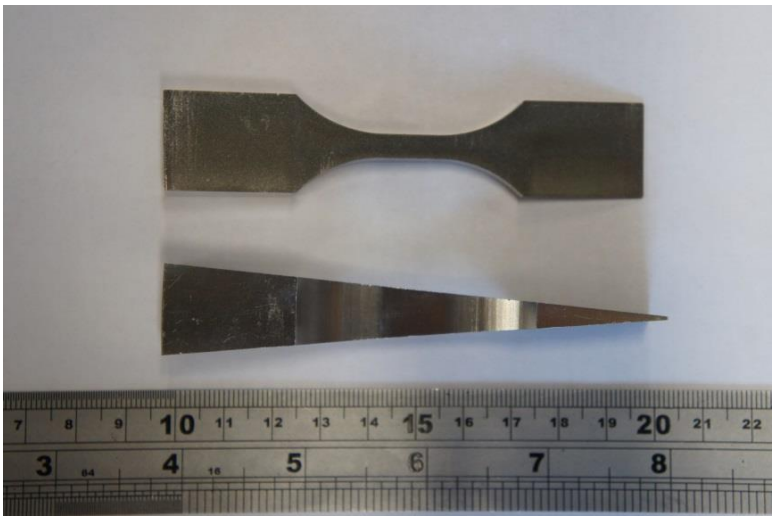

Figure 3-1: Photograph of turned CG RR1000 wedged samples before sectioning into oxidation coupons.

Chapter 4 - Experimental Procedure

The procedural aspects of the experiments conducted were carried out as detailed below:

4.1 Isothermal Oxidation Testing

Isothermal testing was conducted in laboratory air, using an Elite Thermal Systems Ltd single zone tube furnace (model TSH12/50/610-2416CG) or a Carbolite Ltd single zone tube furnace (model CFT 12/65/550) shown in Figure 4-1. The furnace was calibrated to +/- 1°C using an N-type thermocouple. A complete oxidation testing matrix detailing all the times, temperatures and surface conditions used is shown in Table 4-I. Results were collected in one of two ways:

1. Mass change and cross-sectional analysis data collection.
2. Cross-sectional analysis data collection only.

Table 4-I : Oxidation testing matrix for: CG RR1000 with different surface conditions (SP = shot-peening, VP = vibro-peening, PO = polished and TU = Turned) and FG RR1000 with different surface conditions (FG = polished and SW = Swaged)

	24 h	50 h	100 h	200 h	500 h	1000 h	2000 h	4000 h	8000 h
650°C (PO)	x	x	x		x	x	x		
675°C (PO)						x			
700°C (PO)	x	x	x		x	x	x	x	x
725°C (PO)						x			
750°C (PO)	x	x	x		x	x	x		
775°C (PO)						x			
800°C (PO)	x	x	x	x	x	x	x		
800°C (FG)				x					
650°C (SP)	x		x		x	x	x		
700°C (SP)	x		x		x	x	x		
750°C (SP)	x		x		x	x	x		
800°C (SP)	x		x	x	x	x	x		
700ºC (VP)	x		x		x	x	x		
700ºC (TU)	x		x		x	x	x		
700°C (SW)	x		x		x		x		

Mass change and cross-sectional analysis data was only sought on the polished CG RR1000 (PO) and shot-peened CG RR1000 (SP) conditions. In the vibro-peened CG RR1000 (VP), turned CG RR1000 (TU) and swaged FG RR1000 (SW) conditions only cross-sectional analysis was possible as only one side of the specimen had the required surface treatment and therefore any mass change data recorded could not be accurately attributed to the surface treatment. The procedures for both types of testing are very similar. For testing for cross-sectional analysis the specimens were cleaned and degreased in ethanol using an ultrasonic cleaner for a period of 5 minutes. Batches of specimens were placed into open ceramic alumina boats before being placed into the centre of a pre-heated single zone furnace.

Two specimens were removed from the furnace at the required time interval according to Table 4-I and allowed to air cool to room temperature. At each removal from the furnace the specimens were examined for signs of spallation.

For mass gain testing the specimen dimensions were accurately measured using a micrometer before being cleaned and degreased in ethanol using an ultrasonic cleaner for a period of 5 minutes. The specimens were dried and weighed using a sensitive micro balance accurate to ± 0.00001 g (0.01 mg), with the balance being calibrated before every set of measurements using its internal calibration function. Batches of specimens were placed into open ceramic alumina oxide boats before being placed into the centre of a pre-heated single zone furnace. Each specimen was removed from the furnace at 24, 50, 100, 300 and 500 hours. After this point specimens were removed at 500 hour intervals. Specimens were removed from the furnace after the required time and allowed to air cool to room temperature. At each removal from the furnace the specimens were examined for signs of spallation and reweighed and the increase in mass was then used to calculate the nett mass gain. This was normalised to surface area of the specimen. At selected time intervals (Table 4-I) individual specimens were removed for examination before the rest were replaced into the furnace for continued high temperature exposure.

The two specimens that were selected at each time interval allowed one specimen to be used for surface analysis using: confocal microscopy, x-ray diffraction (XRD) and scanning electron microscopy (SEM), and the second specimen for cross-sectional metallography. Individual specimens were not produced for test temperatures of 675°C, 725°C and 775°C as only data on the mass change was sought.

4.2 Heat Treatments

Additional heat treatments were performed on single specimens of both polished and shot-peened CG RR1000 in an inert atmosphere of pure argon at a temperature of 800ºC for 200 hours. This was in addition to those performed during manufacture of the alloys by Rolls-Royce plc. This was performed to investigate whether some grain re-crystallisation is the effect of: temperature, temperature and oxidation or temperature, oxidation and cold work. The furnace was calibrated to +/- 1°C using an N-type thermocouple. Specimens were first cleaned and degreased in ethanol using an ultrasonic cleaner for a period of 5 minutes and wrapped in tantalum foil before being placed into open alumina boats and placed inside a Carbolite Ltd single zone tube furnace (model CFT 12/65/550). The tantalum foil was used due to its high reactivity with oxygen and acts sacrificially to remove any residual oxygen. An inert atmosphere (argon) was passed through the furnace for two hours before it was brought up to the desired temperature. Once the desired time was reached the furnace was switched off and the specimen was pulled out of the hot zone into one of the ends of the silica tube outside the furnace

using Fe-Cr alloy wire, which was attached to the alumina boat before exposure. This ensured quick cooling of the specimen in an inert atmosphere. Heat sinks and fans were added to the ends of the silica tube to improve the cooling rate. The inert atmosphere continued to be passed through the furnace until it reached room temperature.

Figure 4-1: Image of a Carbolite Ltd single zone furnace model CFT 12/65/550)

4.3 Mechanical Testing

Mechanical testing was performed according to the following procedures and parameters:

4.3.1 High cycle fatigue (HCF)

High cycle fatigue testing was performed on both as-received and pre-oxidised four-point bend specimens. Pre-oxidation of specimens occurred on polished CG RR1000 four-point bend specimen which were cleaned and degreased in ethanol ultrasonically for a period of 5 minutes. Specimen dimensions were measured using a micrometer. The dimensions of the specimens were nominally 100 mm x 9 mm x 10 mm. They were then placed on top of two open ceramic alumina boats before being placed into a pre-heated Elite Thermal Systems Ltd. box furnace (Model BSF12/10-2416-2116) at 700°C for two time periods, 2000 hours and 100 hours, in laboratory air. The furnace was previously calibrated using an N-type thermocouple to ± 5°C. The furnace lost ~50°C on opening but regained the required temperature of 700°C within 10 minutes.

In the non-oxidised condition the corners were chamfered to remove the potential for corner crack initiation and cleaned and degreased in ethanol ultrasonically for a period of 5 minutes. Otherwise the specimens were left as-received with the machining marks perpendicular to the direction of applied

force (Figure 4-2). One specimen was also used to test the effect of the aged microstructure, this was performed by taking a specimen pre-oxidised for 2000 hours and removing all of the oxidation damage (external and internal) by grinding using 240 grit paper. Grinding marks were perpendicular to the direction of applied force.

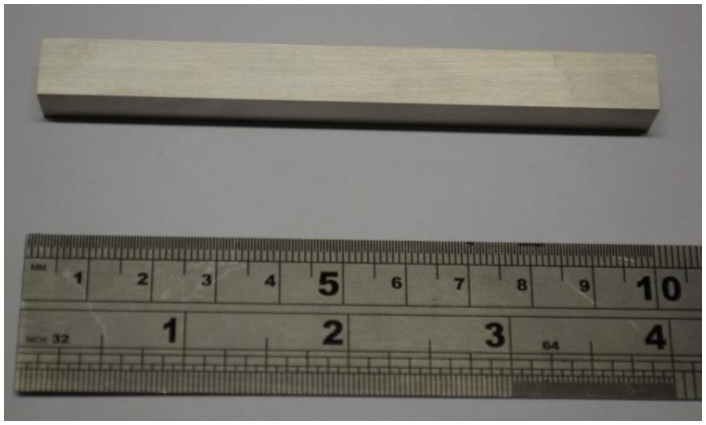

Figure 4-2 : Optical image of an as-received CG RR1000 four-point bend specimen

Table 4-II : High cycle fatigue testing matrix (RT= room temperature)

Specimen ID	Temp °C	Pre-oxidation	R Ratio	Outer fibre Stress [MPa]			Load [kN]		
				σ_{min}	σ_{max}	σ_{mean}	Min	Max	Mean
M09812 SS812 Pos 2	RT	2000h	0.1	70	700.0	385	-0.950	-9.450	-5.200
M09812 SS812 Pos 1	RT	2000h	0.1	80	800.0	440	-1.080	-10.800	-5.940
M09812 SS812 Pos 3	RT	2000h	0.1	80	800.0	440	-1.080	-10.800	-5.940
M09812 SS812 Pos 4	RT	2000h	0.1	80	800.0	440	-1.080	-10.800	-5.940
M09812 SS812 Pos 5	RT	2000h	0.1	80	800.0	440	-1.080	-10.800	-5.940
M09812 SS812 Pos 16	RT	2000h	0.1	83	825.0	454	-1.114	-11.140	-6.125
M09812 SS812 Pos 15	RT	2000h	0.1	85	850.0	468	-1.148	-11.480	-6.320
MER090203 Pos 2	RT	Removed	0.1	90	900.0	495	-1.180	-11.760	-6.470
M09812 SS812 Pos 6	RT	2000h	0.1	90	900.0	495	-1.220	-12.150	-6.690
M09812 SS812 Pos 13	RT	2000h	0.1	90	900.0	495	-1.220	-12.150	-6.690
MER090203 Pos 1	RT	2000h	0.1	100	1000.0	550	-1.350	-13.500	-7.400
MER090203 Pos14	RT	2000h	0.1	100	1000.0	550	-1.350	-13.500	-7.400
M09812 SS812 Pos 7	RT	No	0.1	70	700.0	385	-0.950	-9.450	-5.200
M09812 SS812 Pos 9	RT	No	0.1	80	800.0	440	-1.080	-10.800	-5.940
M09812 SS812 Pos 12	RT	No	0.1	80	800.0	440	-1.080	-10.800	-5.940
MER090203 Pos 16	RT	No	0.1	85	850.0	468	-1.148	-11.480	-6.320
M09812 SS812 Pos 8	RT	No	0.1	90	900.0	495	-1.220	-12.150	-6.690
M09812 SS812 Pos 10	RT	No	0.1	90	900.0	495	-1.220	-12.150	-6.690
MER090203 Pos 22	RT	No	0.1	90	900.0	495	-1.220	-12.150	-6.690
MER090203 Pos 24	RT	No	0.1	100	1000.0	550	-1.350	-13.500	-7.400
MER090203 Pos 6	RT	No	0.1	100	1000.0	550	-1.350	-13.500	-7.400
MER090203 Pos 3	RT	100h	0.1	70	700.0	385	-0.950	-9.450	-5.200
MER090203 Pos 8	RT	100h	0.1	80	800.0	440	-1.080	-10.800	-5.940
MER090203 Pos 9	RT	100h	0.1	90	900.0	495	-1.220	-12.150	-6.690

High cycle fatigue testing was performed on, both as-received and pre-oxidised, CG RR1000 specimens using an Amsler Vibrophore HCF machine with a 20 kN load cell which was set up for

four-point bend testing. The load cells and cycle counters are calibrated yearly to ensure accurate application and measurement. The alignment of the testing fixtures was checked before each test as any misalignment could induce unknown bending loads on the test specimens. A span ratio of 20-60 mm and an R ratio ($\sigma_{min}/\sigma_{max}$) of 0.1 were used throughout. Testing was performed in laboratory air at room temperature. Cycling was performed at the resonant frequency of the specimen, ~75 cycles per second. The testing range is detailed in Table 4-II and an oscilloscope was used to check and adjust the accuracy of the load applied. If the specimens had not failed after $5x10^7$ cycles, the test was defined as a runout and the test was stopped.

4.4 Specimen Preparation Post Testing

Specimens were prepared for detailed cross-sectional analysis of the oxide morphology, composition, depth, the presence of a γ' denuded zone and grain boundary carbide dissolution, as well as characterisation of the parent material. Preparation of oxidised specimens for cross-sectional examination is both difficult and time consuming due to the brittle nature of the oxides formed and the potential to damage the structure. In order to prevent spallation or cracking of the external oxide layer one of two methods of preparation was used:

1. The specimen was mounted in a low shrinkage, low viscosity epoxy resin (Struers epofix), using a Struers Epovac vacuum impregnator at a pressure of 400 mbar (Figure 4-3).
2. The specimen was first sputtered with gold, to produce an electrically conductive layer, and then electroplated with Ni using a "Watt's bath" electrolyte solution (25-40 g/l $NiSO_4 \cdot 6H_2O$, 20-60 g/l $NiCl_2 \cdot 6H_2O$ and 30-45 g/l H_3BO_3) at a temperature of between 45-71ºC with a current density of 1-10 $A.dm^{-2}$. Ni plating helps prevent oxide spallation and damage to the oxide during sectioning. The thin Au layer can be used in the elemental dispersive x-ray spectroscopy (EDX) mapping to delineate where the oxide/alloy ends and the Ni plate begins. Specimens were then mounted as in 1.

The 4-point bend specimens prepared for detailed cross-section analysis by destructive examination of the high cycle fatigued specimens were prepared using one of two methods for the same reasons described above:

1. Specimens were mounted whole in a low shrinkage, low viscosity epoxy resin (Struers epofix), using a Struers Epovac vacuum impregnator at a pressure of 400 mbar. The region of highest stress was then cut out using a Struers Ltd. Accutom-5 precision cutting machine at a low cutting speed (<0.05 mm/min) before being re-mounted in Struers epofix.
   Or
2. A cross-section was milled out using focussed ion beam (FIB) sectioning (a process described later).

In all cases this allowed normal specimen sectioning and preparation to subsequently commence with grinding being performed using progressively finer grades of wet SiC papers before polishing with progressively finer diamond solutions with final polishing being performed using a Struers MD–Chem disc with either OP-S colloidal silica solution or 0.25 μm diamond solution. Specimens were cleaned ultrasonically with ethanol before being sputtered with gold for 60-120 seconds to allow SEM examination. Un-oxidised specimens were hot mounted in conductive Bakelite before being prepared conventionally, as described above. Failed fatigue specimens were treated with care to make sure the fracture surfaces remained un-touched and free from contamination; otherwise no specimen preparation was necessary.

Chemical etching was performed on polished cross-sectioned specimens using two different etchants (compositions in Table 4-III [168, 169]): Kalling's etch was used for grain structure and carbides, and a selective γ′ etchant was used to determine the γ′ area fraction and the size of denuded zones. Specimens were swabbed for 30 seconds in a circular motion with Kallings etchant or immersed in the selective γ′ etchant for 60 seconds.

Figure 4-3. Optical image of Struers vacuum impregnator.

Table 4-III : Composition of the two chemical etchants used

	Gamma prime (γ') Etch	**Kallings Etch**
Chemical composition	Part 1 – 150 ml H_2O, – 150 ml HCl – 2.5 g MoO_3 Part 2 – 15 ml HNO_3 – 25 ml H_2O – 30 ml Part 1	– 100 ml ethanol 96% – 100 ml hydrochloric acid 32% – 5 g copper (II) chloride

4.5 Characterisation of Oxidised and Un-Oxidised Material

Characterisation of the specimens was performed both prior to and after testing using a number of techniques. These are listed in no particular order while giving details of the exact equipment model and procedure.

4.5.1 Confocal microscopy

Confocal microscopy was performed using an Olympus Lext OLS 3100, with a TS-150 table stabilisation unit. It was used to record the arithmetic mean surface roughness of an area, arithmetic mean roughness of a line and mean height of the surface roughness profile peaks (S_a, R_a and R_c respectively) of the specimens. This was performed over an area of 480 x 640 μm, and also used to investigate the times and temperatures that enhanced grain boundary oxidation occurred. This equipment has a manufacturer reported vertical resolution of 0.01 μm and noise and spike reduction corrections were applied. The area size was chosen as it has been found that small areas can distort values reducing the accuracy of the technique. R_a measurements were performed perpendicular to any machining marks where applicable.

4.5.2 Talysurf measurements

The surface roughness measurements (R_a, R_c) obtained from the confocal technique were checked using a Taylor Hobson Form Talysurf, (with vertical resolution of 0.01 μm). The measurement was performed using a stylus angle of 60º, a stylus tip length of 2 μm and an evaluation length of 4.0 mm. The measurements were repeated six times, to give a reproducible average. This was performed to confirm the accuracy of the confocal measurements and the in house measurements performed by Rolls-Royce plc using white light interferometry.

4.5.3 Micro-hardness

Micro-hardness was performed on a cross-section of all conditions using an automated Struers Durascan-50 micro-hardness machine (Vickers hardness, with a 0.3 kg load). The indents were performed at 0.01 mm intervals starting from 0.04 mm from the surface to a depth of 0.1 mm and then at 0.02 mm intervals to a total depth of 0.5 mm. This was performed three times in a diagonal pattern to quantify the hardness affected zone caused by the different surface treatments.

4.5.4 Nano-indentation

Nano-indentation was performed on a cross-section of an oxidised specimen using a Micromaterials Ltd. Platform 3 NanoTest machine. The indents were performed at 1 μm intervals in a diagonal pattern across the specimen, starting within the Ni-plate through the oxide into the bulk alloy. The indents were performed using a Berkovich indenter under a load controlled setting to a maximum load of 30 mN. A loading rate of 1 mNs^{-1} was used. Once the indenter reached the maximum load this was then held for a short period of time (~30 seconds) before being removed from the specimen, giving a

load vs. displacement graph (Figure 4-4). The hardness of the material was then calculated from the slope of the tangent (dP/dh) to the unloading curve using the following equations:

$$H_n = \frac{P_{max}}{A_r} \tag{4.1}$$

where H_n is hardness, P is maximum load and A_r is residual indentation area. For a Berkovich indenter the residual area is:

$$A_r = 3\sqrt{3\,h_c}\,tan^2\theta \tag{4.2}$$

where $\theta = 65.27^o$ and h_c is the depth of the indenter after elastic relaxation and is calculated from the load-displacement graph shown in Figure 4-4 using the following equation:

$$h_c = h_{max} - \varepsilon\frac{\rho_{max}}{dP/dh} \tag{4.3}$$

ε depends upon the indenter geometry and in this case is ~0.75.

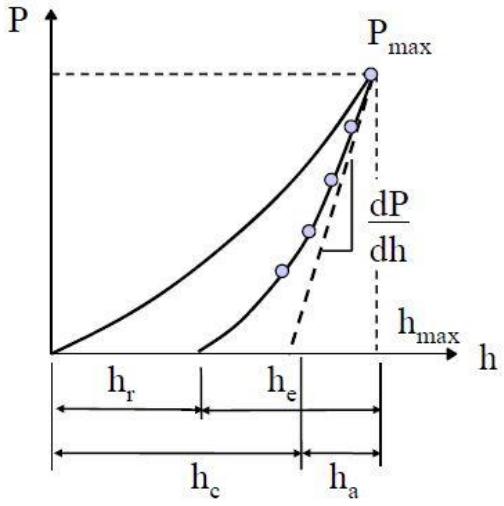

Figure 4-4: Nano-Indentation load against displacement curve used to calculate the hardness of a material [170].

4.5.5 Scanning electron microscopy (SEM)

Scanning electron microscopy (SEM) was performed using either a LaB6 Phillips XL-30 or a field emission gun (FEG) Jeol 7000F, both with Oxford Instruments plc EDX capability. The Jeol 7000F also has wave dispersive x-ray spectroscopy (WDS) capabilities. These were used to examine the planar surface of the oxides and to perform cross-sectional analysis on sections through the specimens. This allowed the oxidation behaviour of the alloy to be characterised. In addition these

instruments were used to analyse the fatigue initiation sites of the fracture surfaces from the high cycle fatigue specimens. An accelerating voltage of 20 KeV was generally used throughout, although when appropriate lower KeVs were used and the probe current was varied according to purpose, i.e. imaging/EDX.

4.5.6 Focused ion beam (FIB)

The focused ion beam (FIB) was used to investigate the presence of voids as sub-surface damage underneath and within the oxide layer, which has been reported in the literature [107]. It was also used to section through cracks penetrating the oxide layer. FIB sectioning was performed using a Quanta 3D dual beam FEG FIB, with a 30 KeV gallium ion source, under the following parameters:

- The specimen was placed on a five axis motorised stage which was tilted to 52° to position the surface perpendicular to the ion beam.
- A protective tungsten layer (~35 x 3 x 4 µm) was deposited on top of the area of interest.
- The specimen was then milled by a series of gallium ion beams at varying currents.
    - First a regular cross section was milled using a 65 nA current.
    - A rectangle was then milled using a 30 nA current.
    - Two clean cross sections were milled using first 7 nA and finally a 1 nA current.
    - This process was repeated with 1 nA (and/or 0.5 nA) current to clean the cross section until the required finish was achieved.

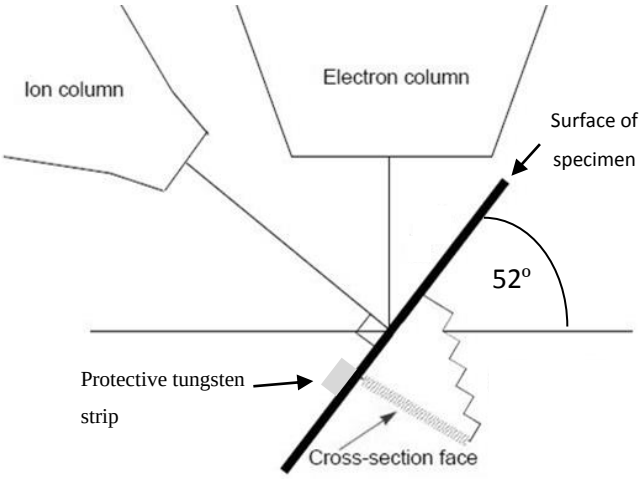

Figure 4-5: Schematic diagram of how the sectioning was achieved on a dual-beam FIB

The dual-beam capability allowed the cross-section to be imaged at every stage using secondary electrons produced by an electron ($SE_{electron}$)[1] beam without tilting the specimen further (Figure 4-5). Further imaging was performed using the secondary electrons produced by the ion beam (SE_{Ion})[2],

[1] $SE_{electron}$ – Secondary electrons produced by the impact of electrons from a field emission gun.
[2] SE_{ion} – Secondary electrons produced by the impact of gallium ions from an ion beam.

where channelling contrast highlights the grain structure of the specimen. Imaging with secondary electrons produced from the ion beam was performed at different incident angles as this affects the contrast of the image because different relative orientations of the ion beam to the crystalline target produce different ion/electron yields. An Everhart-Thorley detector was used to collect the secondary electrons produced from the impact of either the gallium ion or electron beam.

4.5.7 X-ray diffraction (XRD)

An automated Philips XPert x-ray diffractometer (Cu Kα source at 40 Kv and 20 mA) at a scan rate of $2^{o}.min^{-1}$ over the 2θ range of 10-100º was used to identify the oxides present. Phase indexing was performed using the PDF-2 database. This was performed on a range of oxidised specimens and one un-oxidised specimen (Table 4-IV).

Table 4-IV : XRD testing matrix

	24 h	500 h	2000 h
700°C	x	x	x
750°C	x	x	x
800°C	x	x	x
700°C (SP)	x	x	x
750°C (SP)	x	x	x
800°C (SP)	x	x	x
700°C (TU)	x	x	x
700°C (VP)	x	x	x
700°C (SW)	x	x	x

4.5.8 Image analysis

Image analysis was performed on backscattered secondary electron (BSE) images taken at a magnification where the feature analysed (i.e. external and internal oxide or external oxide and γ′ denuded zone) equalled between 25% and 75% of the image. Images were taken from randomly selected areas from the cross-section. A number of different measurements were recorded from the images and these are shown in Figure 4-6 and Figure 4-7 and described below:

1. External oxide scale (chromia)
    - Measurements of the chromia external oxide scale were taken in the direction of the external oxide growth from the air/external oxide scale interface to the external oxide scale/alloy interface, shown as the solid yellow line on Figure 4-7(A&D) as measurement 1. The complex surface profile of the alloy complicates this as does the formation of TiO_2 above the chromia layer. To aid the measurements of chromia thickness, EDX maps were taken for every condition of exposure time and temperature and used to differentiate between chromia and rutile. It was found that

rutile is discontinuous and forms largely in isolated grains at the surface that can be resolved under good contrast (Figure 4-7). It is further complicated by metallic protuberances or metallic regions within the oxide layer. No allowance was made for the presence or absence of these features on the occasions when measurements intersected them. Also no account was made for the small fraction of isolated voids that were encountered. It is estimated that the overall error on chromia thickness due to these factors was an overestimation of <3%.

2. Internal oxide penetration
   - This was measured from the external oxide/alloy interface to the tip of the internal oxide penetration. In the polished condition this is broken down into two measurements, since two distinct penetrations are seen, intragranular and intergranular, shown as the dashed white lines on Figure 4-7(A) as 2a and 2b respectively.
   - In all other conditions one measurement accurately described the damage (measurement 2 in Figure 4-7(D)).
3. γ′ denuded zone
   - This was measured from the external oxide/alloy interface to the depth of the secondary γ′ penetration. In the polished condition this is broken down into two measurements, since two distinct penetrations are seen, intragranular and intergranular, shown as the dotted red lines on Figure 4-7(B) as 3a and 3b respectively.
   - In all other conditions one measurement accurately described the damage (measurement 3 in Figure 4-7(D)).
4. Total oxide damage
   - This was measured from the air/external oxide interface to the depth of the secondary γ′ penetration. In the polished condition this is broken down into two measurements, since two distinct penetrations are seen, intragranular and intergranular, shown as the solid black lines on Figure 4-7(C) as 4a and 4b respectively.
   - In all other conditions one measurement accurately described the damage (measurement 4 in Figure 4-7(D)).
5. Cr-Mo rich grain boundary phase dissolution depth
   - This was measured from the external oxide/alloy interface to the depth of the grain boundary Cr-Mo rich phase dissolution (Figure 4-6).

The measurements were executed using Image J (1.45) software with a grid overlay plugin. The plugin was used to place 5 equally spaced lines horizontally across each image and measurements were recorded point to point at these intersecting points. The measurements of internal oxidation, γ′

denuded zone and carbide dissolution were taken perpendicular to the surface at these intersecting points to allow for an accurate measure of the useful section loss of the alloy, whereas the measurements of external oxide are in the direction of growth. On occasion where the features were infrequent (intergranular penetrations/Cr-rich grain boundary phase dissolution) and did not intersect the sampling lines the measurements were made where appropriate. Before measurements are taken the scale needs to be set using the scale bar stamped on the images. Fifty measurements were taken from ten separate images for all conditions, the large number of measurements allow a reproducible average and standard deviation to be given. The exception to this is in the intergranular internal oxide penetration and Cr-Mo rich phase dissolution, where ten and twenty measurements were produced respectively. The smaller number of measurements was due to the infrequency of this oxide/damage. Measurements were recorded to one decimal place.

Finally, measurements were also taken to analyse the area fraction of secondary γ′ in all un-oxidised conditions. Again Image J was used to calculate the area fraction of secondary γ′ in the centre and surface regions of the specimen. This was done by converting the image to binary before adjusting the threshold, so that an accurate representation of the secondary γ′ particles is seen. A measurement of the area that the secondary γ′ particles cover can then be calculated. This was performed on six images in both regions.

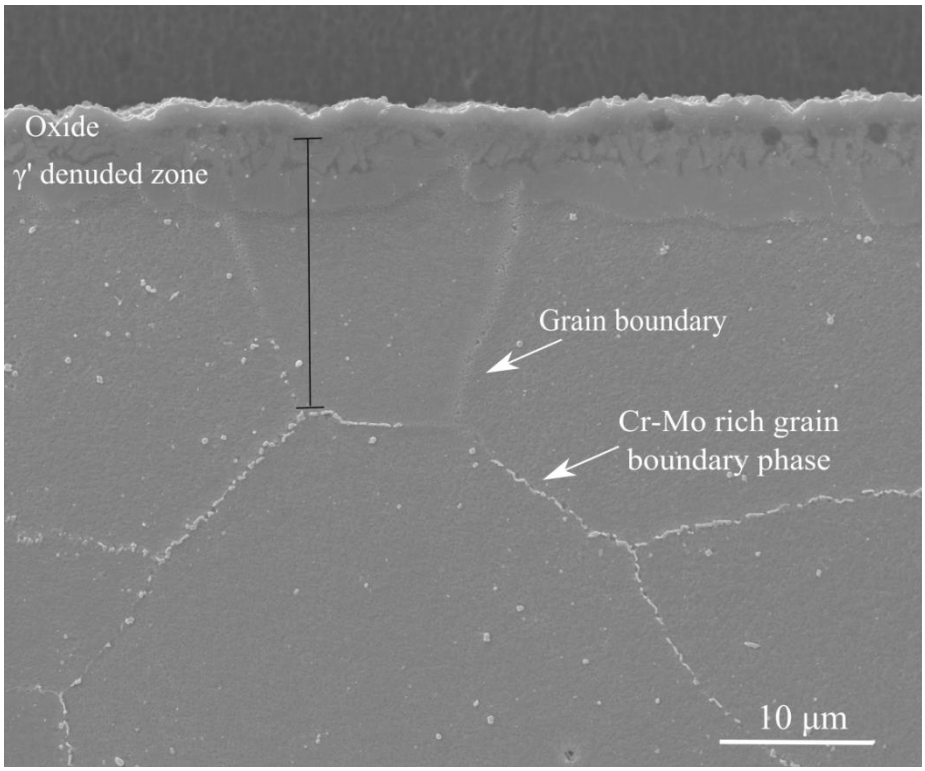

Figure 4-6: SE image of an etched (Kallings reagent) cross-section through a vibro-peened specimen oxidised at 700°C for 2000 hours, illustrating the presence of grain boundary Cr-Mo rich phase (GB) and how this phase dissolution depth was measured.

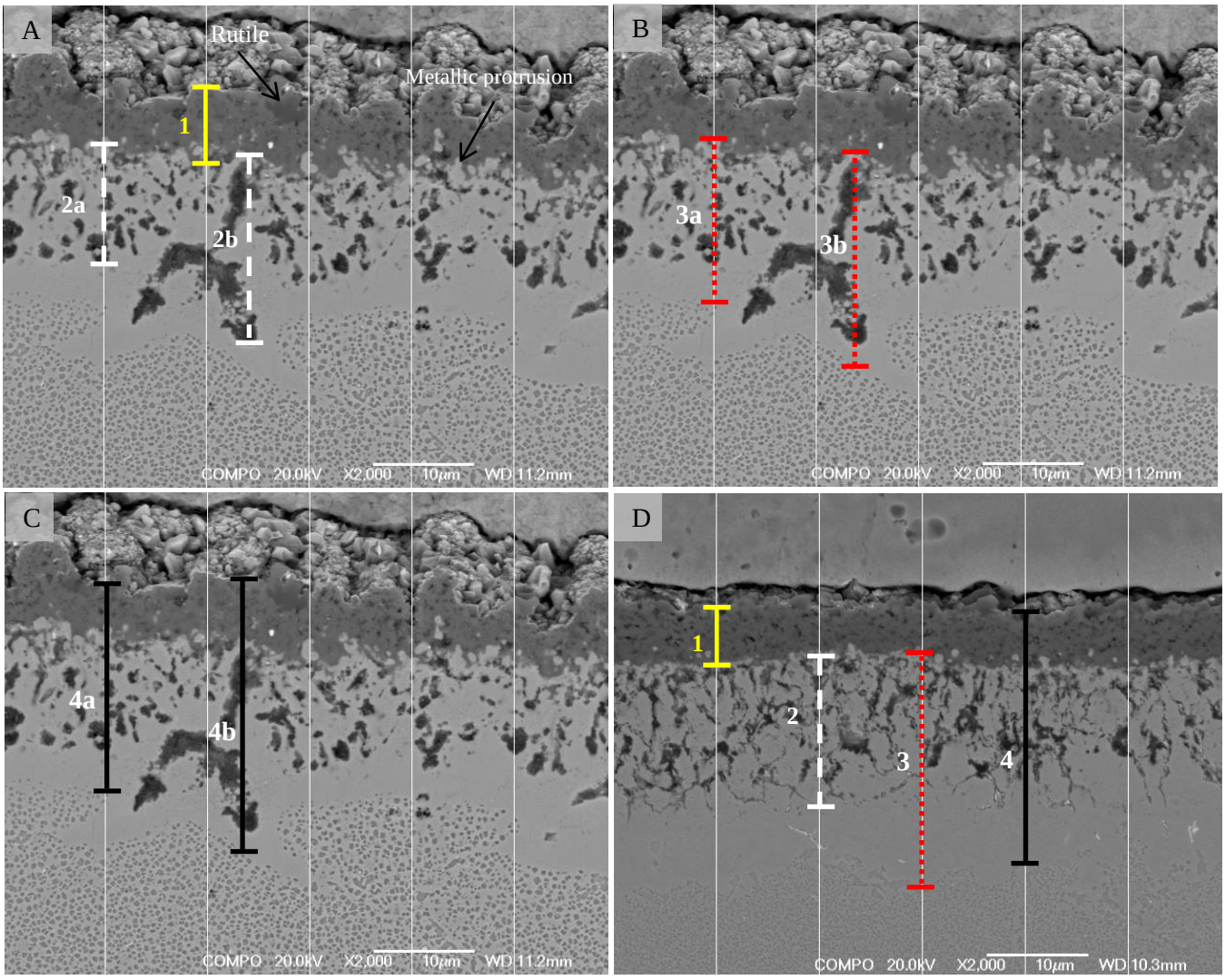

Figure 4-7: BSE micrographs of the γ′denuded zones of oxidised at 800°C for 2000 hours. A) Polished CG RR1000 illustrating how external oxide thickness (1) and intergranular (2b) and intragranular (2a) internal oxide were measured, B) Polished CG RR1000 illustrating how intergranular (3b) and intragranular (3a) γ′denuded zones were measured, C) Polished CG RR1000 illustrating how intergranular (4b) and intragranular (4a) total oxide damage were measured, and D) Shot-peened CG RR1000 illustrating how external oxide thickness (1), internal oxide penetration (2), γ′denuded zones (3) and total oxide damage (4).

Chapter 5 - Oxidation of Ni-based Superalloy, RR1000

5.1 Introduction

Ni-based superalloys have been optimised, compositionally and microstructurally, to operate in the highly stressed conditions occurring in the hot sections of a gas turbine engine. Oxidation resistance has often been an afterthought in the development of these alloys in favour of the high temperature mechanical properties. Engine manufacturers are under a significant amount of market pressure to produce more efficient engines, with higher specific fuel consumptions and reduced NO_x and CO_2 emissions. This necessitates an increase in the compressor discharge and turbine entry temperatures, which will consequently result in accelerated environmental degradation of the rotating components. High temperature oxidation resistance is therefore becoming increasingly important as, when lifing rotating components, the loss of useful metal cross-section, through the formation of internal oxides and depletion of strengthening elements and phases (γ'), have the potential to reduce component lives. For this reason there is a significant need to understand and quantify the oxidation kinetics and damage.

The aim of this research was to investigate and quantify the oxidation kinetics and oxidation damage of coarse-grained (CG) RR1000 in an ideal condition (polished to an arithmetic mean roughness of ~0.3 μm). Most current Ni-based superalloys used for rotor disc applications are characteristic of chromia-forming alloys that consequently suffer from extensive internal oxidation [47, 104, 107, 115]. The formation of internal oxides is undesirable since they can have a significant detrimental effect on the mechanical properties of the alloy especially if it causes strengthening elements to be removed [84]. Therefore significant emphasise was placed on characterising the external and sub-surface oxidation damage at a range of potential operating temperatures. Oxidation kinetics were assessed using both mass gain and metallographic measurements.

5.2 Results and Discussion

5.2.1 Mass gain kinetics of polished CG RR1000

Figure 5-1 shows the change in specimen mass with time over the temperature range tested (650°C-800°C). It is important to stress that no spallation was observed for any of the specimens tested and any mass gain can be attributed to oxidation products. Figure 5-1 clearly shows that the higher the exposure temperature the larger the specimen mass gain, while also illustrates that the rate of mass gain decreases with time at each temperature, concluding that sub-linear growth behaviour is occurring.

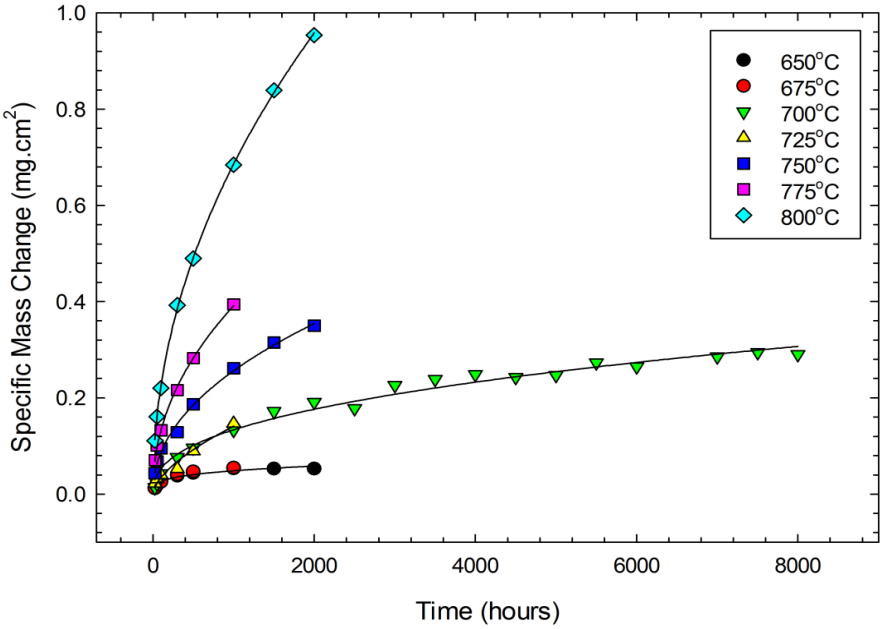

Figure 5-1: Plot of specific mass change against time for each temperature tested in a single zone furnace for a minimum of 1000 hours and a maximum of 8000 hours.

High temperature oxidation kinetics can be reasonably described by the following equation:

$$\left(\frac{\Delta m}{A}\right)^n = k_n\, t \tag{5.1}$$

where $\left(\frac{m}{A}\right)$ is the mass change/surface area (mg.cm^{-2}), exposure time (t) in seconds and k_n is the oxide growth rate constant. The value of n can be determined by plotting log $\left(\frac{m}{A}\right)$ against log t (Figure 5-2).

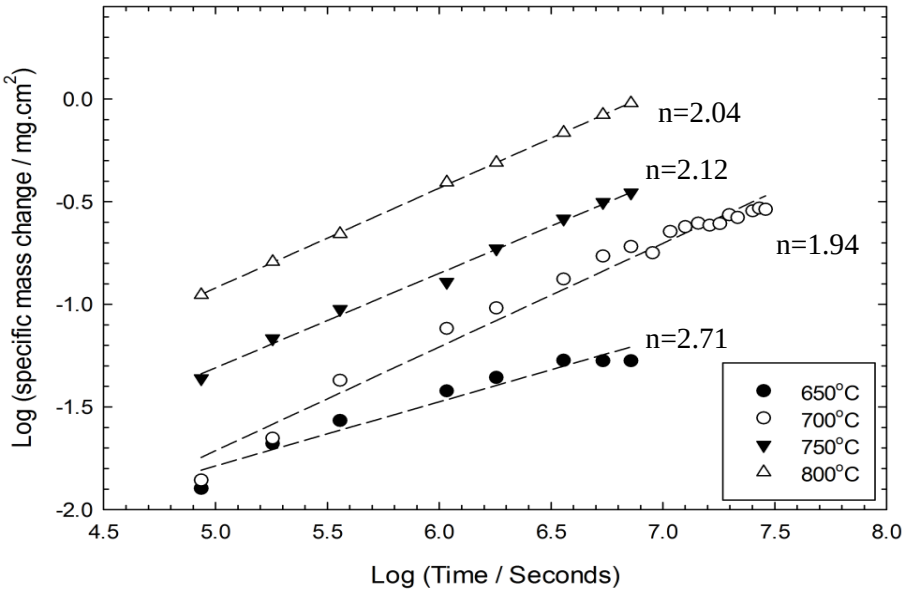

Figure 5-2: Plot of log specific mass change against log exposure time for 650°C, 700°C, 750°C and 800°C showing that the mass gain kinetics can be approximated to parabolic behaviour, n =2.

Figure 5-2 shows the determination of the oxide growth regime (n), for three of the temperatures tested (700, 750 and 800°C). In this way the values of n at each temperature can be evaluated and both Table 5-I and Figure 5-2 show that parabolic behaviour can be reasonably assumed (n = 2) for this alloy between 675°C and 900°C, to give a parabolic rate constant (k_p) in $mg^2cm^{-4}s^{-1}$. At 650°C the behaviour cannot be described accurately assuming parabolic kinetics as the n value indicates significantly sub-parabolic behaviour (n = 2.71). This behaviour is closer to cubic (n = 3) rather than parabolic, but nevertheless a parabolic rate constant has been calculated for 650°C to allow a comparison to other temperatures and conditions. It also tallies well with values from the literature which are regularly approximated according to parabolic behaviour. The parabolic nature of the oxidation kinetics can be illustrated by Figure 5-3, showing the specific mass change raised to a power of n = 2, with the fit of the lines (R^2 values) showing good agreement with parabolic behaviour. A perfect straight line indicates exactly parabolic kinetics.

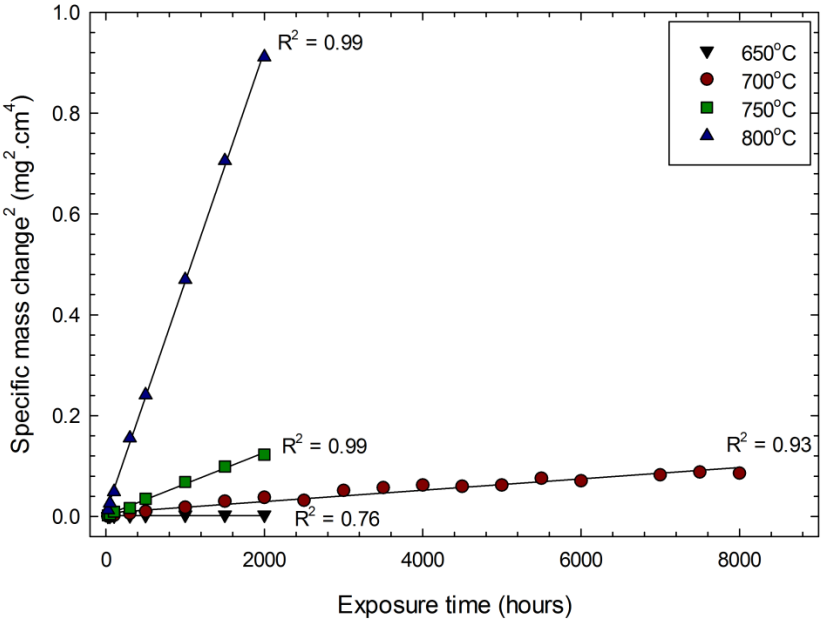

Figure 5-3: Plot of specific mass change squared against time for 650°C 700°C, 750°C and 800°C with R^2 values.

Table 5-I: Best estimate values of the exponent, n, for mass gain kinetics for coarse-grained RR1000 and the mass gain parabolic rate constants determined for coarse-grained RR1000 and pure chromia formation on 20Cr austenitic steel.

Temperature	RR1000	RR1000	20Cr austenitic steel [171]
	n	k_p ($mg^2.cm^{-4}.s^{-1}$)	
650°C	2.71	$5.35x10^{-10}$	-
675°C	2.27	$9.76x10^{-10}$	-
700°C	1.94	$3.48x10^{-9}$	$7.99x10^{-10}$
725°C	2.09	$5.49x10^{-9}$	-
750°C	2.12	$1.77x10^{-8}$	$3.79x10^{-9}$
775°C	2.19	$4.34x10^{-8}$	-
800°C	2.04	$1.29x10^{-7}$	$1.56x10^{-8}$

A comparison of the parabolic rate constants for coarse-grained RR1000 and a pure chromia forming austenitic stainless steel are shown in Table 5-I, clearly showing that RR1000 oxidises much quicker (an order of magnitude) than for the formation of pure chromia on high chromium containing austenitic steel. Figure 5-4(a) illustrates the difference between CG RR1000 and the formation of pure chromia, indicating that other elements are oxidising in CG RR1000. It also shows that the gap between the formation of pure chromia and CG RR1000 narrows with decreasing temperature. The values from the other Ni-based superalloys fall broadly in line with CG RR1000 and demonstrates that all current chromia forming Ni-based superalloys are oxidising faster that the ideal case (Figure 5-4(b)).

An Arrhenius equation (5.2) can be used to calculate the activation energy for the formation of the oxide in both conditions.

$$k_p = k_o \exp\left(\frac{-Q}{RT}\right) \tag{5.2}$$

where k_p is a parabolic rate constant, k_o is a pre-exponential constant, Q is the activation energy for oxide growth ($kJ.mol^{-1}$), R is the gas constant, T is the exposure temperature (K). Figure 5-5(a) shows the full temperature range tested on this alloy, from both testing performed during this program of research and performed in a previous study [115]. A best fit regression line has been plotted through the complete data set and found a good fit (R^2 =0.97) with an activation energy of 296 $kj.mol^{-1}$. The 600^{o}C instantaneous k_p point seems to skew the data and by removing this point, as-shown in Figure 5-5(b) an extremely good fit is found (R^2=0.99), with a single activation energy of 325 $kJ.mol^{-1}$ (650-900^{o}C). The point can legitimately be removed because it was calculated, unlike the rest, from a single data point from one specimen at a single time period. This produces an instantaneous k_p rather than a well described k_p in the other conditions. In addition considering the extremely low mass gain at this temperature (600^{o}C) and time period (1000 hours), the accuracy of this point can be reasonably questioned. In the next section this is considered in more detail with Figure 5-5 showing that as the number of data points and exposure time increases the k_p values tend to decrease slightly. So further testing both in time, number of specimens and number of data points collected at 600^{o}C the growth kinetics could be predicted to fall in line with the best fit regression line produced for the rest of the data and so therefore can legitimately be excluded from the analysis.

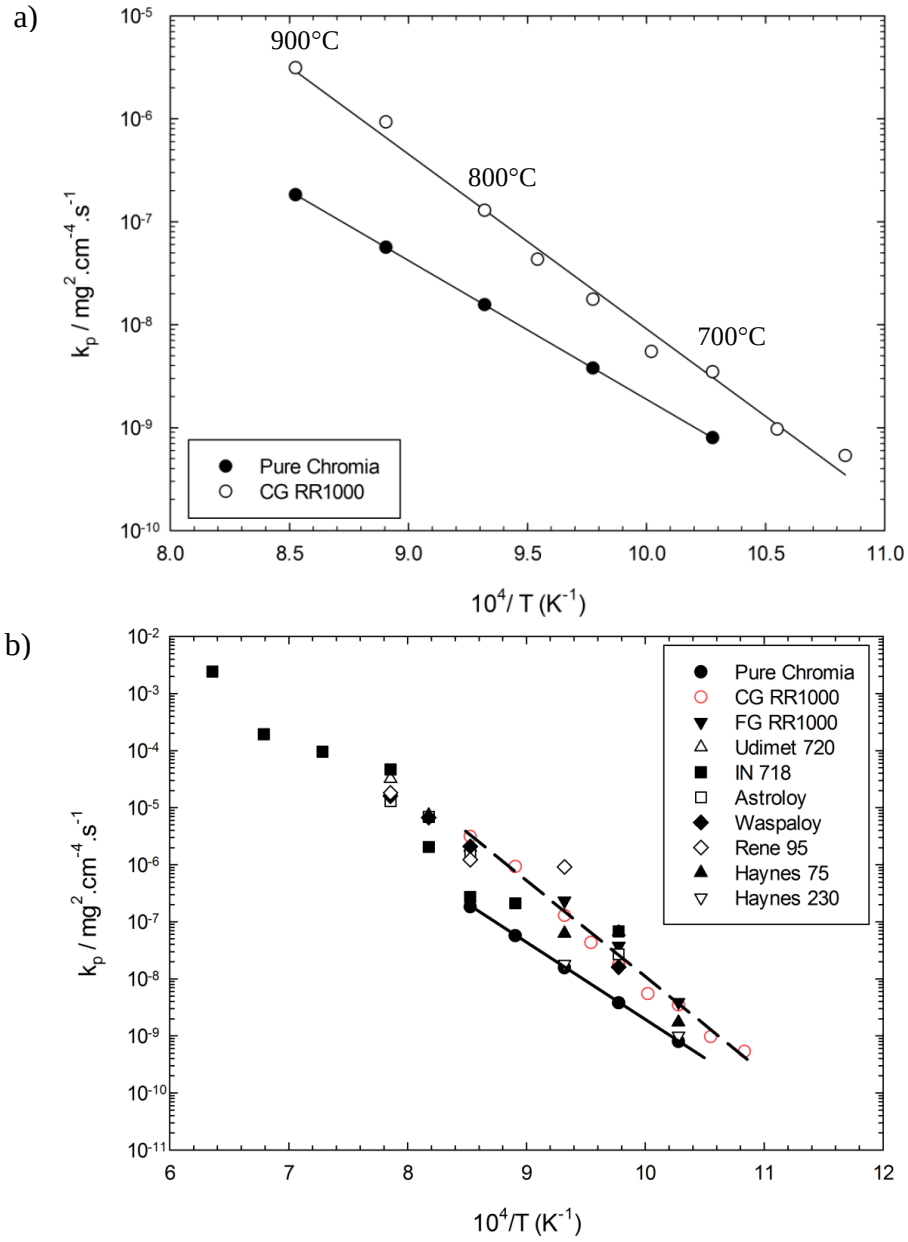

Figure 5-4: Arrhenius plot of k_p values from this study (shown as unfilled circles), compared with a) the expected k_p values for pure chromia growth on a high chromium containing austenitic steel and b) various Ni-based superalloys taken from the literature as well as the expected k_p values for chromia growth from a). Best fit lines for chromia growth and CG RR1000 are provided in both graphs and all exposures were undertaken in a laboratory [104, 107, 112, 113, 149].

Table 5-II: Activation energies of oxide formation on CG RR1000, compared to values from other Ni-based superalloys and pure chromia forming steel, listed along with the temperature range analysed [104, 106, 171].

Alloy	Activation energy (kJ.mol^{-1})	Temperature range tested
CG RR1000	325	650-900°C
FG RR1000	270	700-800°C
Udimet 720	250	750-1000°C
Astroloy	270	750-1000°C
Waspaloy	300	750-1000°C
20Cr austenitic steel	258	700-900°C

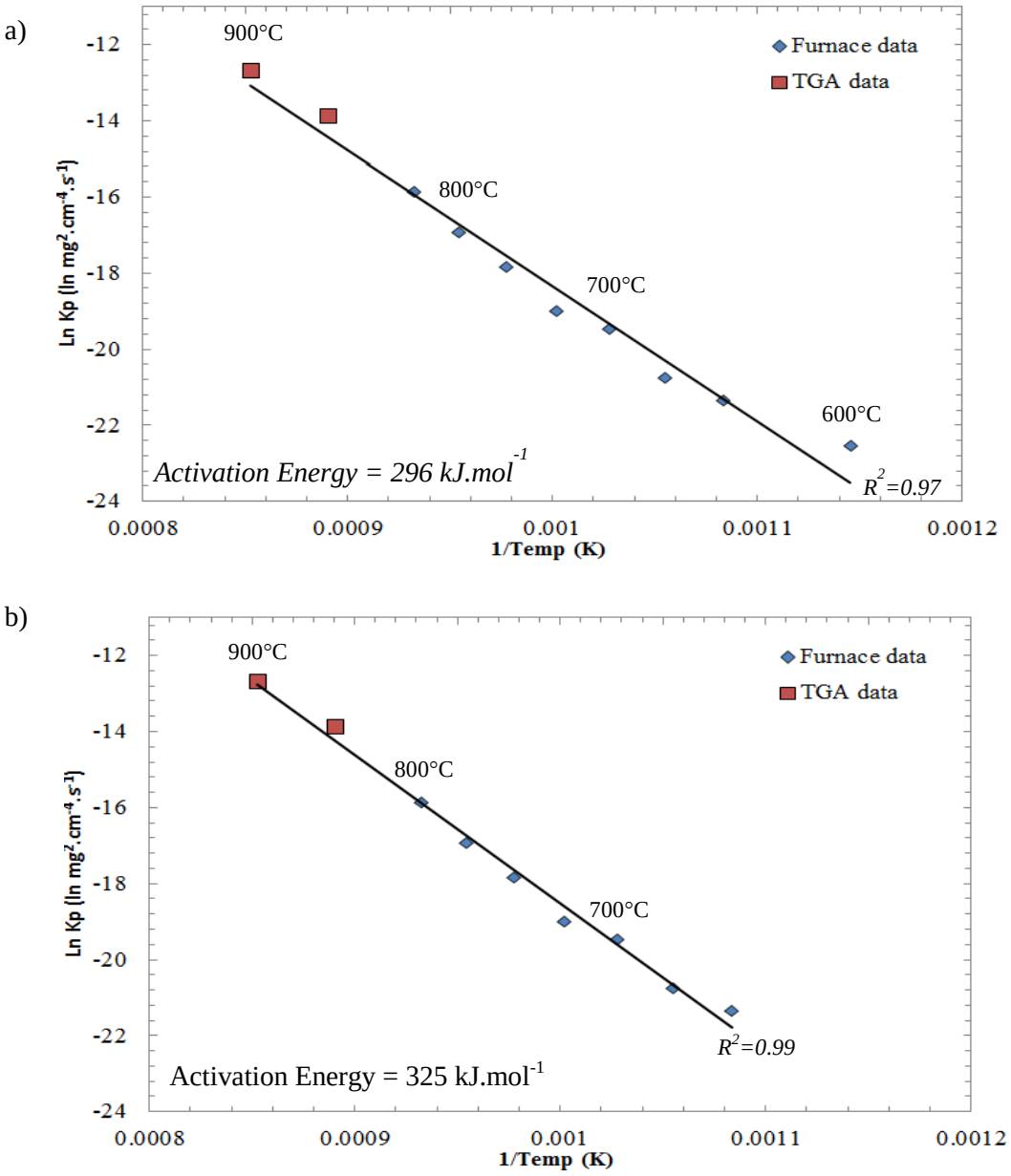

Figure 5-5: Activation energy of oxide formation on CG RR1000 over; a) the full temperature range tested (600-900°C) including a best fit regression lines. b) 650-900°C temperature range. The 850°C and 900°C values are courtesy of M.P. Taylor and are calculated from single specimens using TGA testing. The 600°C is an instantaneous k_p again courtesy of M.P. Taylor for one furnace exposure of 1000 hours.

The thermogravimetic analysis (TGA) data was incorporated at the higher temperatures (850-900°C) into the present data set, however since appreciable mass gain occurs even at these shorter times (100 hours) and being TGA tests, some 500 data points were recorded and used in the evaluation of the reaction kinetics. The activation energies for CG RR1000 are displayed in Table 5-II, along with the temperature range tested. It shows that these are comparable to other Ni-based superalloys used in HP disc applications.

The parabolic rate constants for mass gain are shown as a function of the inverse of the temperature in an Arrhenius plot of Figure 5-4(b) for the present alloy and similar chromia forming Ni-based superalloys [104, 107, 112, 113, 149]. The gradient of the line through this data set yields an activation energy of 325 kj.mol^{-1} and allows an expression for k_p of:

$$k_p = 8.73x10^8 \, exp\left[-\frac{325094}{8.314.T}\right] \; mg^2.cm^{-4}.s^{-1} \tag{5.3}$$

It should be noted that although the term activation energy is used this is not strictly correct since more than one alloy constituent is being oxidised and a single activated event is not occurring. Nevertheless it remains a useful way to describe the temperature dependence of the reaction kinetics and acts as a value for comparison between other chromia forming alloys.

In general the value of the activation energy for Ni-based superalloys is higher than those reported for the growth of pure chromia formation (258 kJ.mol^{-1}) on pure chromium and austenitic steel. The expected k_p values for chromia growth on simple austenitic steel are shown as the solid line in Figure 5-4. These rate constants, expressed in terms of mass gain were obtained from original metallographic data [171], by equating 1 mg.cm^{-2} mass gain to a chromia layer thickness of 6.0 μm. This line forms a lower bound to the Ni-based superalloy data.

The fact that in chromia forming Ni-based superalloys oxide growth rates are higher than those for pure chromia formation are not entirely unexpected since most Ni-based superalloys tend to allow oxidation of more than one element: Ti, Al and Cr, as is the case here. The composition and morphology of the oxide will be discussed at length in the coming pages.

5.2.2 Comparison between TGA and furnace data

A comparison between thermogravametic analysis (TGA) and long term furnace testing has been performed to establish the reliability of each technique. Figure 5-6 shows a comparison between short term thermogravametic analysis (TGA) testing (100 hours) from a previous study [115] and long term furnace exposures (minimum 1000 hours) over a temperature range of 600-900^{o}C. In TGA testing data points can be sampled at regular intervals online, that is while the sample is being oxidised, and can therefore collect around 500 data points in a 100 hour period. In furnace testing a data point can only be recorded when a sample is removed from the furnace and is therefore limited by the number of specimens that are oxidised at each temperature, or the number of times a specimen is removed from the furnace for analysis. Typically this would equate to 3-4 in a 100 hour period and 8-16 in a 1000 hour period. A good agreement is found between the full furnace (up to 8000 hours) and TGA

data and is illustrated in Figure 5-6(a) where the long term furnace measurements lie on top of the TGA measurements.

a) All data available

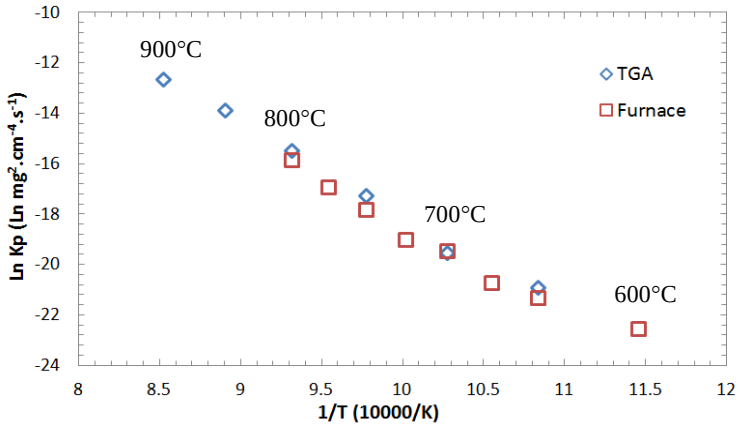

b) Data set from 100h TGA and 100h furnace testing

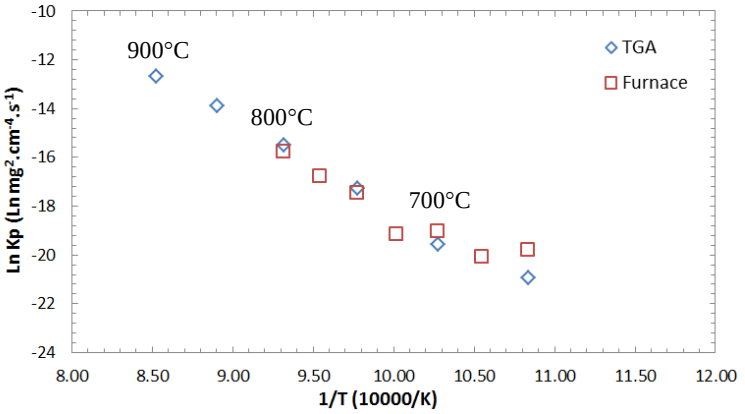

c) Data set from 100h TGA and 1000h furnace testing

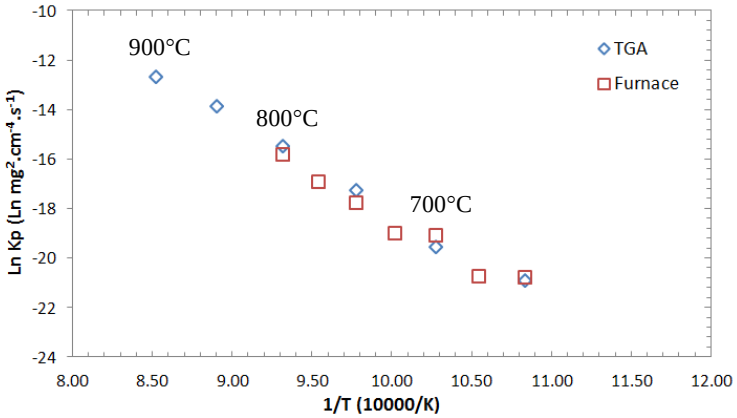

Figure 5-6: Arrhenius plots of the comparison between long term furnace testing and short term thermogravametic testing. a) k_p's calculated from the full data set collected (100h TGA exposures and 1000 or 2000h furnace exposures), b) k_p's from full 100 hour TGA exposures and the first 100 hours of furnace exposures and c) k_p's calculated from the full 100 hour TGA exposures and the first 1000 hours of furnace exposures.

As we move on to a comparison of furnace testing for 100 hours against TGA testing for 100 hours the data points no-longer lie on top of each other but significantly this only occurs at lower temperatures and illustrates that furnace testing is generally not as reliable at lower temperatures (<750^{o}C) at short time periods (Figure 5-6(b)). Once the furnace testing data interval has been increased to 1000 hours the two testing methods show agreement again. As such any furnace testing should be performed over prolonged periods of time (1000 hours). The reason for this is that only a small number of data points are collected during furnace testing compared to TGA testing and therefore TGA data more accurately describes the actual oxide growth as less interpolation in between data points is needed. This is compounded by the extremely low mass changes at short time periods and low temperatures. A further benefit to TGA testing includes an accurate determination of oxide spallation during testing although it is important to note that no signs of spallation have been seen in this alloy.

5.2.3 Surface oxidation

Figure 5-7 illustrates the surface morphology of the typical oxide seen on CG RR1000, showing the individual oxide grains present.

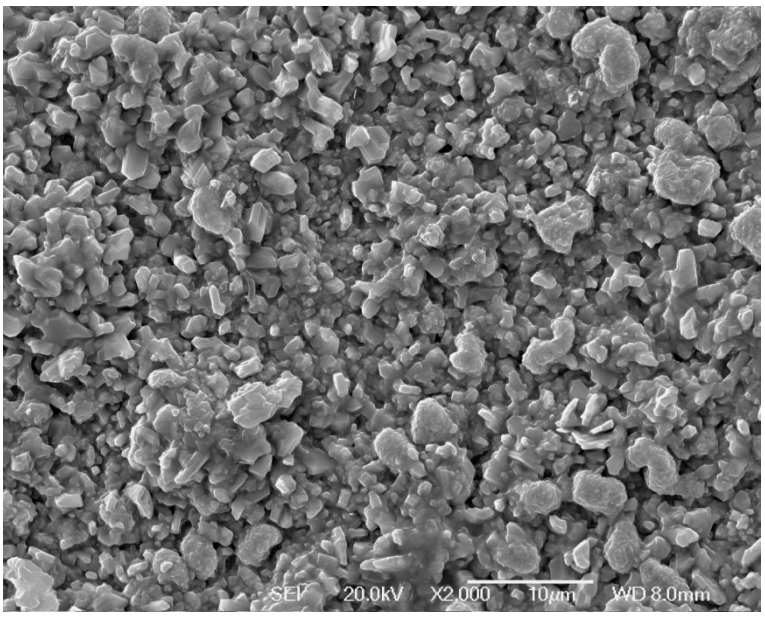

Figure 5-7: SEM micrograph of the surface oxide structure oxidised at 800^{o}C for 2000 hours.

This is followed by Figure 5-8 showing the oxide scale at two different magnifications over a period of time (700^{o}C for 24-2000 hours). An enhancement at the grain boundaries can clearly be seen, these raised regions occurred at regular intervals in circular patterns of 30-50 μm in diameter. This occurred across the entire surface and coincidently 30-50 μm is the grain size of the material and therefore helps to confirm this enhancement is occurring at the grain boundaries.

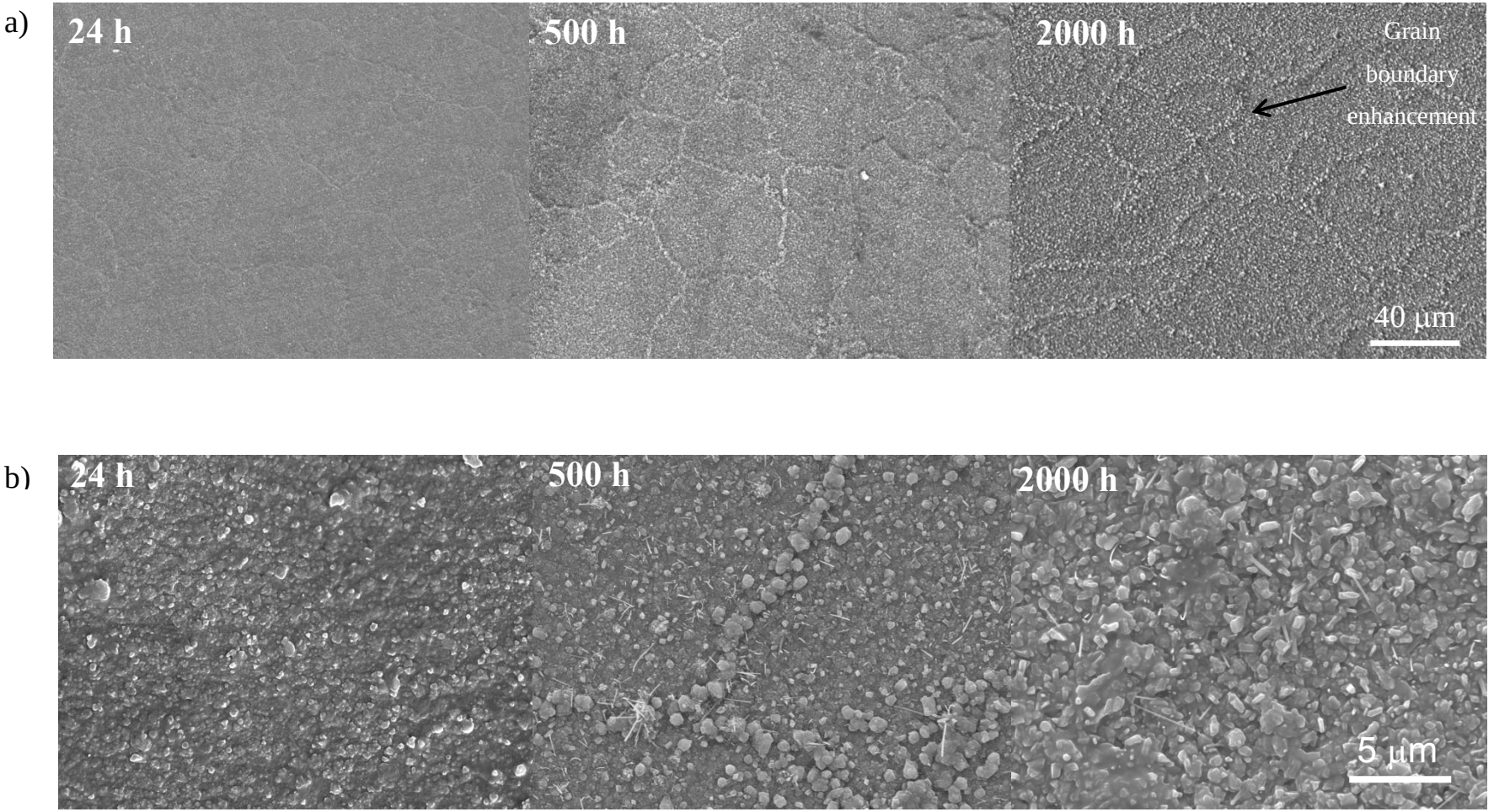

Figure 5-8: SE images of CG RR1000 oxidised in air at 700°C for the times stated on the images. Images were taken at two different magnifications to illustrate the morphology of the oxide.

Again from Figure 5-8 the oxide scale can be seen as a scale made up of individual oxide grains and that these grains increase in size with exposure time. Additionally much larger grains are present on the grain boundaries. A confocal microscope was used to record 3D images of the surface in oxidised CG RR1000 (Figure 5-9). Enhanced external grain boundary oxidation was observed in some conditions e.g. at 700°C from 100 hours onwards and at 800°C at all times up to 500 hours, although from Figure 5-8 enhanced growth at the grain boundaries can be seen at 24 hours but the magnitude of the enhancement is likely to be below the resolution of the confocal microscope to measure. The reported resolution is 0.01 μm but this is reduced dramatically by the roughened surface. Measurements from a number of sites were taken from confocal micrographs of the height of the oxide at the grain boundaries above the rest of the oxide surface, these values +/- standard deviation are recorded in Table 5-III.

Table 5-III: Enhanced grain boundary oxidation, μm (±1 Standard Deviation).

	24h	50h	100h	500h	2000h
700°C	0	0	0.30 (±0.12)	0.40 (±0.1)	0.67 (±0.2)
750°C	0	0.41 (±0.16)	0.82 (±0.34)	0.51 (±0.1)	1.29 (±0.59)
800°C	0.39 (± 0.06)	0.83 (±0.39)	1.19 (±0.23)	3.10 (±0.55)	0

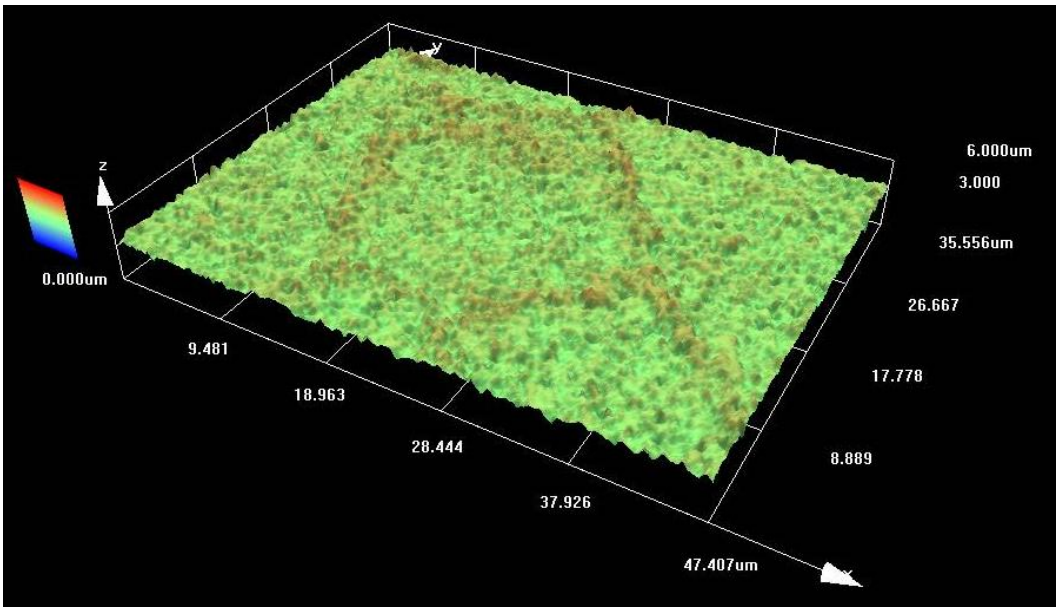

Figure 5-9: Confocal micrograph showing enhanced grain boundary oxidation of a CG RR1000 specimen oxidised in laboratory air at 800°C for 50 hours.

This illustrates that there is enhanced oxidation occurring at the grain boundaries at temperatures above 700°C. The sample that had spent 2000 hours at 800°C did not show any enhanced grain boundary oxidation. This may be due to increased intra-grain oxidation, removing any grain boundary

enhancement. The reason for this enhancement is due to the grain boundaries acting as short circuit diffusion pathways leading to an increased transport of chromium and titanium ions across the oxide scale causing a local increase in growth rate.

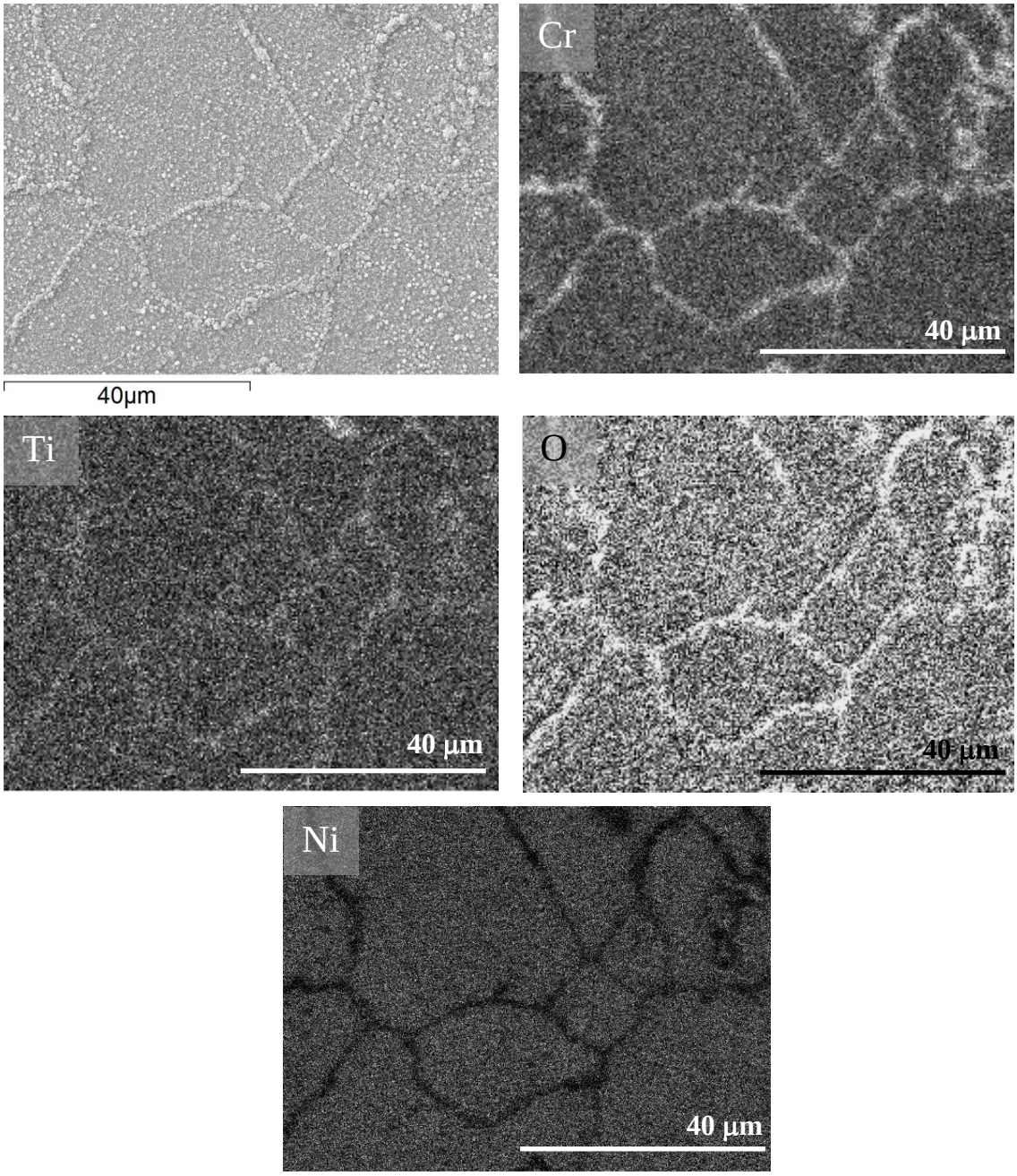

Figure 5-10: EDX map illustrating the surface oxide composition of a CG RR1000 specimen oxidised at 700°C for 500 hours.

The composition of the external oxide scale is chromium and titanium rich with Figure 5-10 again showing enhanced grain boundary oxidation. Rather than illustrating a composition change through the enhanced chromium and titanium counts from the grain boundaries (and deficit of Ni) it shows that the EDX analysis picked up less base material and more oxide at the grain boundaries.

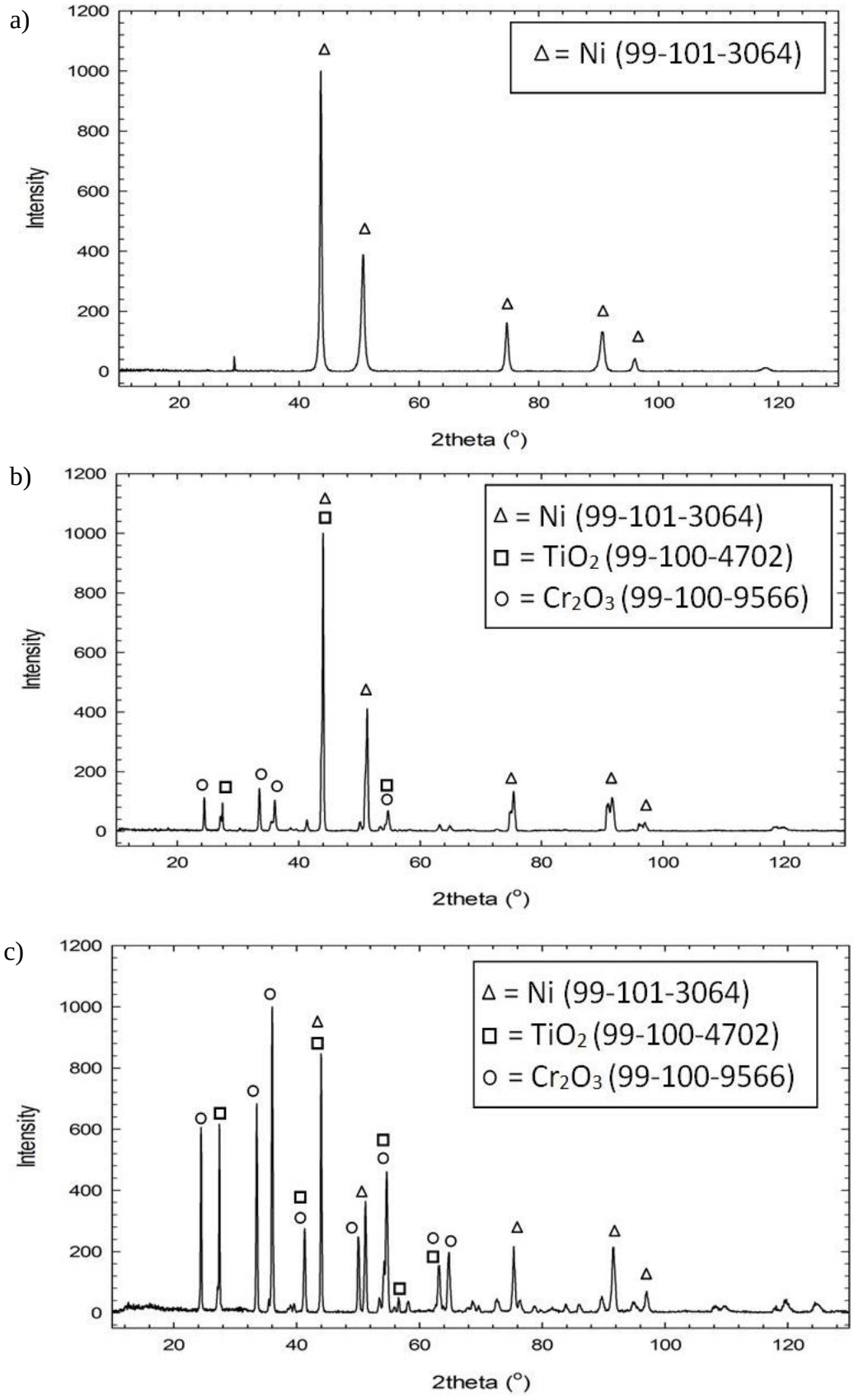

Figure 5-11: XRD traces of specimens held at (a) 700°C, (b) 750°C and (c) 800°C, for 100 h with identification of the peaks between a 2θ of 10–100°. The key contains the ICDD card number of the phases identified.

Further evidence of the external oxide scale composition is provided from the XRD spectra obtained from the surface oxide layer shown in Figure 5-11 for specimens exposed for 100 h at each of 700, 750 and 800°C. From Table 5-IV it can be seen that the chromium and titanium rich oxide consists of chromia and rutile at all temperatures, although the oxide was too thin for XRD scans at the shorter time periods at 700°C and 750°C. Sub-surface oxides could not be detected with confidence in these XRD scans because of their small volume fraction although peaks associated with the substrate alloy were present. Any significant changes in the crystallographic texture of the underlying alloy between the samples would be noticed as the relative intensities of the detected x-rays associated with the phase indexed would vary. No significant crystallographic texture was seen in this polycrystalline alloy.

Table 5-IV: XRD results identifying the oxides present on oxidised CG RR1000

	24h	100h	500h	2000h
700ºC	-	-	TiO_2 & Cr_2O_3	TiO_2 & Cr_2O_3
750ºC	-	TiO_2 & Cr_2O_3	TiO_2 & Cr_2O_3	TiO_2 & Cr_2O_3
800ºC	TiO_2 & Cr_2O_3	TiO_2 & Cr_2O_3	TiO_2 & Cr_2O_3 & $NiCr_2O_4$ (tr)	TiO_2 & Cr_2O_3 & $NiCr_2O_4$ (tr)

5.2.4 Oxidation damage

The oxidation damage of Ni-based superalloy, RR1000, resulting from prolonged high temperature exposure is complex. The typical oxide morphology is shown in the cross-section of Figure 5-12 and shows both a continuous external oxide scale with extensive sub-surface damage. Enhanced grain boundary oxidation of both the external oxide and the internal oxide can also be seen.

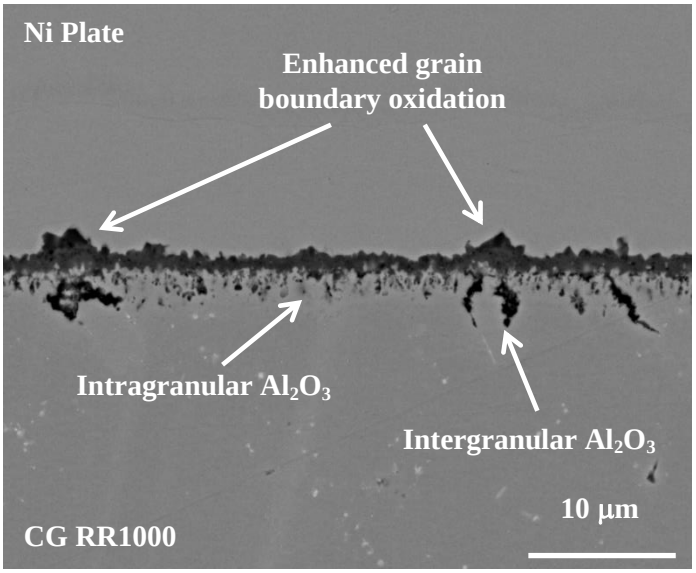

Figure 5-12: SEM micrograph of a sectioned sample of CG RR1000 oxidised in laboratory air at 750°C for 1000 hours, showing intergranular internal alumina oxidation.

Significant sub-surface damage by internal oxidation is present underneath the protective oxide scale. The internal oxide occurs in two distinct precipitations, intergranular and intragranular. The intergranular penetrations are acicular in nature and penetrate to a greater depth than the globular intragranular penetrations (Figure 5-13(a)). These internal oxides are predominantly alumina as can clearly be seen from EDX maps in Figure 5-14. This is similar to what has been found in other chromia forming Ni-based superalloys [47, 104] as well as in this current alloy [115]. The deeper alumina penetrations at the grain boundaries suggest that these sites act as short circuit diffusion pathways [85].

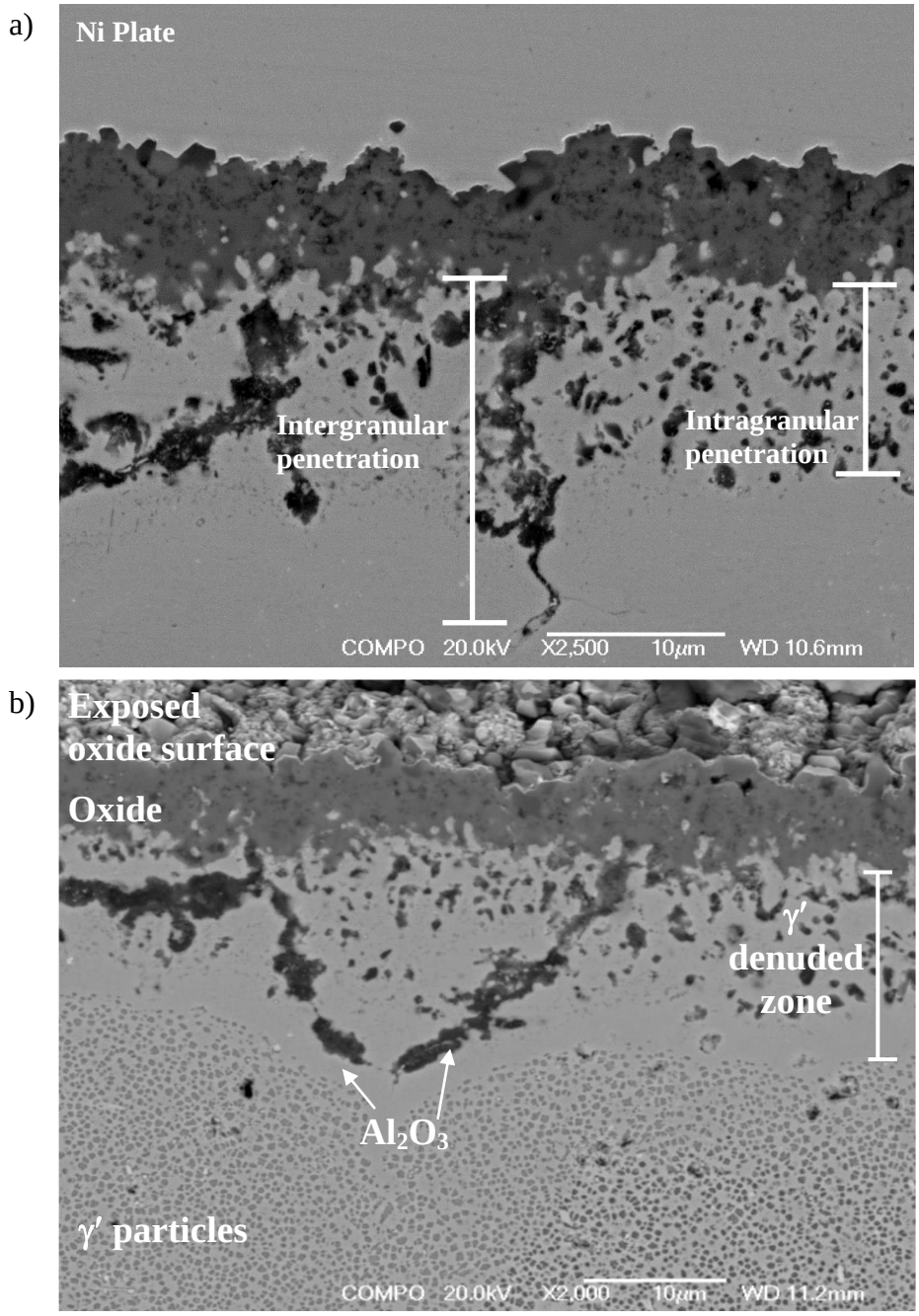

Figure 5-13: BSE images of coarse-grained RR1000 oxidised at 800^{o}C for 2000 hours showing a) the oxide morphology and the two types of internal oxide and b) the γ′ denuded zone (etched with Kallings reagent).

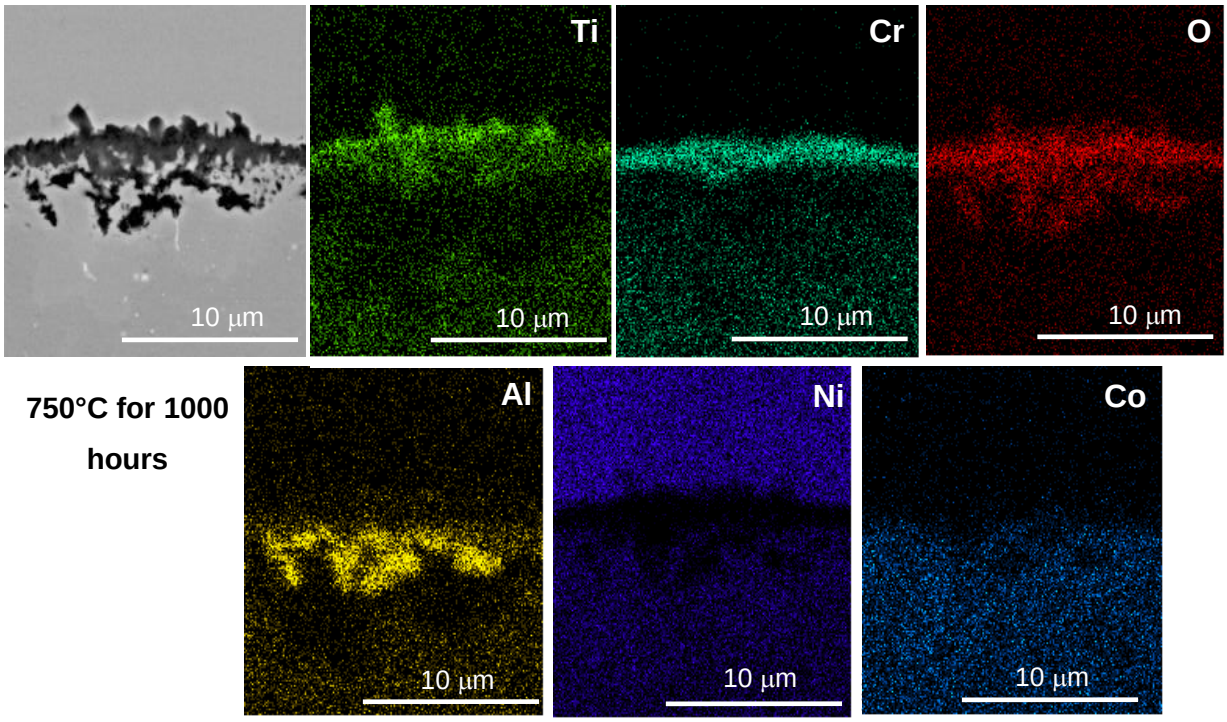

Figure 5-14: BSE image and EDX maps of a section through a specimen held at 750°C for 1000 hours showing the distribution of elements in the oxides formed, as indicated by the presence of oxygen.

Extending underneath this internal oxide is a significant γ′ denuded zone, Figure 5-13(b). This is a region free of γ′ particles, as aluminium depletion due to internal oxide formation has caused the dissolution of γ′ particles and this denuded zone follows the profile of the internal alumina penetrations. No recrystallisation of the grains was found in this alloy within the depletion zone although recrystallisation has been found in both Ni-based superalloys, ME3 and RR1000 (with a fine grained microstructure [4-6 μm]) [47, 107]. In some cases at the higher temperatures (>800^{o}C) TiN particles are formed within the γ′ denuded zone but ahead of the alumina internal precipitates (Figure 5-15). While it is expected that this phase is TiN, it is possible that it could be Ti(C, N) phase and requires further analysis using TEM.

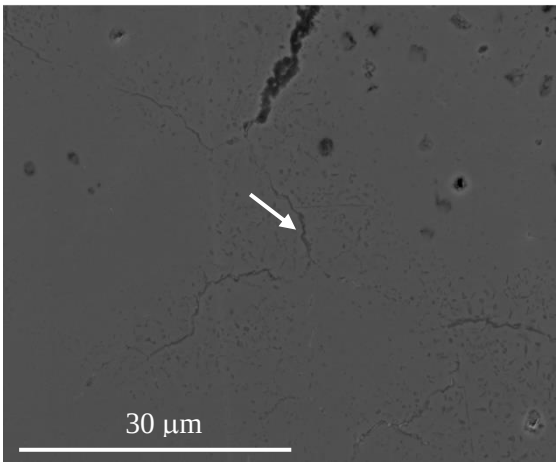

Element	Atomic %
N	10.5
O	0
Al	1.1
Ti	24.4
Cr	10.5
Co	14.6
Ni	36.6

Figure 5-15: BSE image showing the presence of a TiN and the location (white arrow) at which WDS/EDX analysis was performed. Samples was oxidised at 900^{o}C for 100 hours (courtesy of M.P. Taylor).

Underneath this region is a region depleted in Cr-Mo rich grain boundary phases. This is likely to be caused by the depletion of Cr used to supply and form the external chromia scale (Figure 5-16(a)). EDX linescans show that these phases are Mo and Cr rich, Figure 5-16(b), with point analysis recording values of 15 wt. % and 23 wt. % for Mo and Cr respectively compared with 5% and 15% in the bulk alloy. This phase is likely to be either $M_{23}C_6$ or sigma phase, with nominal compositions of $(Cr, Mo)_{23}C_6$ and $(Ni, Co)_x(Cr, Mo)_y$ respectively, which have both been shown to form in this alloy and can both contain significant amounts of Cr and Mo [172, 173].

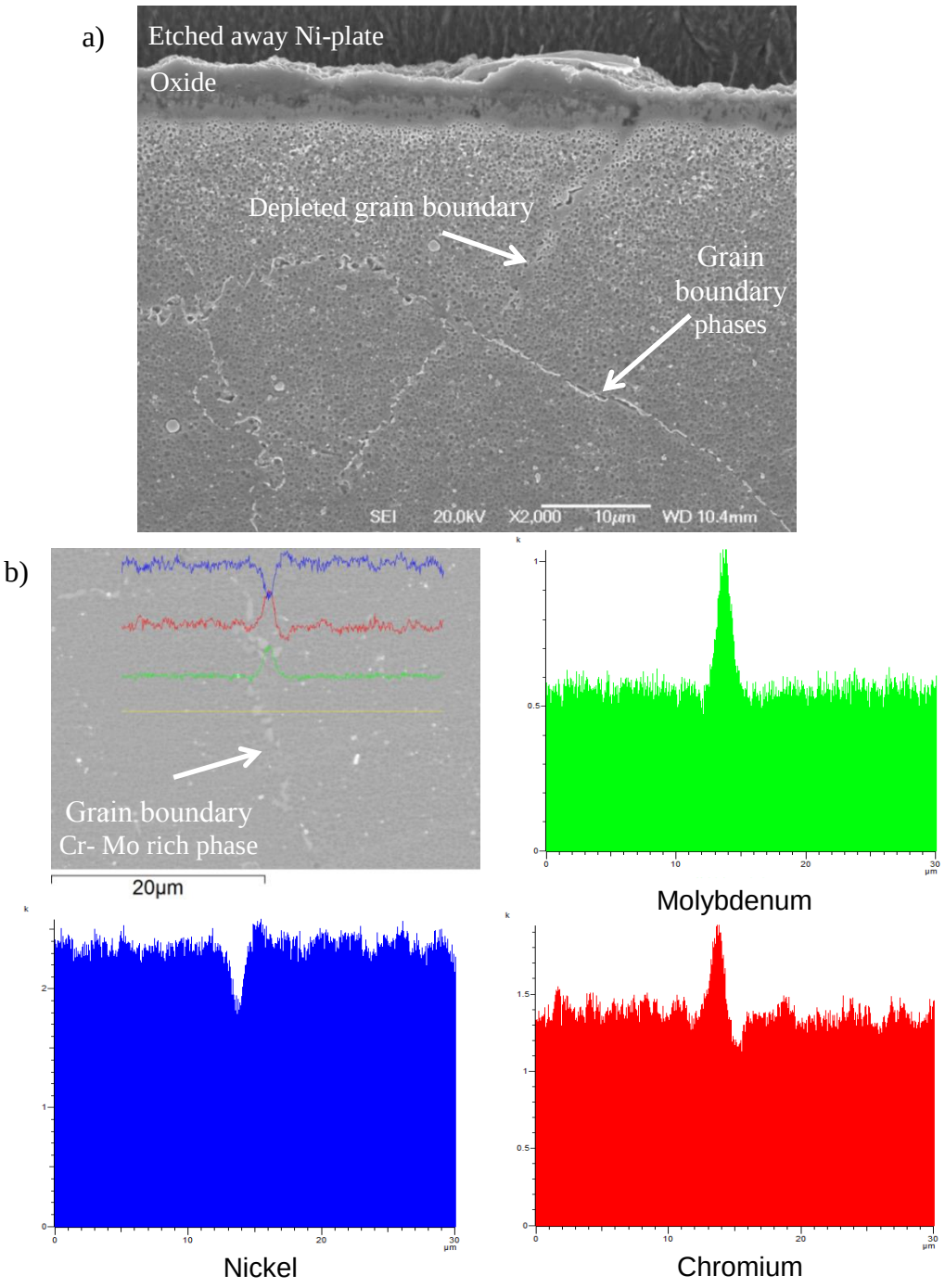

Figure 5-16: a) SE image of the grain boundary phase dissolution of CG RR1000 oxidised at 700°C for 2000 hours. Specimen has been etched with Kallings reagent; b) EDX line scan through a grain boundary phase on CG RR1000 oxidised for 1000 hours at 800°C. Specimen etched using an OP-S polish.

In the similar Ni-based superalloy, ME3, exposed at similar temperatures and times, these phases have been recorded as $M_{23}C_6$ [47]. WDS analysis was used here to try and confirm the presence of carbon but it was unclear whether a slight enhancement of C was found within these particles or whether it was just background C within the SEM, as $M_{23}C_6$ contain relatively small amounts of carbon (~20%) and the probe size of the beam is much larger than the grain boundary particle. It is expected in this case that $M_{23}C_6$ is the predominant grain boundary phase, as sigma phase is not expected to form in RR1000 in significant amounts below 800°C even at prolonged periods of time [172].

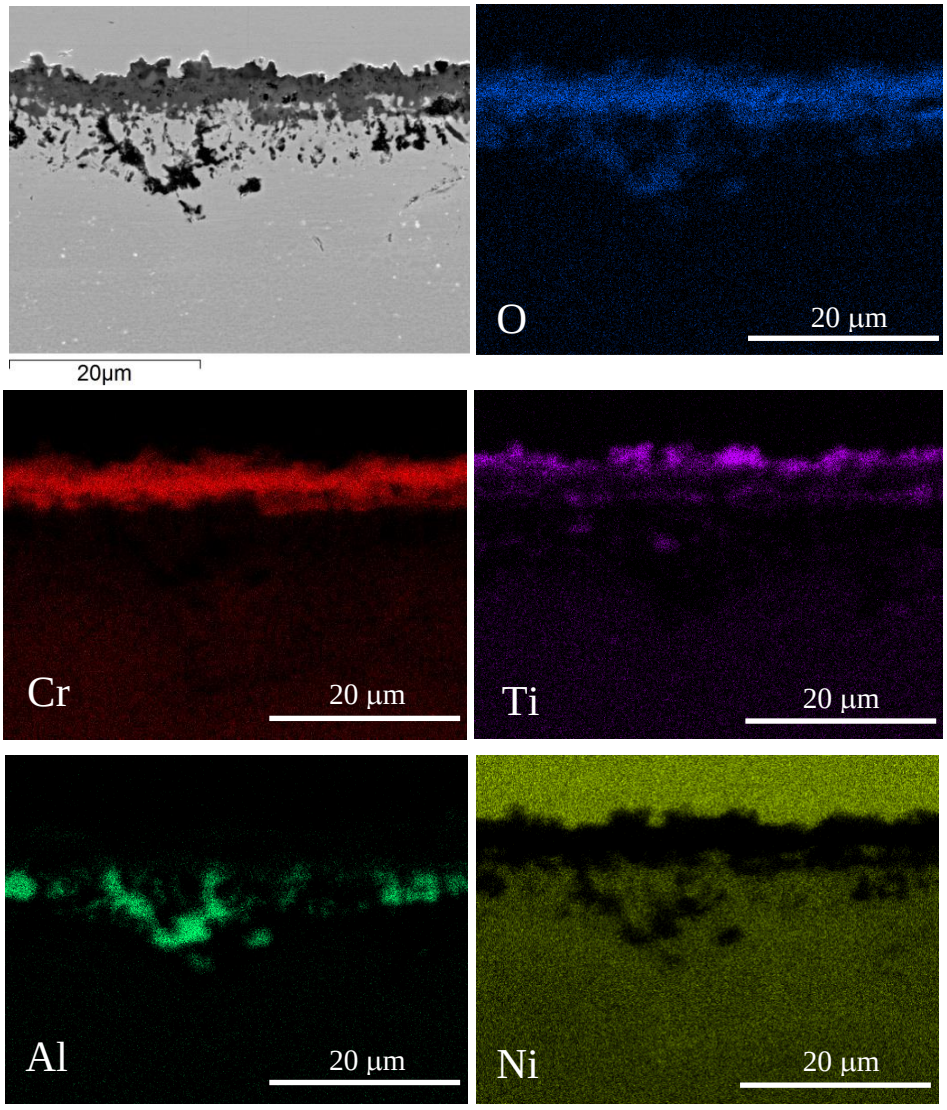

Figure 5-17: EDX elemental map of a specimen oxidised at 800°C for 1000 hours illustrating isolated grains of rutile on the surface and the possible presence of TiN sub-surface.

Closer examination of the EDX maps (Figure 5-14 and Figure 5-17) reveals that the chromium rich surface oxide contained detectable amounts of Ti in addition to there being a separate outer region of Ti rich oxide. It can be inferred from the XRD identified peaks, together with the EDX results, that the outermost surface contained crystals of rutile (TiO_2) but that the thicker chromium-rich oxide

layer was chromia even though titanium was also present. The ability of chromia to dissolve Ti in the oxidised state has been known for some time. It is likely that Ti is incorporated as the Ti^{4+} ion since this has minimal effect on the chromia lattice spacing, even at high dopant levels, which is consistent with the XRD results. The phase equilibrium data of Naoumidis et al. (1991) [41] suggests that for the test temperature of 1000°C, titanium solubility decreases with increasing oxygen partial pressure and is insignificant for $pO_2 > 10^{-18}$. At higher pressures the $Cr_2Ti_3O_9$ phase would be expected. This has a principal XRD peak at 2θ ~28.5° [174] but no evidence was found for this in the present work, even though the specimens were tested in air (pO_2 ~ 0.21) but at lower temperatures. It is suggested reasonably, that the solution characteristics of titanium in the chromia layer are determined by the pO_2 existing at the chromia/alloy interface where the solution process takes place. The oxygen partial pressure here will be much less than 10^{-18} at the present test temperatures. It is also important to note that while a grain boundary enhancement occurs there is not a compositional change associated with this. Furthermore, underneath the external oxide scale, on the alloy/external oxide interface is a Ta rich phase, which only occurs at 800°C at prolonged exposure times. It has been postulated in the literature that this phase could be (Cr, Ta)O_2 [47], although EDX analysis on an SEM could not accurately determine whether the phase found here was an intermetallic or oxide, due to the large probe size compared to the size of the phase being analysed and the close proximity of the external oxide scale. Therefore the oxygen, chromium and nickel could not be excluded from being traces from either the Ti-doped chromia external scale or base alloy. Phase diagrams for the Ni-Ti-Ta system show that it is possible to form a Ni-Ti-Ta rich intermetallic [175].

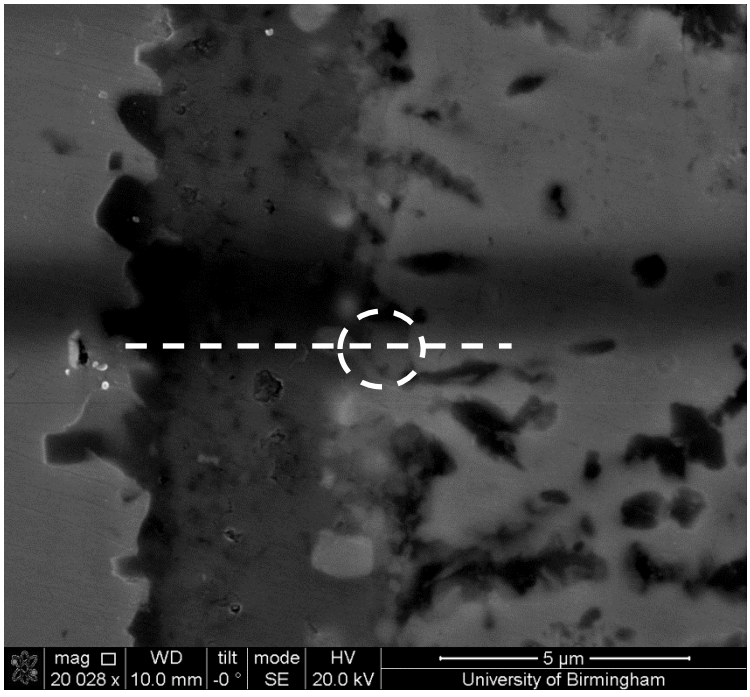

Figure 5-18: SEM image of the location where a TEM foil was taken (dotted line) for the analysis of a Ta-Ti rich phase (highlighted by the dashed circle) formed underneath the external oxide scale on a specimen oxidised at 800°C for 2000 hours (Courtesy of Dr R. Ding).

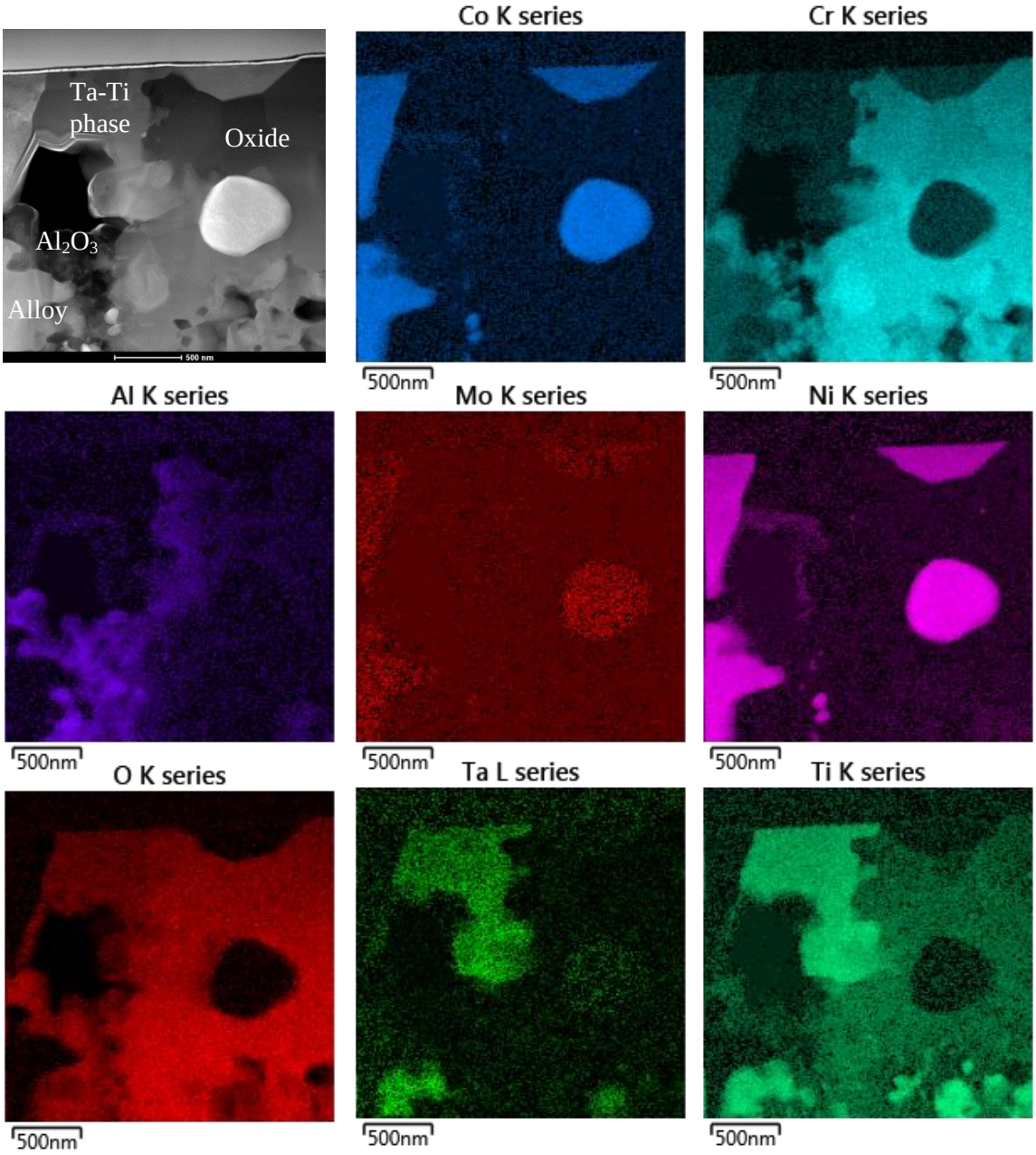

Figure 5-19: STEM image with EDX elemental maps of a TEM foil taken from a specimen oxidised at 800°C for 2000 hours, showing the Ti-Ta rich phase contains oxygen (Courtesy of Dr R. Ding).

Further investigations were, however, performed using TEM analysis courtesy of Dr Rengen Ding. Figure 5-18 shows the location of the Ti-Ta rich phase, with the dotted line indicating where the TEM foil was milled using focussed ion beam (FIB) thinning. An STEM image of this foil is shown in Figure 5-19 along with EDX maps displaying that the phase contains Ta, Ti, Cr and O, illustrating that it is an oxide. An EDX spot analysis was implemented on this oxide with 63.2 at.% oxygen, 20.6 at.% Ti, 4.2 at.% Cr and 12 at.% Ta being present. The ratio of oxygen to Ti, Ta and Cr combined is ~2:1 which corresponds approximately to the MO_2 rutile stoichiometry. This is confirmed by selected area electron diffraction (SAD) which is illustrated in Figure 5-20 and shows that the Ti-Ta-Cr oxide has a similar tetragonal rutile compound MO_2 structure (a = 0.47 nm, c = 0.3 nm) to TiO_2 and TaO_2 tetragonal structures (a = 0.46 nm, c = 0.295 nm and a = 0.47 nm and c = 0.31 nm respectively) [176].

The 010 reflections appear along the $[10\bar{1}]$ zone axis rather than the [100] zone axis due to double diffraction which is missing when imaged along the [100] zone axis. The 100 reflection is a forbidden reflection in the tetragonal rutile structure. Whether or not Cr is actually present is unclear because of the possibility of contamination from the adjacent chromia layer during EDX scan.

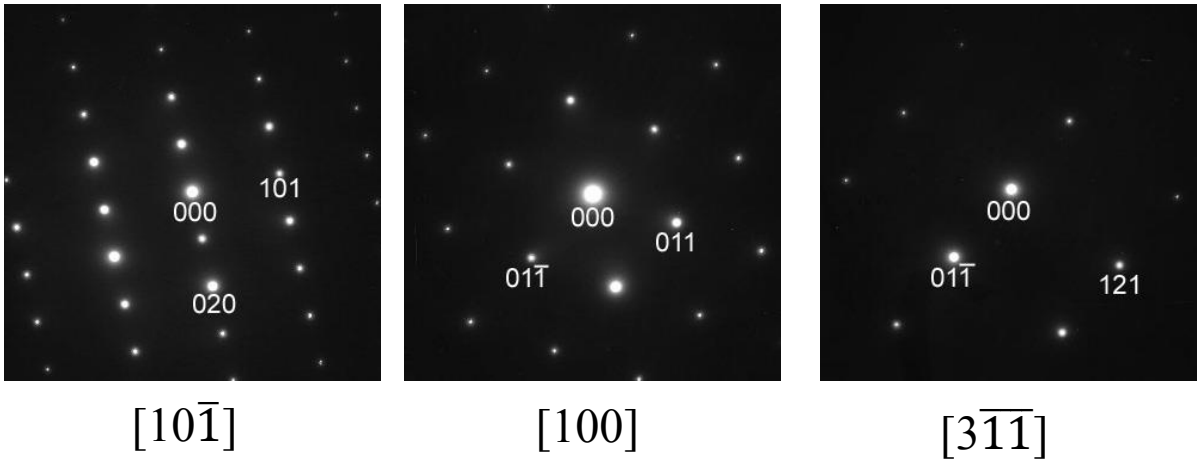

Figure 5-20: Selected area electron diffraction patterns for the $[10\bar{1}]$, [100] and $[3\bar{1}\bar{1}]$ orientations (courtesy of Dr R. Ding).

This provides strong evidence that the phase lying at the external oxide/alloy interface is in fact an oxide with a composition of (Ti, Ta)O_2. Studies on similar Ni-based superalloy, ME3 [47] have reported the presence of a rutile-type phase underlying the outer chromia layer but, in this case, the major metallic constituents were reported to be Ti and Cr.

Figure 5-21(a) shows a cross-section through a specimen and demonstrates the flat surface profile that existed prior to oxidation testing. With increasing exposure time, however, a highly non-planar oxide/metal interface progressively developed, Figure 5-21(b), consisting of protuberances and metallic regions within the outer oxide layer. This morphology may have developed as a result of undercutting by oxide formation [75] or actual protuberances may have developed. In the latter case, they could have formed from outward alloy creep to accommodate the increase in volume resulting from internal oxide formation, as has been suggested for several other alloy systems [70, 73, 77]. The exact composition of these metallic regions was difficult to determine due to their relatively small size compared to the resolution of the SEM probe but EDX analysis suggested they were cobalt and nickel rich, while being depleted in Al, Ti and Cr (Figure 5-22). A TEM section with EDX analysis shows this more clearly in Figure 5-19. This demonstrates that the chromia layer was protective in that the oxygen partial pressure at its base was sufficient to oxidise aluminium and titanium, but not to form oxides of lower thermodynamic stability such as CoO and NiO. This is also consistent with observations in the Ni-based superalloy, ME3 where Ni-Co rich regions were found encapsulated by the surface oxide [47].

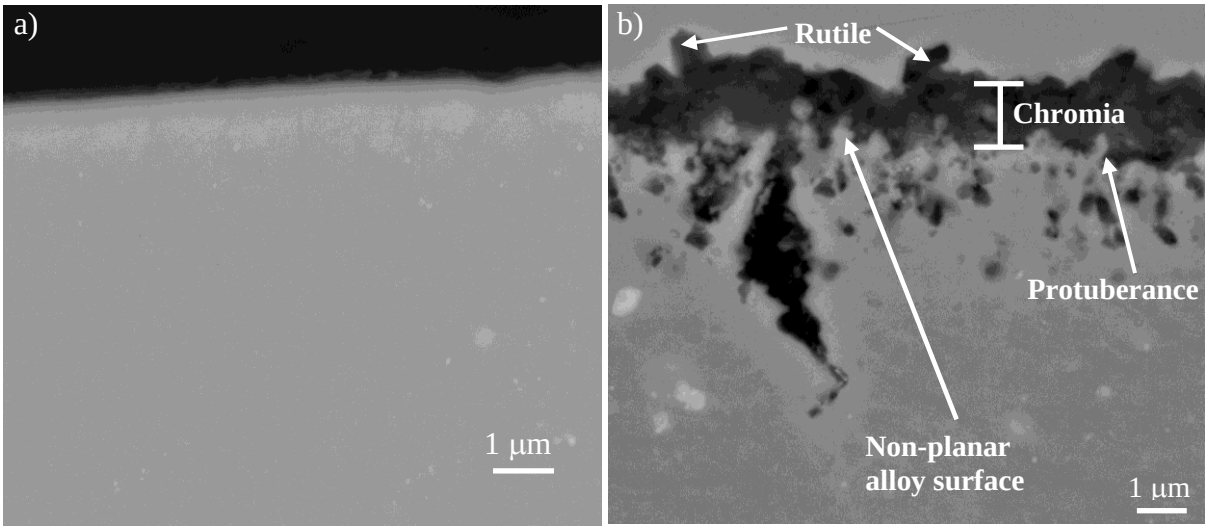

Figure 5-21: a) BSE image through a section through a specimen prior to oxidation testing showing the relatively flat surface profile; b) BSE images at similar magnification of a cross-section through a specimen held at 750°C for 1000 hours illustrating that the oxide/alloy interface becomes non-planar.

With increasing exposure time, the metallic regions could appear to become isolated from the alloy, as can be seen in Figure 5-21 although there may be connectivity with the alloy in the third dimension. Interestingly, the presence of these features did not affect the thickness of the external oxide scale significantly, as can be appreciated from Figure 5-23. The oxidation of elements other than chromium together with the formation of TiN and localised enhanced grain boundary oxides will increase the oxidation mass gain above that expected for the formation of a uniform layer of chromia. To confirm whether these factors account for the higher mass gain parabolic rate constants found, chromia measurements was taken from sections through the tested specimens. A total of 50 measurements were made from 10 micrographs, as described in section 4.5.8. This approach was complicated by the changes in surface profile of the alloy that occurred during oxidation and the formation of TiO_2 above the chromia layer. To aid these chromia measurements, EDX maps were taken for every condition of exposure time and temperature and used to differentiate between chromia and rutile.

Additionally, no allowance was made during measurement for the presence of protuberances on the occasion that the sampling line interested them and no account was made for the small fraction of isolated voids that were encountered. It is estimated that the overall error on chromia thickness due to these factors was an overestimate of <3%. Measurements were also taken to describe the growth of the internal oxide, γ′ denuded zone and Cr-Mo grain boundary phase dissolution.

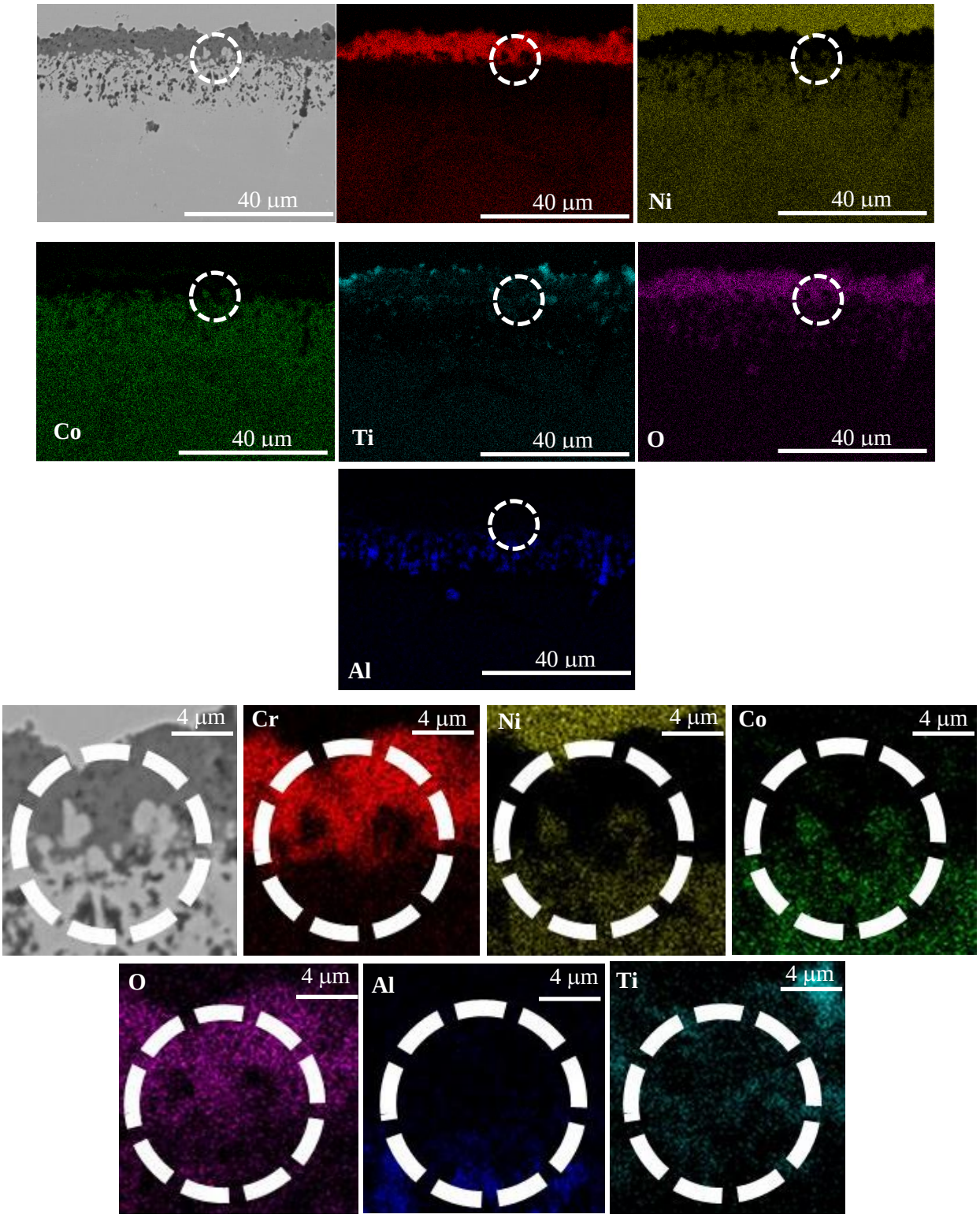

Figure 5-22: EDX elemental maps through a protuberance (highlighted by dashed white ring) in the external scale of a specimen oxidised for 2000 hours at 800°C and the highlighted regions expanded underneath.

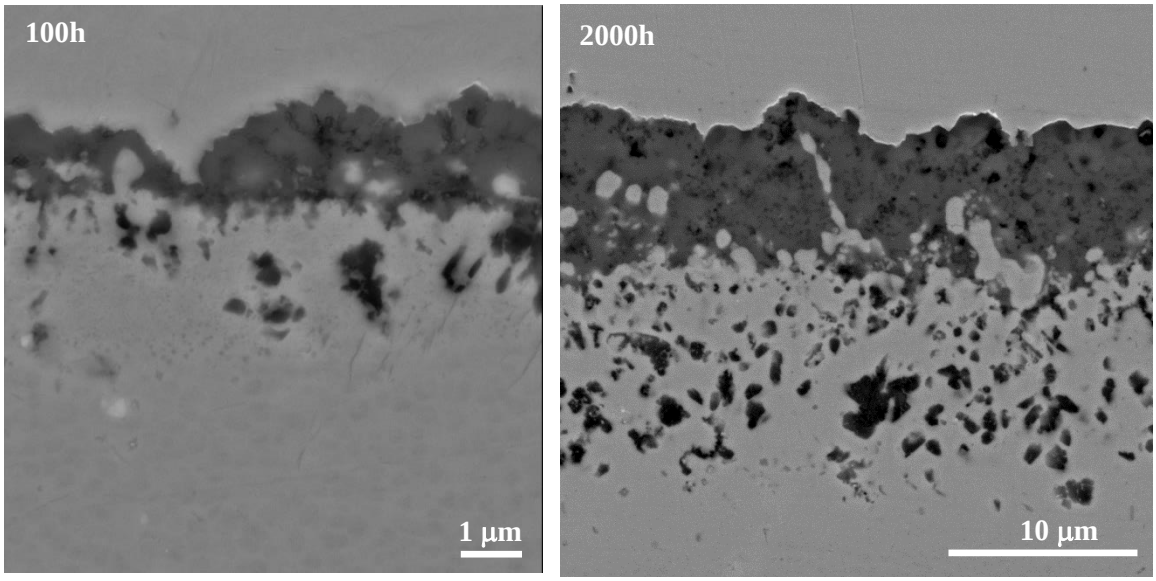

Figure 5-23: BSE images of a specimen oxidised at 800°C showing the evolution of the non-planar oxide/alloy interface.

5.2.5 External oxidation kinetics

The growth of the external oxide scale can be seen from the cross-sections in Figure 5-24. This also shows the development of extensive internal oxidation damage underneath the outer layer illustrating that while the scale is protective the partial pressure of oxygen is still enough to oxidise aluminium. Figure 5-25 shows the change in external oxide scale with time, at the three temperatures in which cross-sectioning of specimens was performed (700, 750 and 800°C), and clearly shows that the higher the exposure temperature the larger the oxide thickness and that the rate of external oxide growth decreases with time at each temperature. This is similar to the mass gain results discussed earlier but it is also not unexpected since we know that a protective external oxide of chromia is formed. This exhibits slow growth since ionic transport across the scale decreases as the scale thickens due to the diffusion distance increasing.

The measurements obtained for the chromia thickness at 700°C together with other measurements taken from the cross-sections of the oxidised specimens are included in Table 5-V. High temperature oxidation kinetics for the external scale can be reasonably described by the following equation:

$$\xi^{n_{ox}} = k_n' \, t \tag{5.4}$$

where ξ is the thickness of the external oxide scale, (assumed to be chromia), k_n' is the growth rate constant for external oxide scale growth, n_{ox} is the growth oxide regime for external oxide scale growth and t is time (in seconds). The value of n_{ox} can then be calculated as before by plotting log ξ against log t (Figure 5-26).

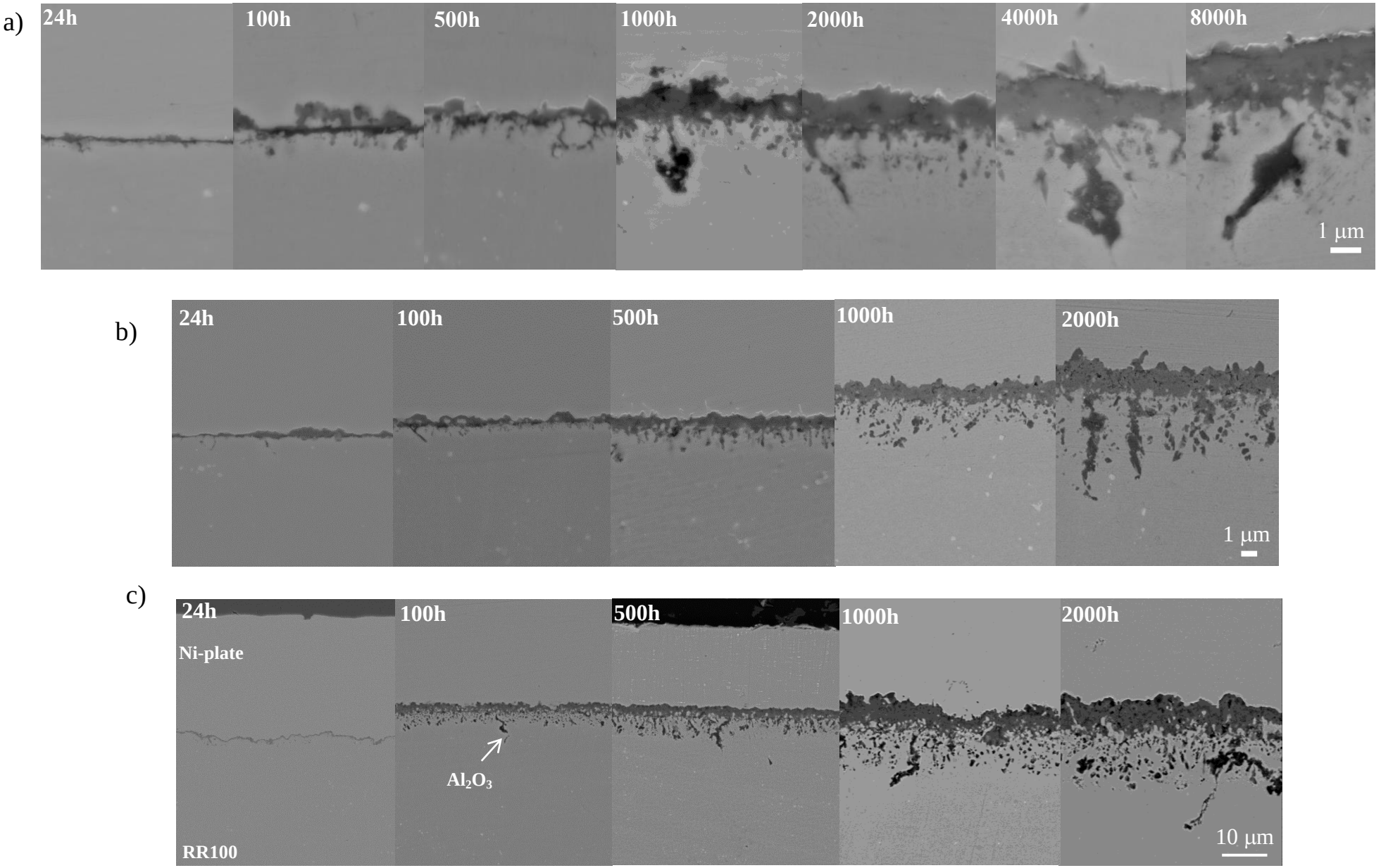

Figure 5-24: BSE images of cross-sections through CG RR1000 oxidised in laboratory air for up to 8000 hours at a) 700°C, b) 750°C and c) 800°C.

Table 5-V: Oxidation damage measurements, in microns, of CG RR1000 oxidised at 700°C for a range of exposure times (±1 standard deviation).

Units in μm	External oxide scale	Internal oxide		γ′ denuded zone		Carbide dissolution
		Intragranular	Intergranular	Intragranular	Intergranular	
24 hours	0.27 (±0.11)	0.09 (±0.06)	0.35 (±0.15)	0.20 (±0.06)	0.57 (±0.07)	-
100 hours	0.84 (±0.21)	0.80 (±0.27)	1.55 (±0.26)	1.04 (±0.29)	2.52 (±0.56)	-
500 hours	1.04 (±0.45)	1.14 (±0.42)	2.31 (±0.53)	1.17 (±0.30)	2.52 (±0.43)	-
1000 hours	1.13 (±0.26)	1.22 (±0.33)	2.53 (±0.50)	1.23 (±0.24)	2.78 (±0.35)	-
2000 hours	1.48 (±0.86)	2.06 (±0.46)	2.92 (±0.48)	2.11 (±0.32)	3.72 (±0.72)	14.50 (±1.81)

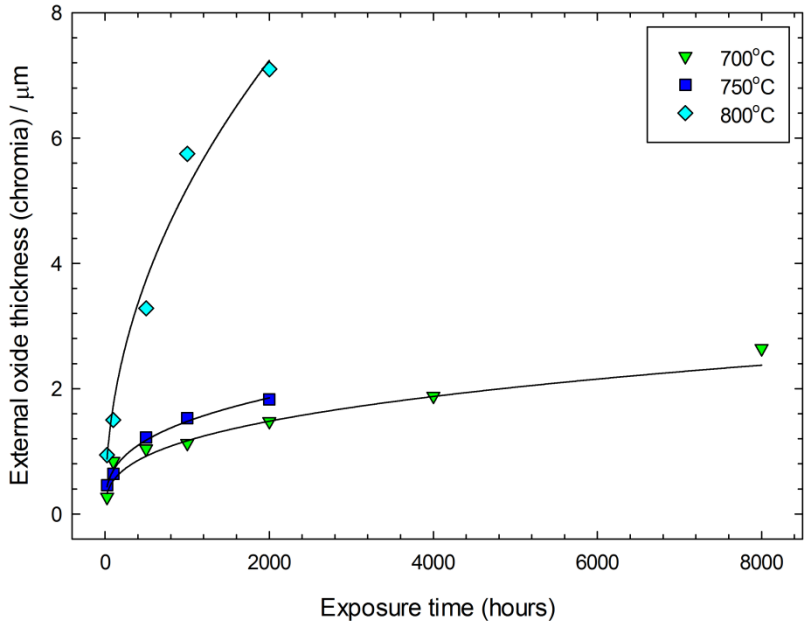

Figure 5-25: Plot of oxide thickness against time for each temperature tested in which sectioning was conducted for a maximum of 8000 hours.

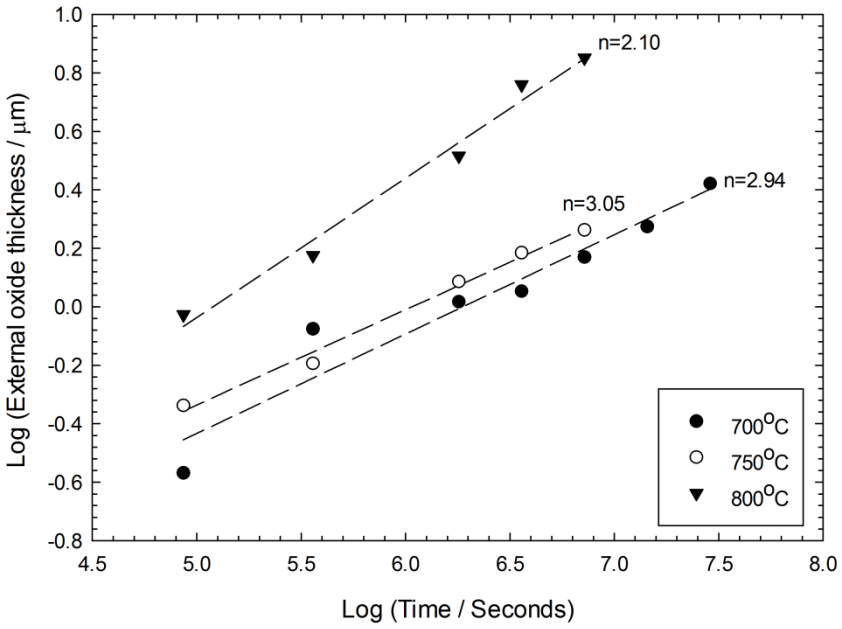

Figure 5-26: Plot of log external oxide thickness against log exposure time for 700, 750 and 800°C.

Figure 5-26 shows the determination of the external oxide thickening growth regime (n_{ox}), for the three temperatures in which extensive measurements were performed (700, 750 and 800°C). In this way the values of n_{ox} can be evaluated for the chromia thickness. At 700 and 750°C the growth can be assumed to be cubic (n=3) with external oxide growth regimes of 2.94 and 3.05 respectively but at 800°C the growth regime switches to parabolic (n_{ox} = 2). The distribution of the external oxide

measurements were checked and confirmed to be normally distributed, using Q/Q plots, histograms (Figure 5-27) and a Shaprio-wilk normality test.

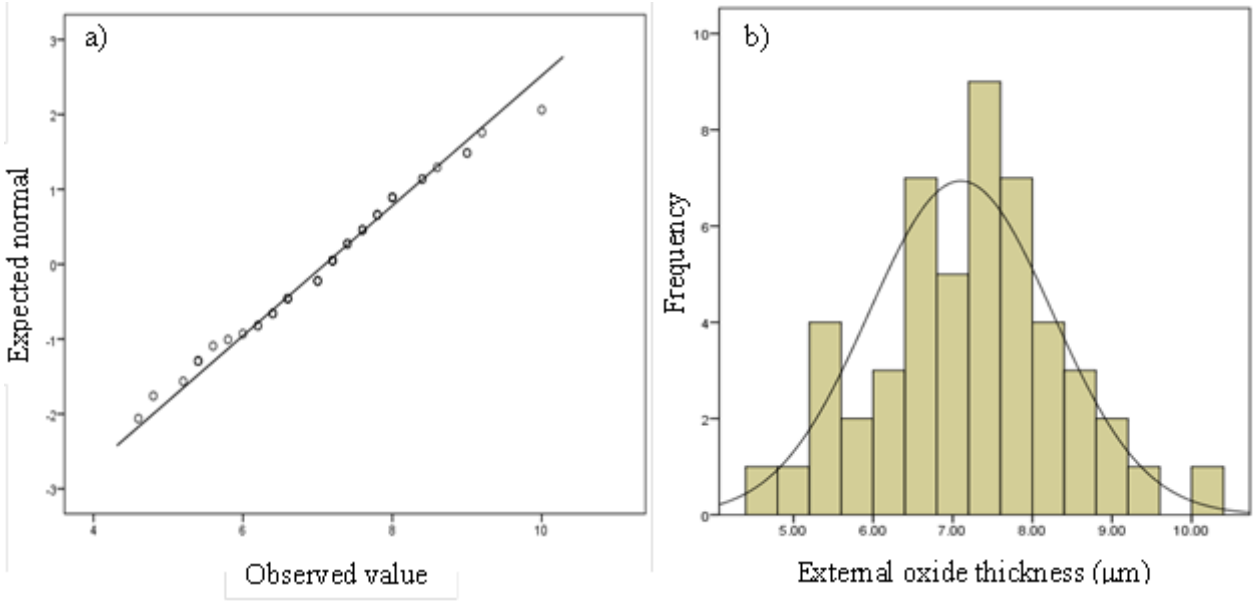

Figure 5-27: Q/Q plot (a) and histogram (b) of all the external oxide measurements taken from a CG RR1000 specimen oxidised at 800°C for 2000 hours, illustrating that the data is distributed normally, with the values being distributed linearly in the Q/Q plot.

Table 5-VI: Best estimates of the exponent, n, for the external oxide scale thickness for coarse-grained RR1000 and the oxidation rate constants of coarse-grained RR1000, the parabolic oxidation rate constants for pure chromia formation on a 20Cr austenitic steel and the cubic oxidation rate constants for Ni-based superalloy ME3 and coarse-grained RR1000.

Temperature	RR1000	RR1000	RR1000	20Cr austenitic steel [171]
	n_{ox}	k_c' ($\mu m^3.s^{-1}$)	k_n' ($\mu m^n.s^{-1}$)	k_p' ($\mu m^2.s^{-1}$)
700°C	2.93	$5.94x10^{-7}$	$5.62x10^{-7}$	$2.94x10^{-8}$
750°C	3.05	$8.56x10^{-7}$	$9.16x10^{-7}$	$1.40x10^{-7}$
800°C	2.10	$4.88x10^{-5}$	$8.81x10^{-6}$	$5.75x10^{-7}$

Temperature	ME3[47]
	k_c' ($\mu m^3.s^{-1}$)
704°C	$2.14x10^{-7}$
760°C	$8.61x10^{-7}$
815°C	$5.28x10^{-6}$

A comparison of the external oxide growth constants of CG RR10000, ME3 and a pure chromia forming austenitic steel are shown in Table 5-VI. It clearly shows that both Ni-based superalloys exhibit significantly (almost an order of magnitude) faster chromia growth than that expected from chromia growth on simpler Ti-free alloys. Figure 5-28 illustrates the difference between the two sets of k_n' and also that shows the pure-chromia forming alloy displays parabolic growth, whereas both

superalloys, RR1000 and ME3, grow sub-parabolically (n = 3). The exception to this is RR1000 at 800°C, where chromia growth is near parabolic and is why the external oxide growth constants of RR1000 are displayed assuming cubic kinetics (k_c') and actual growth kinetics (k_n'). The external oxide growth on RR1000 is similar to that of the similar Ni-based superalloy, ME3, especially when assuming cubic kinetics throughout. When using actual growth kinetics, there is a significant difference at 800°C, which can be attributed to parabolic growth in RR1000 rather than the sub-parabolic cubic growth displayed by ME3, leading to ME3 having a significantly slower oxidation rate at this temperature. An exact comparison cannot be made due to the slight difference in exposure temperatures.

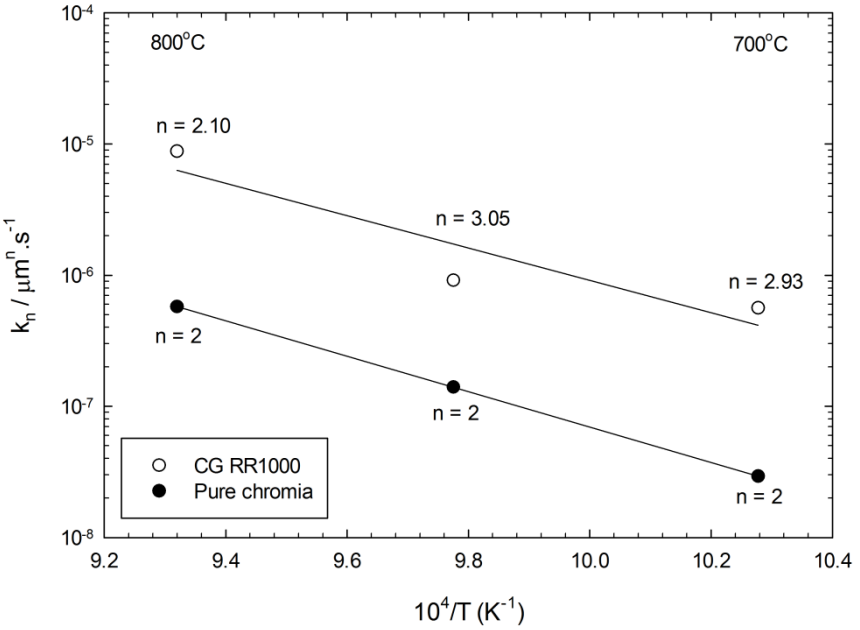

Figure 5-28: Arrhenius plot of k_n' values from this study (shown as unfilled circles) compared to the expected k_p' values for pure chromia formation on a high chromium austenitic steel. Best fit lines for chromia growth on both alloys are provided. Oxidation was performed in laboratory air between 700 and 800°C

The measurements taken from the literature (Ni-based superalloy, ME3) are not pure chromia but include the entire external scale and in some case may contain small amounts of rutile. The values in this present case are for the chromia layer only but the external scale is almost entirely chromia as there is only a small amount of isolated rutile on the surface. So would have a negligible effect on chromia thickness measurements and in this case the terms chromia thickness and external oxide thickness should be used interchangeably.

The external oxide growth for both RR1000 and pure chromia forming steel have been plotted against exposure time since it can be acknowledged from Table 5-VI and Figure 5-29 that chromia growth on RR1000 is significantly quicker than the expected chromia thicknesses grown on pure chromium or high chromium austenitic steel [171]. The parabolic kinetics for pure chromia growth are given by the following equation:

$$k_p' = 2.07x10^6 \exp\left[-\frac{31020}{T}\right] \quad \mu m^2.s^{-1} \tag{5.5}$$

where k_p' is the parabolic rate constant for thickening of the pure chromia layer and T is temperature. From this comparison it can be appreciated that the chromia growth rate observed on the Ni-based superalloy was significantly greater than that expected from chromia growth on simple Ti-free alloys. This increase in rate can be quantified from the slope, dξ/dt, of the chromia thickness/time curves (Figure 5-29) and by evaluating the ratio, 'r', of that for RR1000 (subscript 's' in equation 5.6) and that for the simpler high chromium austenitic steel (subscript 'Cr'):

$$r = \left(\frac{(d\xi/dt)_s}{(d\xi/dt)_{cr}}\right)_{\xi} \tag{5.6}$$

This ratio needs to be evaluated at a given oxide thickness, ξ, to ensure the comparison is made at a given diffusion distance for the chromium defects transporting across the oxide layer. The calculation of the ratio 'r' was made using the best-fit equations for the simple alloy/chromium, equation 5.4 and 5.5 where n = 2, and for each of the three test temperatures using the parameters (n_{ox} and k_n') in Table 5-VI.

The dependence of the ratio, 'r', on oxide thickness and test temperature is shown in Figure 5-30. From this it is clear that the ratio at 700 and 750°C is initially very high, indicating that the rate of defect transport across the chromia layer on the Ni-based superalloy is 2 orders of magnitude quicker than the pure chromia former at an oxide thickness of 0.1 μm. The ratio decreases rapidly with increasing oxide thickness. At an oxide thickness approaching 1 μm the ratio falls to a steady enhancement of around 4. At 800°C this very high initial ratio does not occur and a constant enhancement (~14) at all oxide thicknesses is found. The difference in growth kinetics with the chromia oxide thickness growing parabolically at 800°C, instead of sub-parabolic growth recorded at 700 and 750°C, is a consequence of the same mechanism that is causing a constant enhancement in growth at 800°C.

It has been recognised in various studies [47, 104, 110, 115, 177-182] that titanium, as an alloy constituent, can have a deleterious effect on the oxidation resistance and is known to act both through an impairment of oxide adherence and through the formation of Ti-rich oxides. Rutile formation has been demonstrated previously in this chapter but as mentioned before no spallation has been observed in RR1000 at these test temperatures. Significantly, enhancements of the chromia growth rates have been recorded and it is suggested that these is also a further deleterious effect of titanium, with its retention in the chromia layer. This has been shown in EDX maps in Figure 5-14 and Figure 5-17.

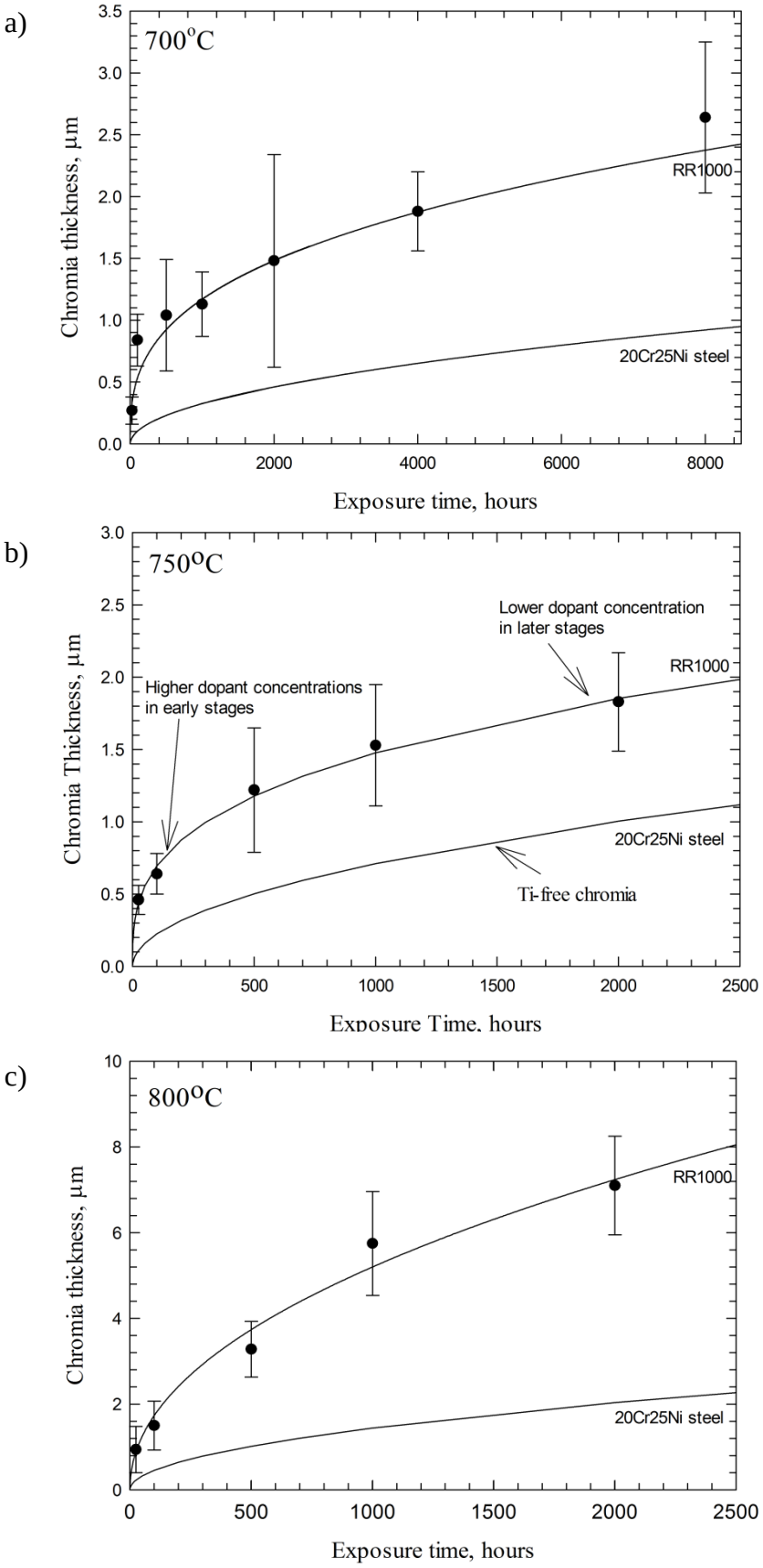

Figure 5-29: Plots of chromia thickness measured on sectioned RR1000 compared with predicted chromia thickness obtained from a pure chromia forming austenitic steel at a) 700°C, b) 750°C and c) 800°C. Oxide thickness measurements for RR1000 are normally distributed and error bars are shown as ± 1 standard deviation.

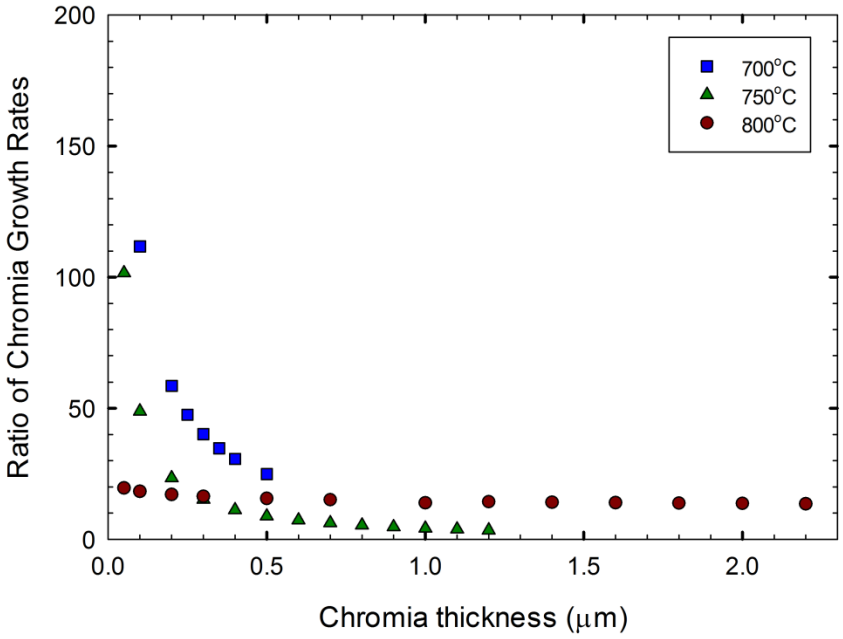

Figure 5-30: The variation of the enhancement ratio with oxide thickness for the three test temperatures at which extensive oxide thickness measurements were undertaken.

A plausible explanation is that this titanium addition in the chromia oxide layer acts as a higher-valent dopant to increase the concentration of chromium vacancies [43, 177, 178, 183]. The ability of chromia to dissolve titanium in the oxidised state has been known for some time [42]. It is likely that Ti is incorporated as the Ti^{4+} ion since this has minimal effect on the chromia lattice spacing, even at high dopant levels, which is consistent with the XRD results. This possibility has been considered in detail by Atkinson et al. [42, 43] in the context of Ti-doped chromium oxide used in sensors for trace gases. A 4-valent titanium ion can be considered to enter the chromium lattice via the dissociation of TiO_2 according to:

$$3TiO_2 \rightarrow 3Ti_{cr}^{\cdot} + V_{Cr}^{'''} + 6O_o^x \qquad (5.7)$$

where the first term on the right hand side of the reaction (equation 5.7) represents the excess positive charge associated with the titanium ion located on a chromium lattice site; $V_{Cr}^{'''}$ is a triply charged chromium vacancy; O_o is the oxygen ion on the oxygen sub-lattice. It should be noted that this simple reaction envisages single chromium vacancies but it may be that these, in fact, form clusters with the titanium ion [42, 43]. The actual defect structure of Ti-doped chromia is unclear but an increase in chromium vacancies is expected as a result of the incorporation of a higher-valent ion. It needs to be assumed, of course, that such concepts will also apply to the oxide grain boundaries since these are likely to remain the main diffusion routes at the temperatures used in this present work. These excess vacancies will increase oxidation rates through increasing diffusion rates of the chromium ion across the oxide layer. It is not possible to quantify this in this work since the titanium concentration within

the chromia layer could not be determined reliably using the SEM because of the thinness of the oxide scale and the proximity of the outer layer of rutile (Figure 5-17). Nevertheless, relatively small quantities of dopants are expected to have a significant effect since the intrinsic vacancy defect population within pure chromia will be small.

It should be recognised that the average quantity of titanium dopant within the chromia layer is likely to decrease as the layer thickens because of the depletion of the element in the adjacent alloy. This holds true at both 700 and 750^{o}C, where a decrease in the enhancement is found, but at 800^{o}C the enhancement ratio stays approximately constant as the oxide thickens. SEM images and EDX traces performed at both 750^{o}C and 800^{o}C for two exposure times (100 or 200 hours and 2000 hours) are shown in Figure 5-31 and Figure 5-32 respectively. In both locations the external oxides, γ' denuded zones and the alloy are labelled. Within the γ' denuded zones illustrated there is some depletion of titanium immediately adjacent to the external oxide scale. The width of this titanium depletion zone is estimated to have increased from 1.5 μm to 5 μm at 750^{o}C. The peaks associated with Ti and Al within the γ' denuded zone appears to be associated with TiN and Al_2O_3.

In Figure 5-31 at 750^{o}C the gradient of the titanium concentration adjacent to the external oxide at 100 hours is positive, indicating that there is a flux of titanium into the growing external oxide. However at 2000 hours the gradient at the interface approaches zero and, thus, the driving force for the diffusion of titanium atoms is greatly reduced as is the flux of titanium into the oxide. Somewhat tentatively, an estimate of the Ti/Cr ratio within the chromia layer can be made comparing the Ti and Cr counts at the peak of the Cr counts. It is found that after 100 hours (Figure 5-31) at 750^{o}C, Ti/Cr ~0.22 but this is reduced to ~0.14 after 2000 hours. This will result in a decreasing rate-enhancement ratio with increasing oxide thickness, as observed in Figure 5-30. It will also ensure that sub-parabolic growth kinetics will result, since the average chromium diffusion coefficient within the oxide will also reduce with increasing oxide thickness. A similar effect would be expected at 700^{o}C. Similar EDX traces occur at 800^{o}C (Figure 5-32), with a positive gradient found at 200 hours illustrating a flux of titanium into the oxide scale and at 2000 hours a depletion profile of titanium and aluminium exists where the concentrations are essentially zero. A corresponding decrease in rate enhancement ratio of the external oxide is not found, and remains at ~14. The reasons for this constant enhancement is currently unclear and further investigations are required to understand why at 800^{o}C a decrease in enhancement does not occur even when a significant depletion of titanium occurs sub-surface. A significant feature appears to be the presence of the (Ti, Ta)O_2 phase discussed earlier (Figure 5-19). Its formation may limit Ti ingress into the chromia layer and thus reduce the doping effect at short time periods, and buffer the release of Ti into the chromia scale at the longer time periods leading to near parabolic kinetics at 800^{o}C.

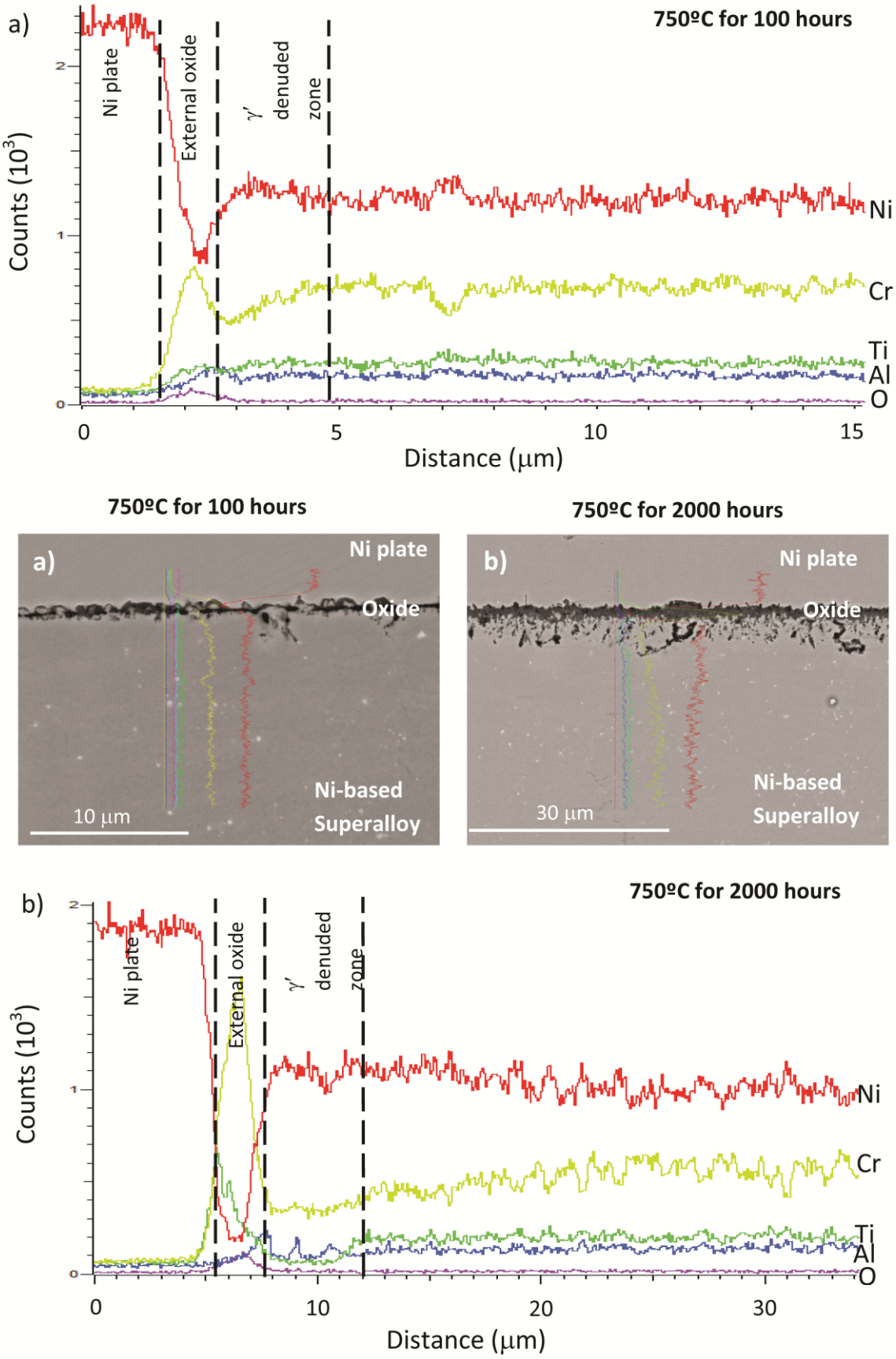

Figure 5-31: EDX linescans (and SE images) of RR1000 oxidised isothermally at 750°C for a) 100h and b) 2000h showing titanium and aluminium depletion underneath the external oxide scale

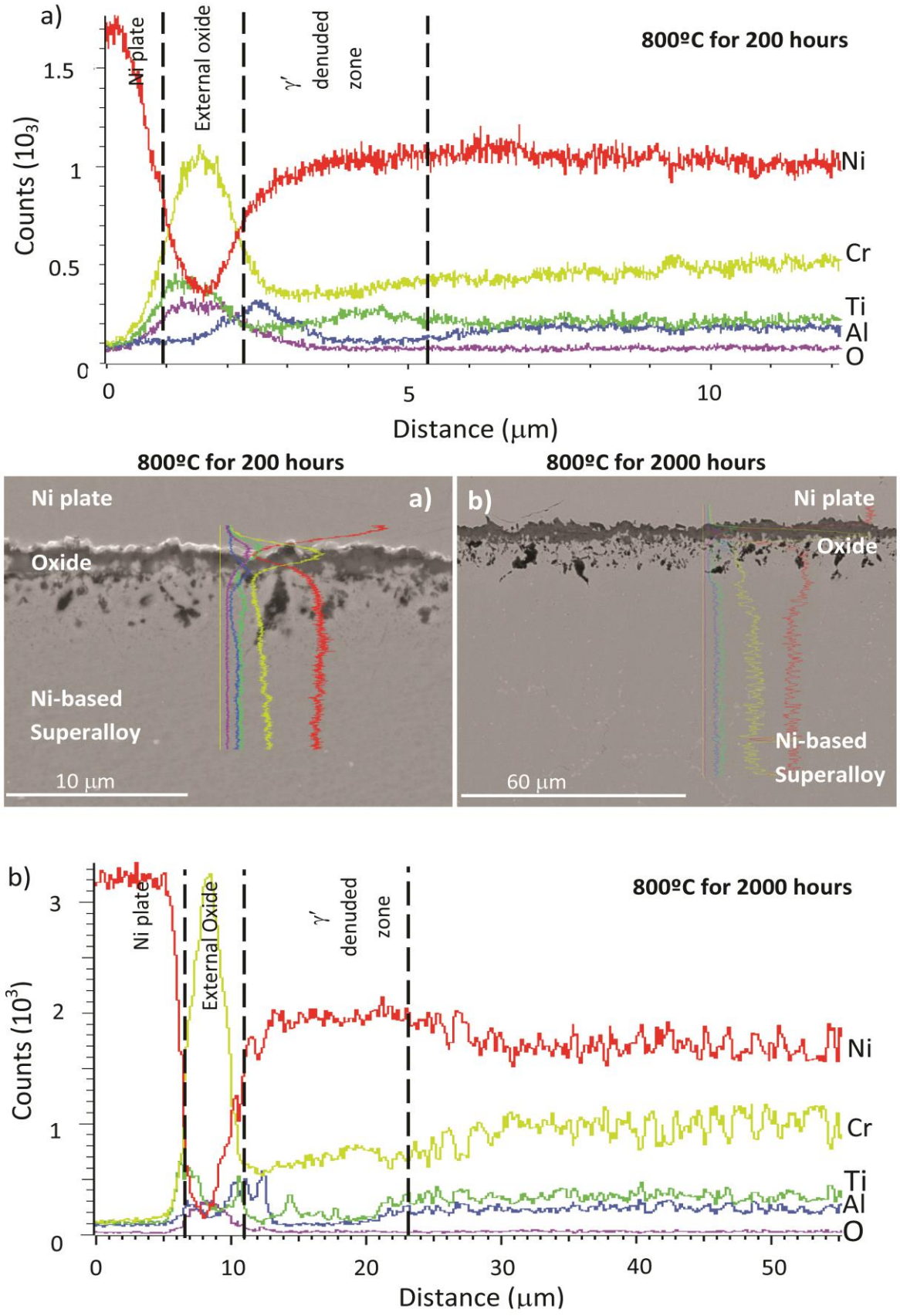

Figure 5-32: EDX linescans (and BSE images) of RR1000 oxidised isothermally at 800°C for a) 200h and b) 2000h showing titanium and aluminium depletion underneath the external scale.

An Arrhenius equation, similar to that used in equation 5.2, can again be used to calculate the effective activation energy for the formation of the external oxide scale.

$$k_n^{'} = k_o \exp\left(\frac{-Q_{ox}}{RT}\right) \quad (5.8)$$

where in this case Q_{ox} is the activation energy for external chromia scale growth (kJ.mol^{-1}), R is the molar gas constant and T is the exposure temperature (K). Figure 5-33 shows the activation energy when assuming cubic kinetics and actual kinetics. This has a large difference on the activation energy quoted 377 kJ.mol^{-1} to 236 kJ.mol^{-1} respectively, it also has a significant effect on the fit of the best fit regression line with R^2 = 0.80 and 0.86 respectively. It must be stressed that this is from only three data points, although well-defined points, further work at additional temperatures is required to define this more comprehensively. Table 5-VII shows the activation energies of RR1000 against those of another similar chromia forming Ni-based superalloy and a pure chromia former. It is important to note that in this case a k_c assuming cubic kinetics has been used for 800^{o}C when it has been shown and described earlier to follow parabolic kinetics is used solely for comparison purposes with the similar Ni-based superalloy, ME3 and to calculate an activation energy from a single growth regime.

Table 5-VII: Activation energy for the formation of the external oxide scale on CG RR1000, Ni-based superalloy ME3 and a 20Cr austenitic steel, listed along with the temperature range analysed.

Alloy	Activation energy (kj.mol^{-1})	Temperature range tested
CG RR1000 (k_n)	236	700-800^{o}C
CG RR1000 (k_c)	377	
ME3	262 (±33)	704-815^{o}C
20Cr austenitic steel	258	700-900°C

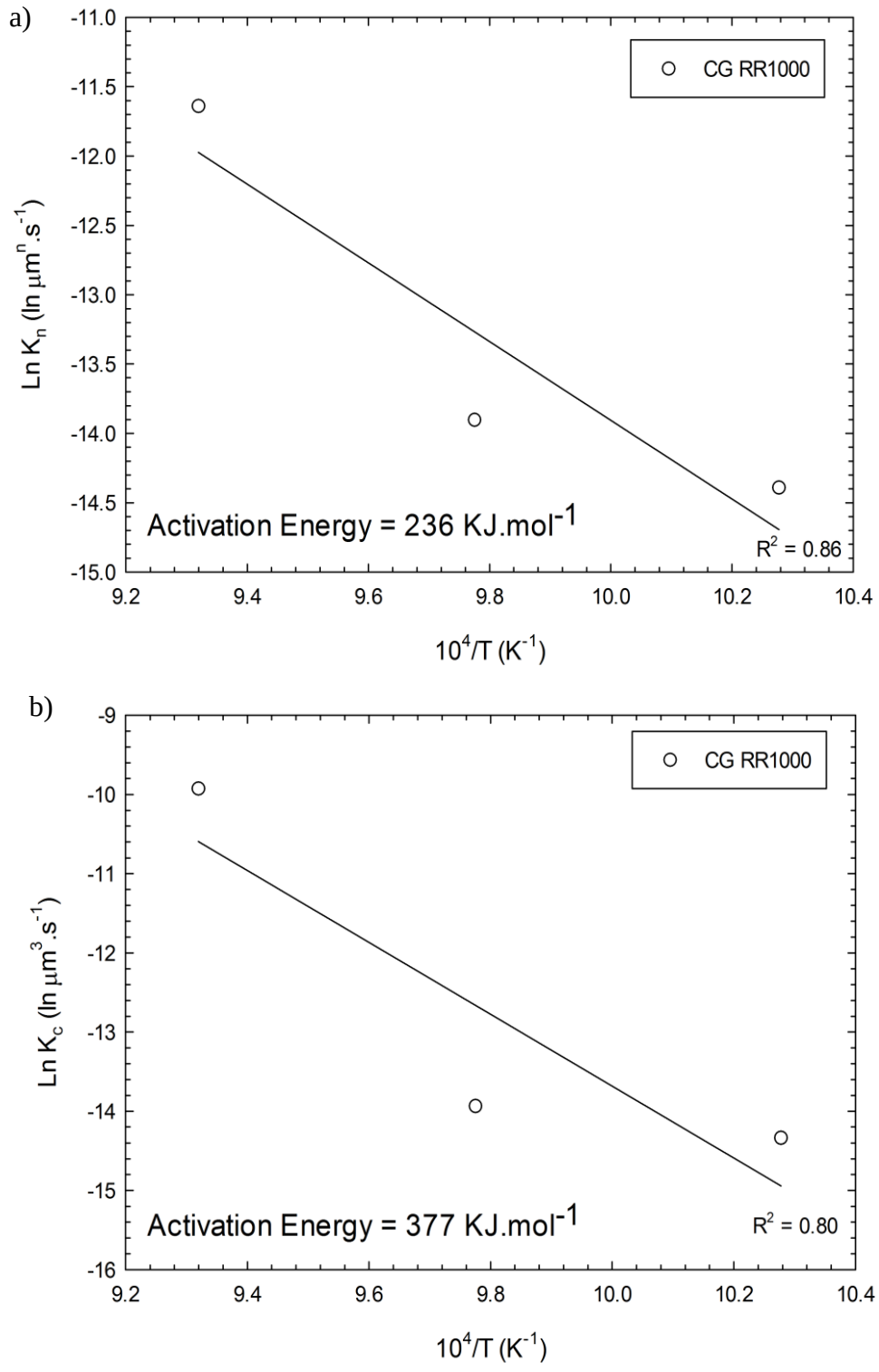

Figure 5-33: Activation energy of external oxide scale formation on CG RR1000 using two different oxide growth regimes: a) k_n values and b) k_c values over the temperature range of 700-800°C. A best-fit regression line is included with an R^2 value describing the fit of the line.

5.2.6 Enhanced grain boundary external oxide kinetics

A significant grain boundary enhancement is seen in the external oxide scale, this has been described earlier and as illustrated in Figure 5-12. The development of the external oxide over time can be seen in Figure 5-34 at the three temperatures in which confocal microscopy was performed (with these measurements of the enhancement above the surface being added to the ones recorded for the oxide thickness during the cross-sections). This clearly shows, like the external intragranular oxide scale that the higher the exposure temperature the larger the oxide thickness and that the rate of external growth decreases with time. This is to be expected as while an enhancement is occurring at the grain boundaries the external oxide scale remains protective. In Figure 5-35 it can evidently be seen that as the intragranular external scale thickness increase that the enhancement at the grain boundaries also increases, up to a point where at which the enhancement is removed completely. It is possible that there is a maximum scale thickness at which the enhancement occurs and it might be expected that an impairment could occur at the grain boundaries with further scale thickening, but additional work would be required to clarify this.

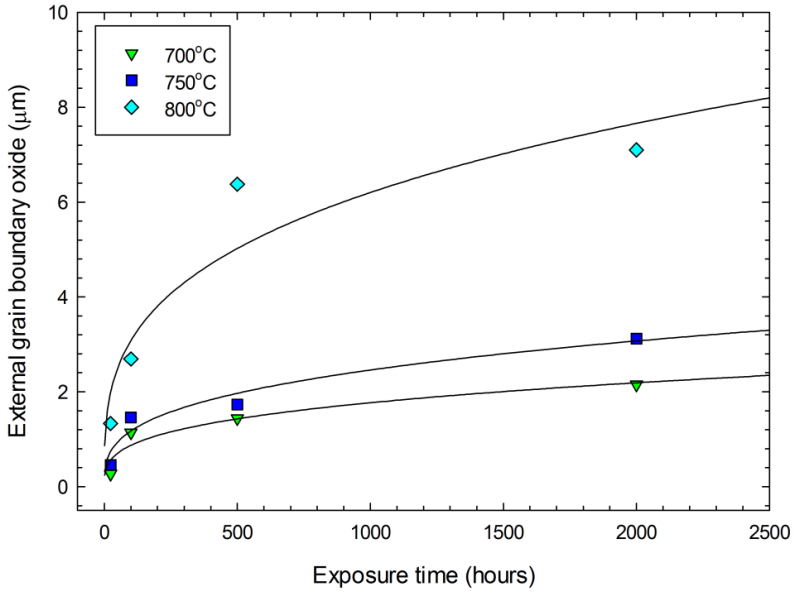

Figure 5-34: Plot of grain boundary enhanced external oxide thickness against time for each temperature tested.

The high temperature oxidation kinetics for grain boundary enhanced external scale growth can be plotted in the same manner as the intragranular external scale, using equation 5.4 replacing k_n' with $(k_n')_{gb}$ and n_{ox} with $(n_{ox})_{gb}$, illustrating the rate constant for oxide growth at the grain boundary and the oxide growth regime at the grain boundary respectively. Likewise the values of $(n_{ox})_{gb}$ can be calculated in the same way by plotting log ξ_{gb} (enhancement plus intragranular oxide thickness) against log t. This is shown in Figure 5-36 and in all cases it illustrates that sub-parabolic growth (Table 5-VIII) is occurring but that the growth is no longer cubic like that found in the intragranular

chromia thickness measurements at both 700°C and 750°C. At 800°C the opposite is true with the growth moving from parabolic to sub-parabolic.

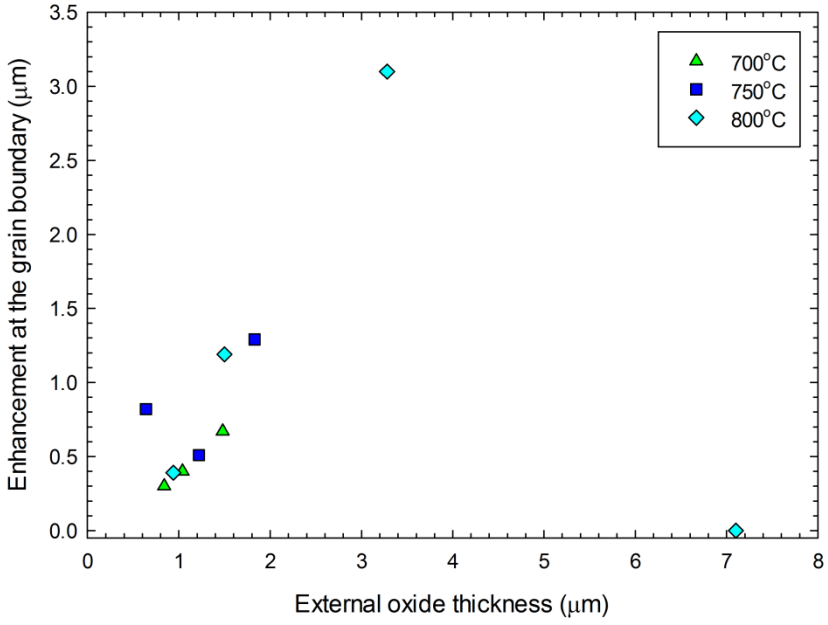

Figure 5-35: Plot of the enhancement of the external scale at grain boundaries against the external oxide thickness.

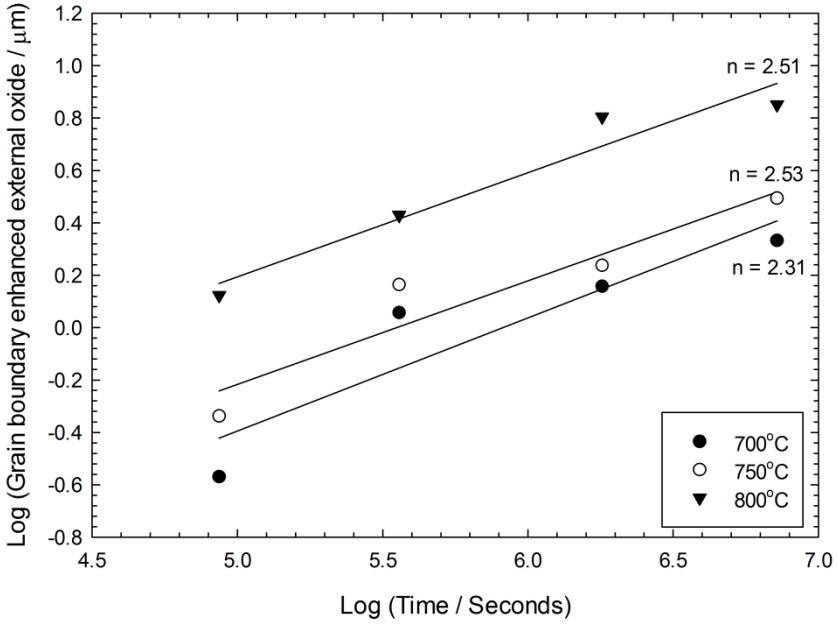

Figure 5-36: Plot of log grain boundary enhanced external oxide against log of exposure time for 700-800°C.

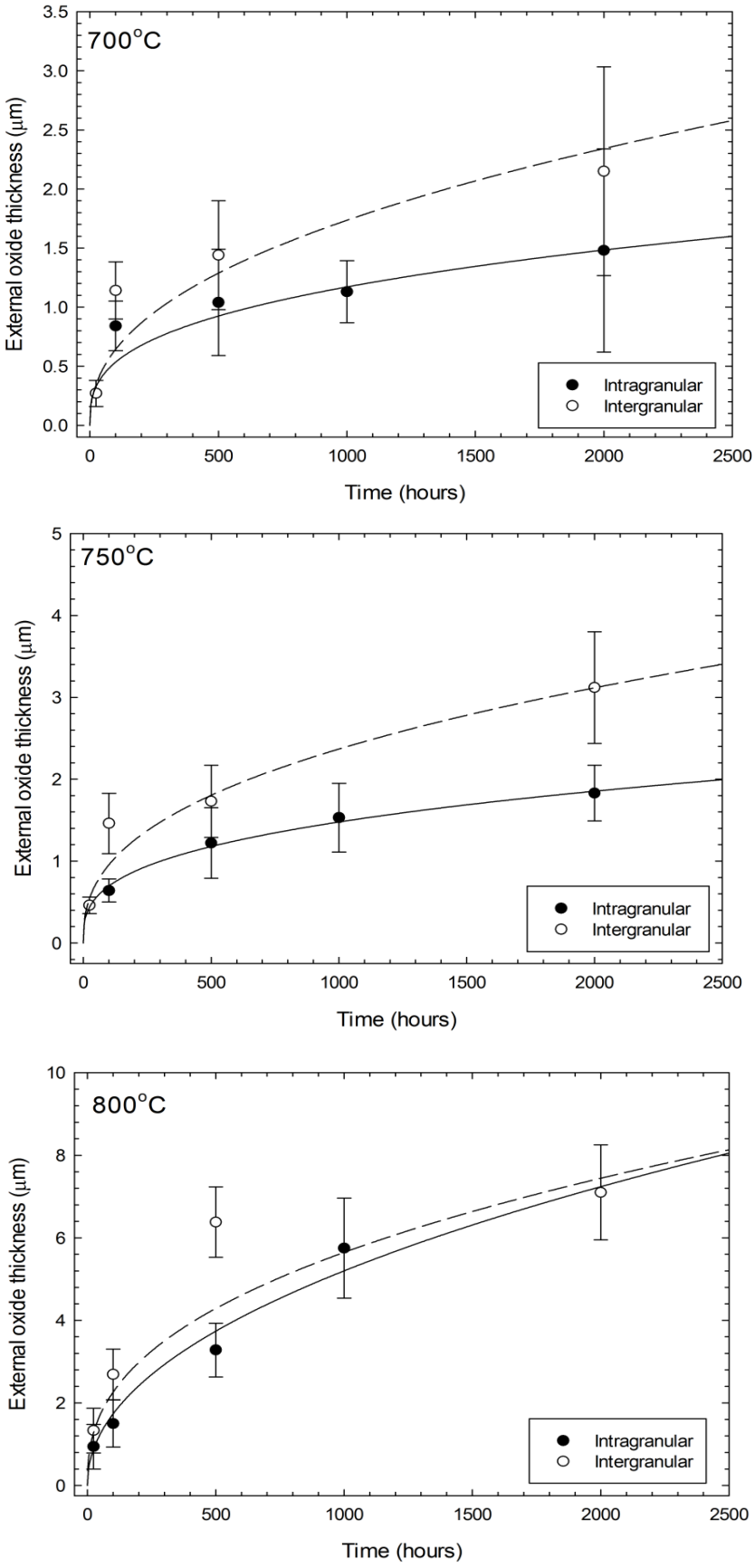

Figure 5-37: Plots of external oxide thickness at both intragranular and intergranular regions, illustrating the enhanced growth at the grain boundaries (±1 standard deviation)

Table 5-VIII: Best estimates for the exponent, n, for the external oxide scale thickness, both inter and intragranular for RR1000 and the oxidation rate constants for both.

Temperature	Grain boundary enhanced		Intragranular	
	RR1000	RR1000	RR1000	RR1000
	$(n_{ox})_{gb}$	$(k_n')_{gb}$ ($\mu m^n.s^{-1}$)	n_{ox}	k_n' ($\mu m^n.s^{-1}$)
700°C	2.31	$9.96x10^{-7}$	2.93	$5.62x10^{-7}$
750°C	2.53	$2.47x10^{-6}$	3.05	$9.16x10^{-7}$
800°C	2.51	$2.15x10^{-5}$	2.10	$8.81x10^{-6}$

Figure 5-37 shows plots of oxide thickness against time for both the intragranular external scale and the grain boundary enhanced external scale. It can be clearly seen that while a significant enhancement is found at 700°C and 750°C, at 800°C the enhancement is present at short times but is removed at the longer time periods. This backs up the results found in Figure 5-35 which shows that the enhancement at the grain boundaries is removed at large intragranular oxide thicknesses. The best fit lines are produced using equation 5.4 and the values of oxide growth rate constants and oxide growth regimes for both conditions. A further comparison of the external growth constants of both intra and intergranular RR1000 can be seen in Table 5-VIII. This provides further evidence that the grain boundaries oxidise quicker than the bulk.

The reason for this occurring is that at lower temperatures and fairly thin scales the grain boundaries act as short-circuit diffusion pathways providing a low energy pathway for diffusion for titanium/chromium to the surface. This leads to enhanced Ti doping at the grain boundaries and therefore enhanced scale growth. At 800°C, this still seems to occur at thin scale thicknesses but as the scale thickens the enhancement disappears. A possible reason for this is that as the chromia scale at the grain boundaries thickens and depletion of chromium and titanium beneath the scale occurs, leading to a larger depletion at the grain boundaries than intragranularly. This causes an increased reduction in the Ti doping at the grain boundaries and the thicker chromia scale acts as a more effective diffusion barrier, as the diffusion distance for Cr across the chromia scale is larger, therefore slower growth ensues. This allows the growth of the intragranular external oxide to outstrip that at the grain boundaries. It is also important to note that the oxide over the grain boundaries is the same composition as the rest and therefore Ti doping is still occurring.

The temperature dependence of the respective rate constants for external oxide formation are shown in the Arrhenius plot to obtain an activation energy for oxide formation at the grain boundaries. This was performed both assuming parabolic kinetics and using actual growth kinetics (Figure 5-38). This has a large effect on the activation energy produced 212 $kJ.mol^{-1}$ to 265 $kJ.mol^{-1}$ respectively, while having little effect on the fit of the best fit regression line with $R^2 = 0.93$ and 0.93 respectively. It must

be stressed that this is from only three data points and only from 6 measurements of grain boundary enhancement at each time period. Table 5-IX shows the activation energy of the Ni-based superalloy RR1000, both intragranularly and intergranularly, along with values for the similar Ni-based superalloy, ME3 and pure chromia formation.

The activation energy of the grain boundary enhanced external oxide is lower than all the other alloys if assuming parabolic kinetics. This occurs because the grain boundaries acts as low energy short-circuit diffusion pathways thereby enhancing the diffusion of chromium and titanium to the surface [52, 53]. As the rate controlling step in a chromia scale is reportedly dominated by the transport of chromium ions across the growing scale a quicker growth rate will ensue at the grain boundaries due to the increase in chromium supplied via short circuit diffusion compared with that supplied intragranularly by bulk lattice diffusion [53]. Additionally, as discussed before, the doping of the chromia scale with Ti leads to an enhanced growth rate over pure chromia formation. A comparison between intragranular and intergranular external oxide growth is difficult, as the intragranular external scale grows in a cubic manner at 700°C and 750°C before switching to parabolic growth at 800°C, whereas parabolic kinetics can be assumed for the growth of the grain boundary (intergranular) enhanced external oxide at all temperatures. This means the determination of the activation energy is skewed in the intragranular condition and it is entirely possible that a new activated process is occurring at 800°C.

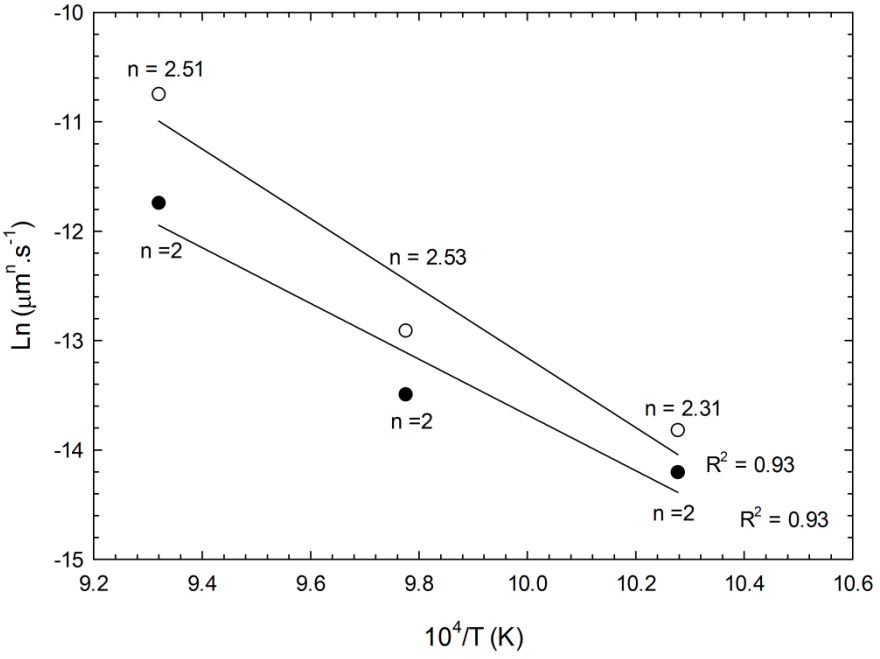

Figure 5-38: Activation energy of oxide formation on grain boundary enhanced external oxide formation between 700-800°C assuming both parabolic and actual kinetics.

The enhancement of the chromia growth rate at the grain boundaries of RR1000 against the chromia oxide thickness on pure chromium or 20Cr25Ni austenitic steel (calculated using equation 5.5) is

shown in Figure 5-39. Clearly the enhancement of the external scale at the grain boundaries occurs at 700°C, 750°C and 800°C. In all cases this enhancement decreases with increasing oxide thickness, in the same way that it occurs in the intragranular external oxide. The only difference is that where a constant enhancement occurred at 800°C intergranularly, a large initial enhancement is recorded which decreases with oxide thickness. The enhancement occurs through the same Ti doping mechanism and decreases because of Ti depletion sub-surface.

Table 5-IX: Activation energies (kJ.mol^{-1}) of external oxide scale formation both intra and intergranularly, with values from the literature.

Alloy	Activation energy (kj.mol^{-1})	Temperature range tested
Intergranular RR1000 (k_p)	212	700-800°C
Intergranular RR1000 (k_n)	265	
RR1000 (k_n)	236	
RR1000 (k_c)	377	
ME3	262 (±33)	704-815°C
20Cr austenitic steel	258	700-900°C

The activation energy provides a useful means of predicting the temperature dependence of the formation of the external oxide scale and allows the following expression for grain boundary enhanced oxide growth kinetics to be developed:

$$(k_p')_{gb} = 1.35 \text{ x} 10^5 \exp\left[-\frac{211925}{8.314T}\right] \quad \mu m^2.s^{-1} \tag{5.9}$$

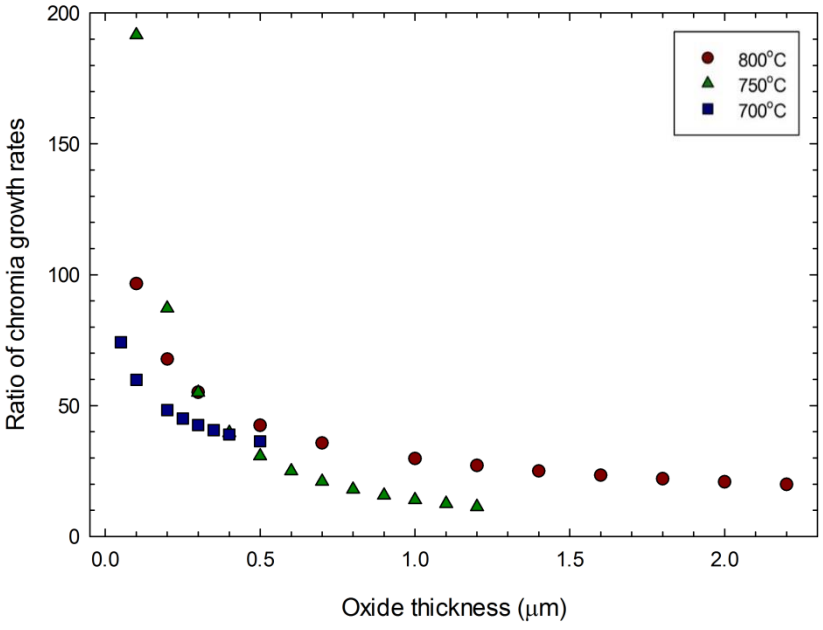

Figure 5-39: The variation of the enhancement ratio with oxide thickness for the three test temperatures at which grain boundary enhanced oxide thickness measurements were undertaken.

5.2.7 Internal oxide and γ′ denuded zone kinetics

Extensive measurements of the thicknesses of the internal oxidation zone (IOZ) and γ′ denuded zone (DZ) at 700, 750 and 800°C for up to 2000 hours have been performed, as described in section 4.5.8. These measurements were normally distributed as displayed in the Q/Q plots and histograms shown in Figure 5-40. A Shaprio-wilk test was used to confirm normality. The average values for 2000 hours at each temperature are included in Table 5-X and measurements for 700°C at all exposure times are included in Table 5-V.

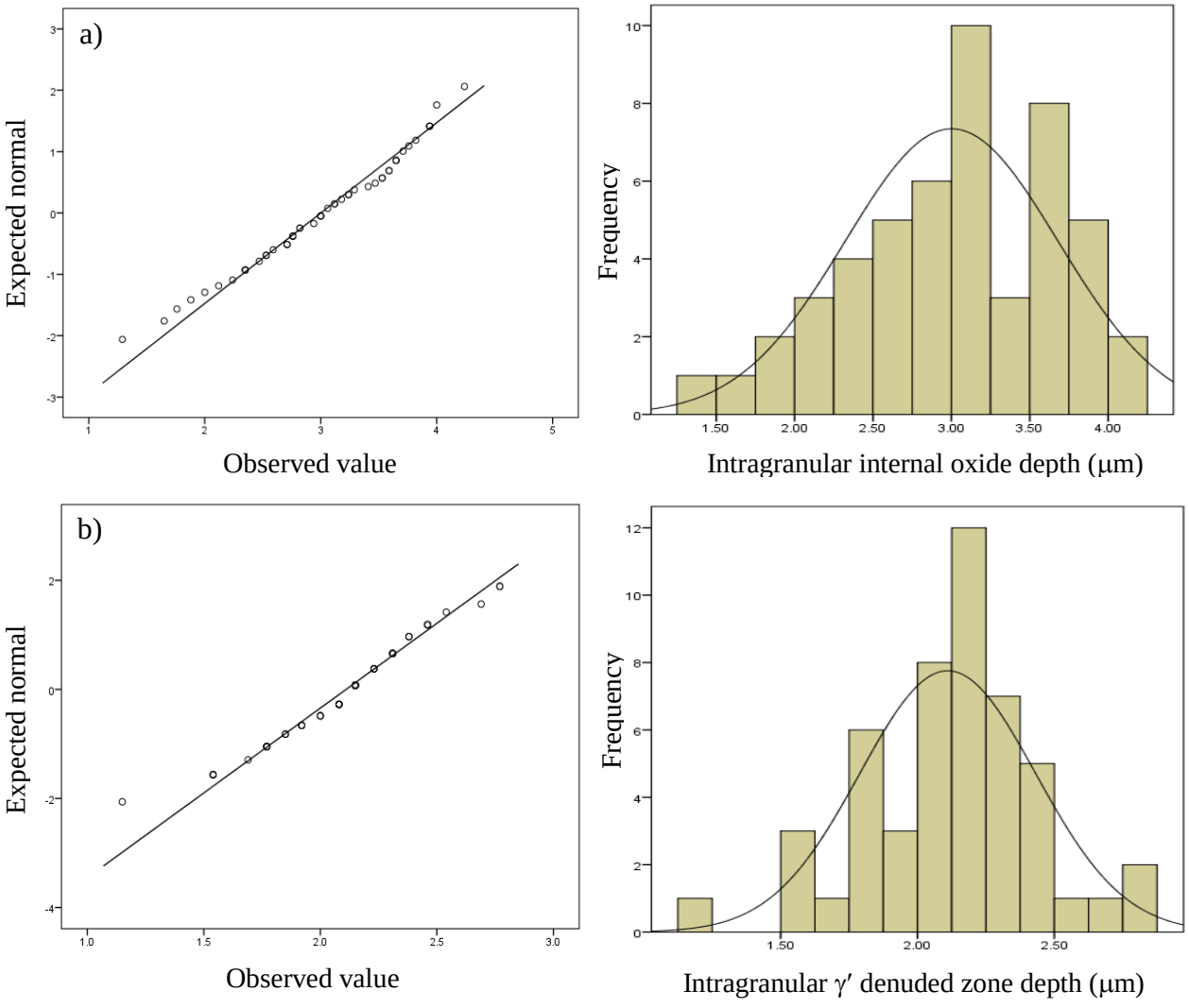

Figure 5-40: Q/Q plot and histogram of all a) the internal intragranular oxide measurements taken from a CG RR1000 specimen oxidised at 750°C for 2000 hours, illustrating that the data is normally distributed. b) The intragranular γ′ denuded zone measurements taken from a CG RR1000 specimen oxidised at 700°C for 2000 hours, illustrating that the data is normally distributed.

Table 5-X: Subsurface damage measurements for both intragranular and intergranular internally oxidised internal oxide penetrations and γ′ denuded zone, with ± 1 standard deviation

Units / μm	Average Al_2O_3 penetrations		Average γ′ denuded zone	
	Intragranular	**Intergranular**	**Intragranular**	**Intergranular**
Number of measurements	50	10	50	10
Distribution of values	Normal	Normal	Normal	Normal
700°C for 2000h	2.06 (± 0.46)	2.92 (± 0.48)	2.11 (± 0.32)	3.72 (± 0.72)
750°C for 2000h	3.00 (± 0.68)	5.42 (± 0.93)	3.69 (± 0.89)	6.99 (± 0.79)
800°C for 2000h	11.07 (±2.04)	16.42 (±2.24)	14.75 (±2.00)	21.59 (±1.54)

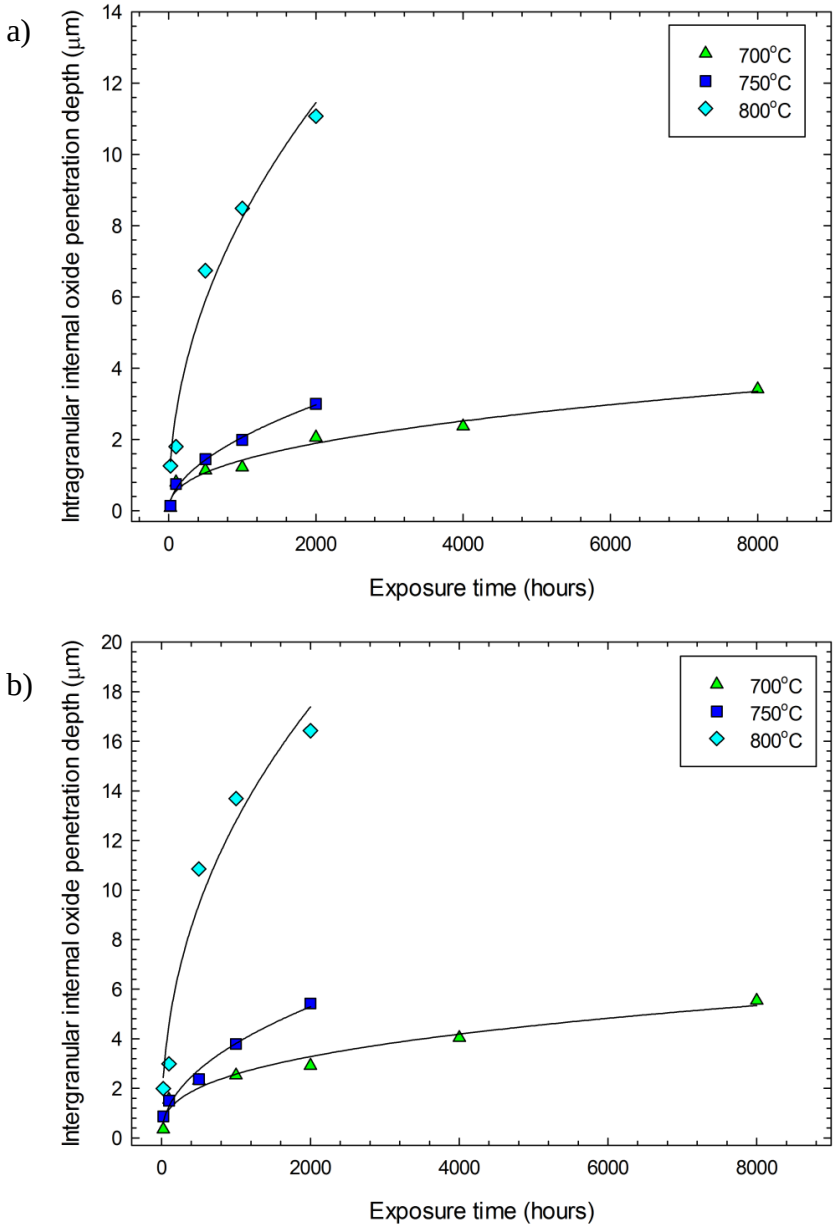

Figure 5-41: Plot of a) Intragranular alumina penetration and b) Intergranular alumina penetration against time for each temperature tested.

Table 5-XI: Subsurface damage measurements taken from the literature on Ni-based superalloy ME3 for both internal oxide penetrations and γ′ denuded zone, with ± 1 standard deviation [47]. A single depth of penetration was reported in ME3.

Units / μm	Average Al_2O_3 penetrations	Average γ′ denuded zone
Number of measurements	24	24
Distribution of values	Normal	Normal
704°C for 2020h	2.97 (± 0.41)	3.11 (± 1.03)
760°C for 2020h	5.71 (± 0.41)	5.80 (± 1.27)
815°C for 2020h	9.97 (±1.23)	10.58 (±0.89)

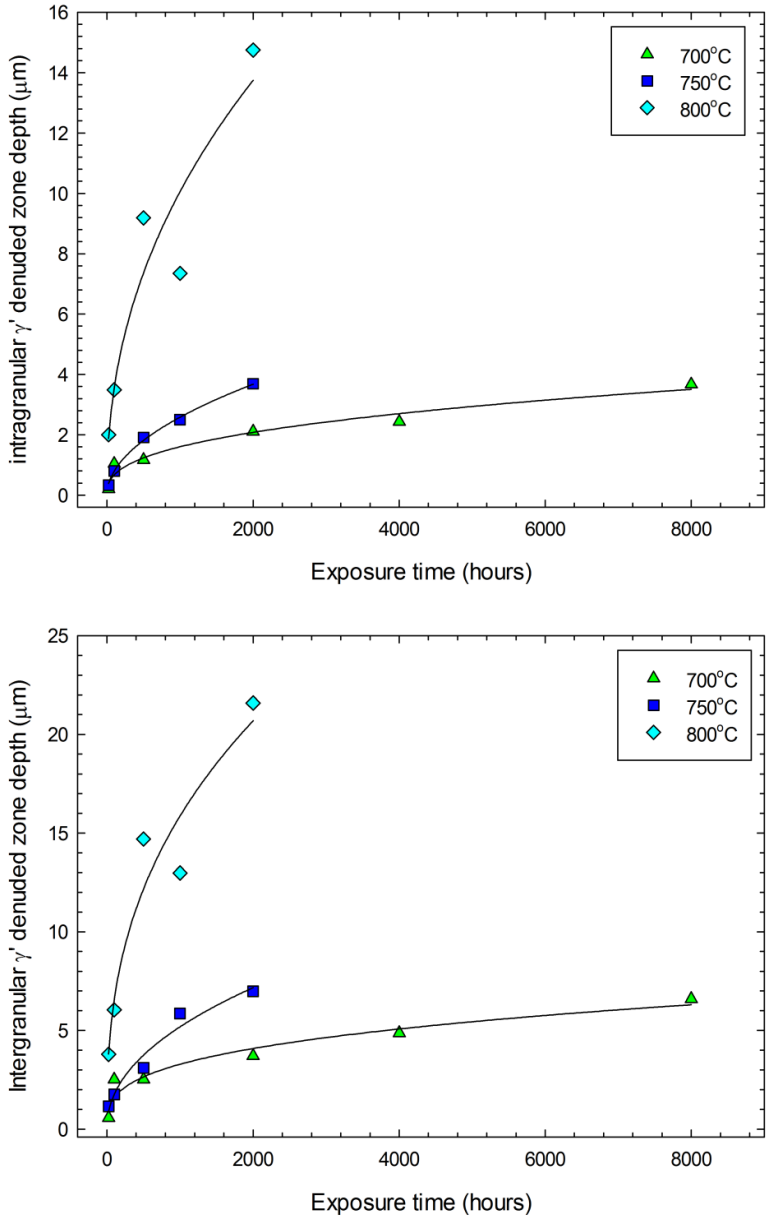

Figure 5-42: Plot of a) Intragranular γ′ denuded zone and b) Intergranular γ′ denuded zone against time for each temperature tested on CG RR1000.

Figure 5-41 clearly shows, like the external oxide growth, that the higher the exposure temperature and time the larger the magnitude of both the internal oxide penetration (both intragranular and intergranular), while also illustrating that the rate of internal oxide growth decreases with time and temperature. The same is shown for the γ′ denuded zone in Figure 5-42. Oxide measurements for the three test temperatures for both RR1000 (present study) and ME3 [47] are shown in Table 5-X and Table 5-XI. While each study used slightly different times and temperatures the results recorded are comparable at 700°C and 750°C but RR1000 illustrates a worse performance at 800°C which follows a similar form to the external oxide measurements. Additionally, only a single type of penetration was reported in ME3 compared to the two distinct types (intragranular and intergranular) seen in the present study, here, on RR1000.

High temperature kinetics for the internal oxide penetration depth, ℓ, can be approximated reasonably using the following equations:

$$\ell_{gb} = \left[(k_{n\ell})_{gb} t\right]^{1/n_{ioz(gb)}} \tag{5.10}$$

$$\ell_{tr} = \left[(k_{n\ell})_{tr} t\right]^{1/n_{ioz(tr)}} \tag{5.11}$$

Where $k_{n\ell}$ are the appropriate growth rate constants for internal oxidation, for intergranular, $(k_{n\ell})_{gb,}$ and intragranular, $(k_{n\ell})_{gb}$. n_{ioz} is the oxide growth regime for both intergranular (gb) and intragranular (tr). The values of n_{ioz} can then be evaluated by plotting log ℓ against log t (Figure 5-43). A similar approach can be performed for the γ′ denuded zone with growth rate constants, $(k_{ny})_{tr}$ and $(k_{ny})_{gb}$ describing the intragranular and intergranular denuded zones respectively. Additionally, n_{dz} can be evaluated in the same way to describe the denuded zone growth regime. Figure 5-43(a) shows the determination of the internal oxide growth regime, with the values being displayed in Table 5-X. Figure 5-43(b) shows the determination of the γ′ denuded zone growth regime, with the values also being displayed in Table 5-X. In both cases parabolic behaviour can reasonably be assumed. Although the growth of the intergranular γ′ denuded zone can be considered to be sub-parabolic, with all n values being significantly over 2. In this case it will be assumed to be parabolic strictly for comparison purposes between the other alloying conditions.

Figure 5-44 and Figure 5-45 show the growth of the alumina penetrations and the γ′ denuded zone and indicate that the intergranular penetrations grow faster than the intragranular penetrations in both cases. This is highlighted again by the parabolic rate constants shown in Table 5-XIII. The best fit lines in Figure 5-44 and Figure 5-45 are produced using equations 5.10 and 5.11 and the values in Table 5-XIV show a good fit with the experimental data.

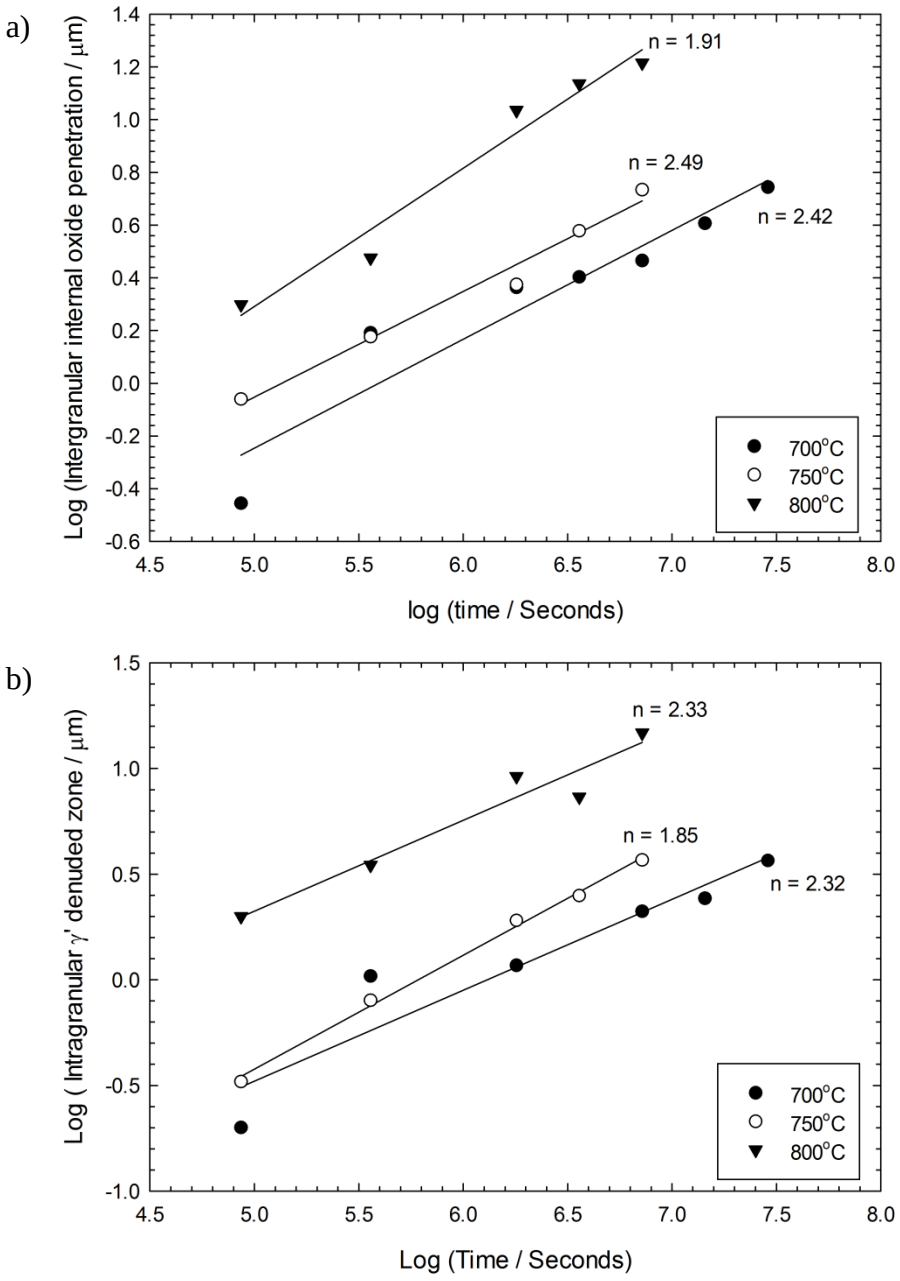

Figure 5-43: Plot of a) log intergranular internal oxide penetration against log time and b) log intragranular γ′ denuded zone depth for 700°C, 750°C and 800°C showing that the growth kinetics can be approximated to parabolic behaviour, n = 2.

Table 5-XII: Best estimates values of the exponent, n, for the internally oxidised zone and the γ′ denuded zone, both intragranularly and intergranularly for coarse grained RR1000.

	Al_2O_3 penetrations		γ′ denuded zone	
	Intragranular	**Intergranular**	**Intragranular**	**Intergranular**
700°C	1.84	2.42	2.34	2.84
750°C	1.53	2.49	1.85	2.38
800°C	1.86	1.91	2.33	2.59

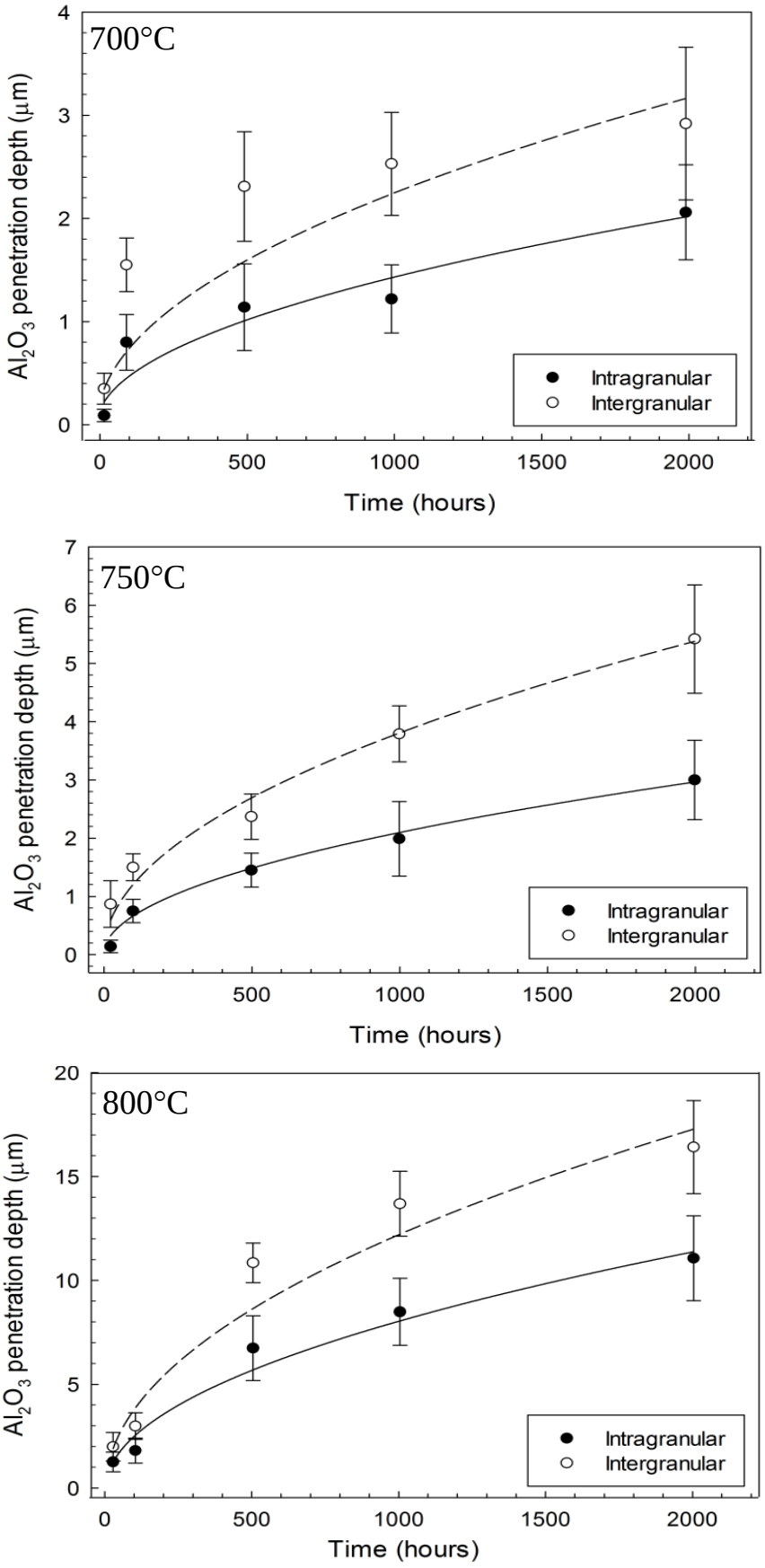

Figure 5-44: Plots of intergranular and intragranular internal oxide penetrations against time at 700, 750 and 800°C.

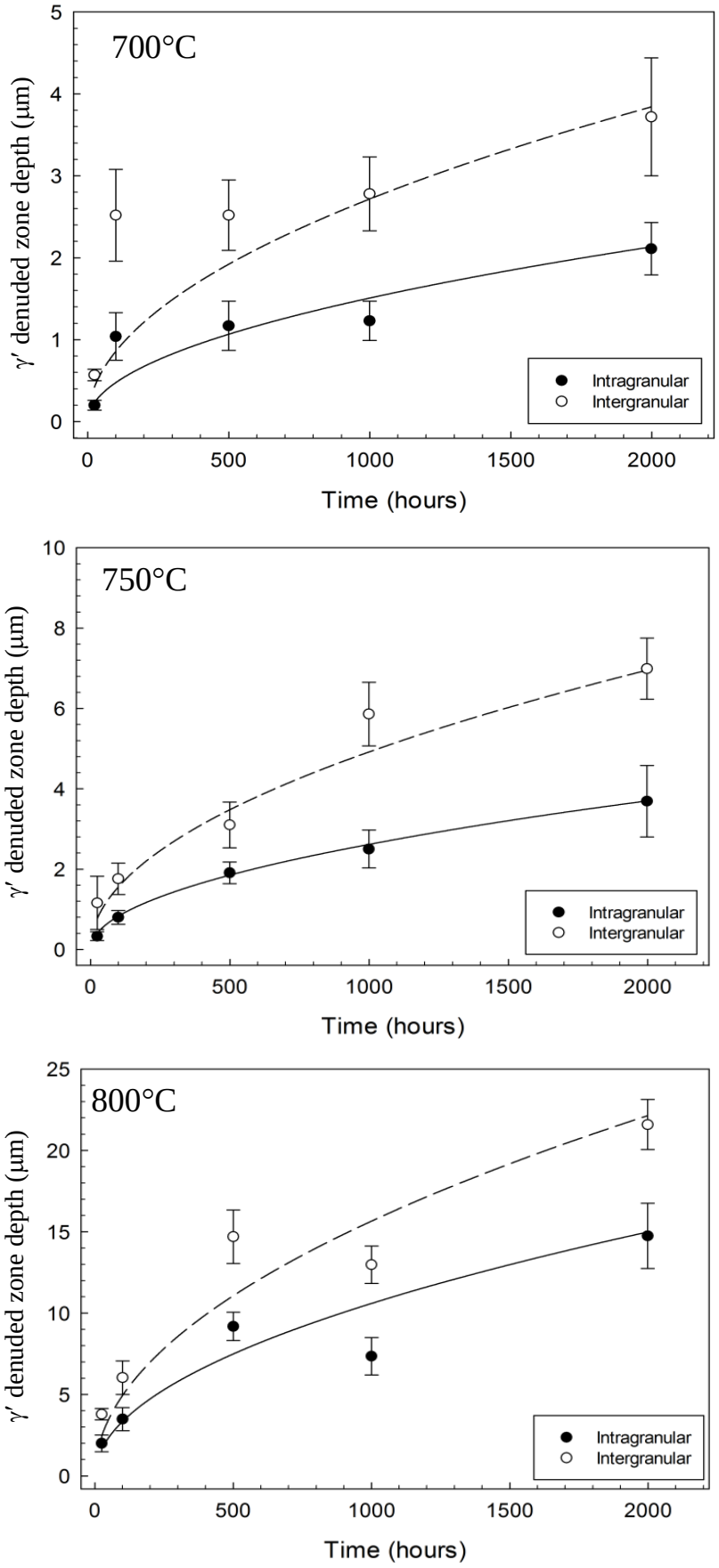

Figure 5-45: Plot of intergranular and intragranular γ′ denuded zone depth against time at 700, 750 and 800°C.

Table 5-XIII: Parabolic rate constants for both intragranular and intergranular internal oxide and γ′ denuded zones for CG RR1000.

Units / $\mu m^2.s^{-1}$	Al_2O_3 penetrations		γ′ denuded zone	
	Intragranular	**Intergranular**	**Intragranular**	**Intergranular**
700°C	$4.1x10^{-7}$	$1.1x10^{-6}$	$4.6x10^{-7}$	$1.6x10^{-6}$
750°C	$1.2x10^{-6}$	$4.0x10^{-6}$	$1.9x10^{-6}$	$7.2x10^{-6}$
800°C	$1.8x10^{-5}$	$4.2x10^{-5}$	$2.8x10^{-5}$	$6.4x10^{-5}$

Table 5-XIV: Parabolic and cubic rate constants for both internal oxide and γ′ denuded zones for Ni-based superalloy, ME3.

	Al_2O_3 penetrations	γ′ denuded zone
	$\mu m^2.s^{-1}$	$\mu m^3.s^{-1}$
704°C	$1.4x10^{-6}$	$5.3x10^{-7}$
760°C	$3.9x10^{-6}$	$2.1x10^{-6}$
815°C	$1.4x10^{-5}$	$1.4x10^{-5}$

Interestingly a comparison with ME3 can be made using the data in Table 5-XIV. The rate constants for the single type of alumina penetrations in ME3 are higher than the intergranular penetrations at ~700°C, in between the two type penetrations at ~750°C and lower than both at ~800°C. This illustrates that the performance of the similar Ni-based superalloy, ME3, improves relative to RR1000 as the temperature increases. It could also be expected that the performance of ME3 improves slightly as the exposure temperature in all cases was marginally higher. The γ′ denuded zone cannot be compared directly as they assume cubic growth rather than the parabolic growth assumed here, and so an accurate comparison cannot be drawn. As expected the rate constants for the γ′ denuded zone are larger than the corresponding rate constants for internal oxidation and using the square root of the ratio of rate constants in Table 5-XIII indicates that the intragranular γ′ denuded zone is approximately 6% deeper than the IOZ at 700°C and approximately 25% deeper at 800°C; the corresponding values for the intergranular penetration are approximately 21% and 23% at 700°C and 800°C respectively.

The temperature dependences of the respective rate constants for internal oxide formation are shown in the Arrhenius plot of Figure 5-46. The present results are obviously limited (three test temperatures only) and do not lie on a particularly convincing line (although $R^2 = 0.94$ for intergranular and 0.89 for intragranular). Nevertheless, they fall within the overall trend displayed by other similar alloys as can be seen in the figure. The values of activation energies obtained from the slopes of the broken lines shown in Figure 5-46 are given in Table 5-XV; for intergranular penetration the intragranular penetrations has a higher value at 325 $kJ.mol^{-1}$ compared with 314 $kJ.mol^{-1}$. The best fit rate equations for each morphology are given below as equations 5.12 and 5.13:

$$(k_{n\ell})_{tr} = 9.07x10^{10} \exp\left[-\frac{325371}{8.314T}\right] \quad \mu m^2.s^{-1} \tag{5.12}$$

$$(k_{n\ell})_{gb} = 6.20x10^{10} \exp\left[-\frac{313598}{8.314T}\right] \quad \mu m^2.s^{-1} \tag{5.13}$$

The temperature dependence of the growth of the γ′ denuded zone was similarly obtained from an Arrhenius plot to obtain the values of activation energy. These are a little higher than those found for the growth of the IOZ, but reflect a combination of the temperature dependences of the IOZ growth, of aluminium diffusion into the IOZ and also the local aluminium concentration for γ′ solution. It is a complex situation that cannot be defined by a singly activated process. Nevertheless, the activation energy provides a useful means of predicting the temperature dependence of the γ′ denuded zone growth as given in equations 5.14 and 5.15:

$$(\mathrm{k}_{ny})_{tr} = 3.71x10^{12} \exp\left[-\frac{354056}{8.314T}\right] \quad \mu m^2.s^{-1} \tag{5.14}$$

$$(\mathrm{k}_{ny})_{gb} = 2.24x10^{11} \exp\left[-\frac{320612}{8.314T}\right] \quad \mu m^2.s^{-1} \tag{5.15}$$

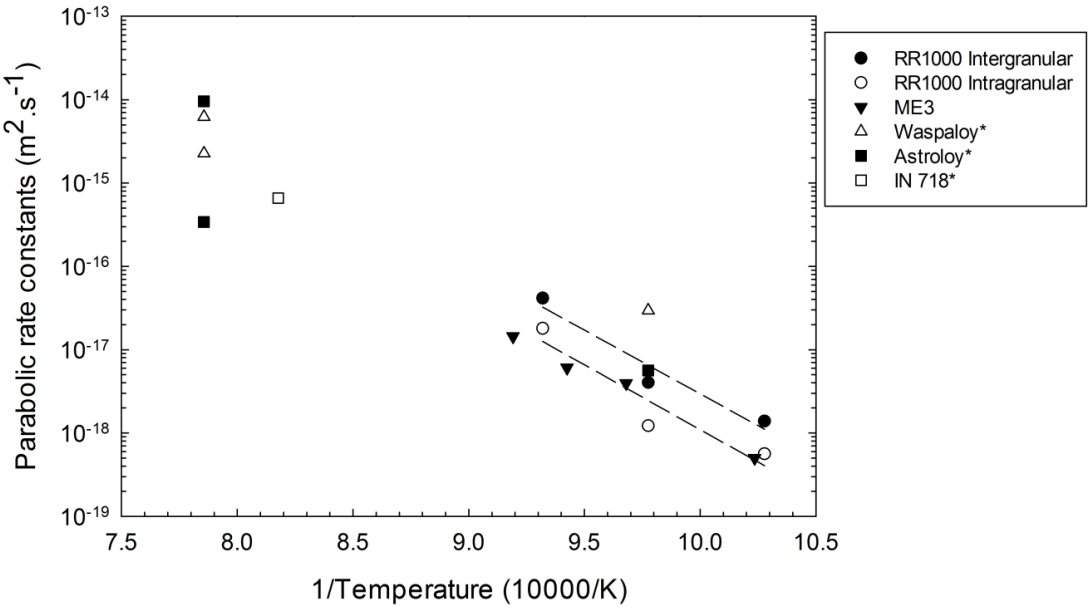

Figure 5-46: Arrhenius plot of both intergranular and intragranular internal oxide penetrations with measurements of several other similar Ni-based superalloys for comparison: some of the values were recorded from single measurements taken from the literature and so are recorded as instantaneous parabolic rate constants [47, 104, 114]. The dotted lines indicate the expected values for k_p' according to equation 5.12 and 5.13.

Table 5-XV: Activation energies (kJ.mol^{-1}) of both internal oxidation and γ′ denuded zones for the present study on RR1000.

Al_2O_3 penetrations		γ′ particle free zone	
Intragranular	**Intergranular**	**Intragranular**	**Intergranular**
325 kJ.mol^{-1}	314 kJ.mol^{-1}	354 kJ.mol^{-1}	321 kJ.mol^{-1}

Internal oxidation of alloys is usually considered to be controlled by the rate of diffusion of oxygen within the alloy. This is likely to be the case in the absence of a surface oxide layer, as considered initially by Wagner [45]. In the presence of a protective surface layer, the diffusion model becomes more difficult but Maak [82] has provided a solution for the case where the surface oxide thickens parabolically. Direct application of this model to the present tests cannot be undertaken reliably, however, because the surface oxide thickens with sub-parabolic kinetics and the model requires the measurements to be taken from the original surface. Estimating the position of the original surface is difficult in this alloy due to the formation of metallic protrusions onto the surface oxide. Maak's treatment again envisages diffusion within the alloy to be rate determining whereas, in principle, the rate of internal oxidation could be determined by the rate of transport through the surface layer. This becomes more likely when the surface oxide is protective as in the present case. It is also clear that a depletion profile of aluminium develops ahead of the region of internal oxidation, as evidenced by a γ′ denuded zone, as shown in Figure 5-13 and Figure 5-47. The EDX scan of Figure 5-47 demonstrates that the aluminium concentration within the alloy falls rapidly from the bulk value (horizontal line) as the γ′ denuded zone boundary is crossed and before the internally oxidised region is reached. Since the formation of a particle of new oxide within the alloy requires that the solubility product of alumina is exceeded, it is possible, in principle, for the supply of aluminium, rather than oxygen, to control the rate of thickening of the internal oxidation zone.

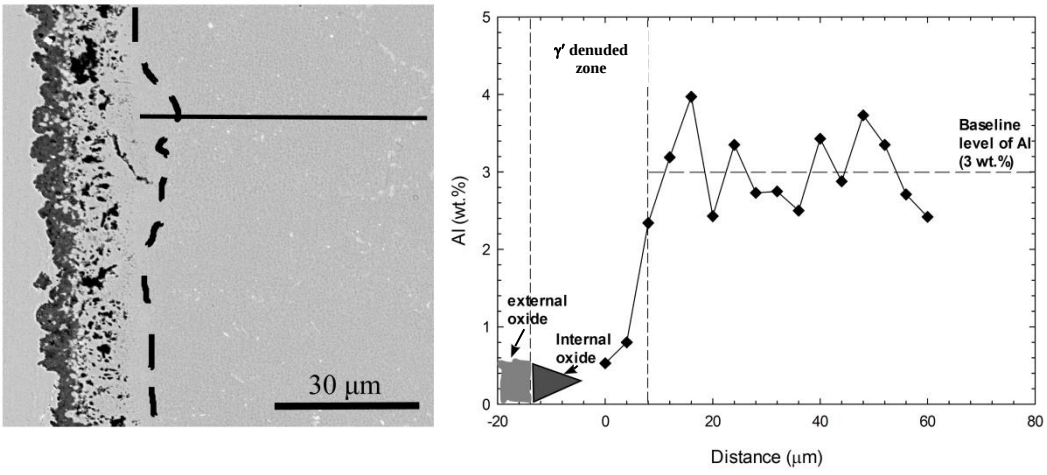

Figure 5-47: EDX analysis showing diffusion profile of aluminium concentration at 4 μm increments of a specimen oxidised at 800°C for 2000 hours: dashed line on micrograph indicates limits of γ′ denuded zone; boundaries of various zones and baseline level of aluminium in the alloy are indicated on the profile; oxygen was not detected in this profile.

The activation energies for the thickening of the IOZ in the present tests for both intergranular and intragranular penetration are shown in Table 5-XV, with intergranular penetration having a lower activation energy. This is a not a surprising result since, if oxygen transport within the alloy were rate controlling, it would be expected that the faster rate of penetration down alloy grain boundaries would have been associated with a lower activation energy commensurate with a fast diffusion path. The process controlling the development of the sub-surface damage is unclear, but it is likely to be a

combination of: oxygen transport through the surface oxide, oxygen transport into the alloy and aluminium diffusion to the reaction front. It needs to be emphasised, however, that these values are based on measurements obtained at only three test temperatures and a more comprehensive data set is required and so further work is required in this area.

5.2.8 Total oxidation damage kinetics (both intragranular and intergranular)

The kinetics of growth of both the external oxide and the γ′ denuded zone are combined to give total oxidation damage at both the grain boundaries and transgranularly. This is not quite the same as section loss as some rutile/chromia growth will sit on the surface of the alloy, rather than remove useful load-bearing cross-section, but still provides a most valuable tool in lifing a component.

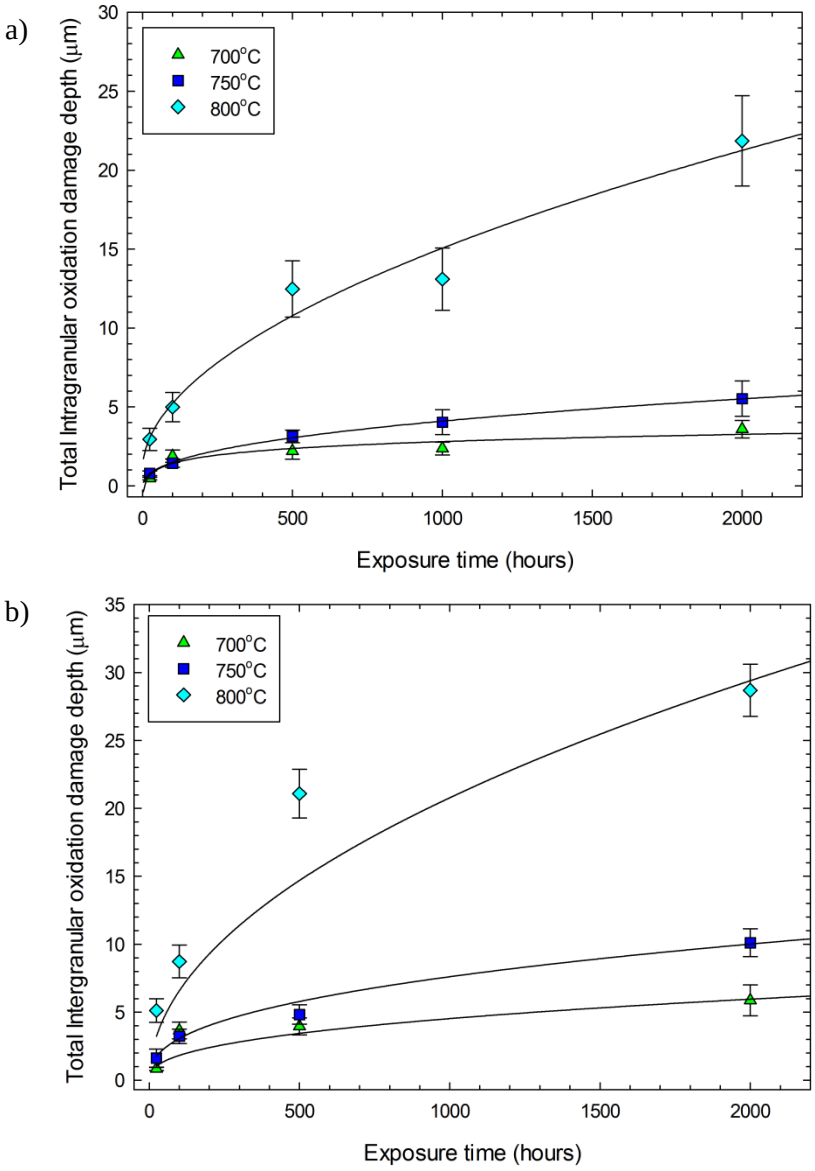

Figure 5-48: Plot of total oxidation damage depth against time at a) intragranular locations and b) intergranular locations that extensive metallographic measurements were performed.

Figure 5-48 shows that as the exposure temperature and time increases so does the magnitude of the oxidation damage. This is not unexpected since it is a composite of the damages discussed earlier in this chapter which all show a similar pattern. It can also clearly be seen that the damage intergranularly is significantly larger at all temperatures tested than that at intragranular locations, which is not unexpected. The depth of total oxidation damage is driven largely by the internal damage (internal oxide and γ′ denuded zone) as this makes up over half of the total oxidation damage produced by prolonged exposures at high temperatures. This means that while the enhancement of the external oxide scale is removed as the scale thickens at 800°C for the longer time periods, the growth of the internal damage at the intergranular locations still outstrips that of the intragranular damage. Therefore the total oxidation damage intergranularly continues to grow at a faster rate than that occurring intragranularly.

High temperature kinetics for the total oxidation damage, τ, both intergranularly and intragranularly can be approximated reasonably using the following equations respectively:

$$\tau_{gb} = \left[(k_{n\tau})_{gb}\, t\right]^{1/(n_{\tau o})_{gb}} \quad (5.16)$$

$$\tau_{tr} = \left[(k_{n\tau})_{tr}\, t\right]^{1/(n_{\tau o})_{tr}} \quad (5.17)$$

Where $(k_{n\tau})_{gb}$ and $(k_{n\tau})_{tr}$ are the appropriate growth rate constants for total oxidation damage, for intergranular, and intragranular respectively. $n_{\tau o}$ is the oxide growth regime for both intergranular (gb) and intragranular (tr). $n_{\tau o}$ can be determined by plotting log τ against log of time (Figure 5-49). The values for $n_{\tau o}$, $(k_{n\tau})_{gb}$ and $(k_{n\tau})_{tr}$ are shown in Table 5-XVI. Although sub-parabolic kinetics are found in all cases, parabolic kinetics are assumed, to allow for comparison between the other surface conditions (Chapter 6). Figure 5-50 shows the growth of the total oxidation damage and indicates that the oxide damage at the grain boundaries grows faster than that intragranularly. This is highlighted again by the parabolic rate constant values displayed in Table 5-XVI. The best line fits in Figure 5-50 are produced using equations 5.16 and 5.17 with the values in Table 5-XVI and shows a good fit with experimental data. The temperature dependence of the respective rate constants is shown in Figure 5-51, with activation energies of 329 and 274 kJ.mol^{-1}, for the intragranular and intergranular locations respectively. The large reduction in activation energy in the intergranular location is caused by the grain boundaries acting as short-circuit diffusion pathways allowing faster transport of oxygen, aluminium and chromium to the internal oxidation reaction front and to the external scale/alloy interface. Enhancement at the grain boundaries both internally and externally has also been seen in the Ni-Al system [79].

The rate controlling process for oxidation in RR1000 is complex and, as mentioned previously, there is likely to be a combination of processes occurring. It is likely that chromium diffusion through the Ti-doped chromia oxide scale is controlling the growth of chromia scale on RR1000. The activation energy of Cr through a single crystal of chromia (280kJ.mol^{-1}) compares reasonably well with those reported in this alloy (236 kJ.mol^{-1}) and those reported for pure chromia formation (258 kJ.mol^{-1}), although the contribution of O diffusion through chromia cannot be discounted. No values for the activation energy for O diffusion in chromia were found in the literature. The single crystal of chromia was reported to have Si as an impurity that reacts in a similar doping mechanism to Ti in this alloy ($3SiO_2 \rightarrow 3Si_{cr}^{\cdot} + V_{Cr}^{'''} + 6O_o^x$) and so is particularly relevant in this comparison. The activation energy for Cr diffusion down chromia grain boundaries is much higher, at 675kJ.mol^{-1}. This is partly due to the inability for single crystals to be produced free of impurities/defects therefore accounting for the lower activation energy [184]. It is also important to note the much higher temperature used in these studies compared with the one here. Sub-surface it is likely that no-single process is rate controlling and that different processes ensues for the growth of the internal oxide and γ′ denuded zone. Table 5-XVII displays the activation energies, taken from the literature, for O in Ni, Cr through chromia, Ti and Al in Ni-Ti-Al ternary alloys and Cr in 20Ni-25Cr steel or Ni-16Cr-7Fe. While the values for oxygen diffusion are significantly below those reported here for both lattice and grain boundary diffusion in the internally oxidised zone (325 and 314 kJ.mol^{-1} respectively) and the γ′ denuded zone (354 and 321 kJ.mol^{-1} respectively). This is likely to be due to oxygen having to diffusion through a protective chromia scale and therefore a higher activation energy would be expected. In all cases the activation energy shown here is much larger than those for possible rate controlling processes in Table 5-XVII. Oxygen diffusion through the chromia scale or diffusion of Al, to the internal oxidation reaction front is likely to be controlling the rate of internal oxidation and further analysis is required to illicit the correct mechanism. It is reasonable that the diffusion of Al to the internal reaction front induces the dissolution of the γ′ particles and therefore controls the γ′ denuded zone growth, although again further work is required.

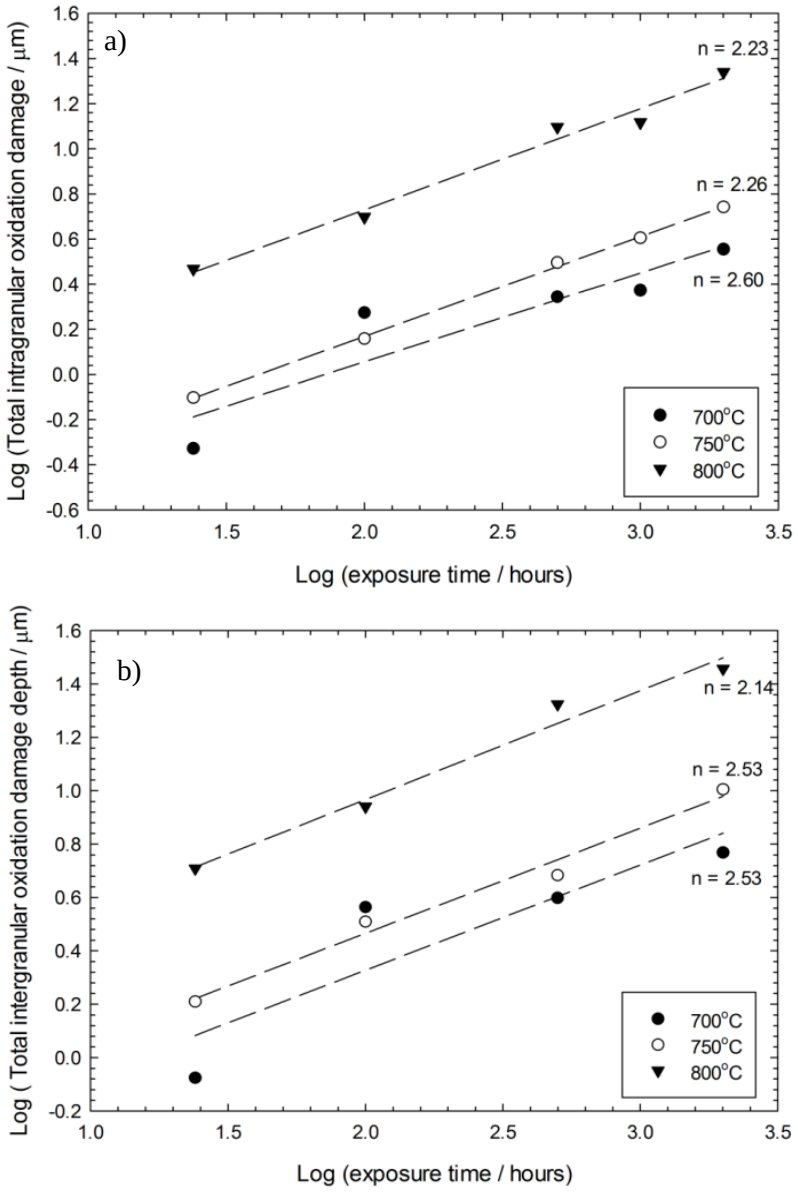

Figure 5-49: Plot of log total oxide thickness against log of exposure time for 700-800°C at a) intragranular and b) intergranular locations, illustrating that parabolic behaviour can be assumed (n = 2).

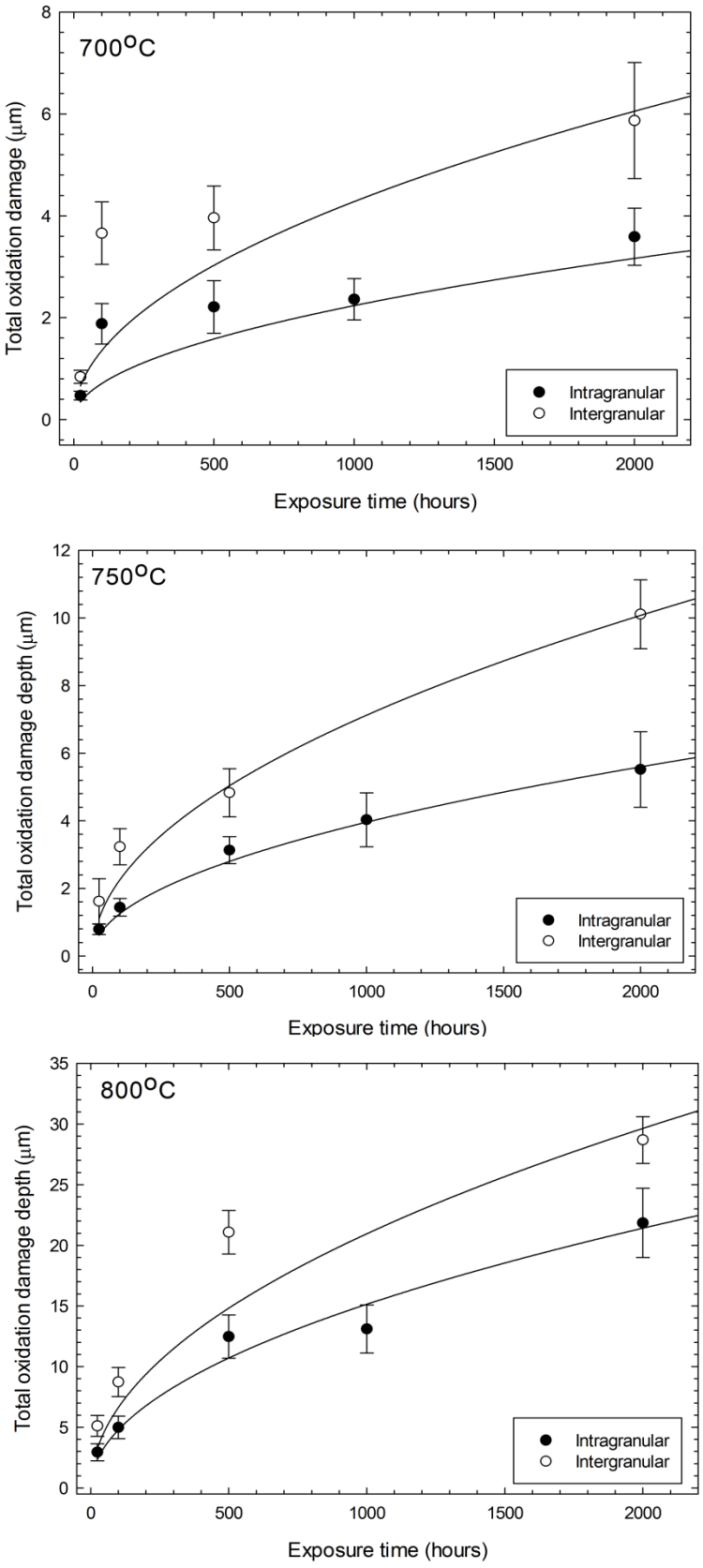

Figure 5-50: Plots of total oxide damage depth at both intragranular and intergranular regions, illustrating the enhanced growth at the grain boundaries (±1 standard deviation).

Table 5-XVI: Both exponent, n_{To}, and parabolic growth rate constants for both intergranular and intergranular total oxide damage depth for CG RR1000.

Temperature	Intragranular		Intergranular	
	$(n_{to})_{tr}$	$(k_{p\tau})_{tr}$ ($\mu m^2.s^{-1}$)	$(n_{to})_{gb}$	$(k_{p\tau})_{gb}$ ($\mu m^2.s^{-1}$)
700°C	2.60	$1.39x10^{-6}$	2.53	$5.09x10^{-6}$
750°C	2.26	$4.35x10^{-6}$	2.53	$1.41x10^{-5}$
800°C	2.23	$6.37x10^{-5}$	2.14	$1.22x10^{-4}$

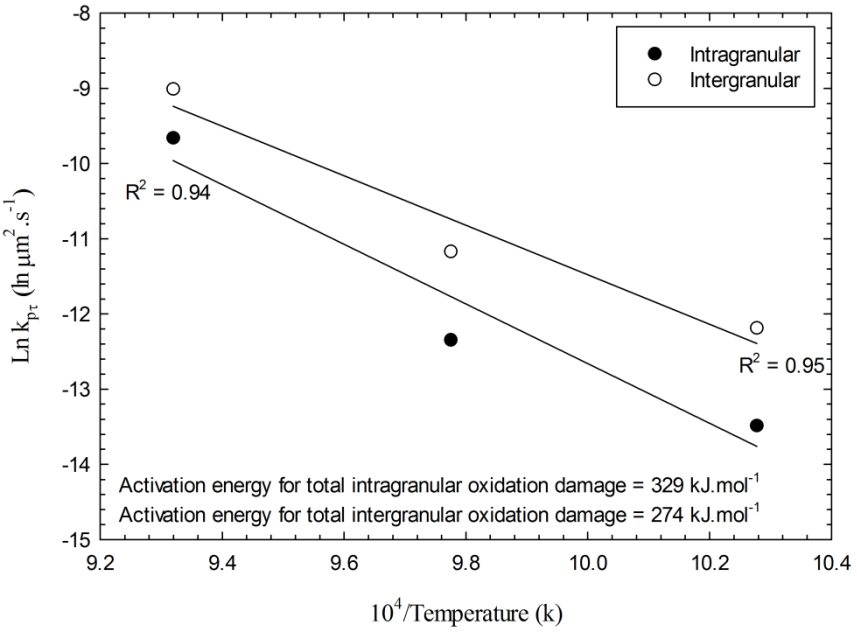

Figure 5-51: Activation energy of the total oxide damage on CG RR1000 both intergranularly and intragranularly. A best fit regression line is included with an R^2 values describing the fit of the line.

Two equations have been produced to describe the oxidation damage at both intergranular $(k_{p\tau})_{gb}$ and intragranular $(k_{p\tau})_{tr}$ and are displayed below:

$$(k_{p\tau})_{tr} = 5.19x10^{11} \exp\left[-\frac{329542}{8.314T}\right] \quad \mu m^2.s^{-1} \tag{5.18}$$

$$(k_{p\tau})_{gb} = 2.16x10^{9} \exp\left[-\frac{274127}{8.314T}\right] \quad \mu m^2.s^{-1} \tag{5.19}$$

These equations can be used to predict the kinetics of total oxidation damage at any temperature within the temperature range tested (700-800°C), allowing the quantification of the depth of oxide damage produced by a high temperature exposure.

Table 5-XVII: The activation energies, taken from the literature, for O in Ni, Ti and Al in Ni-Ti-Al ternary alloys and Cr in 20Ni-25Cr steel or Ni-16Cr-7Fe. The studies with the most appropriate temperature range to the one used here (973-1073 K) were selected.

Diffusion species	Metal/Alloy	Temperature range (K)	Activation energy / Q ($kJ.mol^{-1}$)	Reference
Oxygen	Nickel	623-1273	240	[185]
Oxygen	Nickel	950-1600	192	[185]
Oxygen	Nickel	1123-1673	164	[186]
Oxygen (lattice)	Nickel	500-1726	158	[185]
Oxygen (grain boundary)	Nickel	500-1726	108	[185]
Al (lattice)	Ni-Al-Ti steel	1173-1473	266	[187]
Ti (lattice)	Ni-Al-Ti steel	1173-1473	278	[187]
Cr (lattice)	20Ni-25Cr steel	823-1173	246	[188]
Cr (grain boundary)	20Ni-25Cr steel	823-1173	187	[188]
Cr (lattice)	Ni-16Cr-7Fe	858-1346	283	[189]
Cr (grain boundary)	Ni-16Cr-7Fe	858-1346	201	[189]
Cr	Chromia (Single crystal)	1473-1723	280	[190]
Cr	Chromia (Polycrystalline)	1473-1573	675	[184]

5.2.9 Grain boundary phase dissolution zone

The deepest form of oxidation damage can be considered to be the dissolution of grain boundary phases. In the as-received alloy MC carbides reside on the majority of the grain boundaries (Figure 5-52(a)). These decompose according to the following equations 5.20 and 5.21 during high temperature exposure to form Cr-Mo rich phases; these are most likely $M_{23}C_6$ at these temperatures [172]. It is also possible that Cr and Mo rich sigma phase could be forming as it is nominally $(Ni\text{-}Co)_x(Cr, Mo)_y$ [172].

$$MC + \gamma \rightarrow M_{23}C_6 + \gamma' \quad (5.20)$$

$$MC \rightarrow M_{23}C_6 + \sigma \quad (5.21)$$

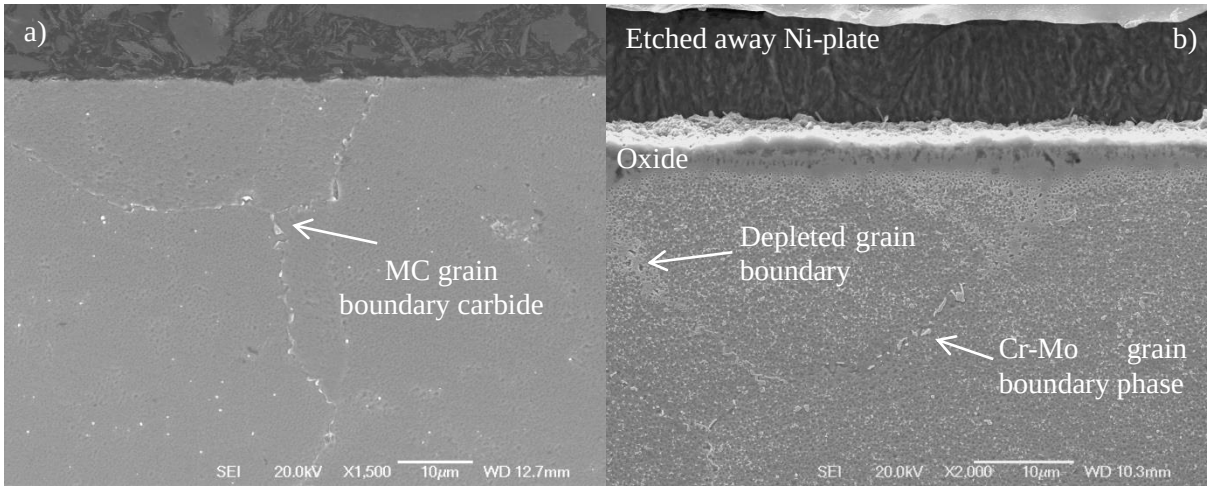

Figure 5-52: SEM images of a cross-section through a) as-received CG RR1000, showing grain boundary carbides and b) the grain boundary phase dissolution of CG RR1000 oxidised at 700°C for 2000 hours. Both specimens were etched using Kallings reagent.

These phases then dissolve to form a dissolution region underneath the external oxide scale (Figure 5-52(b)). The dissolution of these phases is likely to be caused by the depletion of chromium underneath the external chromia scale. The depth of the grain boundary phase dissolution zone after exposure at 700°C for 2000 hours can be seen in Table 5-V at an average depth perpendicular to the surface of 14.50 μm. Chromium carbide dissolution has been shown to occur in both chromia forming steels and superalloys [47, 62-65, 191]. This generally leads to a weakened region at the surface but in some cases can also cause an increase in the number of carbides in the centre of the specimen, as carbon diffuses there, improving the creep strength of the alloy [62, 64, 65]. The dissolution region here is significantly larger than that found in ME3 with a fine grain size, with 9.6 μm [47]. This is not to be unexpected since the frequency of the grain boundaries and number of grain boundary phases is likely to be larger with a fine grain structure, leading to a larger reservoir of chromium on the grain

boundaries in the near surface region. Thus, a greater number of grain boundary phases have to dissolve to achieve the same overall dissolution depth [191]. These grain boundary phases are likely to contain a high proportion of $M_{23}C_6$ since sigma phase would not be expected in large quantities below 800^{o}C, even at prolonged periods of time [172]. Even so a more detailed analysis is required at several temperatures and exposure times to allow detailed kinetics for the formation and dissolution of these grain boundary phases, as is the need for detailed compositional analysis via transmission electron microscopy (TEM), allowing the determination of the exact structure of the grain boundary phase that is dissolving. As stated previously analysis using WDS on an SEM was not conclusive.

5.3 Concluding Summary

The oxidation kinetics and oxidation damage of coarse-grained Ni-based superalloy, RR1000, has been comprehensively studied through the use of mass gain and metallographic measurements and the following conclusions can be made:

- Mass gain kinetics show parabolic growth behaviour across all temperatures tested, with parabolic rate constants being comparable to similar chromia forming Ni-based superalloys.

- An activation energy of 325 kJ.mol^{-1} was recorded over a temperature range of 650-900^{o}C and is similar to other Ni-based superalloys but is considerably more than pure chromia formation, which is to be expected since in RR1000 more than one element (Cr, Ti and Al) is oxidising.

- The oxide comprises of an external oxide scale of Cr_2O_3 with isolated grains of TiO_2 on the outer surface. Sub-surface is significant internal Al_2O_3, which occurs in two distinct morphologies: intergranular and intragranular. Beneath this the presence of TiN occurs but only at higher temperatures and prolonged times (e.g. 800^{o}C for 2000 hours).

- A significant γ' denuded zone is observed underneath the internal oxidised region. In addition, beneath this layer depletion of the grain boundaries of chromium and molybdenum rich carbide occurs and this is the furthest extent of the oxidation damage recorded in this alloy. Protuberances of base alloy were recorded within the external oxide scale and are thought to have formed from outward creep of the depleted γ' denuded region to accommodate the increase in volume resulting from the formation of internal oxides.

- The external oxide scale grows significantly faster than pure chromia. This enhancement decreases with oxide thickness at 700^{o}C and 750^{o}C and can be as much as two orders of magnitude for thin scales (~0.1 μm) although decreases to a value of around 6 at oxide thickness of 2 μm. This enhancement occurs at 800^{o}C as well but rather than decreasing with thickness it stays constant at a relatively low level, with a value of 14. This shows that the chromia enhancement is less dependent on oxide thickness at 800^{o}C than it is at lower temperatures. Further investigations are required to understand the reason for this occurring as it is not currently understood.

- The increased oxidation rate of the external oxide scale in RR1000 is attributed to increased ionic transport caused by doping of the chromia layer by titanium and the consequent creation of vacancies on the chromium sub-lattice.

- The growth rates of internal oxidation damage (internal oxidation and γ′ denuded zone) can be approximated accurately by parabolic behaviour. Equations to describe the development of the internal oxidation damage have been produced. The process controlling the development of the subsurface damage is unresolved, but it likely to be a combination of: oxygen transport through the surface oxide, oxygen transport into the alloy and aluminium diffusion to the reaction front. Further work with more advanced compositional analysis is needed.

- Significant enhancement of the oxidation damage at the grain boundaries has been recorded both externally and internally, with these acting as potential short circuit diffusion pathways and providing lower activation energy paths for diffusion.

- Limited characterisation of the grain boundary chromium-molybdenum phase dissolution was performed with it forming the deepest component of internal oxidation damage, penetrating significantly further that the γ′ denuded zone. Further detailed analysis to provide kinetics and to pinpoint whether it is sigma phase or the more likely $M_{23}C_6$ is required.

Chapter 6 - Oxidation of Ni-based Superalloy, RR1000, with Different Surface Modifications

6.1 Introduction

It has been established that surface modifications, e.g. shot-peening, can have a significant effect on the high temperature oxidation performance of an alloy. This can occur through the earlier formation of a protective scale, enhanced oxide growth or change in oxide composition [119-123]. Most oxidation studies, especially those on Ni-based superalloys are performed in the ground or polished condition rather than the actual condition the component would enter service and since high temperature oxidation has been shown to reduce component lives [84, 152] it is important to quantify the effect that different surface modifications have. Little work has been done to investigate the effect of different surface conditions in Ni-based superalloys, specifically different surface treatments that would be present in the real life application, as well as having different levels of surface damage.

The aim of this research was to investigate and quantify the effect different surface modifications (Shot-peeing, Vibro-peening, Turning and Swaging) have on the oxidation kinetics and oxide oxidation damage of the Ni-based superalloy, RR1000. This includes a detailed analysis of the composition, oxidation kinetics and oxidation damage of the alloy having undergone prolonged (up to 2000 hours) high temperature (700-800^{o}C) exposure to laboratory air.

6.2 Results and Discussion

A comparison between the different surface modifications has been made in the as-received condition using several different techniques before comparing the oxidation kinetics and damage caused during a prolonged high temperature exposure (700-800^{o}C for up to 2000 hours).

6.2.1 Surface roughness

The surface roughness of all the different surface conditions (Polished, Shot-peening, Vibro-peened and Turned) has been calculated with, in the case of the polished and shot-peened CG RR1000 conditions, both confocal and Talysurf measurements being performed. This was done to check the validity of the confocal technique used in all the conditions. The surface roughness was recorded as R_a, S_a and R_c, with the terms defined in both the experimental procedure and appendix. It is important to record the surface roughness as it has been shown to affect the oxide morphology, composition and growth rates [108, 130-135] and needs to be accounted for when comparing mass gain measurements due to the increase in surface area it causes.

The surface roughness measurements (Table 6-I) on the shot-peened variant are similar using both techniques and compare well with data reported in the literature for shot-peened Udimet 720Li [116] and those found internally at Rolls-Royce plc, using white light interferometry. In contrast there is a clear discrepancy between the roughness measurements obtained on the polished specimens; this is thought to be due to excessive background noise with the confocal technique at low surface roughnesses perhaps produced using back reflection. In this case Talysurf measurements are likely to be more reliable and show the surface to be particularly flat.

The surface roughness of all the surface modifications show significant increases in the surface roughness compared with the polished condition, with the turned surface having the roughest surface. The fact that both the shot-peened and vibro-peened conditions started with a 1200 grit surface finish is important, as Table 6-I illustrate that both shot-peening and vibro-peening increase the surface roughness of the 1200 grit ground surface. Shot-peening removes any semblance of the ground finish underneath, while vibro-peening does not with most of the ground surface still being visible in the vibro-peened image (Figure 6-1). The reason behind this is that vibro-peening is a less aggressive surface treatment and therefore the increase in surface roughness over the ground surface is largely due to the process modifying the ground finish, rather than removing it. Therefore the pre-vibro-peening surface condition is important in determining the surface finish of the component. The swaged condition was polished to the same surface finish as the polished condition and so is not included in Table 6-I.

Table 6-I : Confocal microscope surface roughness measurements of coarse-grained RR1000, compared with Talysurf results, μm (± standard deviation).

	Confocal Measurements		**Talysurf Measurements**	
	Polished CG RR1000	**Shot-peened CG RR1000**	**Polished CG RR1000**	**Shot-peened CG RR1000**
S_a	0.43 (±0.16)	1.57 (±0.01)	-	-
R_a	0.31 (±0.12)	1.48 (±0.18)	0.01 (±0.005)	1.42 (±0.01)
R_c	1.00 (±0.46)	3.81 (±0.64)	0.10 (±0.05)	4.66 (±0.96)

	Confocal Measurements		
	Vibro-peened CG RR1000	**Turned CG RR1000**	**1200 grit CG RR1000**
S_a	1.84 (±0.07)	2.37 (±0.12)	1.24 (±0.11)
R_a	1.69 (±0.26)	2.33 (±0.23)	1.19 (±0.16)
R_c	4.49 (±0.94)	7.65 (±0.88)	3.23 (±0.39)

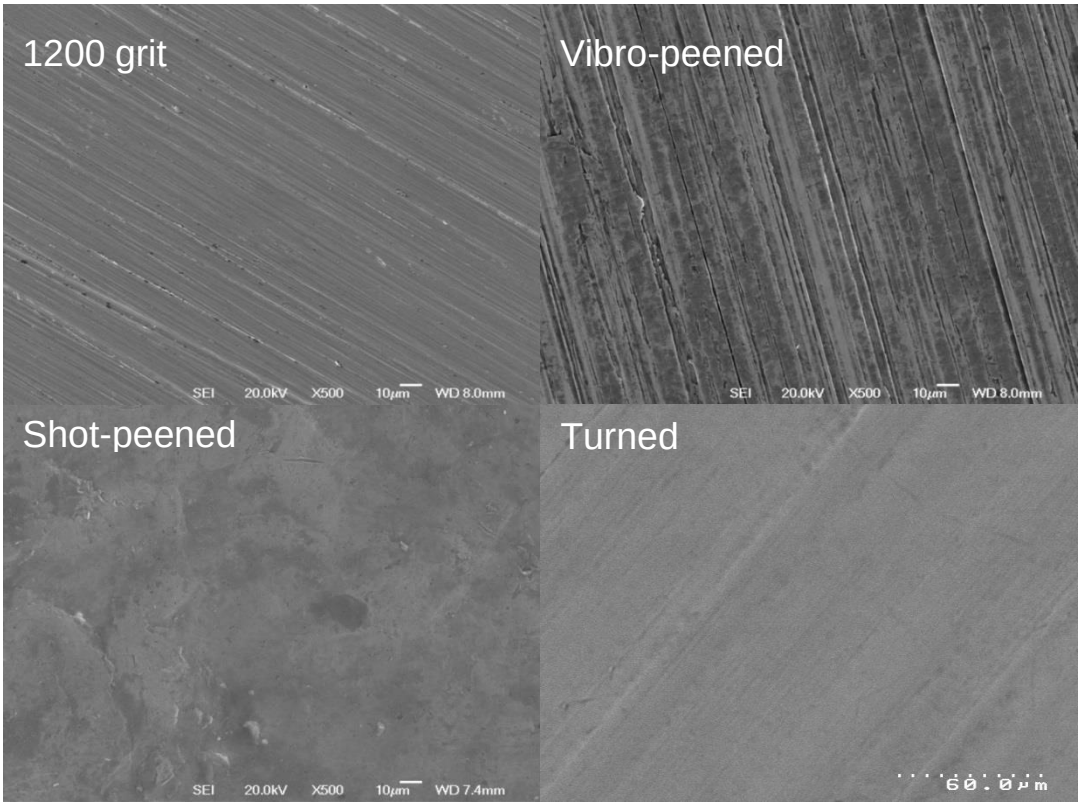

Figure 6-1: Secondary electron images of the surface of as-received specimens for oxidation after the prescribed surface treatment.

The surface roughness of the polished un-oxidised samples is significantly smoother than that of the other surface conditions (Table 6-I). The oxidation reaction is often described by mass gain per unit specimen area. This is conventionally taken as geometric area, but where significant surface roughness exists it is desirable to make the estimate of an increased surface area for use in the calculation of specific mass gain. As a first approach, the actual surface area of the shot-peened samples was calculated by assuming the surface roughness followed a sinusoidal profile. The effective increase in line length was then estimated by calculating the arc length using the roughness data obtained earlier. This arc length is given by equation (6.1) below:

$$l_c = \int_0^{\omega} \sqrt{1 + \left(\frac{dy}{dx}\right)^2}\ \mathrm{dx} \tag{6.1}$$

where l_c is the length of the curve, x is the linear coordinate between 0 and the wavelength, ω, and y is given by:-

$$y = A\ sin\frac{2\pi x}{\omega} \tag{6.2}$$

where A is the amplitude (half R_c of 3.81 μm), ω is the wavelength (24 μm). This gives:-

$$y = 1.9 \sin\frac{2\pi x}{24} \quad (6.3)$$

Differentiating this gives:-

$$dy/dx = 0.4974 \cos\frac{\pi x}{12} \quad (6.4)$$

Inputting equation (6.4) into Equation 6.1 then gives:

$$l_c = \int_0^{24} \sqrt{1 + \left(0.4974 \cos\left(\frac{\pi x}{12}\right)\right)^2}\, dx \quad (6.5)$$

This integral was evaluated numerically to give a 5.9% increase in length over the roughness wavelength using software available at www.wolframalpha.com/input/?i=integral. This corresponds to an increase in surface area of 12.2%. This increase in surface area was then applied to the geometric surface area recorded on the shot-peened specimens. This approach is only relevant to mass-gain measurements, as any detailed oxide thickness measurements will be applied in the direction of oxide growth. As such this approach was only applied to shot-peened system, as no mass gain measurements were recorded in the other surface conditions.

6.2.2 Micro-hardness

Figure 6-2 shows the effect of the different surface conditions on the hardness profile of the specimen. The hardness at the surface region of the specimen, in the shot-peened condition is raised significantly and extends to a depth of around 140-150 μm into the alloy. From the error bars it can be seen that there is a significant amount of scatter which is down to the discrete γ/γ′ microstructure. The depth of this hardness affected zone compares well with previous research [116] performed on the Ni-based superalloy, Udimet 720Li where a zone depth of 140 μm was reported. In that study, the effect of a range of shot-peening conditions was investigated, and that included the conditions used here. This increase in hardness indicates an increase in dislocation density in the surface region of the material and, through the use of EBSD, Child et al. [116] showed that the level of surface deformation is half the hardness affected zone (71 μm). Thus, a similar depth of surface deformation would be expected in the shot-peened condition here. Figure 6-3 shows that shot-peening severely affects the microstructure in the outer 1-2 μm zone but the Hv depth profile shows a significant effect further

into the alloy. The deformation caused to the microstructure could be the reason why the area immediately below the surface could not be characterised using EBSD in Child et al [116]. The vibro-peened condition, turned condition and swaged condition show different levels of hardness affected zones, with the vibro-peened condition showing little if any increase at hardness near the surface. The turned condition shows a hardness affected zone of around 80 μm and the swaged condition shows a significant constant enhancement throughout the specimen cross-section.

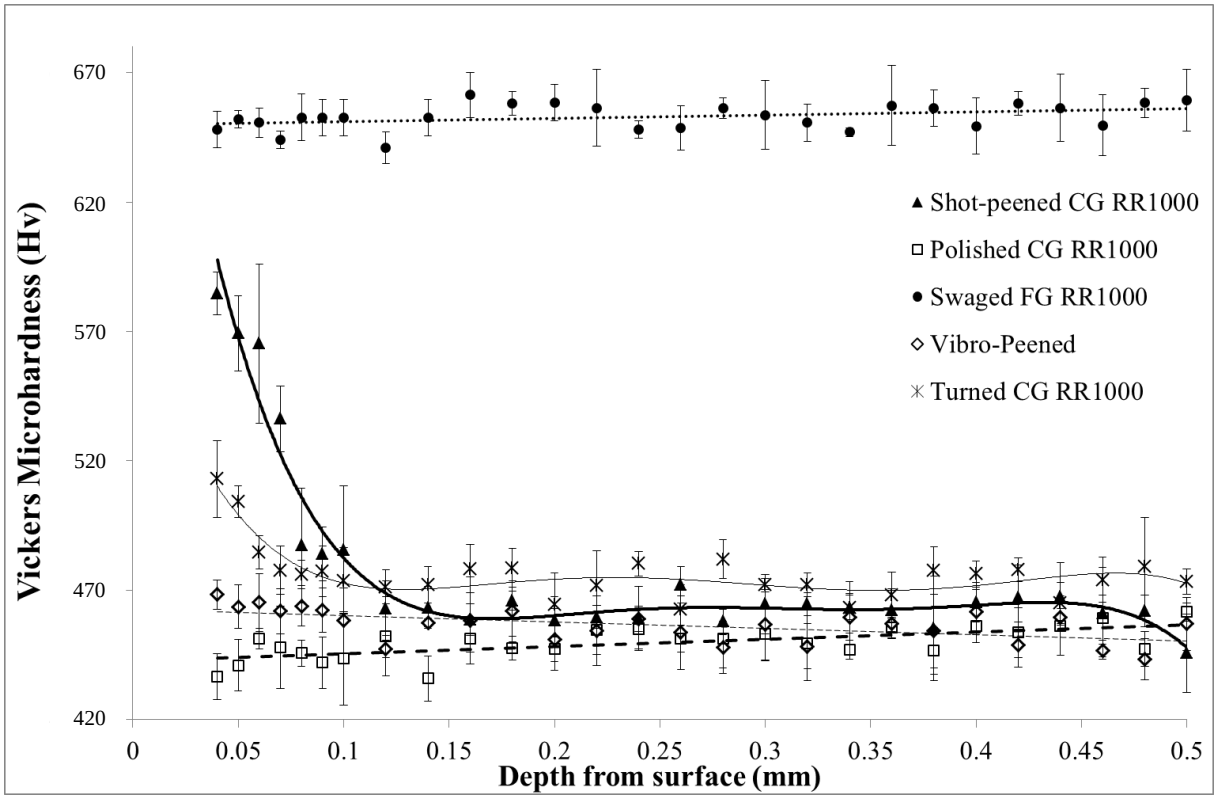

Figure 6-2: A micro-hardness trace of sectioned RR1000, with different surface modifications (±1 standard deviation)

Table 6-II: Residual stress and cold work values for RR1000 each with different surface modifications courtesy of Rolls-Royce plc.

	Residual stress			**Cold work**
	Max (MPa)	Type of stress	Depth (μm)	Max
Vibro-peened (CG)	1000-1200	Compressive	~200	20%
Shot-peened (CG)	~1500	Compressive	~200	40%
Swaged (FG)	~700	Compressive	Constant	30-33%
Turned (CG)	~1600	Tensile	~20	25%
Polished (CG)	-	-	-	-

Table 6-II includes both residual stress and cold work measurements performed using XRD analysis provided by Rolls-Royce plc. Cold work is inferred from the full width at half maximum (FWHM) measurements using XRD based on measurements conducted on FG RR1000 with known amounts of strain (errors in this are around ±10%). The polished condition is thought to have minimal surface residual stress and close to zero cold work, due to the polishing technique used. The turned specimen has a tensile residual stress at the surface before becoming significantly compressive after around 20 microns, this compressive residual stress reached a maximum at a value of 1000 MPa and reached a depth of 150 μm. Interestingly vibro-peening introduces a similar level of compressive residual stress as shot-peening but with considerably less cold work and this is reflected in the hardness traces, with minimal if any hardness affected zone being found in the vibro-peened specimen. Swaging is by far the most aggressive surface condition, with the process causing a total reduction in specimen cross-sectional area of 31.3 % and this is reflected in the microhardness traces, with the swaged specimen having a considerably increased hardness throughout the cross-section of the material and through the large constant residual stress induced in the material. Interestingly the level of residual stress seems to have little bearing on the hardness affected zones, although the specimens with the largest percentage cold work show the largest enhancement in hardness. The depth of the hardness affected zone also has little bearing on the depth of the residual stress, with the shot-peened condition tallying fairly well (Hardness affected zone = 150 μm and residual stress depth = 200 μm) as does the swaged condition, whereas the opposite is true in the vibro-peened and turned conditions.

6.2.3 Microstructure

The grain structure of the material, in either the near surface region or centre, does not seem to be affected by the shot-peening and has a grain size of ~ 30-50 μm. Table 6-III shows there is also no significant difference in secondary γ′ volume fraction due to the shot-peening process nor between central and surface regions. The grain structure of the material does not seem to be affected by any of the other surface treatments and has a grain size of around 30-50 μm in the coarse grained alloy (Figure 6-4). In addition it is important to note that none of the surface conditions, by themselves i.e. as-treated/un-oxidised, seem to induce any recrystallisation in the near surface region with the grain size remaining as intended. In the FG swaged sample the grain size also remains the same at ~4-6 μm, although swaging does introduce a significant amount of deformation throughout which can be seen in the vast number of slip bands throughout the specimen (Figure 6-4). The FG alloy also shows the presence of primary γ' particles. There is also deformation of the secondary γ′ particles with significant deformation being present in the shot-peened (1-2 μm), turned (~3 μm) and swaged (1-2 μm) conditions (Figure 6-3). A minimal amount (<1 μm) is found in the 1200 grit surface finish and the vibro-peened surface condition. The deformation caused to the microstructure could be the reason

why the area near the surface could not be characterized using EBSD in [116]. It is interesting to note that the deformation at the surface of the shot-peened condition looks much less severe than the deformation seen in the FG swaged condition, even though the level of cold work is larger in the shot-peened condition. A similar level of deformation in the secondary γ′ particles is seen but the presence of significant slip bands within the grains is not. Table 6-III shows there is no significant difference in secondary γ′ area fraction due to any of the surface modification processes, nor between the surface and central regions of the samples.

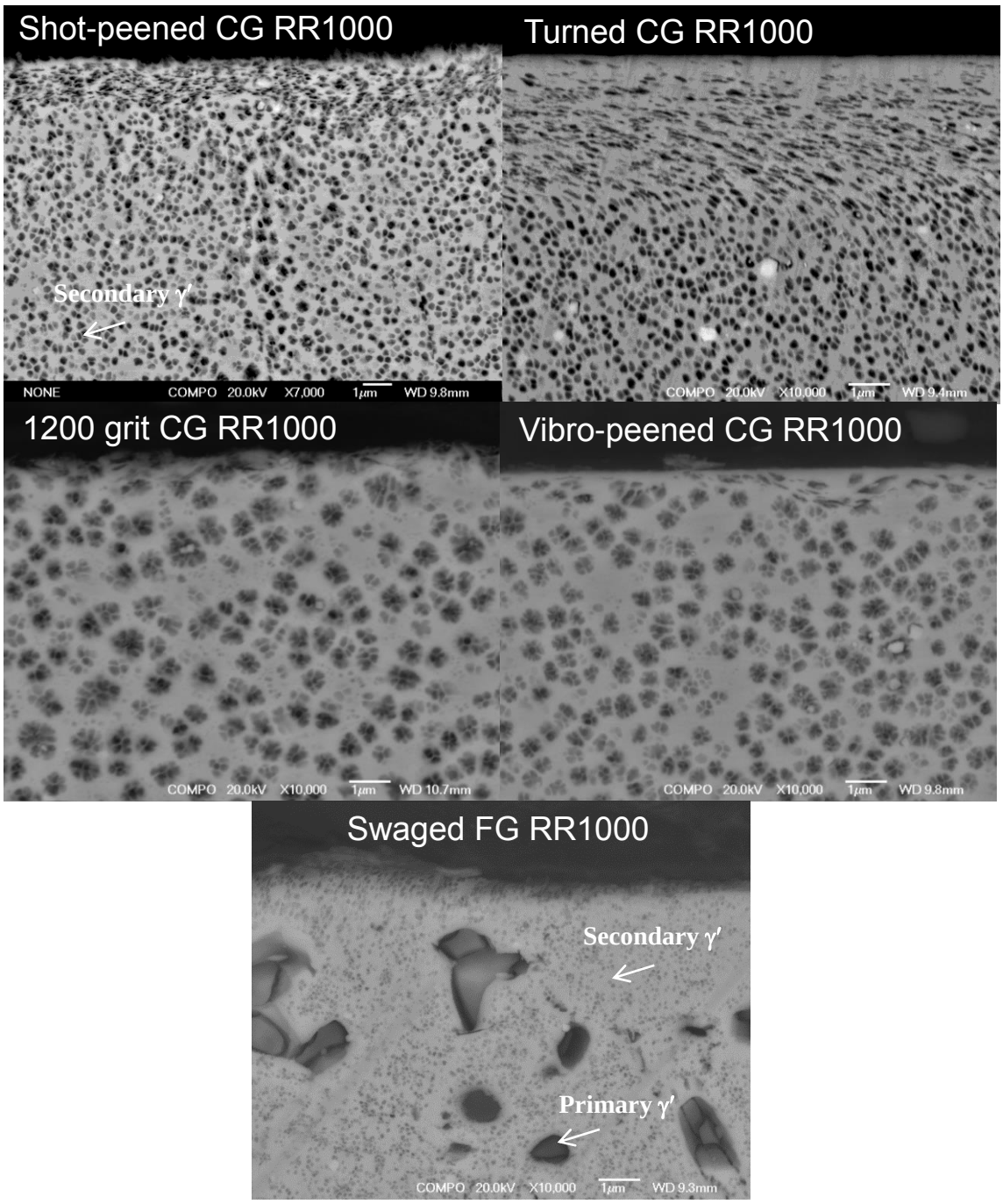

Figure 6-3: BSE images of the γ′ morphology at the surface of sectioned RR1000 specimens with different surface modifications. Specimens were etched with a selective γ′ etchant. Primary γ′is only found in the FG alloy.

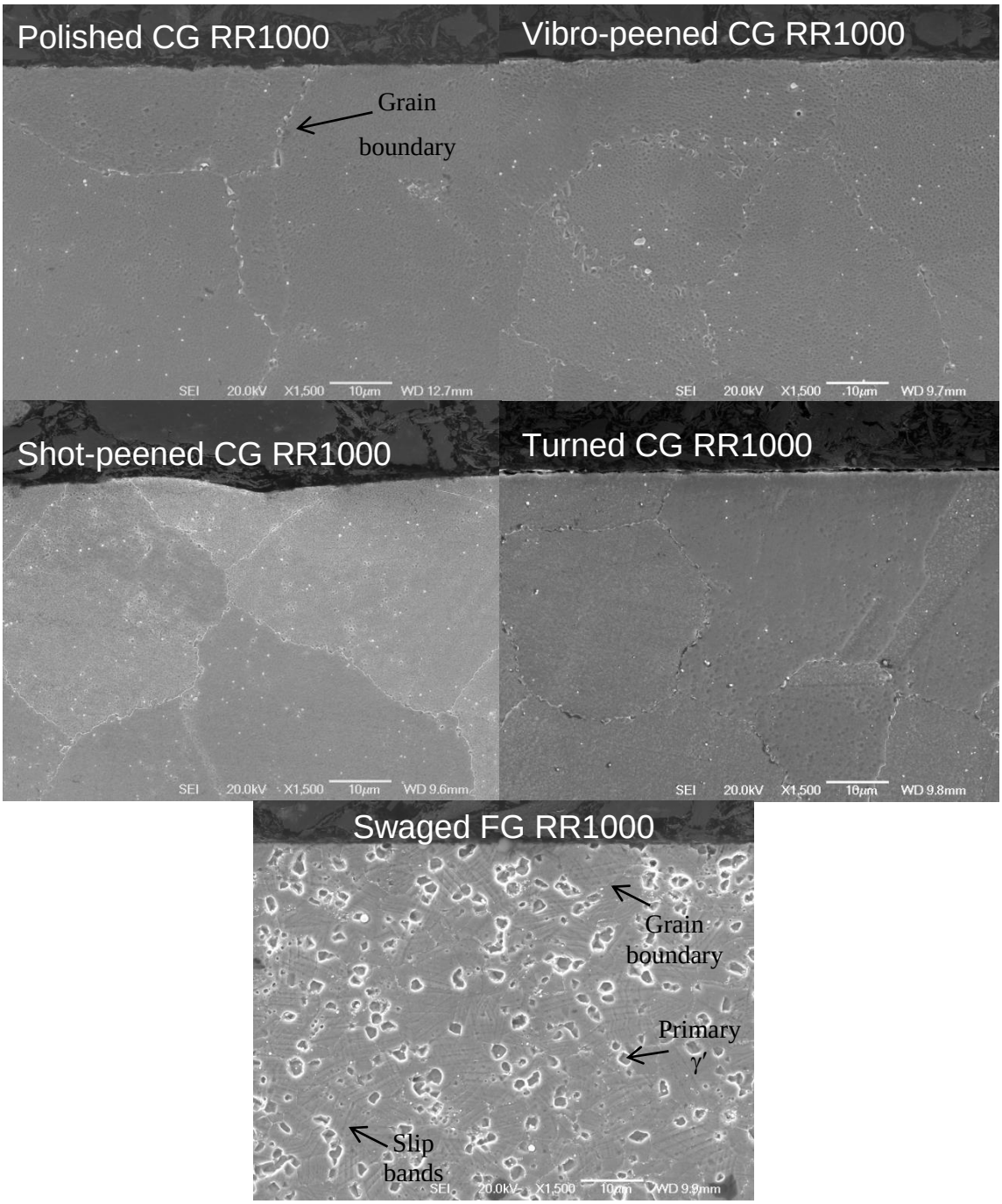

Figure 6-4: Secondary electron images of the grain structure at the surface of sectioned RR1000 with different surface modifications. Specimens were etched using Kallings etchant.

Table 6-III: Area fraction of secondary γ′ in RR1000, with different surface modifications, in the surface and centre regions of a cross-sectioned sample.

	Polished CG RR1000	**Shot-peened CG RR1000**	**Vibro-peened CG RR1000**	**Turned CG RR1000**
Surface	40% (±3)	46% (±5)	42% (±2)	42% (±1)
Centre	41% (±3)	46% (±5)	42% (±3)	42% (±1)

6.2.4 Mass gain kinetics of shot-peened CG RR1000

Figure 6-5 shows the change in specimen mass with time over the temperature range tested (650-800°C). It is important to stress that no spallation was observed for any of the specimens tested and that any mass gain can be attributed to oxidation products. Figure 6-5 clearly shows that, similar to the polished condition, the higher the exposure temperature the larger the specimen mass gain, while also illustrating that the rate of mass gain decreases with time at each temperature, concluding that sub-linear growth behaviour is occurring. As mentioned before a correction was applied to account for the additional surface roughness induced by shot-peening to produce an actual surface area rather than geometric surface area. This actual surface area (12.2% increase on the geometric surface area) was used in the calculation of any mass change measurements.

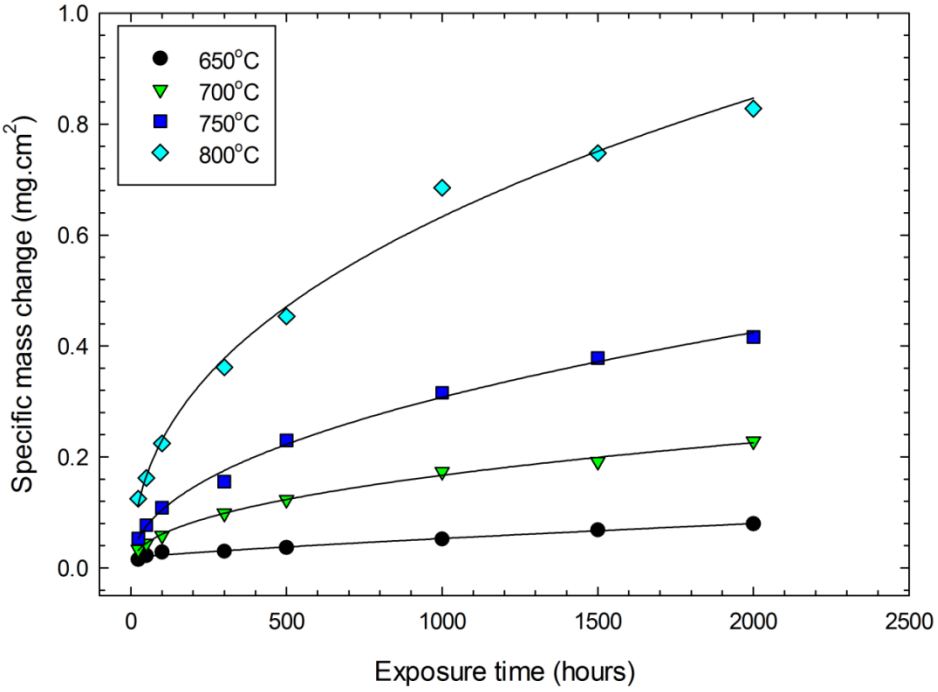

Figure 6-5: Plot of specific mass change against time for each temperature tested in a single zone furnace for 2000 hours.

High temperature oxidation kinetics can be reasonably described by the following equation:

$$\left(\frac{\Delta m}{A}\right)^n = k_n\, t \tag{6.6}$$

where $\left(\frac{m}{A}\right)$ is the mass change/surface area (mg.cm^{-2}), exposure time (t) in seconds and k_n is the oxide growth rate constant. The value of n can be determined by plotting log $\left(\frac{m}{A}\right)$ against log t. Figure 6-6 shows the determination of the oxide growth regime (n), for the four temperatures tested (650°C, 700°C, 750°C and 800°C). In this way the values of n at each temperature can be evaluated and both

Table 6-IV and Figure 6-6 show that like the polished condition, parabolic behaviour can be reasonably assumed (n = 2) for this alloy between 700°C and 800°C, to give a parabolic rate constant (k_p) in $mg^2.cm^4.s^{-1}$. At 650°C the behaviour cannot be described accurately assuming parabolic kinetics, as the growth regime indicates that sub-parabolic behaviour is occurring (n = 2.9). This behaviour is close to cubic (n = 3) similarly to the polished condition. Nevertheless a parabolic rate constant has been calculated for all temperatures tested to allow for a comparison between other temperature and other conditions both in this programme of research and with the literature.

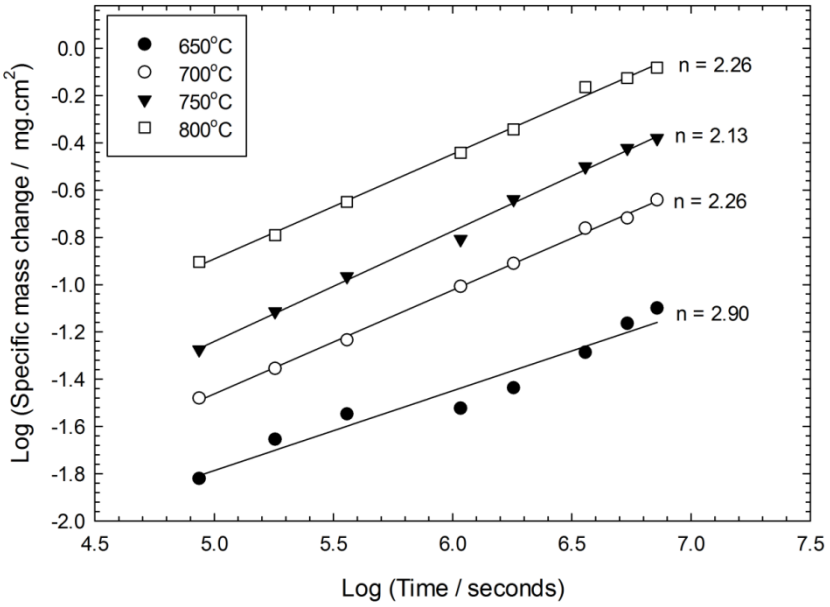

Figure 6-6: Plot of log specific mass change against log exposure time for 650°C 700°C, 750°C and 800°C showing the oxide growth regime.

A comparison of the parabolic rate constants for CG RR1000, in the polished condition and the shot-peened condition, is shown in Table 6-V. A comparison has also been drawn between these and values for chromia formation on an austenitic stainless steel and FG RR1000 taken from the literature [88, 107]. The kinetics of both conditions are similar with parabolic conditions being assumed for both between 700°C and 800°C and cubic at 650°C.

Table 6-IV: Oxide growth regimes for CG RR1000 with and without shot-peening. Parabolic kinetics (n = 2) are a reasonable approximation.

	Polished CG RR1000	**Shot-peened CG RR1000**
650°C	2.7	2.9
700°C	1.9	2.3
750°C	2.1	2.1
800°C	2.0	2.3

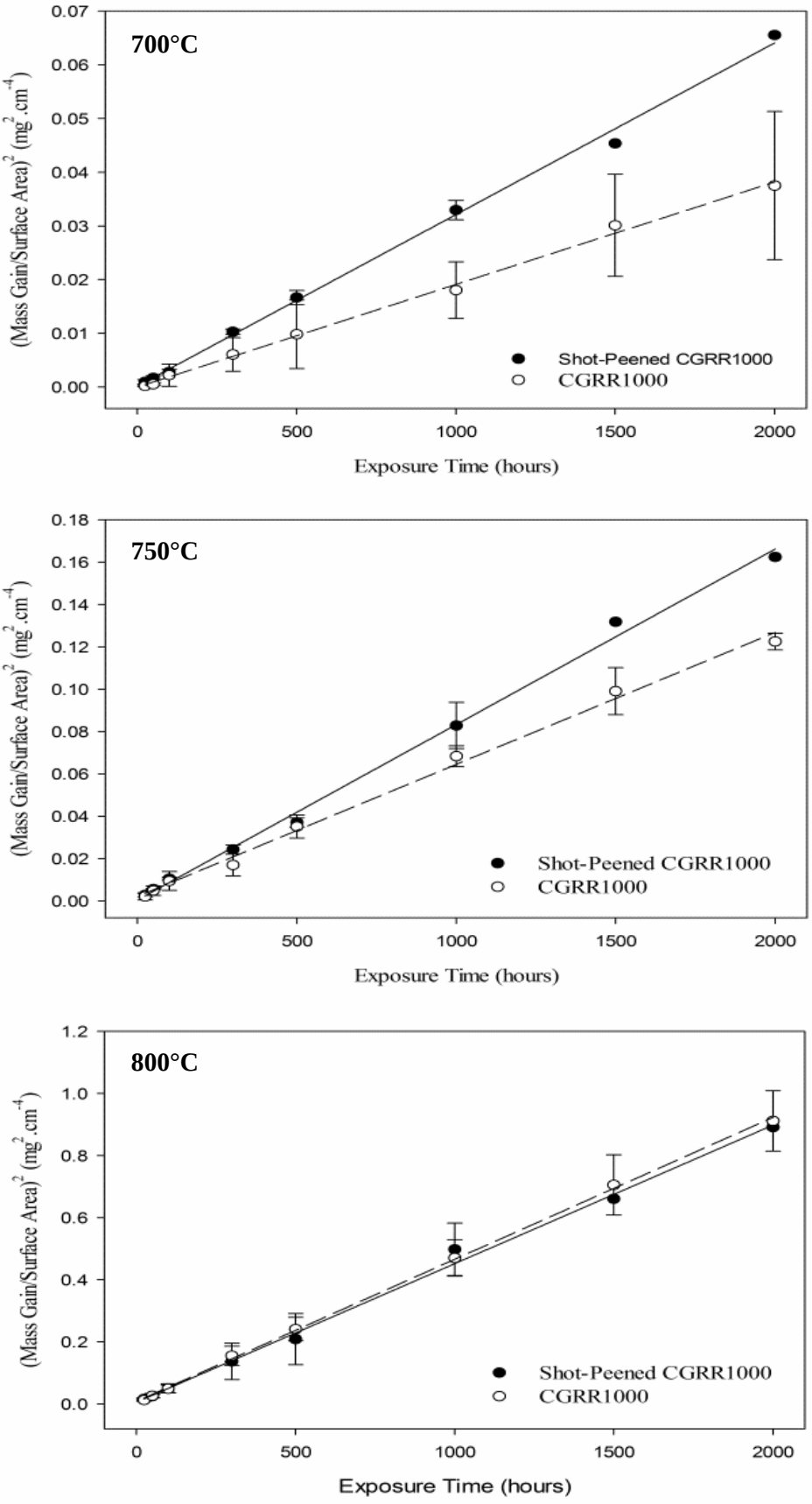

Figure 6-7: k_p graphs of CG RR1000 in the polished or shot-peened condition at 700°C, 750°C and 800°C (±1 standard deviation).

Table 6-V: Parabolic rate constants ($mg^2.cm^{-4}s^{-1}$) for CG RR1000 with and without shot-peening, including fine grained RR1000 and a chromia forming steel.

	CG RR1000	Shot-peened CG RR1000	FG RR1000 [107]	Chromia [88] formation
650°C	$5.35x10^{-10}$	$8.51x10^{-10}$	-	-
700°C	$3.48x10^{-9}$	$7.41x10^{-9}$	$3.89x10^{-9}$	$7.99x10^{-10}$
750°C	$1.77x10^{-8}$	$2.55x10^{-8}$	$3.79x10^{-8}$	$3.79x10^{-9}$
800°C	$1.29x10^{-7}$	$1.05x10^{-7}$	$2.33x10^{-7}$	$1.56x10^{-8}$

The parabolic rate constants in Table 6-V illustrate that, like the polished condition described in the chapter before, the shot-peened surface condition oxidises much quicker than a chromia forming steel. Some internal oxidation of silica occurs in the chromia forming steel as does the internal oxidation of alumina in RR1000, so a fair comparison can be made. The difference between shot-peened and polished condition is shown in Figure 6-7. This shows that shot-peening has no effect on the reaction rate at 800°C but has a detrimental effect at both 750°C and 700°C. It has previously been shown that shot-peening can have a beneficial effect on the oxidation kinetics [119, 122, 123]. This was attributed to the early formation of chromia due to shot-peening providing short-circuit pathways for diffusion of chromium. Shot-peening of CG RR1000 does provide short-circuit paths for diffusion of chromium, but also for other alloy constituents, such as titanium and aluminium accounting for the higher mass gains. Thus, shot-peened CG RR1000 forms a protective layer of Cr_2O_3, as does the polished condition and the potential strength of shot-peening is not realised.

Table 6-VI: A comparison of activation energies of the parabolic rate constants for mass gain in CG RR100 with and without shot-peening, with other similar Ni-based superalloys and a high Cr containing steel.

Alloy	Activation energy ($kJ.mol^{-1}$)	Temperature range tested
CG RR1000	301	650-800°C
Shot-peened CG RR1000	302	650-800°C
FG RR1000	270	700-800°C
Udimet 720	250	750-1000°C
Astroloy	270	750-1000°C
Waspaloy	300	750-1000°C
20Cr austenitic steel	258	700-900°C

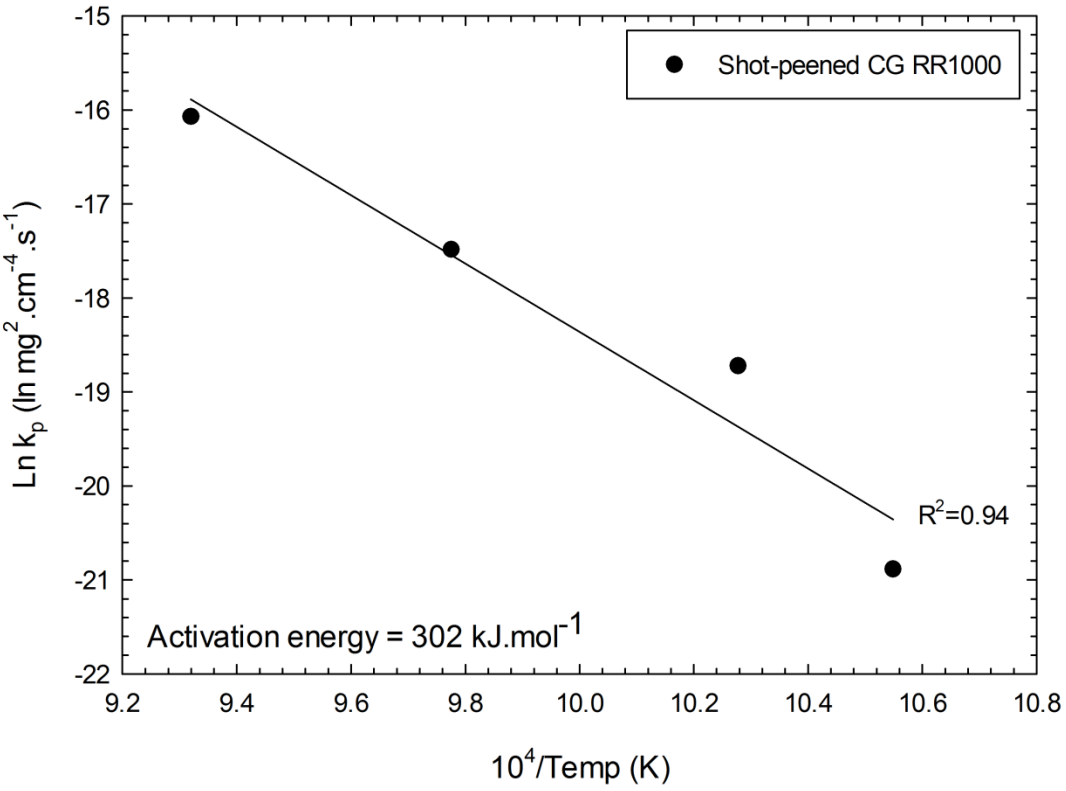

Figure 6-8: Activation energy graph of oxide formation on shot-peened CG RR1000 over a temperature range of 650°C-800°C.

An Arrhenius equation (6.7) can be used to calculate the activation energy for the formation of the oxide in both conditions.

$$k_p = k_o \exp\left(\frac{-Q}{RT}\right) \quad (6.7)$$

where k_p is a parabolic rate constant, k_o is a pre-exponential constant, Q is the activation energy for oxide growth (kJ.mol^{-1}), R is the gas constant, T is the exposure temperature (K). Figure 6-8 shows a best fit regression line through the complete mass gain data set for shot-peened CG RR1000 and found a good fit (R^2 = 0.94) with an activation energy of 302 kJ.mol^{-1}. It is worth noting again that the term activation energy is not strictly correct as more than one element is oxidising and a single activated event is not occurring but it is a useful term to describe the temperature dependence of the reaction kinetics and acts as a value for comparison between other similar alloys. As can be seen in Table 6-IV the activation energy for both conditions is very similar and fits in reasonably well with other similar Ni-based superalloys although it is significantly higher than those reported for chromia formation on Cr or high Cr containing austenitic steel. This is not entirely unexpected as explained in the previous results chapter that most Ni-based superalloys tend to allow oxidation of more than one

element: Ti, Al and Cr, as is the case here. The composition and morphology of shot-peened CG RR1000 will be discussed in detail in the following pages.

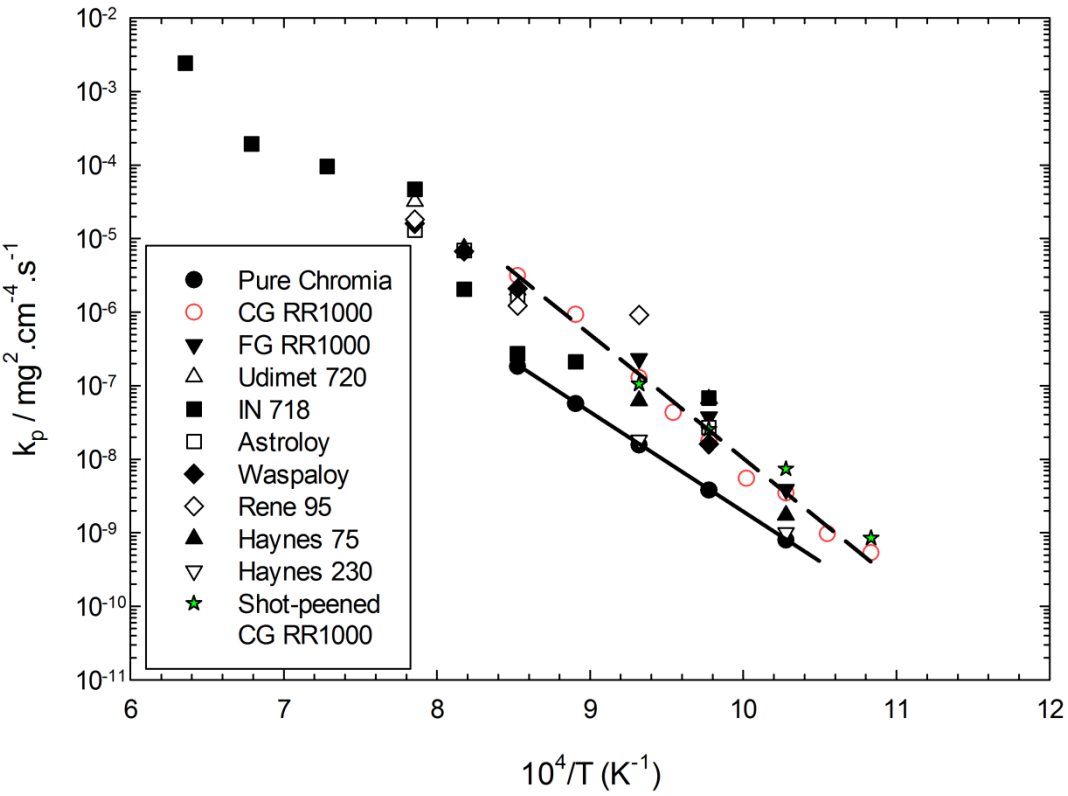

Figure 6-9: Arrhenius plot of kp values from this programme of research (polished CG RR1000 shown as unfilled red circles and shot-peened CG RR1000 as filled green stars), compared with values from the literature of other similar Ni-based superalloys and chromia formation on a high chromium containing austenitic stainless steel.

The parabolic rate constants for mass gain are shown as a function of inverse of temperature in the Arrhenius plot of Figure 6-9 for the present alloy, similar chromia forming superalloys and chromia formation on an austenitic stainless steel. It can be seen that chromia formation provides a lower bound for the data, with the values for both shot-peened and polished CG RR1000 falling within a band of similar Ni-based superalloys. The shot-peened mass gain parabolic rate constants lie on the upper side of this band at the lower temperatures (650°C and 700°C) but fall within the band at 750°C and 800°C. It illustrates the detrimental effect that shot-peening has on CG RR1000 at the lower temperatures. The gradient of the line through this data set yields an activation energy of 302 kJ.mol^{-1} for the shot-peened condition and allows for an expression of k_p of:

$$k_p = 6.52x10^7 \ exp\left[-\frac{302247}{8.314.T}\right] \ mg^2.cm^{-4}.s^{-1} \quad (6.8)$$

This allows the calculation of a k_p at any temperature required within the temperature range tested 650-800°C and is a useful way of describing the oxidation kinetics of the shot-peened alloy.

6.2.5 Surface images

Figure 6-10 illustrates the surface morphology of the typical oxide seen on CG RR1000 with different surface modifications over a period of time (24-2000 hours at 700°C) showing the individual oxide grains present. In all surface conditions the grains increase in size over time. It is important to note the difference in surface oxide morphology between the surface conditions as well as noticing that no grain boundary enhancement was found. The shot-peened condition shows a similar morphology to the polished condition, with fairly uniform grains and the occasional thin rod shaped oxide. The vibro-peened condition shows a similar grain morphology that follows the machining marks of the pre-peening surface preparation (1200 grit ground). The turned condition is similar but machining marks are further apart and the swaged condition shows a different oxide morphology, while a continuous layer of oxide is formed, some regions are thicker than others, with this patchy appearance reducing with time as the regions become interconnected. In none of the conditions does a change in oxide composition occur.

The composition of the external oxide scale was evaluated using XRD at all test temperatures (700-800°C for shot-peened and 700°C for other surface modifications) at 500 and 2000 hours. XRD spectra confirmed that like the polished condition the external oxide, in all surface conditions and temperatures, is rutile and chromia (Table 6-VII). Sub-surface oxides could not be detected with confidence in these XRD scans because of their small volume fraction although peaks of the substrate alloy were present.

Table 6-VII: XRD results for oxide composition on RR1000 with different surface modifications oxidised for 700°C.

	500h	**2000h**
CG RR1000	$TiO_2 + Cr_2O_3$	$TiO_2 + Cr_2O_3$
Shot-peened CG RR1000	$TiO_2 + Cr_2O_3$	$TiO_2 + Cr_2O_3$
Vibro-peened CG RR1000	$TiO_2 + Cr_2O_3$	$TiO_2 + Cr_2O_3$
Turned CG RR1000	$TiO_2 + Cr_2O_3$	$TiO_2 + Cr_2O_3$
Swaged FG RR1000	$TiO_2 + Cr_2O_3$	$TiO_2 + Cr_2O_3$

a) Shot-peened CG RR1000

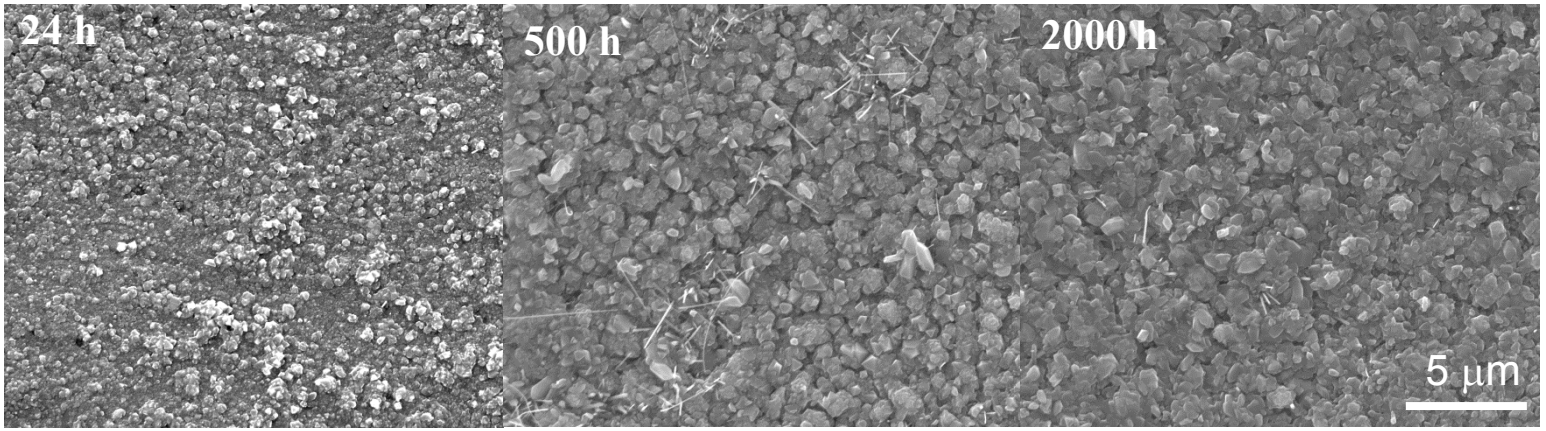

b) Vibro-peened CG RR1000

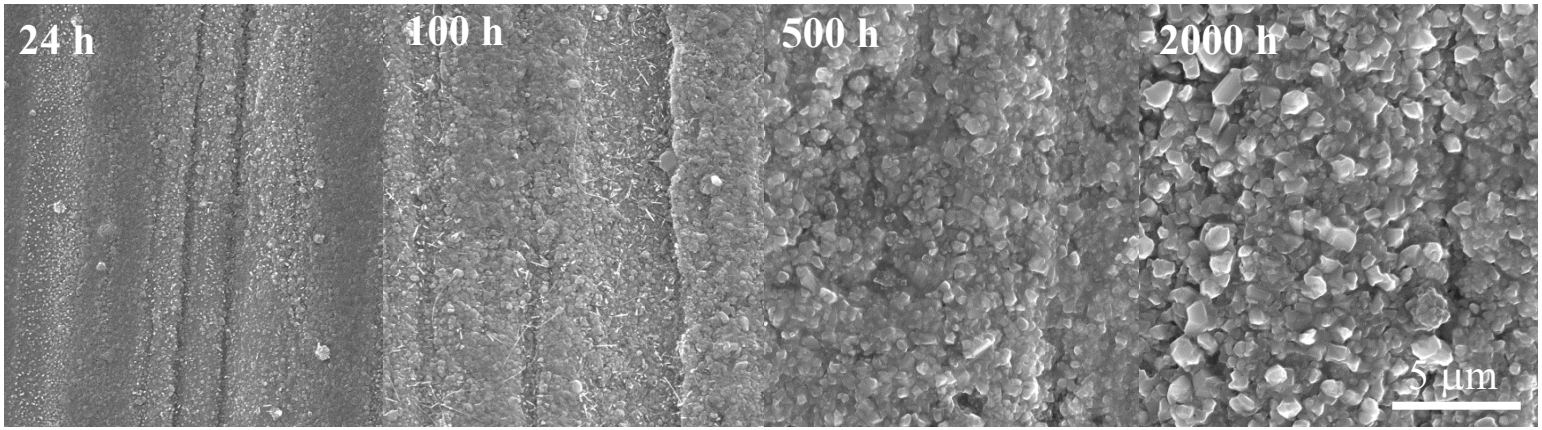

c) Turned CG RR1000

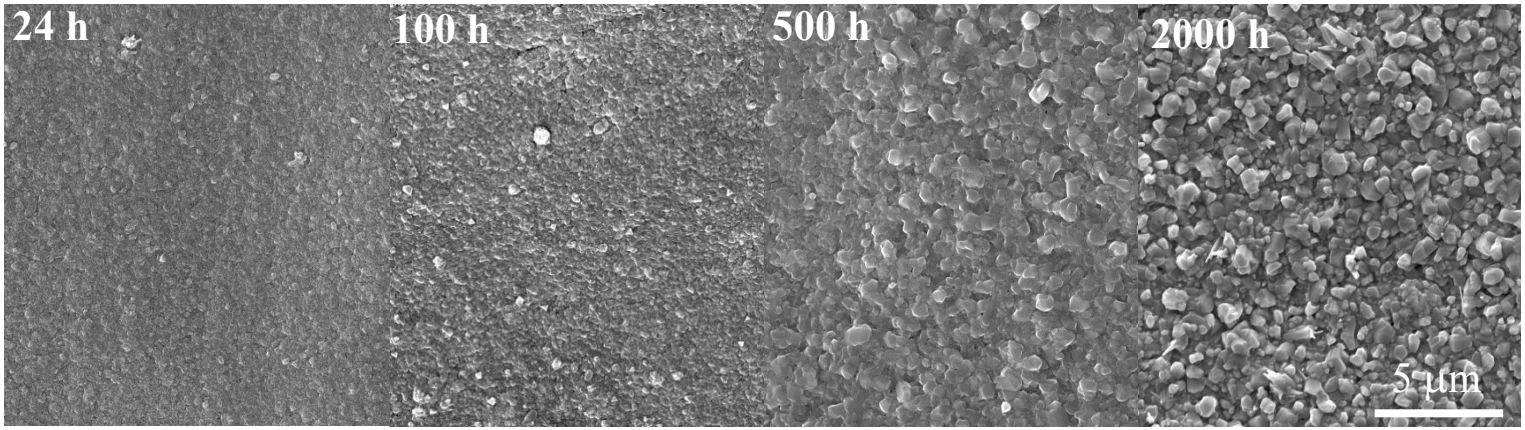

d) Swaged FG RR1000

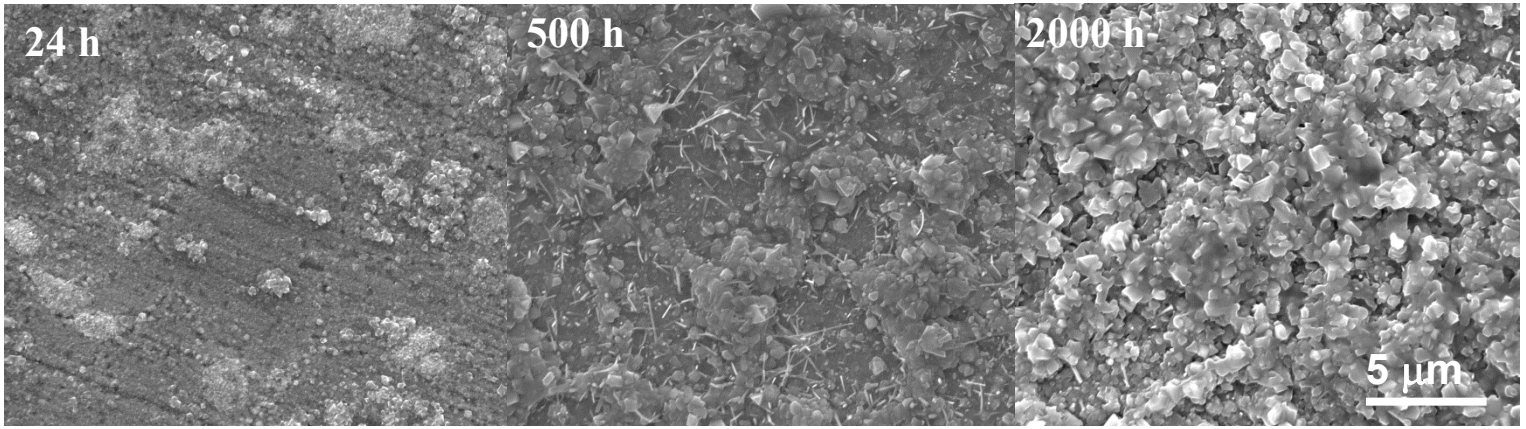

Figure 6-10: Secondary electron images of the surface of oxidised RR1000, with different surface modifications a) Shot-peened CG RR1000, b) Vibro-peened CG RR1000, c) Turned CG RR1000 and d) Swaged FG RR1000. Specimens were oxidised at 700°C in laboratory air for the exposure time illustrated in the image.

6.2.6 Oxidation damage

The oxidation damage of Ni-based superalloy, RR1000, with different surface modifications resulting from prolonged exposure to high temperatures is complex. The typical oxide morphology and composition was described in Figure 5-12, showing a continuous external oxide scale with an extensive sub-surface damage; the shot-peened surface condition is shown here in Figure 6-11. The different surface modifications applied to the alloy cause in most cases only a change in the morphology of the oxidation damage. This is particularly apparent in the significant sub-surface internal oxide that is present underneath the protective oxide scale, with it precipitating in a different manor depending on the surface condition before oxidation (Figure 6-12).

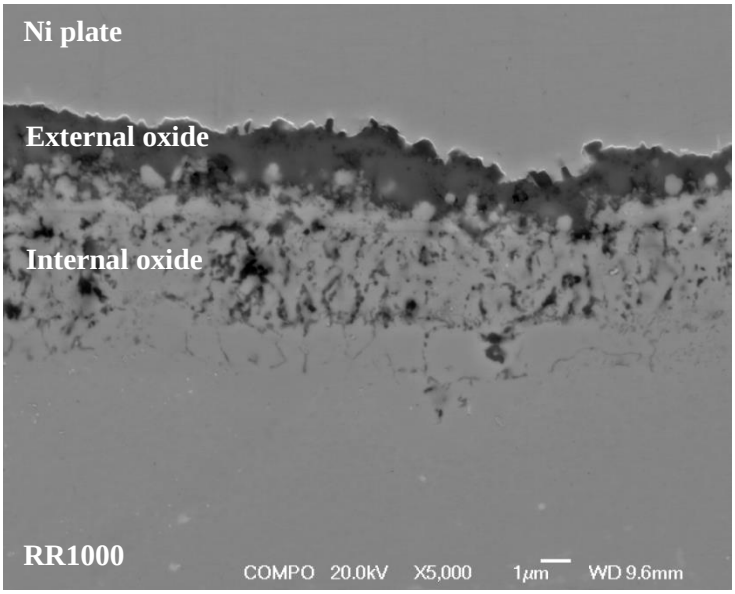

Figure 6-11: BSE image of a cross-section through shot-peened RR1000 specimen oxidised at 750°C for 2000 hours.

In all surface conditions, the external oxide scale consists of a chromia scale with isolated grains of TiO_2 on the surface (Figure 6-11 and Figure 6-13). The internal oxides are predominantly alumina as can clearly be seen from the EDX maps/linescans in Figure 6-13. This is similar to what has been found in other similar Ni-based superalloys [47, 104, 115] and in the polished condition (Chapter 5). Whereas in the polished condition two types of precipitates were found, one intragranular and one intergranular, this is not the case here with a much more frequent but continuous depth penetration being present in all the surface condition (Figure 6-11 and Figure 6-12). Slight changes are found in the alumina penetration in the swaged condition, as it is fine grained with a large amount of cold work and contains primary γ' particles. The internal oxide precipitation is less frequent that in the other surface conditions but more frequent that polished CG RR1000, with the alumina intrusions forming down the grain boundaries (Figure 6-12(d)). The penetration front is still uniform across the cross-section. Figure 6-14 shows the dissolution of a primary γ' particle leading to the formation of a fine dispersion of internal alumina oxides.

a) Shot-peened CG RR1000

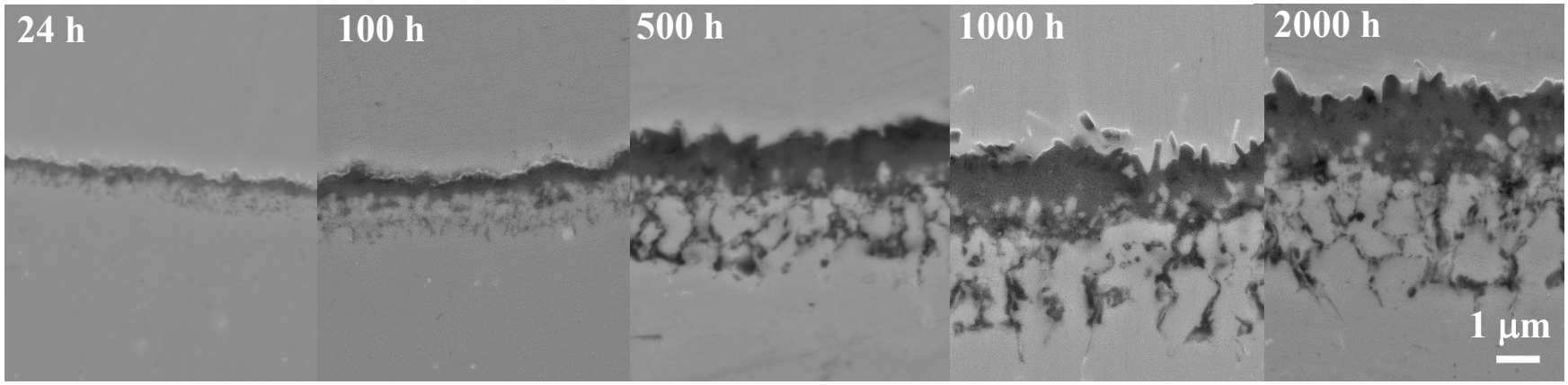

b) Vibro-peened CG RR1000

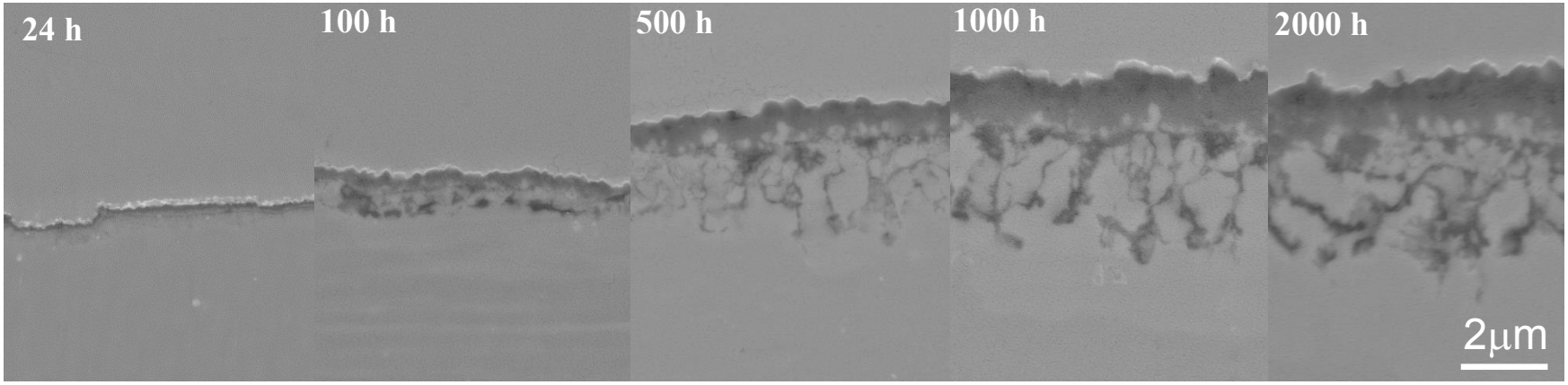

c) Turned CG RR1000

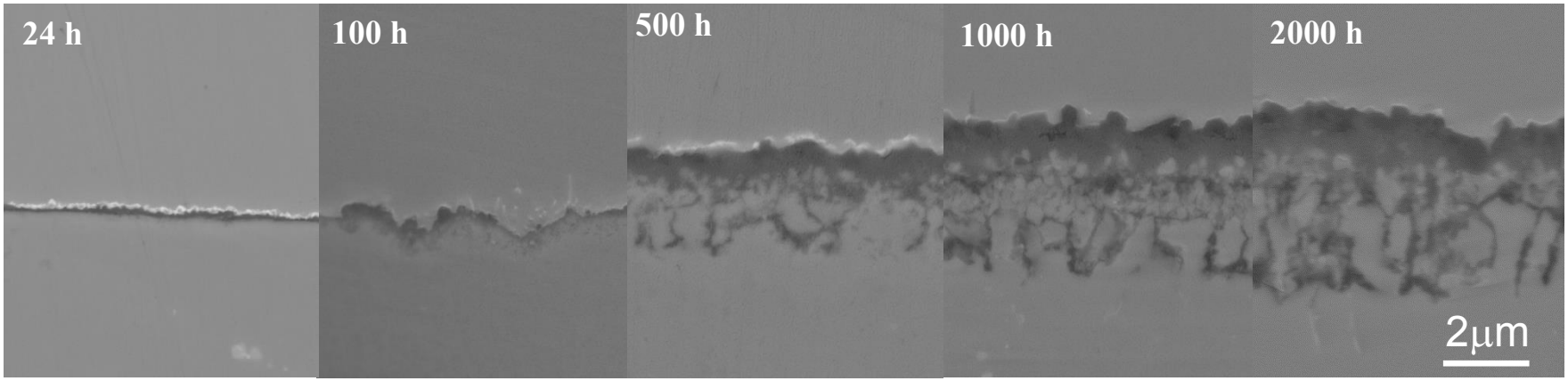

d) Swaged FG RR1000

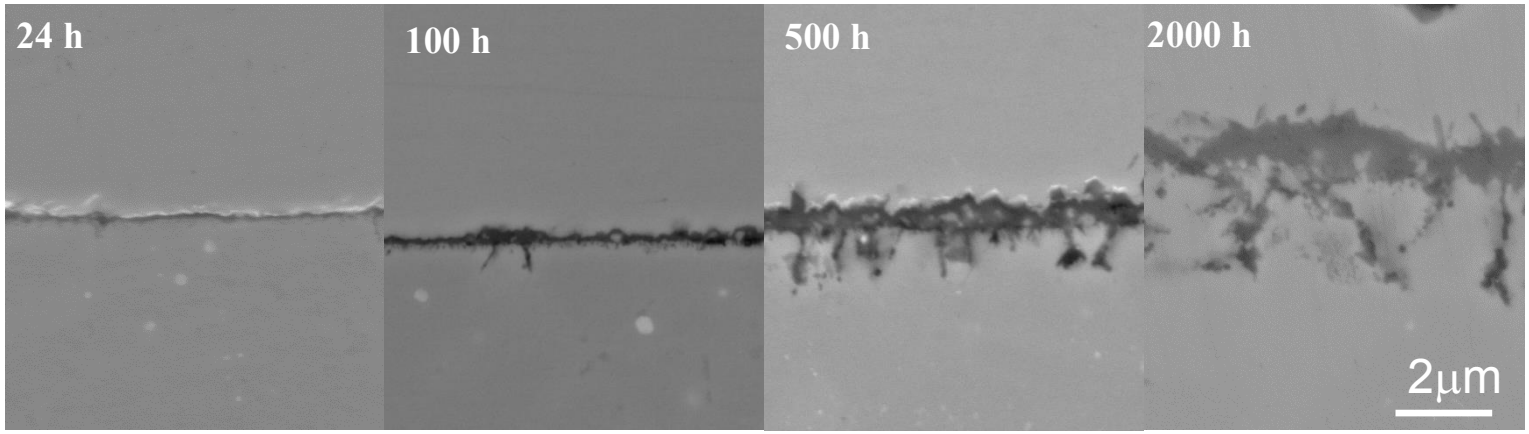

Figure 6-12: BSE images of cross-sectioned RR1000, with different surface modifications a) Shot-peened CG RR1000, b) Vibro-peened CG RR1000, c) Turned CG RR1000 and d) Swaged FG RR1000 illustrating the oxidation damage. Specimens were oxidised at 700°C in laboratory air for the exposure time illustrated in the image.

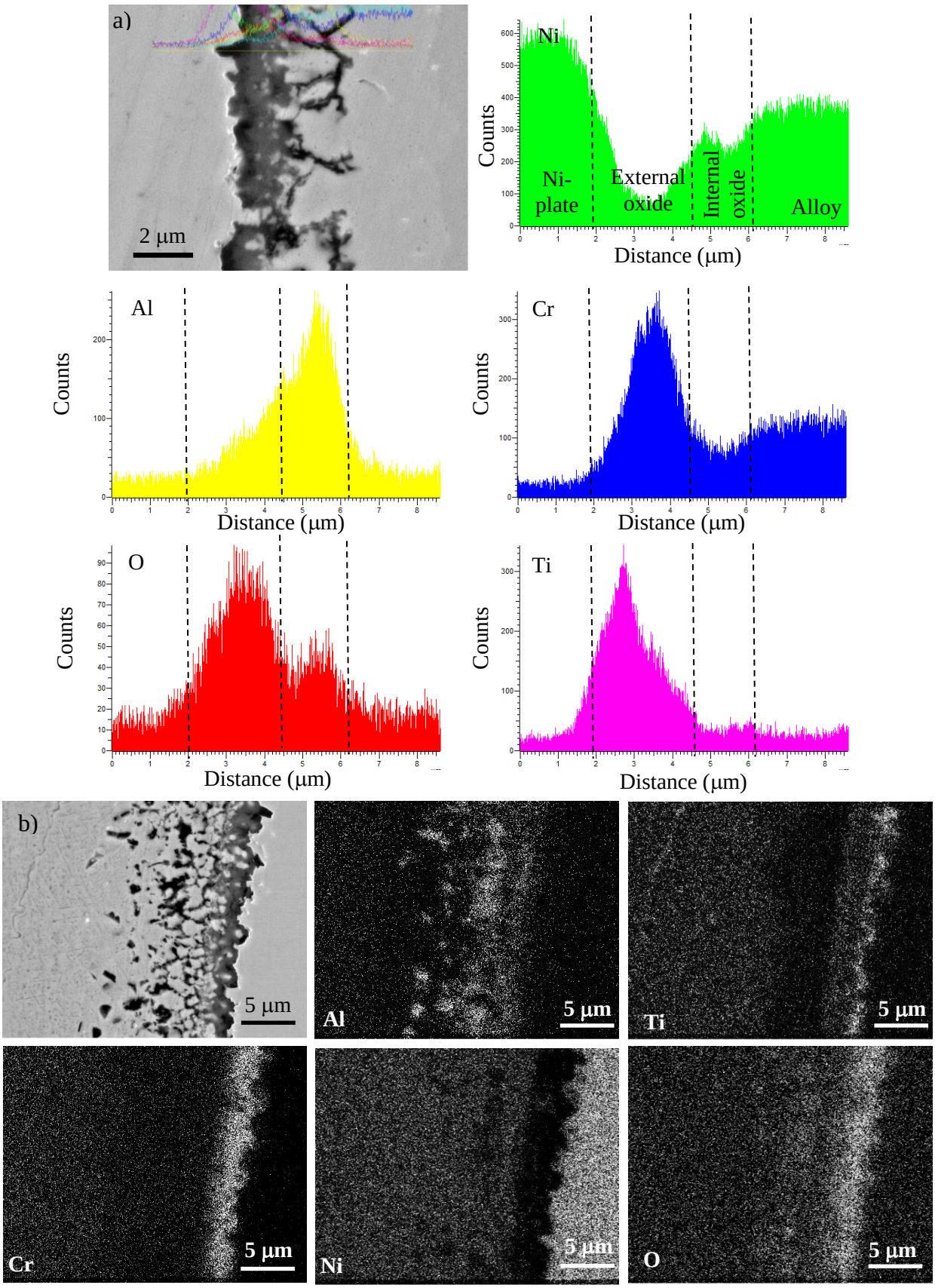

Figure 6-13: a) BSE image, with energy dispersive x-ray analysis linescan of a section through a vibro-peened CG RR1000 oxidised in laboratory air at 700°C for 2000 hours. b) SEM image, with energy dispersive X-ray analysis maps, of a section through a shot-peened CG RR1000 sample held in laboratory air at 800°C for 500 hours.

Extending beneath this internal oxide is a significant γ′ denuded zone, illustrated in Figure 6-15. This again like in the polished condition is a region free of γ′ particles, as aluminium depletion due to internal oxide formation has caused the dissolution of the γ′ particles. This denuded region follows the profile of the internal alumina intrusions and so in general forms a uniform front, unlike the polished condition, where two distinct depths of dissolution are found.

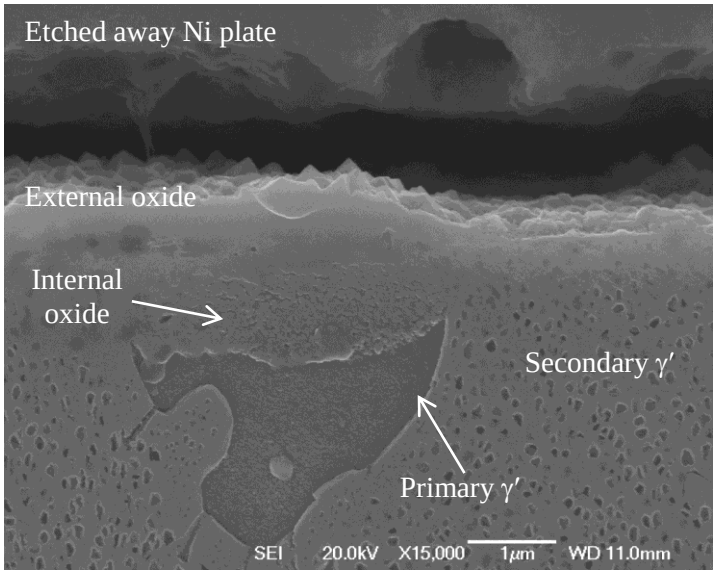

Figure 6-14: Secondary electron image of the Internal oxidation of a primary γ′ particle of a swaged FG RR1000 specimen oxidised at 700°C for 100 hours etched using a selective γ′etchant.

In the shot-peened condition at the higher exposure temperatures (750°C and 800°C) TiN's precipitates are formed within the γ′ denuded zone but ahead of the internal alumina penetrations. This is similar to the polished condition although TiN was found at 750°C during exposure times of >1000 hours rather than only occurring at 800°C in the polished condition. EDX analysis shows the presence of a Ti rich phase ahead of the grain boundaries which was confirmed using WDS in Chapter 5 as a TiN particle (Figure 6-16). Figure 6-17 shows that recrystallisation occurs, in the shot-peened condition, within this γ′ denuded zone, with a large number of micron sized grains (0.6 – 2.5 μm) formed. Recrystallisation typically requires two things: a minimum amount of deformation to provide the driving force for the reaction and growth of the grains and also high temperature [192]. It is thought that in this case a combination of cold work, high temperature and elemental depletion is required in order for this to occur. As it was not seen in the polished condition (Figure 6-17 (b)), which displayed no cold work, or in the aged condition, where the high temperature exposure was performed in an argon atmosphere so that no oxidation took place. It only occurs in the γ′ denuded zone as the secondary γ′ particles would be expected to hinder recrystallisation by exerting a significant Zener pinning effect [192] and the cold work in most cases is only displayed in the near surface region. This recrystallisation has been shown to occur within the γ′ denuded zone in the fine grained RR1000 [106] and in the similar Ni-based superalloy, ME3 [47] when undergoing a high

temperature (>700°C) exposure in air. The surface condition of ME3 was low stress ground with a surface roughness of ~1 μm and therefore unlike the polished condition used here, cold work may still be present sub-surface. As the surface condition of fine-grained RR1000 was similar to that used here in the polished condition, the variation in recrystallisation between the alloy grain sizes could be a grain size effect. Confirmation of recrystallisation in the vibro-peened, swaged and turned conditions has not been performed but a similar effect to that found in the shot-peened condition would be expected.

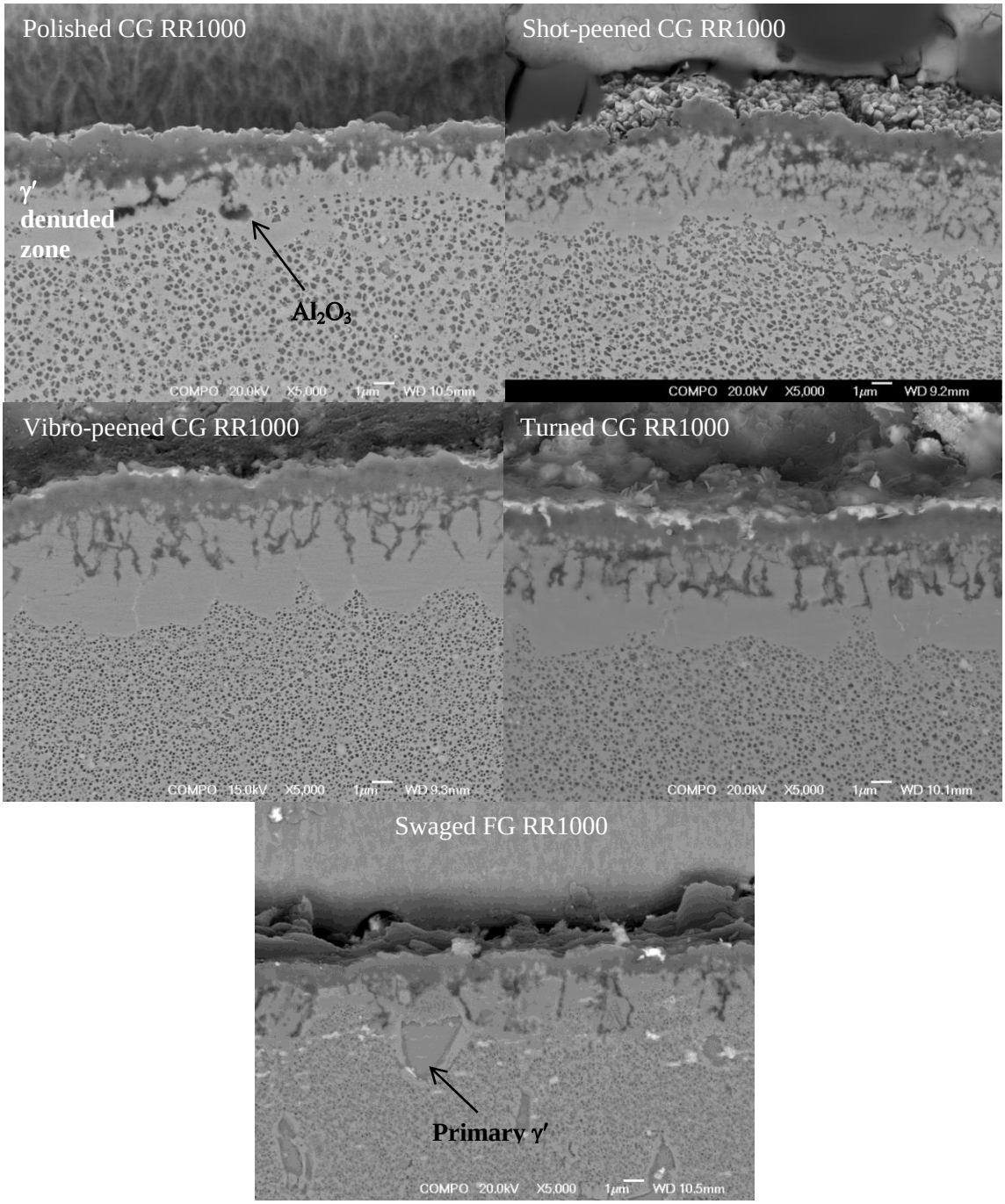

Figure 6-15: Secondary electron images of γ′ denuded zone of RR1000 with different surface modifications oxidised in laboratory air at 700°C for 2000 hours, etched with a selective γ′ etchant.

This is one of the likely reasons for the change in morphology of the internal alumina penetrations, with recrystallisation causing a large increase in the number of grain boundaries within the γ′ denuded zone. These act as short circuit diffusion pathways, thus creating numerous low energy diffusion pathways for both Al and O to the reaction front leading to a more frequent and uniform precipitation of internal oxide. The large number of slip bands from the cold work induced in the surface region by the surface modifications applied, could act as short circuit diffusion pathways, but would be expected to be relaxed out via the recrystallisation process within this γ′ denuded zone.

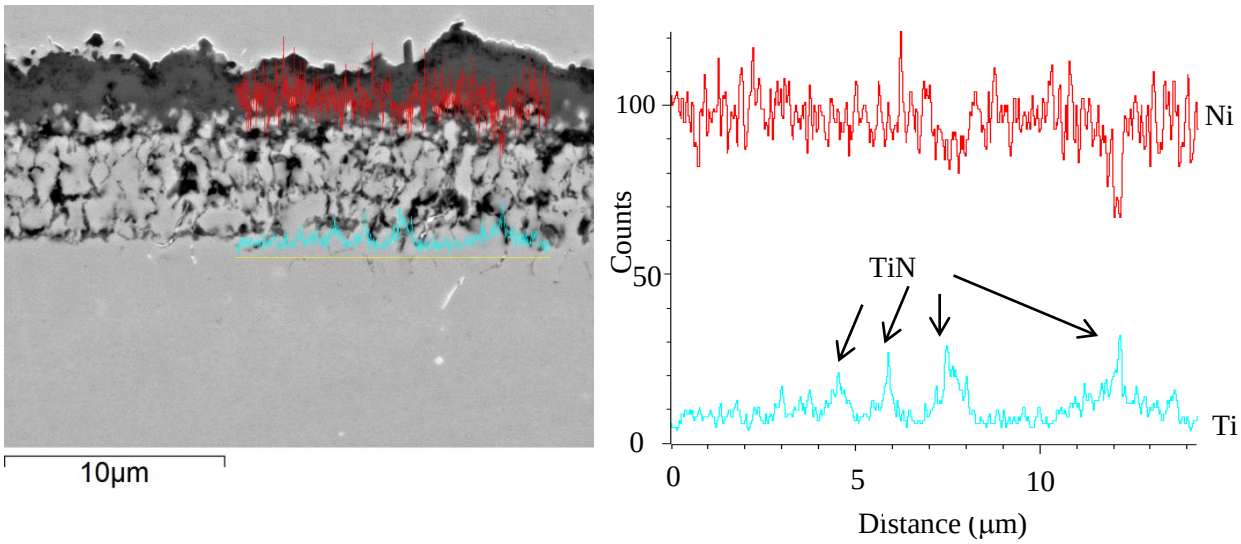

Figure 6-16: BSE image and EDX maps showing the presence of TiN particles in shot-peened CG RR1000 specimen oxidised at 750°C oxidised for 2000 hours.

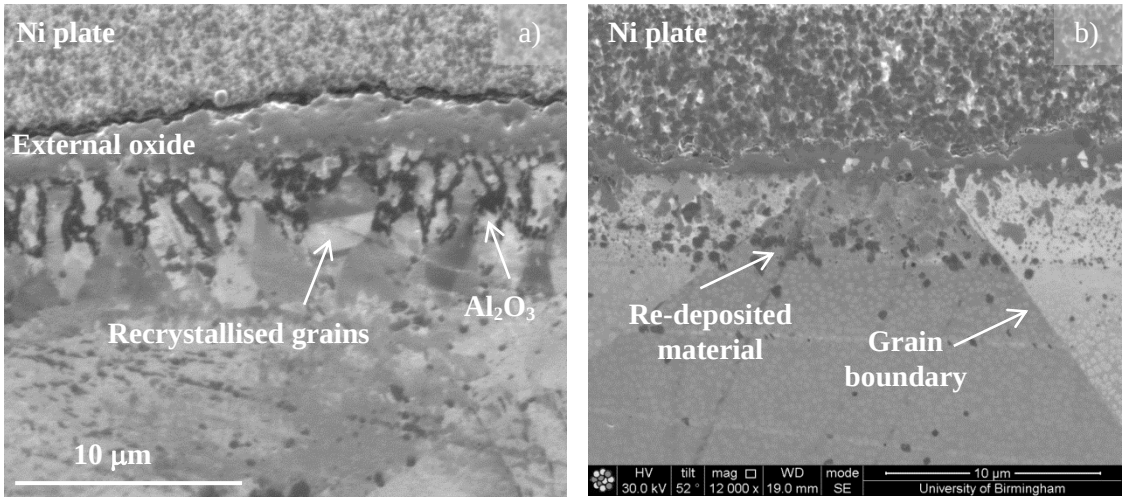

Figure 6-17: Secondary electron images using ion channelling contrast of both a) shot-peened RR1000 and b) polished RR1000 showing the occurrence of recrystallised grains within the γ′ denuded zone in the shot-peened condition and the normal grain structure in the polished condition. Samples were oxidised in laboratory air at 800°C for 200 hours. Some re-deposited materials is present in b) from the FIB milling.

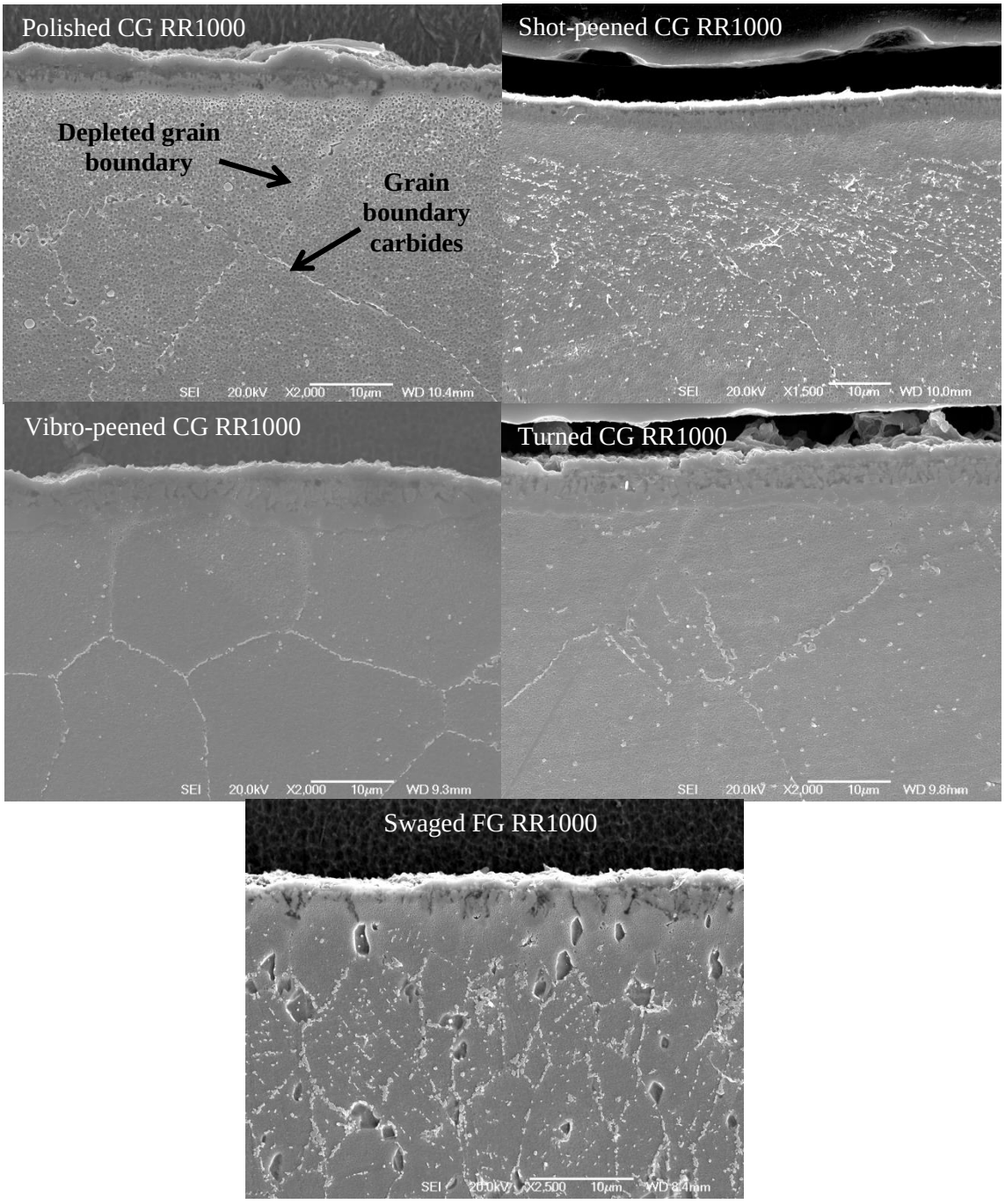

Figure 6-18: Secondary electron images of the carbide dissolution in the near surface region of RR1000 with different surface modifications oxidised in laboratory air at 700°C for 2000 hours.

Underneath this region is a region of depleted Cr-Mo rich grain boundary phases, this has been discussed in detail for the polished condition in Chapter 5. The dissolution of this phase occurs due to depletion of Cr used to supply the chromia external scale (Figure 6-18). The precipitation in most cases is limited to the grain boundaries. The MC carbides which reside on the grain boundaries of all the as-received surface conditions (Figure 6-4) decompose according to equations 5.20 and 5.21 to form Cr-Mo rich phases. These can either be sigma phase $(Ni\text{-}Co)_x(Cr,Mo)_y$ or $(Cr, Mo)_{23}C_6$ carbides. At 700°C these are most likely $(Cr, Mo)_{23}C_6$ carbides, as sigma phase would not be expected to form

in large quantities below 800°C in Ni-based superalloys with similar compositions to CG RR1000 [172]. In the swaged and shot-peened condition, $M_{23}C_6$ carbides are not only found on the grain boundaries but also within the grains, along slip bands. The dissolution of carbides due to the depletion of chromium in the near surface region leads to a large amount of carbon being released into solution. A diffusion gradient into the centre of the alloy is produced and the slip bands act as nucleation sites for $M_{23}C_6$ formation below the dissolution region. These conditions display the largest and deepest amount of deformation in the microstructure giving a potential reason why it only occurs in the swaged and shot-peened conditions. The formation of a higher percentage of carbides underneath a carbide dissolution region has been described previously in the literature [62, 63].

A couple of additional things to note within the external oxide scale in the shot-peened condition are the presence of a (Ta, Ti)O_2 phase forming at the external oxide alloy interface at the higher temperatures ~800°C (Figure 6-19). Figure 6-19 shows an EDX point analysis of the oxide showing an increased amount of Ta, along with Ti, Al, Cr and O. The oxides exact composition is hard to determine using EDX on an SEM, due to its small size and the large probe size used picking up large amounts of the external and internal oxides. TEM analysis was used in the polished condition to confirm the (Ta, Ti)O_2 structure and the same is expected here. This was described in more detail in Chapter 5. In the shot-peened condition this oxide is found in the same location but in significantly smaller amounts. The tests on the other conditions would not be expected to produce this oxide due to the lower exposure temperature.

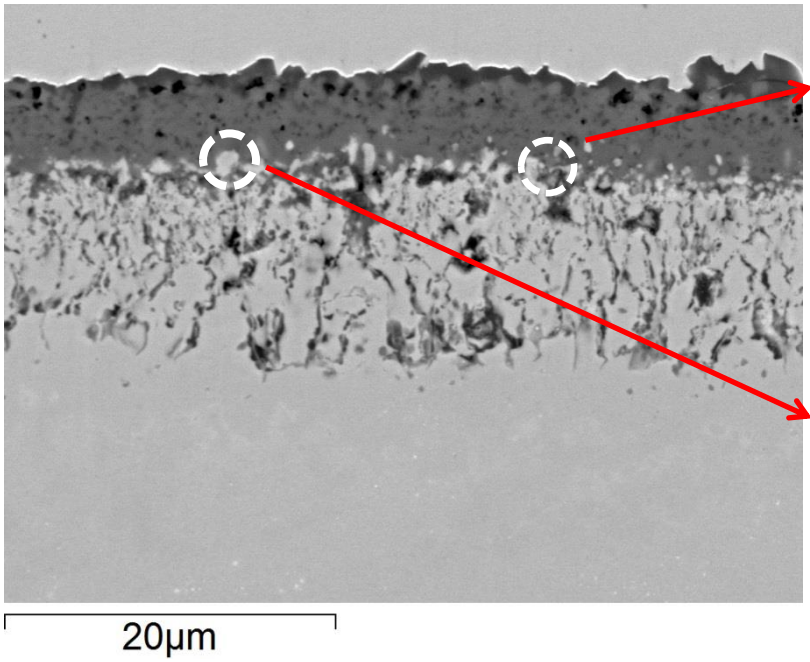

(Ta, Ti)O_2

Element	wt. %	at. %
O	23.2	51.6
Al	5.8	7.7
Ti	11.4	8.5
Cr	26.2	17.9
Co	5.6	3.4
Ni	13.3	8.1
Ta	14.5	2.9

Ni-Co rich protuberance

Element	wt. %	at. %
O	9.1	27.0
Al	0.8	1.3
Ti	1.2	1.2
Cr	19.7	18.0
Co	19.6	15.8
Ni	39.7	32.1
Mo	8.3	4.1
Ta	1.6	0.4

Figure 6-19: SE image and EDX point analysis of a cross-section through a shot-peened CG RR1000 specimen, illustrating the presence of a (Ta, Ti)O_2 forming underneath the chromia external scale, oxidised at 800°C for 2000 hours.

Furthermore, as in the polished condition the presence of Ti throughout the chromia scale can be noted in the shot-peened and vibro-peened conditions in Figure 6-13(a&b), in addition to isolated grains of TiO_2 on the outer surface. This in fact occurs in all surface conditions of RR1000. In Chapter 5 it was demonstrated that Ti has the ability to dissolve within the chromia scale as Ti^{4+} ions without affecting the chromia lattice spacing enough to be picked up via XRD [42]. It is also important to notice the non-planar surface that develops during oxidation and the encapsulation of metallic regions within the external oxide scale shown in Figure 6-19. These encapsulated metallic regions have been reported in polished RR1000 in Chapter 5 and in the similar Ni-based superalloy, ME3 as Ni-Co rich protuberances [47]. They have also been described in several chromia forming alloys [73, 77]. Moreover the mechanism for their formation would be expected to be the same in RR1000 regardless of the surface treatment applied and this was described in detail in Chapter 5. As stated in both the method and Chapter 5, no allowance for these metallic protuberances, nor the small amount of isolated voids found in the external scale, was made during measurement.

6.2.7 External oxide kinetics

The growth of the external oxide scale from cross-sections can be seen in Figure 6-12. This also shows the development of the extensive internal oxidation of alumina, illustrating that, like the polished condition, the scale is protective while also allowing the partial pressure of oxygen sub-surface to be high enough to oxidise aluminium. The measurements obtained for chromia thickness at 700°C for all the conditions at an exposure time of 2000 hours are shown in Table 6-VIII. High temperature oxidation kinetics for the external scale can be reasonably described by the following equation:

$$\xi^{n_{ox}} = k_n' \, t \tag{6.9}$$

where ξ is the thickness of the external oxide scale, (assumed to be chromia), k_n' is the growth rate constant for external oxide scale growth, n_{ox} is the growth oxide regime for external oxide scale growth and t is time (in seconds). Figure 6-20(a) shows the thickness of the external oxide scale with time, at 700°C in all the different surface conditions tested. Clearly all conditions show a similar trend, with the rate of external oxide growth decreasing with time. The vibro-peened condition forms a lower bound (blue dashed line) with the shot-peening condition forming the upper bound (green dotted line). All the other conditions fall within these lines and generally fall within each other's ± 1 standard deviation error bars. This would suggest that there is no significant difference between any of the conditions, although using a one-way ANOVA with Tukey analysis the oxide thickness on the shot-peened surface condition has been found to be significantly larger ($p<0.05$), when oxidised at 700°C for 2000 hours, than the vibro-peened, swaged and polished surface conditions.

In the shot-peened condition the change in external oxide thickness with time, at 700, 750 and 800°C is shown in Figure 6-20(b). This shows a similar trend to the polished condition and to mass gain results discussed earlier in this chapter, with the oxide thickness being larger as exposure temperature increases and that the rate of external oxide growth decreases with time at each temperature. A t-test was used to confirm that a significant difference ($p<0.05$) was present between the shot-peened and polished condition when oxidised at 2000 hours at both 750 and 800°C. Homogeneity of variance was tested for and found to be violated.

a) 700°C – All surface conditions

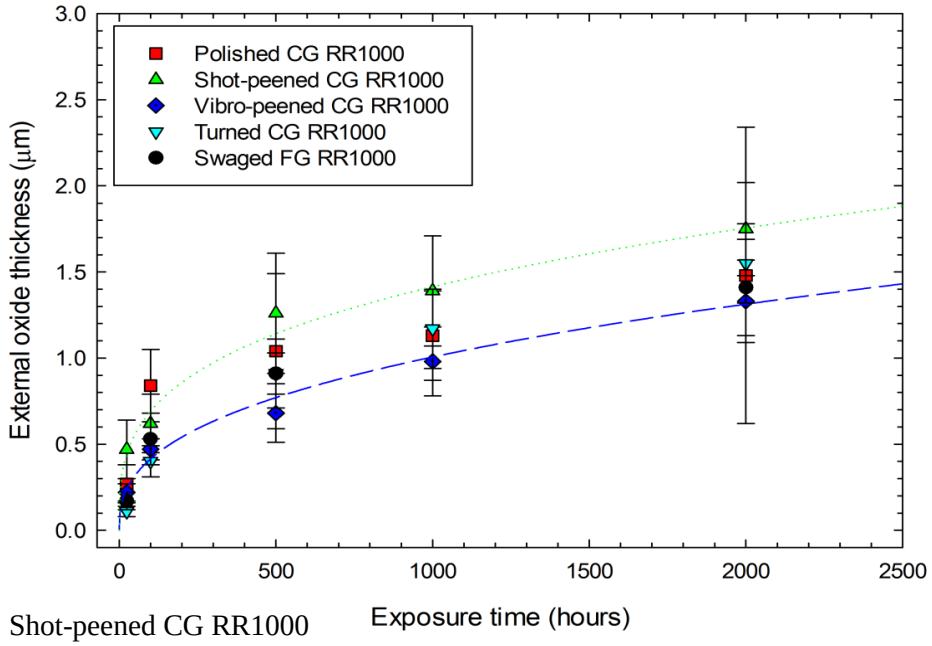

b) Shot-peened CG RR1000

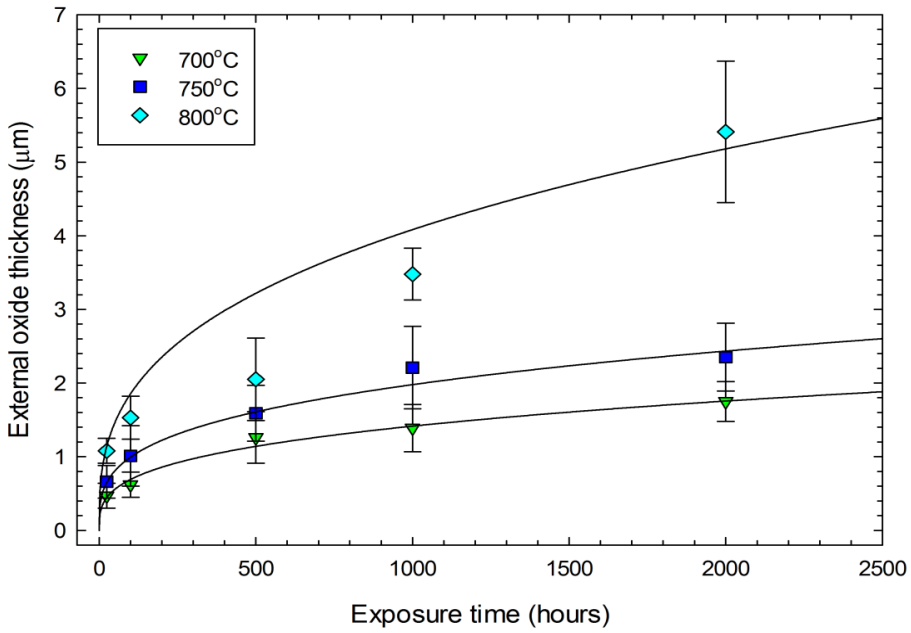

Figure 6-20: Plot of oxide thickness against time for a) each surface condition tested at 700°C and b) for shot-peened CG RR1000 at 700, 750 and 800°C. Best fit lines are produced for the shot-peened and Vibro-peened in a) as these form upper and lower bounds and for all data sets in b). Best fit lines were plotted according to Equation 6.9, with values for n_{ox} and k_n' being taken from Table 6-X.

The normality of the external oxide measurements were checked and confirmed to be normally distributed, using Q/Q plots, histogram and a Shaprio-wilk normality test. The Q/Q plots and histogram for vibro-peened condition oxidised at 700°C for 1000 hours is shown in Figure 6-21.

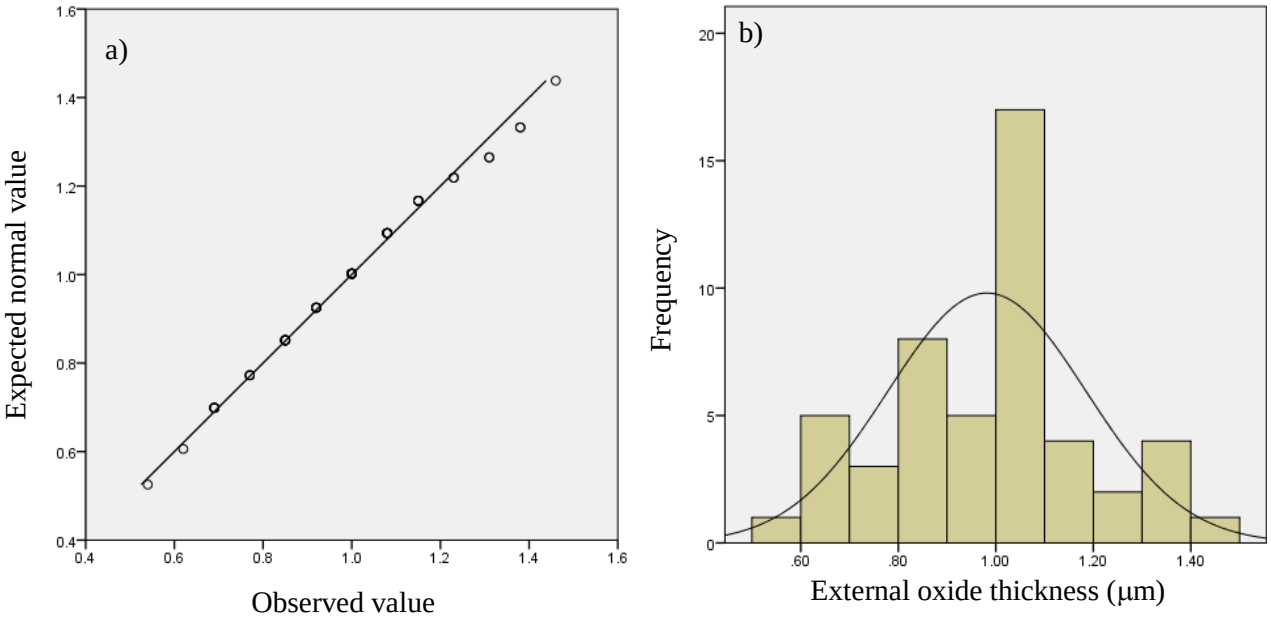

Figure 6-21: Q/Q plot (a) and histogram (b) of all the external oxide measurements taken from a vibro-peened CG RR1000 specimen oxidised at 700°C for 1000 hours, illustrating that the data is distributed normally, with the values being distributed linearly in the Q/Q plot.

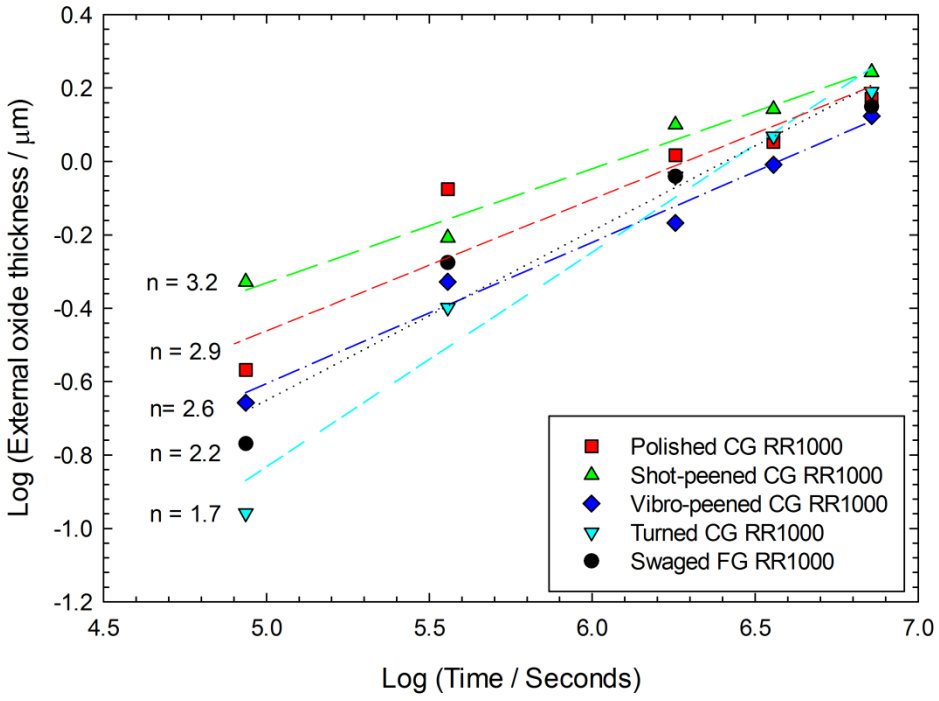

Figure 6-22: Plot of log external oxide thickness against log exposure time for each surface condition tested at 700°C.

Table 6-VIII: Oxidation damage measurements, in microns, oxidised at 700°C for 2000 hours for all the surface modifications applied to RR1000 (±1 standard deviation).

		External oxide (μm)	Internal oxide (μm)	γ′ denuded zone (μm)	Carbide dissolution (μm)
CG RR1000	**Intragranular**	1.48 (±0.86)	2.06 (±0.46)	2.11 (±0.32)	14.50 (±1.81)
	Intergranular		2.92 (±0.48)	3.72 (±0.72)	
Shot-Peened CG RR1000		1.75 (±0.27)	2.91 (±0.37)	2.82 (±0.57)	11.77 (±1.22)
Vibro-peened CG RR1000		1.33 (±0.24)	2.15 (±0.56)	4.47 (±0.71)	15.25 (±2.90)
Turned CG RR1000		1.55 (±0.23)	2.25 (±0.30)	4.03 (±0.75)	15.09 (±2.43)
Swaged FG RR1000		1.41 (±0.28)	2.64 (±0.62)	2.78 (±0.35)	7.44 (±0.75)

Table 6-IX: Best estimates of the exponent, n, oxidation kinetics of RR1000 for the oxidation damage with different surface modifications oxidised at 700°C in laboratory air, assuming parabolic or cubic behaviour.

		External oxide		Internal oxide		γ′ denuded zone	
		n_{ox}	k_c' ($\mu m^3.s^{-1}$)	n_{ox}	k_{pl} ($\mu m^2.s^{-1}$)	n_{ox}	k_{py} ($\mu m^2.s^{-1}$)
CG RR1000	**Intragranular**	2.9	$5.94x10^{-7}$	1.8	$4.11x10^{-7}$	2.3	$4.64x10^{-7}$
	Intergranular			2.4	$1.10x10^{-6}$	2.8	$1.57x10^{-6}$
Shot-Peened CG RR1000		3.2	$7.62x10^{-7}$	1.8	$1.23x10^{-6}$	1.9	$1.38x10^{-6}$
Vibro-peened CG RR1000		2.6	$3.07x10^{-7}$	2.3	$7.16x10^{-7}$	1.8	$2.48x10^{-6}$
Turned CG RR1000		1.7	$4.98x10^{-7}$	1.5	$7.58x10^{-7}$	1.6	$2.44x10^{-6}$
Swaged FG RR1000		2.2	$3.91x10^{-7}$	2.0	$9.45x10^{-7}$	1.7	$1.05x10^{-6}$

Table 6-X: Best estimates of the exponent, n, and actual oxidation kinetics of RR1000 for the oxidation damage with different surface modifications oxidised at 700°C in laboratory air and the external oxide scale kinetics of the shot-peened condition at 700, 750 and 800°C.

Temperature	Shot-peened CG RR1000		20Cr austenitic steel [171]
	n_{ox}	k_p' ($\mu m^2.s^{-1}$)	K_n' ($\mu m^n.s^{-1}$)
700°C	3.22	$2.94x10^{-8}$	$8.48x10^{-7}$
750°C	3.34	$1.40x10^{-7}$	$2.72x10^{-6}$
800°C	2.92	$5.75x10^{-7}$	$1.68x10^{-5}$

		External oxide		Internal oxide		γ′ denuded zone	
		n_{ox}	K_n' ($\mu m^n.s^{-1}$)	n_{ioz}	K_{nl} ($\mu m^n.s^{-1}$)	n_{dz}	K_{ny} ($\mu m^n.s^{-1}$)
CG RR1000	**Intragranular**	2.9	$5.63x10^{-7}$	1.8	$3.45x10^{-7}$	2.3	$6.95x10^{-7}$
	Intergranular			2.4	$2.16x10^{-6}$	2.8	$7.12x10^{-7}$
Shot-Peened CG RR1000		3.2	$8.48x10^{-7}$	1.8	$1.02x10^{-6}$	1.9	$1.23x10^{-6}$
Vibro-peened CG RR1000		2.6	$2.82x10^{-7}$	2.3	$8.50x10^{-7}$	1.8	$1.77x10^{-6}$
Turned CG RR1000		1.7	$3.16x10^{-7}$	1.5	$5.12x10^{-7}$	1.6	$1.78x10^{-6}$
Swaged FG RR1000		2.2	$3.02x10^{-7}$	2.0	$9.05x10^{-7}$	1.7	$6.90x10^{-7}$

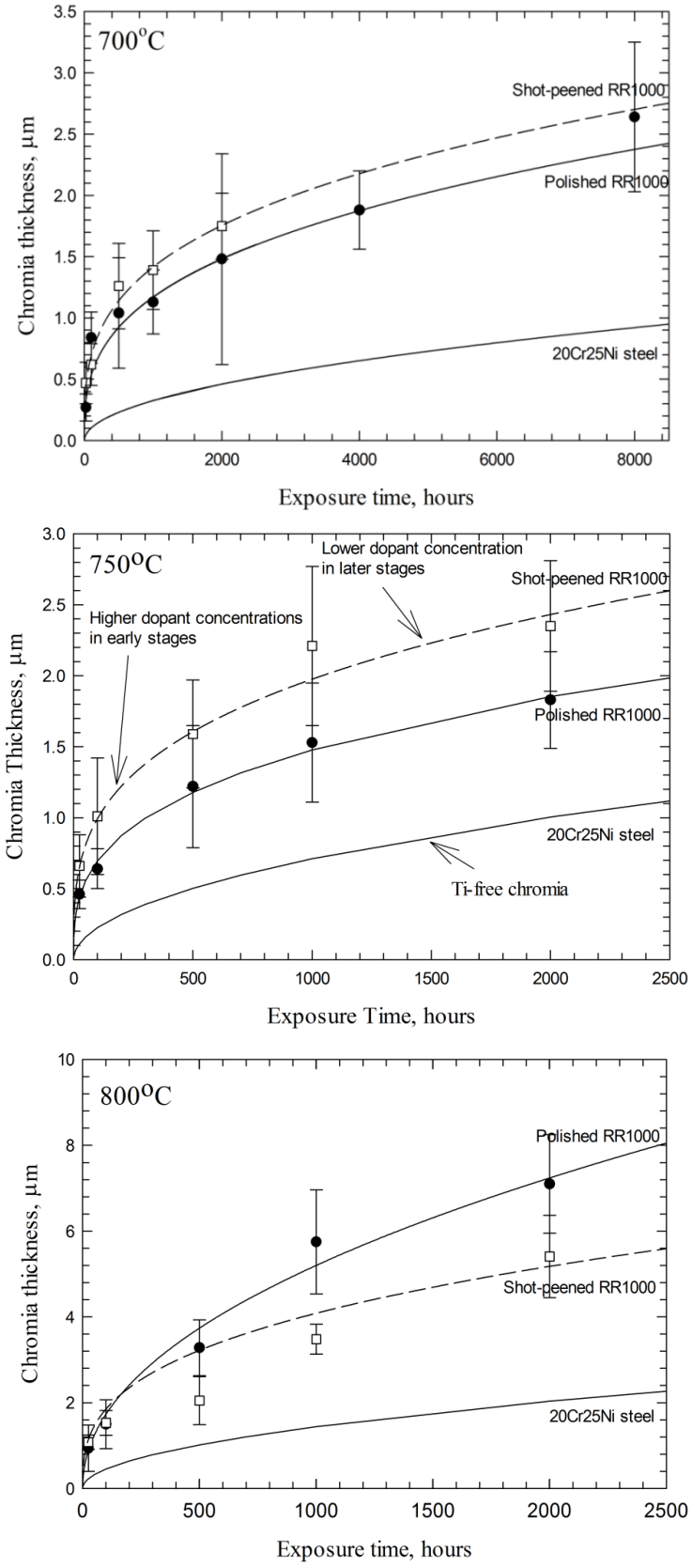

Figure 6-23: Plot of chromia thickness measured on both RR1000, with and without shot-peening, at 700°C, 750°C and 800°C compared with Ti-free austenitic steel/pure chromia. Error bars are shown as ±1 standard deviation. Hollow squares are measurements for shot-peened RR1000 and filled circles are polished RR1000. Best fit lines for RR1000 are produced using equation 6.9 and the n_{ox} and k_n' values in Table 5-VI and Table 6-X. Pure chromia was plotted according to equation 5.5.

Figure 6-22 shows the determination of the external oxide thickening growth regime (n_{ox}) for each of the surface conditions tested at 700°C. In all cases sub-parabolic kinetics are recorded apart from turned CG RR1000 where the kinetics are slightly quicker than parabolic (Table 6-IX). In the shot-peened case significantly sub-parabolic growth can be assumed at the three temperatures, 700, 750 and 800°C (Table 6-XI). Cubic kinetics for the chromia growth have been assumed to allow for a comparison to be made between the different surface conditions applied to RR1000 as well as the similar Ni-based superalloy, ME3.

Table 6-XI: Best estimate for the exponent, n, for the external oxide scale thickness and the sub-parabolic oxidation rate constants for polished and shot-peened CG R1000. The parabolic rate constants for pure chromia formation on a 20Cr austenitic steel and the sub-parabolic oxidation rate constants for Ni-based superalloy, ME3 are also included.

Temperature	Shot-peened CG RR1000		Polished CG RR1000		20Cr austenitic steel [171]
	n_{ox}	k_c' ($\mu m^3.s^{-1}$)	n_{ox}	k_c' ($\mu m^3.s^{-1}$)	k_p' ($\mu m^2.s^{-1}$)
700°C	3.22	$7.62x10^{-7}$	2.93	$5.94x10^{-7}$	$2.94x10^{-8}$
750°C	3.34	$2.05x10^{-6}$	3.05	$8.56x10^{-7}$	$1.40x10^{-7}$
800°C	2.92	$1.92x10^{-5}$	2.10	$4.88x10^{-5}$	$5.75x10^{-7}$

Temperature	ME3[47]
	k_c' ($\mu m^3.s^{-1}$)
704°C	$2.14x10^{-7}$
760°C	$8.61x10^{-7}$
815°C	$5.28x10^{-6}$

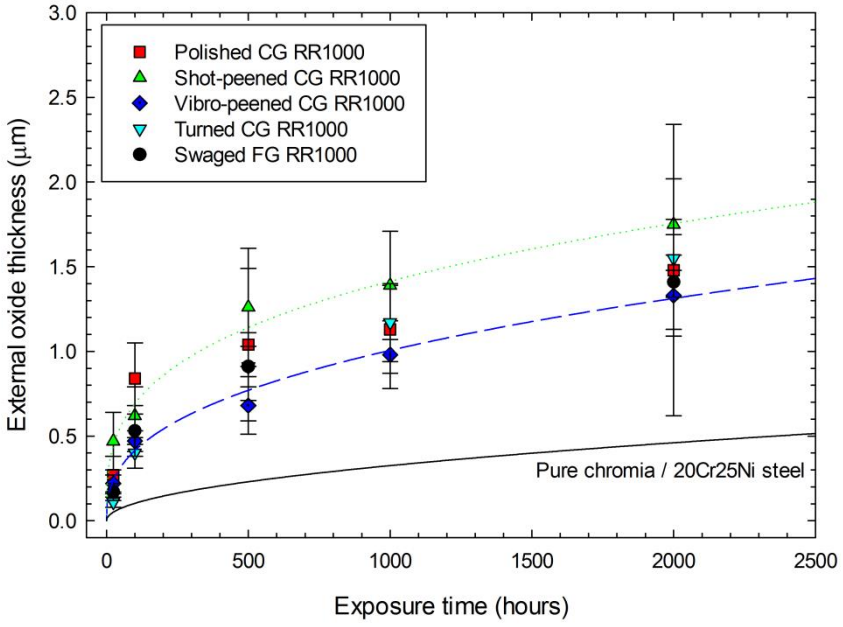

Figure 6-24: Plot of chromia thickness measure on RR1000 with several different surface modifications at 700°C compared with a pure chromia forming 20Cr austenitic steel. Error bars are ±1 standard deviation. Best fit lines for RR1000 are produced using equation 6.9 and values in Table 6-X. Pure chromia was plotted according to equation 5.5.

A comparison of the external oxide growth constants at 700°C for all of the surface conditions are shown in Table 6-IX. It clearly shows similar results to Figure 6-20 (a) with shot-peening having the largest growth rate and vibro-peening having the slowest and in all conditions the growth rates are significantly faster than for pure chromia growth. The growth rates for the external oxide on RR1000 are similar to that of the similar Ni-based superalloy, ME3, although ME3 has a lower growth rate at 815°C when compared with RR1000 at 800°C (regardless of the surface condition). An exact comparison cannot be made due to the slight difference in exposure temperature.

The external oxide growth for shot-peened RR1000 at three different temperatures is shown in Figure 6-23 evidently showing the external scale not only grows quicker than the polished condition at 700 and 750°C, but that shot-peening has a beneficial effect at 800°C mirroring the mass gain results.
Figure **6-24** shows the same external oxide thickness measurements against time in RR1000 with several different surface modifications displaying again that the chromia growth on RR1000 regardless of the surface preparation is significantly faster than pure chromia growth on either chromium or a high chromium containing steel. The lines for chromia growth were taken from the expected chromia thickness, Equation 5.5 in Chapter 5, grown on pure chromium or high chromium containing austenitic steel recorded in the literature (shown below).

$$k_p' = 2.07x10^6 \exp\left[-\frac{31020}{T}\right] \quad \mu m^2.s^{-1} \tag{5.5}$$

where k_p' is the parabolic rate constant for thickening of the pure chromia layer and T is temperature. Similar to that performed in Chapter 5, the enhanced growth rate observed on RR1000 regardless of the surface condition was significantly greater than that expected from pure chromia growth on simple Ti-free alloys. This increase in rate can be quantified using Equation 5.6 in Chapter 5 (shown below).

$$r = \left(\frac{(d\xi/dt)_s}{(d\xi/dt)_{cr}}\right)_{\xi} \tag{5.6}$$

Again the calculation of the ratio 'r' was performed for all conditions using best fit Equations 6.9 and the parameters (n_{ox} and k_n') given Table 6-X. The dependence of the ratio 'r' on oxide thickness (ξ) and test temperature or surface condition is shown in Figure 6-25 and shows a significant enhancement in chromia growth rate in RR1000. A plausible explanation for the enhancement of the chromia scale in the polished condition has been explained in detail in Chapter 5. This is caused by an increase in chromium vacancies within the chromia scale as a result of the incorporation of a higher-valent ion, leading to an increase in the oxidation rate through increased diffusion rates of chromium ions across the oxide [42-44, 62, 178, 183].

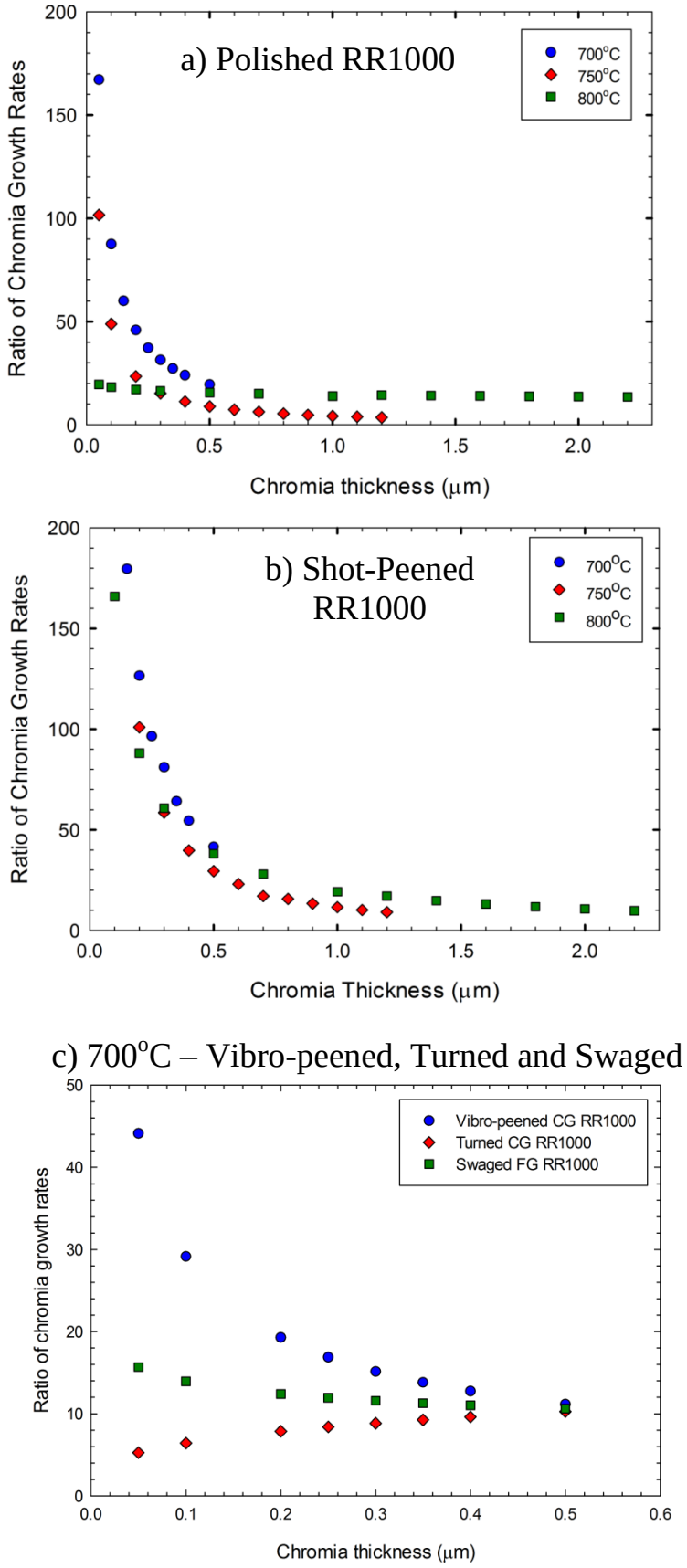

Figure 6-25: The variation of the enhancement ratio with oxide thickness in a)polished CG RR1000, b) shot-peened CG RR1000 for 700°C, 750°C and 800°C and in c) for swaged FG RR1000, turned CG RR1000 and vibro-peened CG RR1000 at 700°C

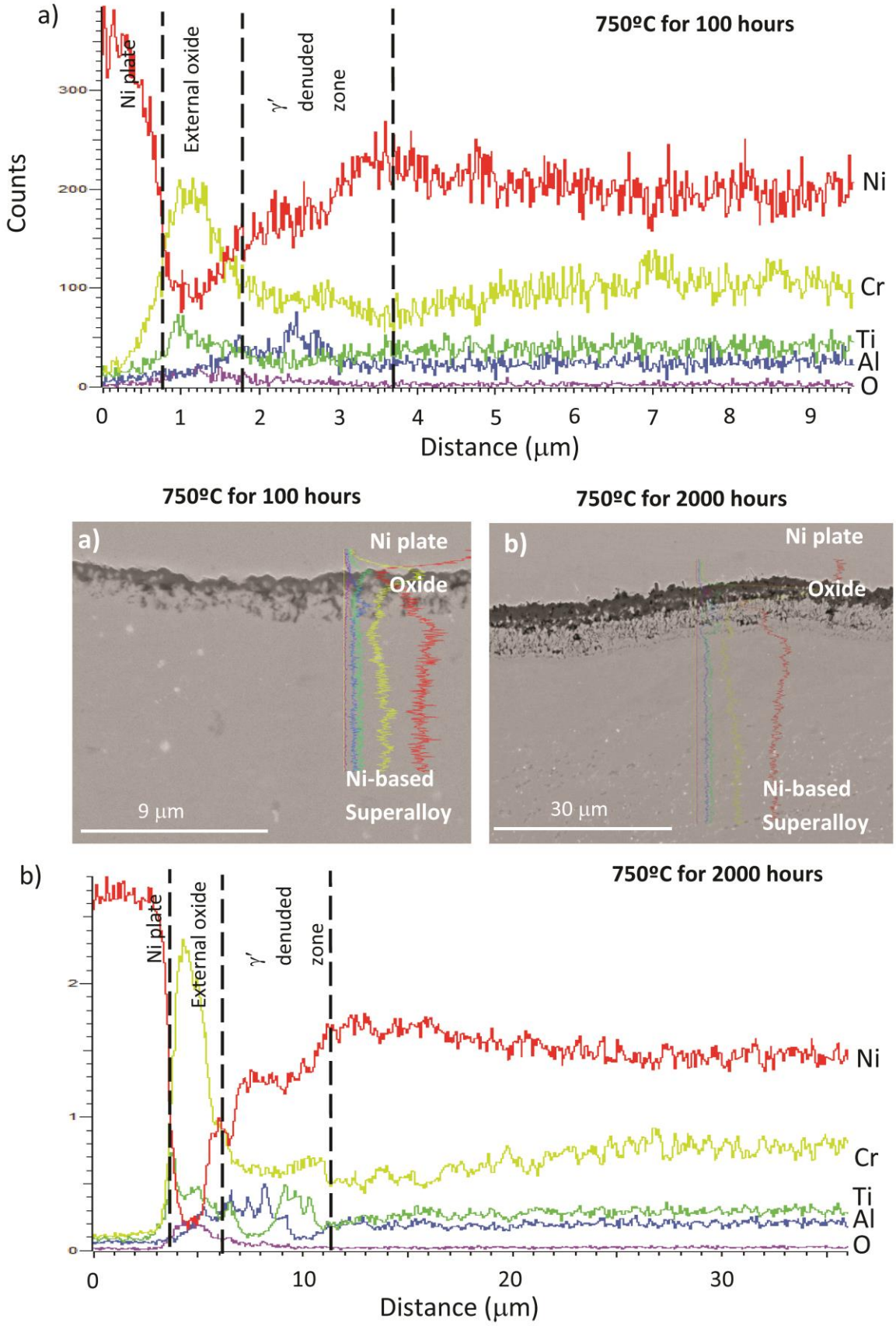

Figure 6-26: EDX linescans (and BSE images) of shot-peened RR1000 oxidised isothermally at 750°C for a) 100 hours and b) 2000 hours showing titanium and aluminium depletion underlying the external oxide scale.

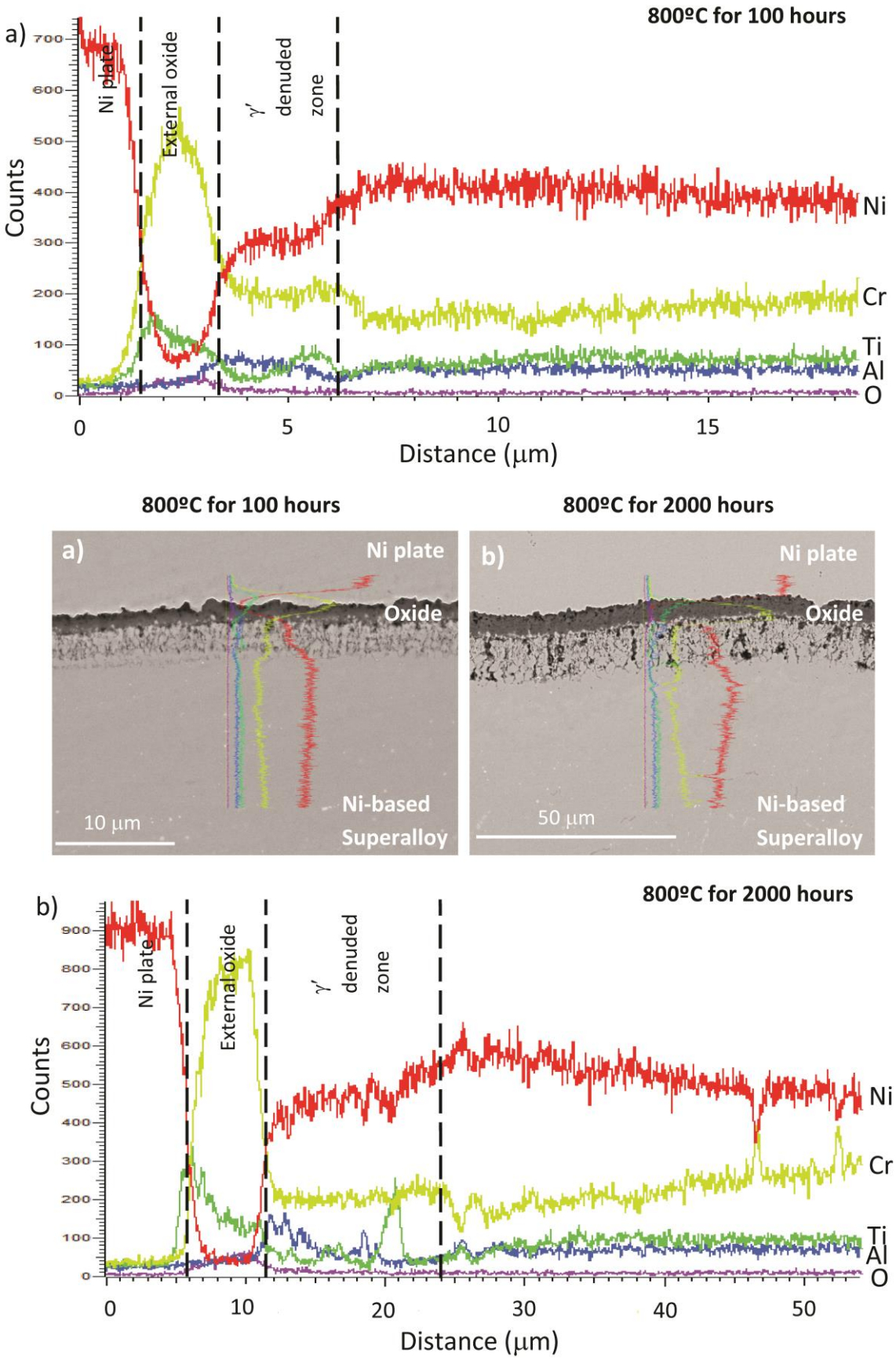

Figure 6-27: EDX linescans (and BSE images) of shot-peened RR1000 oxidised isothermally at 800°C for a) 100 hours and b) 2000 hours showing titanium and aluminium depletion underlying the external oxide scale.

This would also hold true for the shot-peened condition. As the external oxide thickens and depletion of Ti underneath the external oxide scale ensues, the driving force for Ti into the oxide scale is reduced. This causes a corresponding reduction in the rate-enhancement ratio as the oxide thickness increases (Figure 6-25(b)). This is illustrated by Figure 6-26 and Figure 6-27 which shows SEM images and EDX linescans for both 750 and 800^{o}C. In all cases the location of the external oxides, γ' denuded zone and the alloy are labelled. It can be seen within the γ' denuded zone there is some depletion of both aluminium and titanium adjacent to the external oxide scale. At shorter time periods, 100 hours (

Figure **6-24** (a) and Figure 6-27(b)), a positive gradient of Ti concentration is found adjacent to the oxide scale, indicating that there is a flux of Ti into the growing oxide scale. At the longer time periods (Figure 6-26(b)) and Figure 6-27(b)) there is a significant depletion of Ti within the γ' denuded zone along with the near zero gradient of Ti concentration neighbouring the growing oxide scale, although the profile for Ti in (Figure 6-26(b)) and Figure 6-27(b) is complicated by the inclusion of TiN within the γ' denuded zone. This near zero gradient causes a reduction in driving force for titanium into the oxide scale and therefore the reduction in rate-enhancement ratio with increasing chromia thickness, seen in Figure 6-25(a & b), as the doping effect is reduced. The reduction in the Ti concentration within the chromia scale in the shot-peened condition can be made tentatively, like in the polished condition, in Chapter 5, by calculating an estimate of the Ti/Cr ratio within the chromia layer by comparing the Ti and Cr counts at the peak of the Cr counts. It is found that after 100 hours (Figure 6-26(a)) at 750^{o}C, Ti/Cr ~0.22 but this is reduced to ~0.14 after 2000 hours (Figure 6-26(b)). This is remarkably exactly the same values as the polished condition.

It can be noted that there is a significant difference between the polished and the shot-peened condition at 800^{o}C. At 800^{o}C in the shot-peened condition the mechanism described above holds true. It is unclear why the lack of the reduction in the rate-enhancement occurs in the polished condition, with it displaying a small constant enhancement. As stated before in both cases the depletion of the Ti underneath the doped chromia scale, at the longer time periods, is significant with the only notable difference between the alloys being the inclusion of a smaller amount of (Ti, Ta)O_2 adjacent to the external oxide scale in the shot-peened condition. Its formation does not seem to have the same effect as that found in the polished condition in that it produces the same decreasing rate-enhancement ration with increasing chromia thickness rather than the constant enhancement found in the polished condition at 800^{o}C. This is likely to be due to the much smaller amount of the phase.

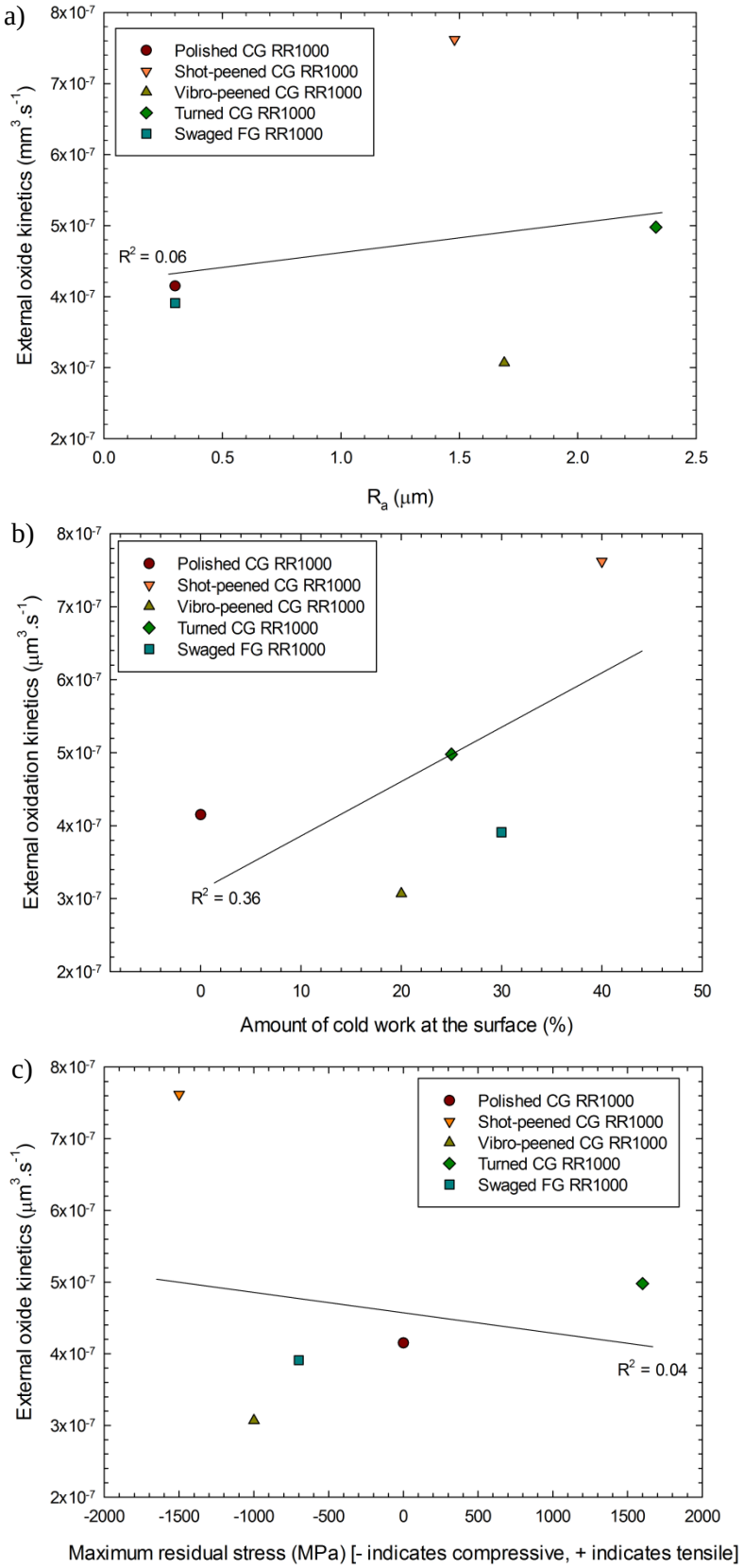

Figure 6-28: Plot of oxidation kinetics against a) surface roughness, b) cold work and c) residual stress for all the surface condition tested at 700°C.

In addition the shot-peened condition shows an enhancement in Cr concentration within the γ′ denuded zone at both short (100 hours) and long (2000 hours) exposure times (Figure 6-26 and Figure 6-27) at both 750°C and 800°C. This is in contrast to the polished condition which shows a monotonic decrease in Cr concentration from the bulk alloy through the depletion zone towards the oxide/metal interface. The difference between the polished and shot-peened condition is unclear and merits further study. One possibility is that recrystallised grain boundaries acts as short circuit diffusion pathways enhancing diffusion of Cr in the γ′ denuded zone compared to the bulk alloy leading to the step down in Cr concentration at the γ′ denuded zone/alloy interface.

In the case of the other surface conditions (Vibro-peened, Turned and Swaged) the rate-enhancement ratio with chromia thickness is shown in Figure 6-25(c). The vibro-peened condition shows a similar effect but a much smaller enhancement in growth initially, with a maximum rate-enhancement of ~40 (at a chromia thickness of 0.1 μm). This is not surprising as this condition shows the lowest growth rate and would therefore be expected to show a smaller enhancement than either the polished or shot-peened condition. The swaged condition again shows similar, although with a much smaller enhancement is recorded initially (~15). Again the swaged sample displays a slow growth rate that is slightly larger than the vibro-peened sample. It is not clear why vibro-peening or swaged surface treatment causes the smallest chromia growth rates, although the growth rates are still comfortably within the same order of magnitude as those recorded on the shot-peened or polished alloy. The mechanism for chromia being doped with Ti, described above, would be expected to hold true in these cases.

The turned specimen shows the opposite with a very small increasing rate-enhancement as chromia thickness increases. While the chromia growth rate of this surface condition falls comfortably within the other surface conditions (
Figure **6-24**), initially the chromia growth rate is small, sitting on the lower bound for the alloy, before increasing to the upper bound. This gives an exponent for chromia growth significantly greater than parabolic (n=1.5), meaning that while an enhancement between turned CG RR1000 and pure chromia formation is recorded in all cases, the difference between the growth rates increases, rather than decreases as in the other surface conditions. The reason why this occurs only in the turned surface condition is currently unclear.

A comparison of the chromia growth rates are plotted against the amount of residual stress, cold work and surface roughness each condition has is demonstrated in Figure 6-28 and illustrates that there is no real trend in either the amount of residual stress (R^2 of 0.04) or in the surface roughness (R^2 of

0.06). There is, however, a loose trend in the cold work (R^2 of 0.36) with the larger the amount of cold work the larger the external oxidation kinetics. The enhancement could be caused by an increase in the diffusion of Cr and Ti due to recrystallisation and the production of slip bands in the near surface region providing low energy diffusion pathways. Support is provided by numerous studies that have found that increased levels of cold work can lead to enhanced diffusion of Cr. In some cases this has a beneficial effect, by causing the formation of protective oxides in alloys that otherwise formed non-protective oxides [124, 125]. Whereas in others, like the surface conditions used here, a detrimental effect is found with an increase in diffusion of Cr leading to enhanced growth kinetics for alloys already forming protective oxides [126, 128]. In one study shot-peened has been found to cause a localised plastic zone in the near surface region [120] and another an ultra-fine microstructure was found [122], similar to that found in the recrystallised region in this alloy, with both leading to an enhancement in chromium diffusion. It is unclear why the supply of Cr to the oxide/alloy interface would increase the growth rate of chromia as Cr ion transport across the chromia scale is usually the rate controlling process. In this high Cr alloy (~15 wt.%) the supply of Cr to this interface is unlikely to be rate controlling. This increased supply of Ti could reasonably lead to an enhanced doping effect and therefore an enhancement in chromia growth rates. There is also a significant amount of error (±10%) in the cold work measurements due to the method used to calculate them and so the accuracy of the trend should be questioned. Additionally a much better trend is found with the amount of residual stress if the values are taken solely as magnitude irrespective of whether it is a tensile or compressive stress ($R^2 = 0.28$), indicating that only the magnitude of the stress matters and illustrates, like the effect of cold work, that the larger the residual stress the larger the external oxide growth rates. It is hard to break down the effect of each of these factors have, as they are inter-related, on the oxidation kinetics as any differences in growth rate are likely a combination of all three.

Figure 6-29 illustrates the determination of the activation energy assuming, n=3, sub-parabolic kinetics. An activation energy of 278 $kJ.mol^{-1}$ is recorded for the shot-peened condition, this is slightly higher than that attained on similar Ni-based superalloy, ME3. It is also larger than that found for pure chromia. Even the activation energy in this case was performed only from three well defined points a good fit between them was found with an R^2 of 0.94. The value for polished condition is significantly lower than that achieved in pure chromia formation, the shot-peened condition and ME3. Although this value is dubious as two significantly different exponents, n=3 (700, 750^{o}C) and n=2 (800^{o}C) were found, but sub-parabolic kinetics (n=3) were assumed for the calculation of the activation energy. It is possible two different activation processes are occurring, in the polished condition, one for the lower temperatures (700-750^{o}C) and one at the higher range (800^{o}C) meaning this is not an accurate determination of the activation energy for external oxide formation, so a comparison to the shot-peened condition cannot accurately be made. Although differences in the activation energies are apparent these are minor differences, with all the values fitting in reasonably

well with pure chromia formation and that of similar Ni-based superalloy, ME3 [47]. The activation energy for Cr ion transport across chromia is similar to the values for chromia growth found here at 280 kJ.mol^{-1} and indicates that this is the rate controlling process in all conditions [190]. A more detailed analysis of the rate controlling processes is available in Chapter 5. Using the activation energy determined using Figure 6-29, an equation has been produced to describe the external oxide growth rate constants in the shot-peened CG RR1000 condition and is displayed below:

$$k'_c = 5.18x10^8 \exp\left(\frac{278092}{8.314\,T}\right)\ \mu m^3.s^{-1} \quad (6.10)$$

Table 6-XII: Activation energy for the formation of the external oxide scale on shot-peened CG RR1000, polished CG RR1000, Ni-based superalloy ME3 and pure chromia formatting 20Cr austenitic steel listed along with the temperature range analysed.

Alloy	Activation energy (kj.mol^{-1})	Temperature range tested
Polished CG RR1000	236	700-800°C
Shot-peened CG RR1000	278	700-800°C
ME3	262 (±33)	704-815°C
20Cr austenitic steel	258	700-900°C

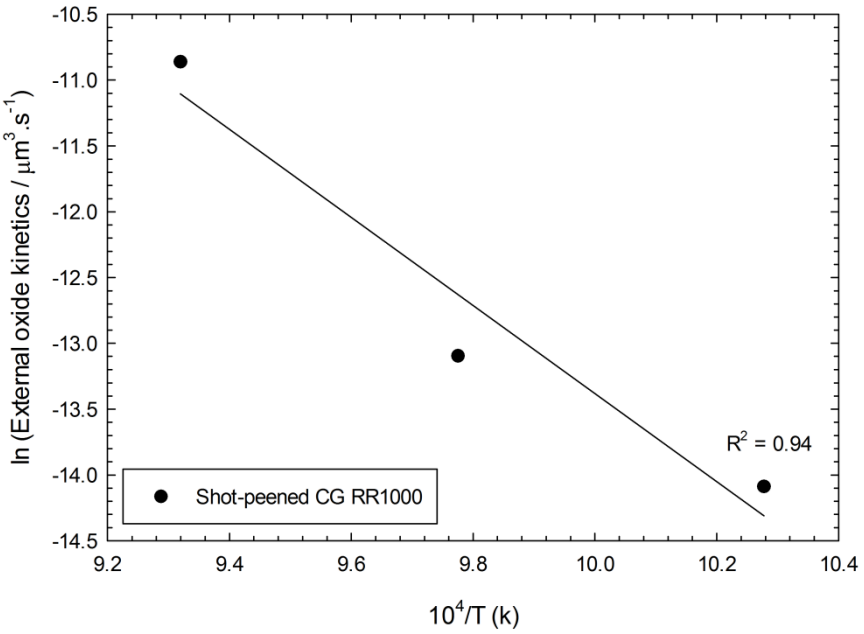

Figure 6-29: Activation energy of external oxide scale formation on shot-peened CG RR1000 over a temperature range of 700°C-800°C. A best fit regression line is included with a R^2 value describing the fit of the line.

6.2.8 Internal oxide and γ′ denuded zone kinetics

The growth of the internal oxide (Figure 6-12) and γ′ denuded zone has been investigated at 700°C in all the surface conditions and additionally at 750 and 800°C in the shot-peened condition. Extensive measurements of both the internal oxide penetration (IOZ) and the γ′ denuded zone have been performed. The average measurements for 700°C at 2000 hours are displayed in Table 6-VIII. These measurements were normally distributed as displayed in the Q/Q plots and histograms shown in Figure 6-30. This was performed in conjunction with a Shaprio-wilk test to confirm normality.

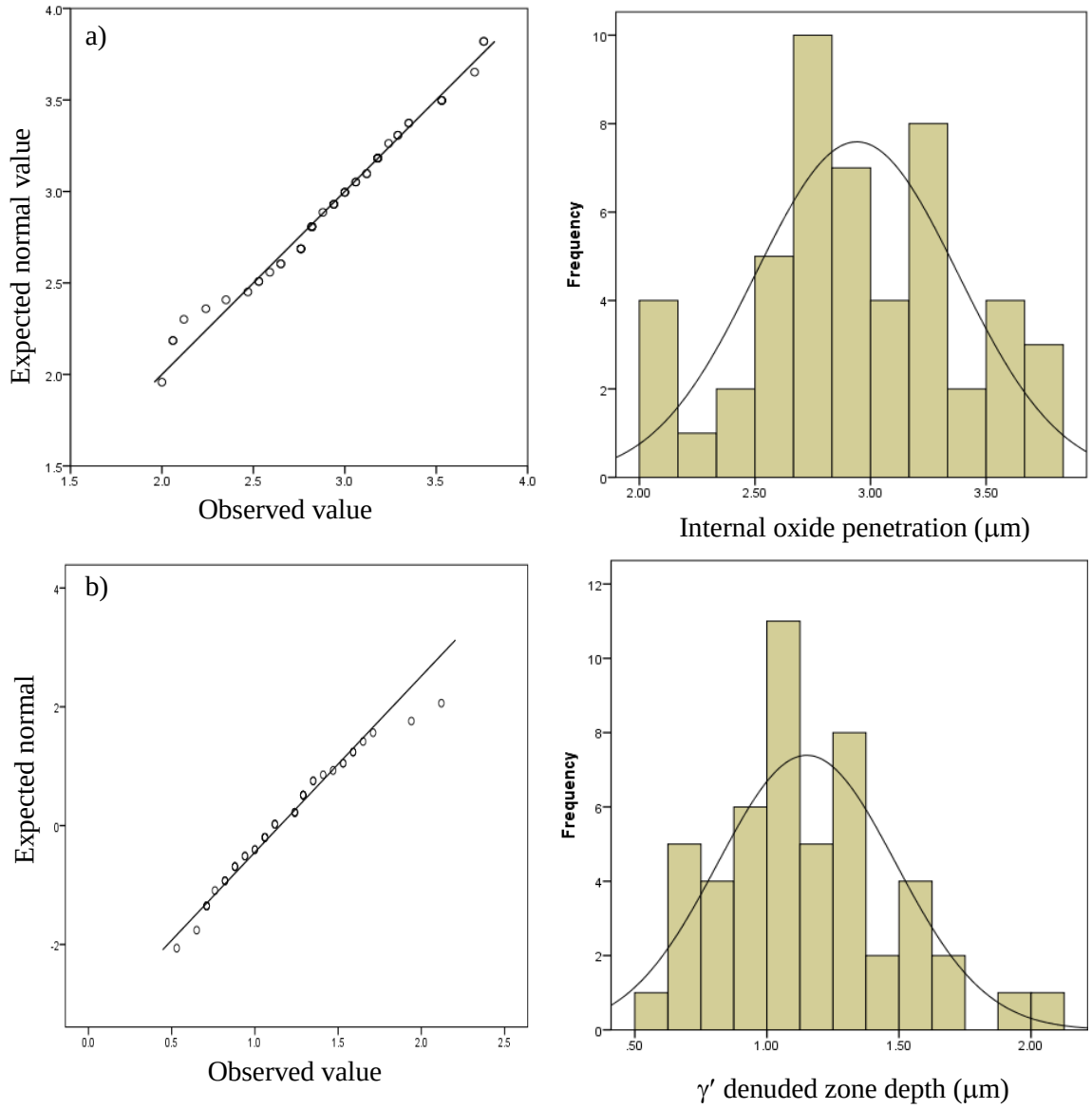

Figure 6-30: Q/Q plot and histogram of (a) all the internal oxide measurements taken from a shot-peened CG RR1000 specimen oxidised at 75°C for 500 hours. b) All the γ′ denuded zone measurements from a swaged FG RR1000 specimen oxidised at 700°C for 500 hours. Both a) and b) illustrate that the data is distributed normally, with the values being distributed linearly in the Q/Q plot.

Figure 6-31(a) clearly shows that the growth of the internal oxide at 700°C is the largest in the shot-peened and intergranular polished condition, with the alumina penetration in the intragranular polished condition being the smallest. All the other conditions fall in between these. Figure 6-32 shows the fit of the trend lines through the measurements at each time for each surface condition. In Figure 6-31(b) the alumina penetration depth in shot-peened condition is shown plotted against time at the three temperatures at which testing was performed and evidently shows, like in the polished condition and the external chromia scale, that the higher the exposure temperature the larger the magnitude of the internal alumina penetration. This also holds true for the γ′ denuded zone in the shot-peened condition at the three test temperatures (700-800°C) shown in Figure 6-33(b).

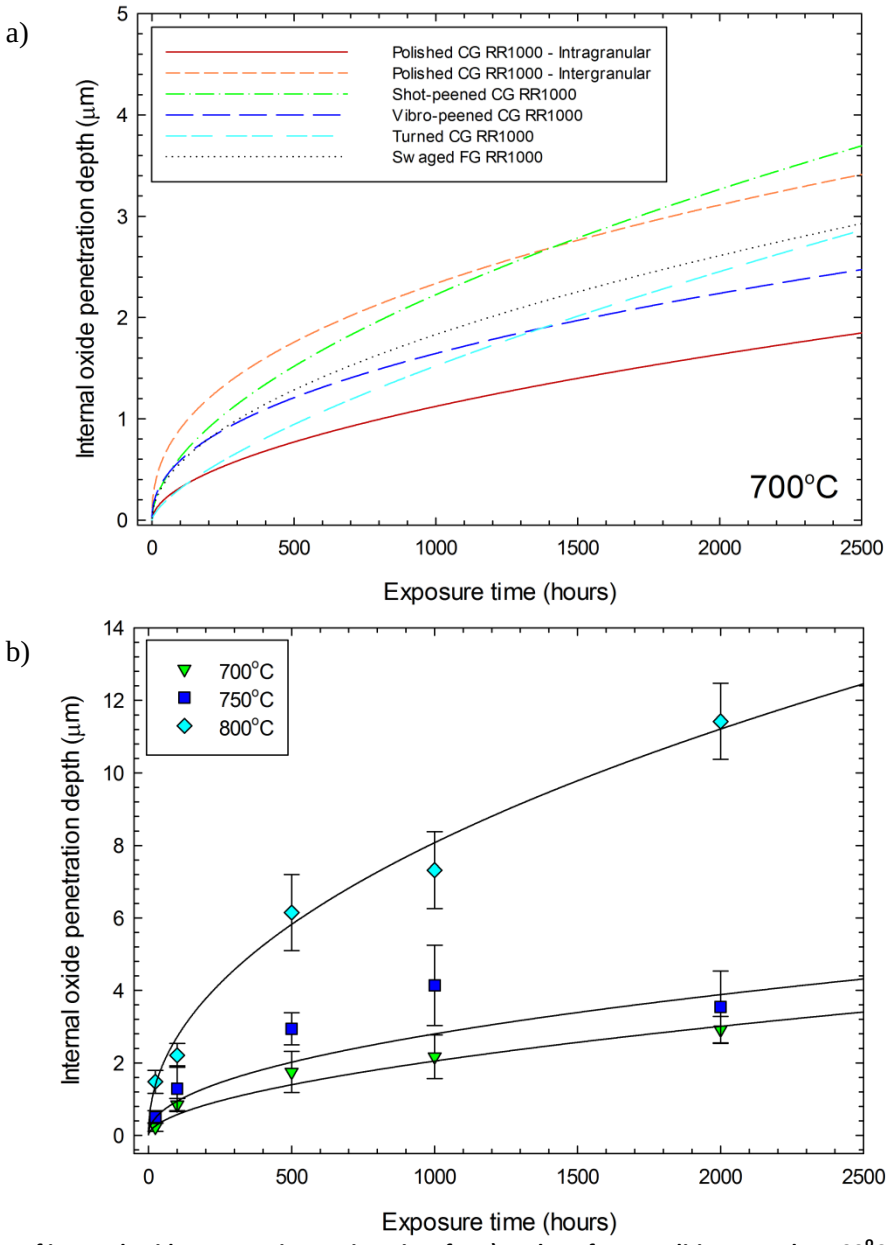

Figure 6-31: Plot of internal oxide penetration against time for a) each surface condition tested at 700°C and b) for shot-peened CG RR1000 at 700, 750 and 800°C. The full data set is shown in Figure 6-32. The lines in a) are produced using best fit kinetics using equation 6.11 and the values for n_{ioz} and k_{nl} in Table 6-X and Table 6-XIII.

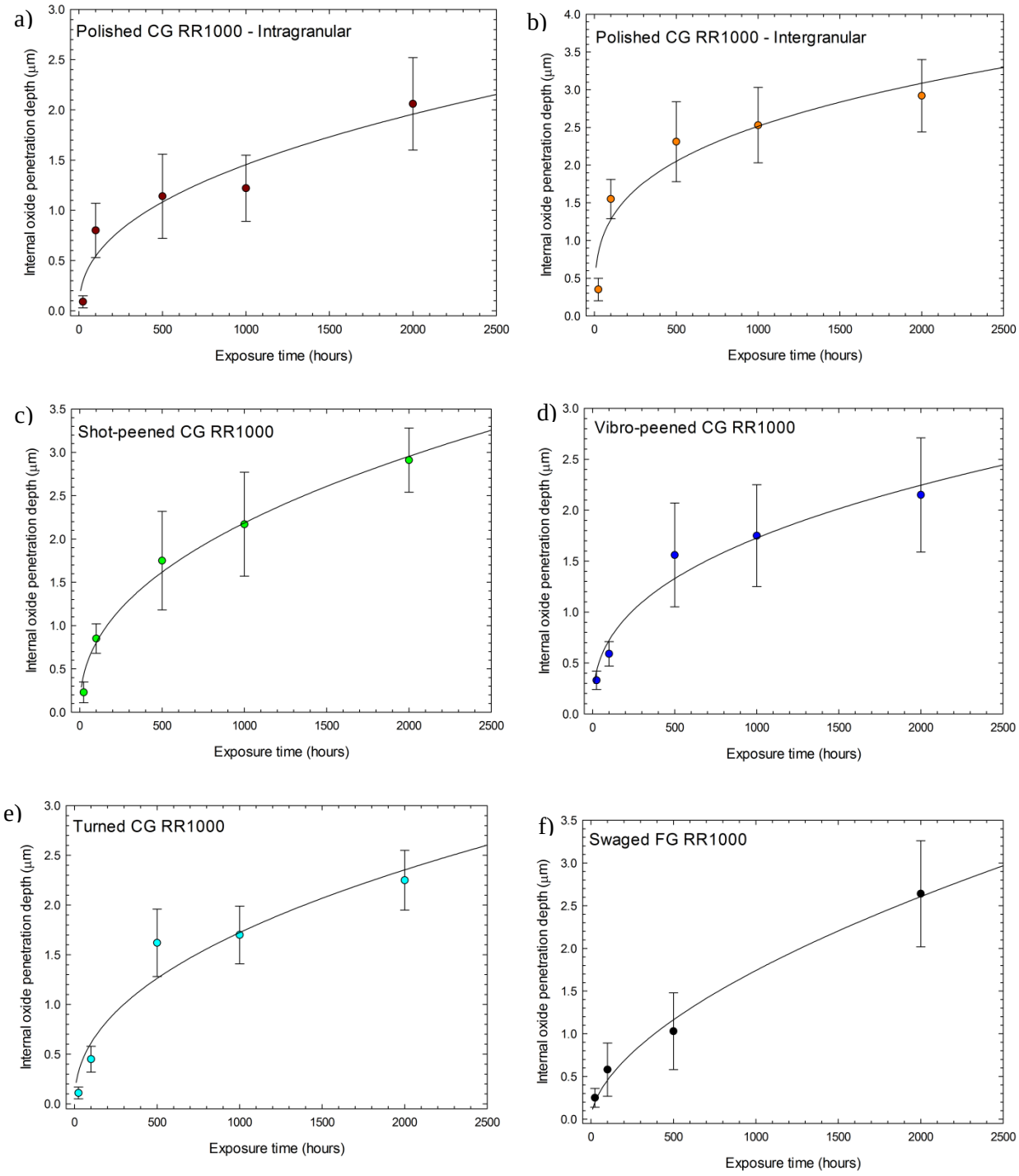

Figure 6-32: Plot of internal oxide penetration against time for a) intragranular polished condition, b) intergranular polished condition, c) shot-peened condition, d) vibro-peened condition, e) turned condition and f) swaged condition at 700°C. Best fit lines were produced using equation 6.11 and the corresponding values for n_{ioz} and k_{nl} in Table 6-X.

A one-way ANOVA with Tukey analysis was used to investigate if any significant differences ($p<0.05$) were found between the alumina penetration of the individual surface conditions when oxidised at 700°C for 2000 hours. The intragranular penetration of Al_2O_3 in the polished condition are significantly smaller than the intergranular Al_2O_3 intrusions in the polished condition as well in the Al_2O_3 intrusions in both the shot-peened and swaged conditions. The shot-peened and polished intergranular internal alumina penetrations are also significantly deeper than those in the swaged, vibro-peened and turned conditions and finally the swaged condition is significantly deeper than those in the vibro-peened and turned condition.

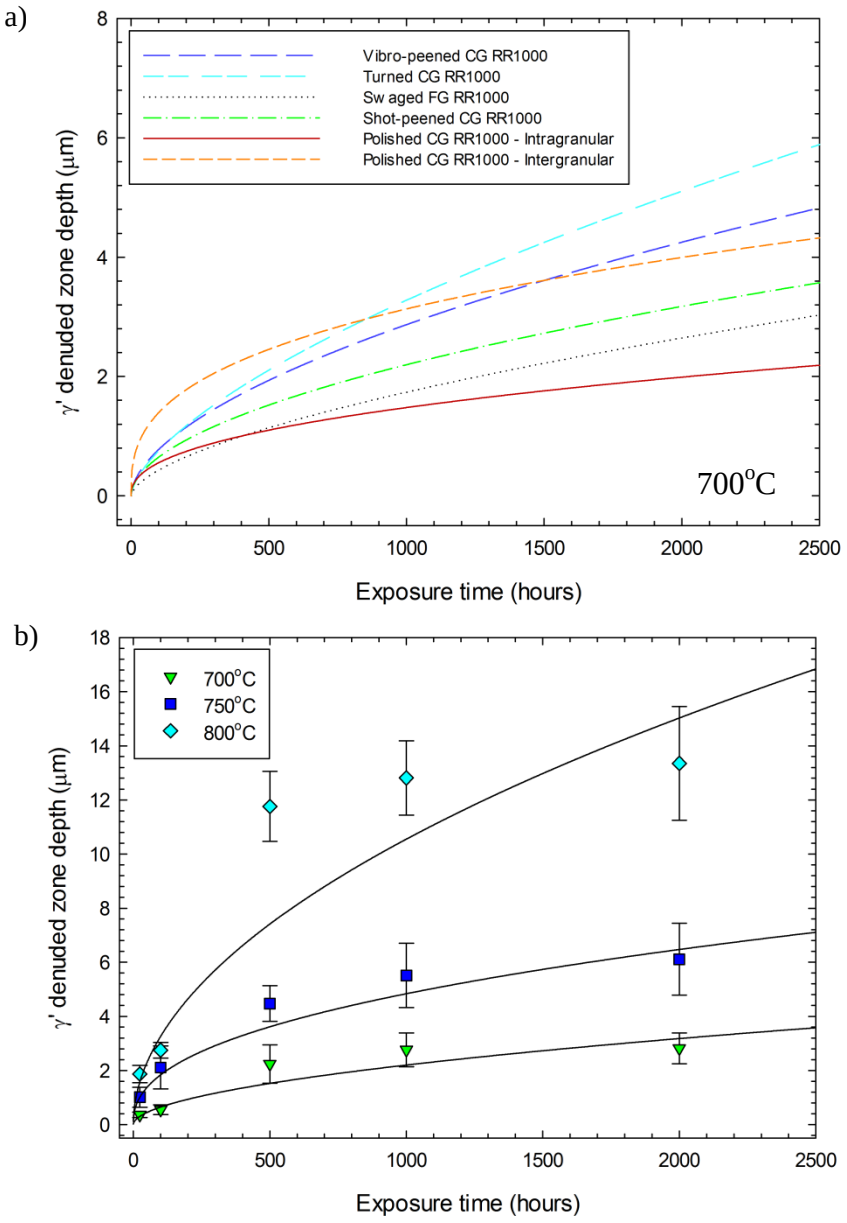

Figure 6-33: Plot of γ′ denuded zone depth against time for a) each surface condition tested at 700°C and b) for shot-peened CG RR1000 at 700-800°C. The lines in a) are produced using best fit kinetics.

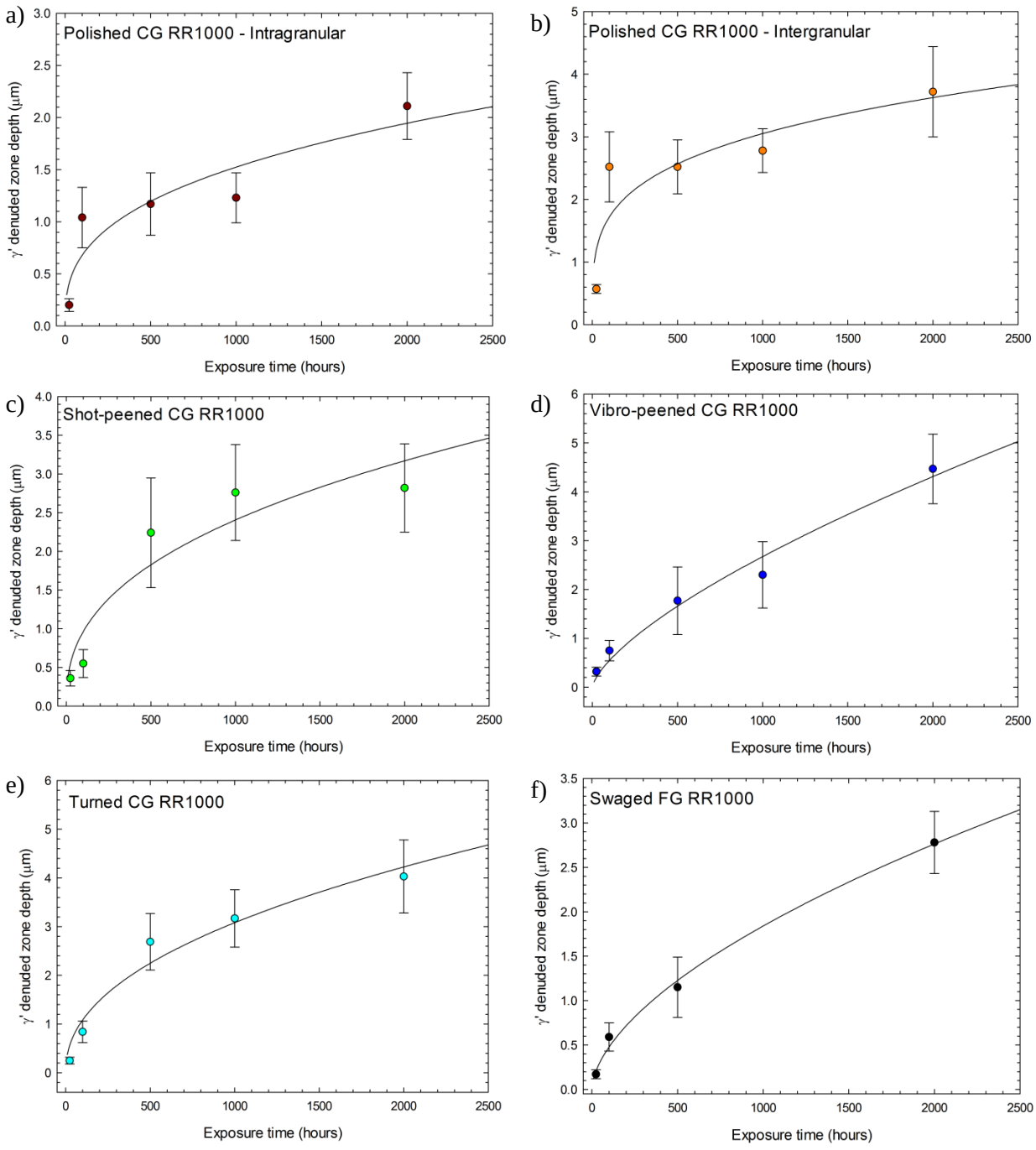

Figure 6-34: Plot of depth of the γ' denuded zone against time for a) intragranular polished condition, b) intergranular polished condition, c) shot-peened condition, d) vibro-peened condition, e) turned condition and f) swaged condition at 700°C. Best fit lines were produced using equation 6.11 and the corresponding values for n_{ioz} and k_{nl} in Table 6-X.

This trend is not repeated with the depth of the γ′ denuded zone at 700°C. Here, the vibro-peened condition and the turned condition show the largest γ′ denuded zones with the intragranular polished condition showing the smallest and acting as the lower bound (Figure 6-33 and Figure 6-34). This is supported by the significant differences ($P<0.05$) recorded in the depth of the γ′ denuded zone, using a one-way ANOVA with Tukey analysis, for all the conditions using the average measurement taken at an exposure time of 2000 hours. The vibro-peened and turned surface conditions have significantly deeper γ′ denuded zone than all the other conditions. The depth of the γ′ denuded zone in intragranular polished condition is significantly smaller than this zone in all the other conditions and the swaged and shot-peened surface conditions have γ′ denuded zone that are significantly smaller than those in the intergranular polished condition.

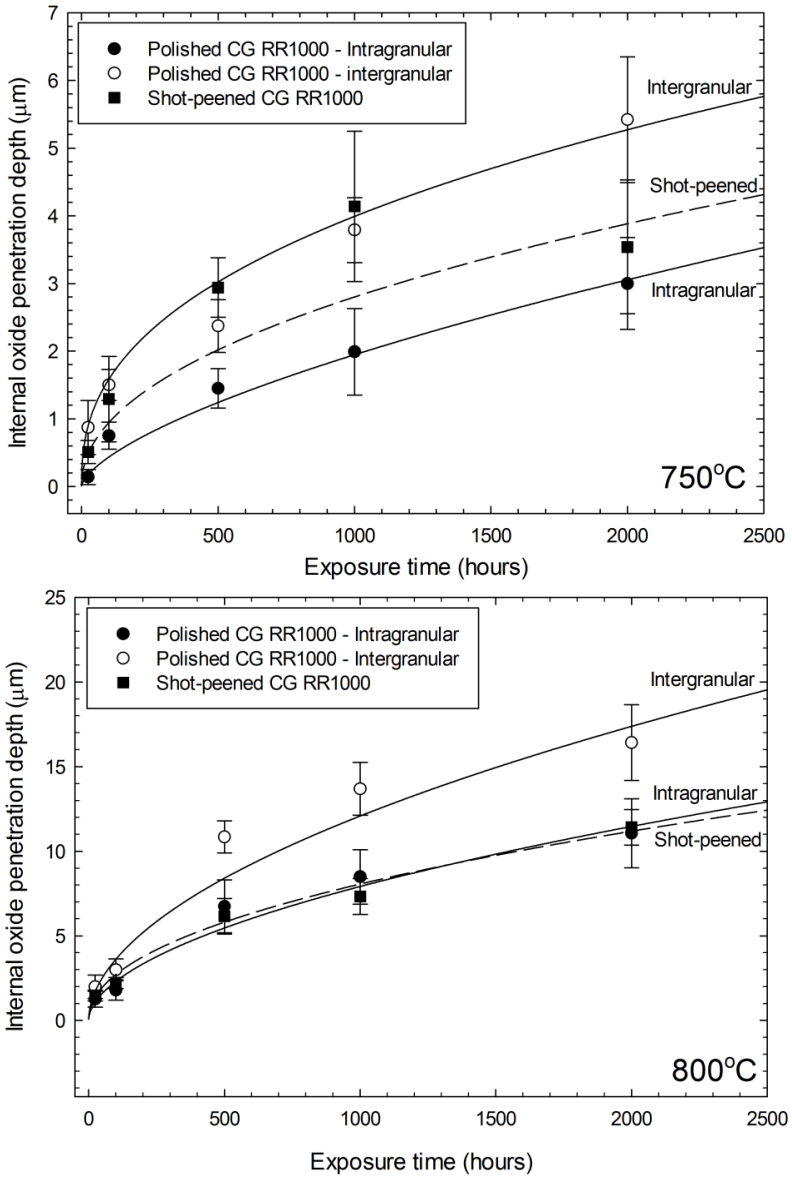

Figure 6-35: Plot of the depth of internal oxide penetrations against time for polished and shot-peened CG RR1000 at 750°C and 800°C. Best fit lines were produced using equation 6.11 with input values shown in Table 6-XIII.

Figure 6-35 shows that the depth of the internal oxide penetrations in the shot-peened condition falls within these for intergranular and the intragranular locations in the polished condition. At 700°C the shot-peened condition is almost the same as the intergranular intrusions, while at 750°C it falls directly in between the two and at 800°C it is almost the same as the intragranular intrusions. This illustrates that as the temperature increases the depth of penetration in the shot-peened condition increases at a lower rate than in the polished condition. The same effect is found in the depth of the γ′ denuded zone (Figure 6-36). It is likely that there is a larger volume of alumina in the shot-peened condition at 700 and 750°C, as while the intergranular penetrations in the polished condition are slightly larger, their infrequent nature would lead to a larger volume of alumina being present in the shot-peened condition. At 800°C there is likely to be a similar volume, as the shot-peened condition shows a similar internal oxide penetration depth to the intragranular penetrations, mirroring the mass gain results.

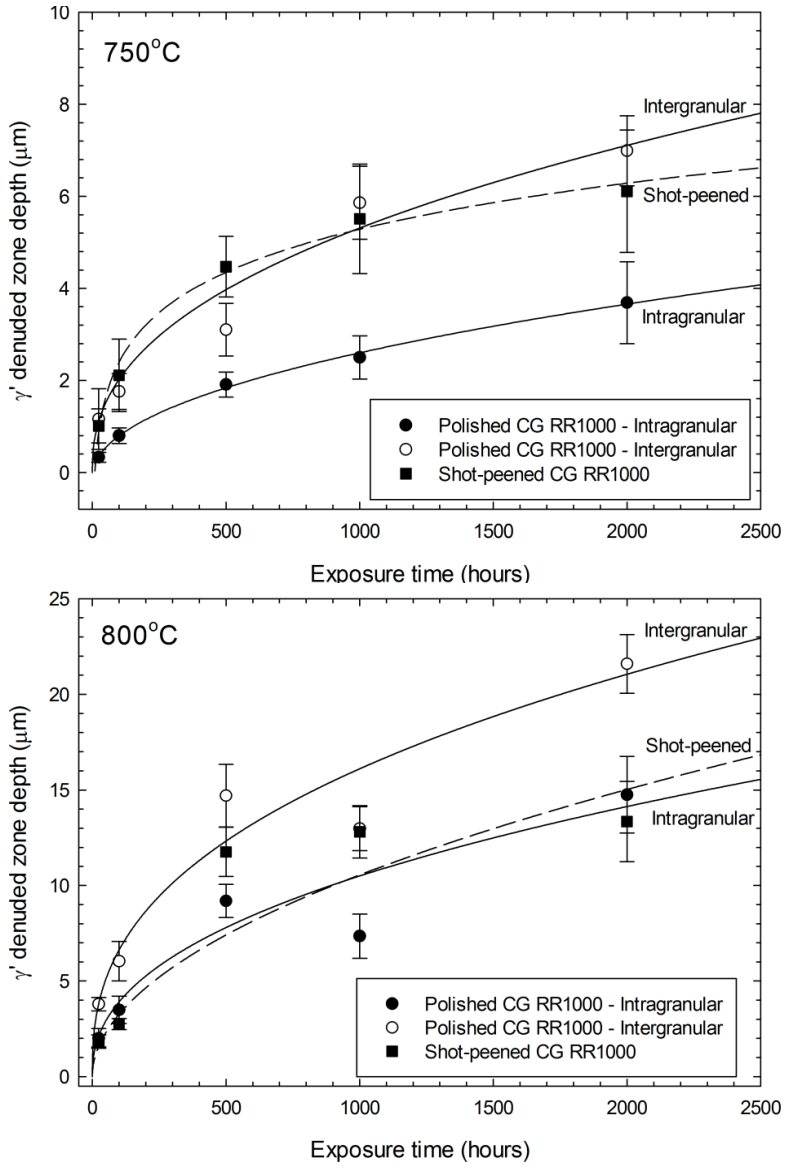

Figure 6-36: Plot of γ′ denuded zone depth against time for polished and shot-peened CG RR1000 at 750°C and 800°C. Best fit lines were produced using equation 6.11 with input values shown in Table 6-XIII.

High temperature kinetics for the internal oxide penetration depth, ℓ, can be approximated reasonably using the following equations:

$$\ell = [k_{n\ell}\, t]^{1/n_{ioz}} \tag{6.11}$$

where $k_{n\ell}$ are the appropriate growth rate constants for internal oxidation and n_{ioz} is the oxide growth regime. A similar approach can be performed for the γ′ denuded zone with the growth rate constant $k_{n\gamma}$. The growth kinetics in all cases, both the internal oxide penetration and the γ′ denuded zone can be approximated to parabolic behaviour (n=2). This can be shown for all conditions at 700°C in Table 6-IX and in Table 6-XIV for the shot-peened and the polished conditions at all test temperatures. The parabolic rate constants shown in Table 6-XV and Table 6-XVI report similar results to those discussed previously for the external oxide kinetics in this section, in that, ME3 has internal oxide growth kinetics that are greater at 700 and 750°C but at >800°C the kinetics of shot-peened CG RR1000 overtake those of ME3. The performance of similar Ni-based superalloy, ME3, improves relative to RR1000 as the temperature increases. A comparison cannot accurately be performed using the γ′ denuded zone depth because the study assumes cubic growth rather than the parabolic growth assumed here.

The parabolic rate constants (Table 6-IX) emulate the results discussed previously in this section and shown in Figure 6-31(a) and Figure 6-33(a). These values have been used to calculate the effect of surface roughness, cold work and residual stress on the internal oxidation kinetics, which is illustrated in Figure 6-37. There is no correlation with surface roughness, illustrating that it has no effect on the penetration depth of the internal oxide. A very small correlation with both residual stress and cold work was recorded, illustrating that the larger the percentage cold work the larger the internal oxide penetration growth rate. This is also the same with increasing compressive residual stress. A different effect might be recorded if the volume of internal oxide was calculated rather than the depth and would possibly allow the changes in morphology of the internal oxides to be quantified. Again it is unlikely that these factors work in isolation as they are interrelated and any cause of increased internal oxide growth rates could be due to a combination of all three.

Interestingly, the depth of the γ′ denuded, in Figure 6-38, zone shows a number of different trends with a reasonable correlation being found when comparing surface roughness with the parabolic rate constants (R^2 = 0.66). This illustrates that as the surface roughness increases so does the growth rate constants for the γ′ denuded zone. Furthermore no trends were found when comparing the residual stress (R^2=0.07) or the amount of cold work (R^2=0.08) unless the direction of the residual stress is removed i.e. whether it is compressive or tensile. Using the magnitude of the stress only, the trend

increases to an R^2 of 0.37, with the larger the stress the faster the kinetics. This is interesting as it shows significantly different results to the other surface conditions, where the amount of cold work has typically been the main correlating factor. It is possible that the depth of the γ′ denuded zone is related more closely to the volume of the internal oxide rather than the penetration depth and that a rougher surface may induce a larger volume of internal oxide to form. As stated before it is improbable that these factors are working in isolation as the change in kinetics in an alloy with the same composition is probably driven by the production of low energy diffusion pathways, which can be a by-product of all three factors, as the surface roughness, cold work and residual stress can easily be inter-related.

Table 6-XIII: Both exponent, n, and growth rate constants, k_n, for the internal oxide penetration and γ′ denuded zone of shot-peened CG RR1000 oxidised between 700-800°C.

Temperature	Shot-peened CG RR1000			
	Internal oxidised zone		γ' denuded zone	
	n_{ioz}	k_{nl} ($\mu m^n.s^{-1}$)	n_{dz}	$k_{n\gamma}$ ($\mu m^n.s^{-1}$)
700°C	1.8	$1.02x10^{-6}$	1.9	$1.23x10^{-6}$
750°C	2.1	$2.47x10^{-6}$	2.4	$1.18x10^{-5}$
800°C	2.1	$2.30x10^{-6}$	2.0	$2.82x10^{-5}$

The temperature dependence of the respective rate constants for the internally oxidised zone are shown in Figure 6-39 for all surface conditions tested. The activation energy for shot-peened CG RR1000 is significantly less that that recorded for either the intragranular or intergranular locations on polished CG RR1000 (Table 6-XVII), however it is very similar to ME3. While the activation energy is not a singly activated process, nevertheless it remains a useful means of predicting the temperature dependence of the shot-peened condition. An equation has been produced to describe the internal oxide penetration and γ′ denuded zone in the shot-peened CG RR1000 condition and is displayed below:

Internal oxide penetration kinetics

$$k_{p\ell} = 2.01x10^6 \exp\left[-\frac{229309}{8.314\,T}\right] \quad \mu m^2.s^{-1} \tag{6.12}$$

γ′ denuded zone kinetics

$$k_{py} = 4.34x10^8 \exp\left[-\frac{270453}{8.314\,T}\right] \quad \mu m^2.s^{-1} \tag{6.13}$$

Table 6-XIV: Best estimate values of the exponent for the internally oxidised zone (n_{ioz}) and the γ′ denuded zones (n_{dz}) for both polished and shot-peened CG RR1000.

	Shot-peened CG RR1000		Polished CG RR1000			
	Al_2O_3 penetrations	γ′ denuded zone	Al_2O_3 penetrations		γ′ denuded zone	
			Intragranular	Intergranular	Intragranular	Intergranular
700°C	1.81	1.88	1.84	2.42	2.34	2.84
750°C	2.12	2.38	1.53	2.49	1.85	2.38
800°C	2.11	1.96	1.86	1.91	2.33	2.59

Table 6-XV: Parabolic rate constants for the internal oxide and γ′ denuded zones for polished CG RR1000 (intragranularly and intergranularly) and for shot-peened CG RR1000.

	Shot-peened CG RR1000		Polished CG RR1000			
Units / $\mu m^2.s^{-1}$	Al_2O_3 penetrations	γ′ denuded zone	Al_2O_3 penetrations		γ′ denuded zone	
			Intragranular	Intergranular	Intragranular	Intergranular
700°C	$1.2x10^{-6}$	$1.4x10^{-6}$	$4.1x10^{-7}$	$1.1x10^{-6}$	$4.6x10^{-7}$	$1.6x10^{-6}$
750°C	$2.5x10^{-6}$	$6.1x10^{-6}$	$1.2x10^{-6}$	$4.0x10^{-6}$	$1.9x10^{-6}$	$7.2x10^{-6}$
800°C	$1.8x10^{-5}$	$3.1x10^{-5}$	$1.8x10^{-5}$	$4.2x10^{-5}$	$2.8x10^{-5}$	$6.4x10^{-5}$

Table 6-XVI: Parabolic and cubic rate constants for the increase in depth for both the internal oxide and the γ′ denuded zones, respectively, for Ni-based superalloy, ME3 [47].

	Al_2O_3 penetrations $\mu m^2.s^{-1}$	γ′ denuded zone $\mu m^3.s^{-1}$
704°C	$1.4x10^{-6}$	$5.3x10^{-7}$
760°C	$3.9x10^{-6}$	$2.1x10^{-6}$
815°C	$1.4x10^{-5}$	$1.4x10^{-5}$

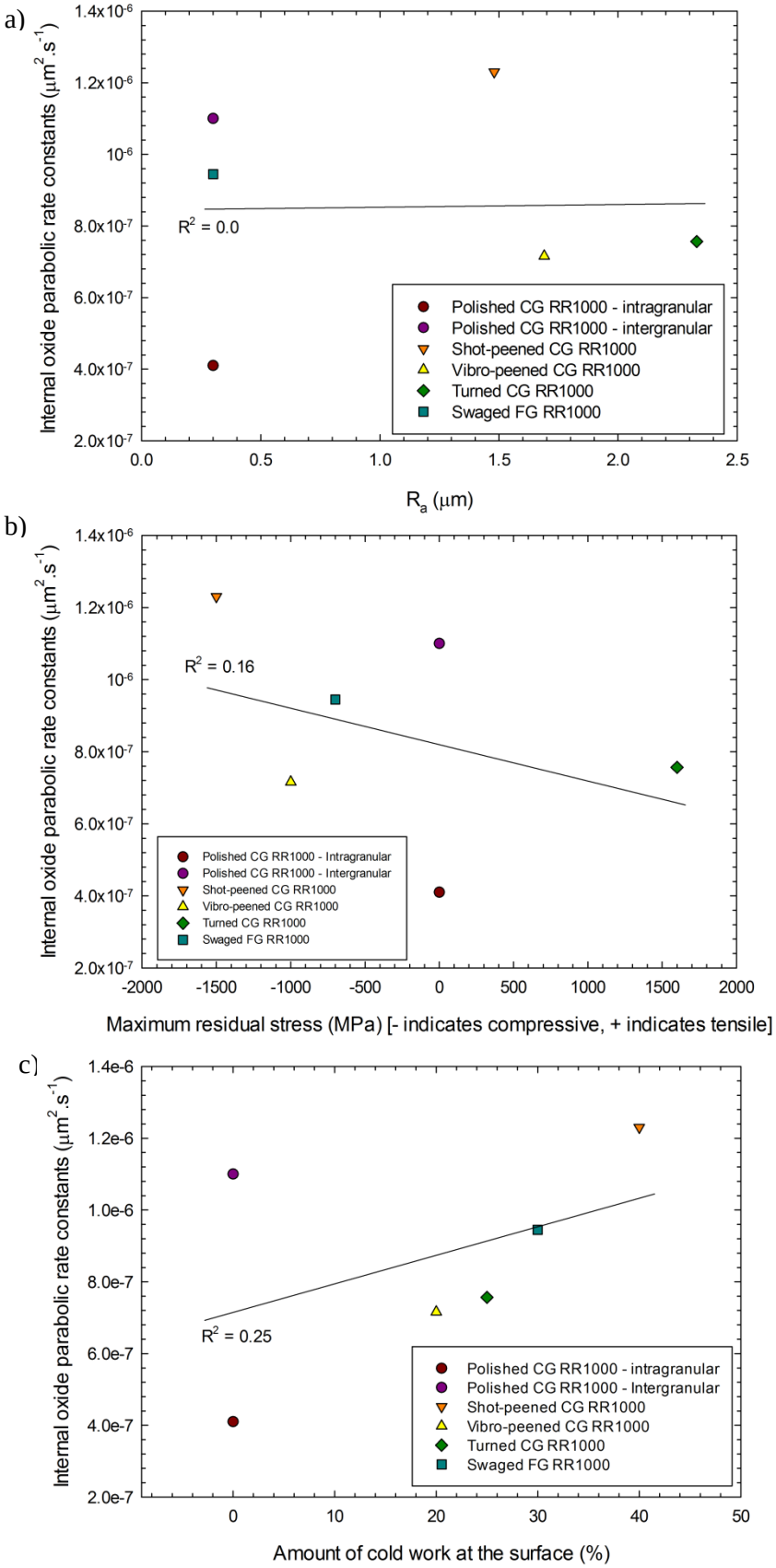

Figure 6-37: Plot of internal oxidation kinetics against a) surface roughness, b) residual stress and c) cold work for all the surface conditions tested at 700°C.

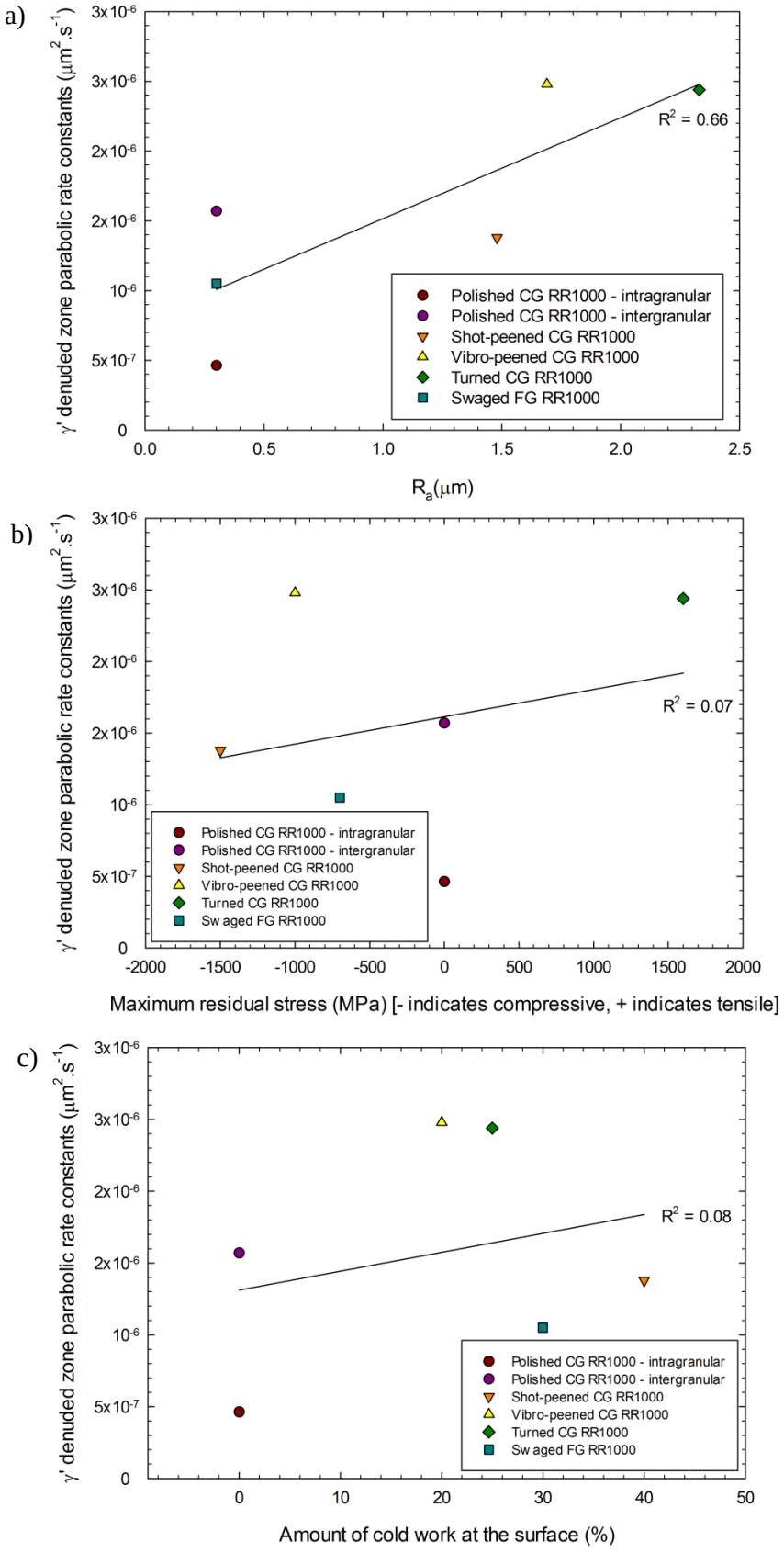

Figure 6-38: Plot of γ′ denuded zone kinetics against a) surface roughness, b) residual stress and c) cold work for all the surface conditions tested at 700°C.

Table 6-XVII: Activation energies (kJ.mol^{-1}) of shot-peened CG RR1000, polished CG RR1000 and ME3 for the internal oxidised zone and the γ′ denuded zone.

Shot-peened CG RR1000		Polished CG RR1000			
Al_2O_3 penetrations	γ′ denuded zone	Al_2O_3 penetrations		γ′ denuded zone	
		Intragranular	Intergranular	Intragranular	Intergranular
229 kJ.mol^{-1}	270 kJ.mol^{-1}	325 kJ.mol^{-1}	314 kJ.mol^{-1}	354 kJ.mol^{-1}	321 kJ.mol^{-1}

ME3[47]	
Al_2O_3 penetrations	γ′ denuded zone
218 (±18) kJ.mol^{-1}	285 (±35) kJ.mol^{-1}

The rate controlling process for internal oxidation and γ′ particle dissolution is complex. Oxygen diffusion through the external chromia scale and through the IOZ, diffusion of Al to the reaction front and dissolution of γ′ particles are all possible rate controlling processes. The activation energy of oxygen diffusion through Ni is between 108-240 kJ.mol^{-1} and the diffusion of Al through Ni is 266 kJ.mol^{-1} [185-187]. Both these are reasonable for the rate controlling processes in shot-peened RR1000. It is likely that the values for oxygen diffusion are lower than those found in this alloy because oxygen has to diffuse through a protective chromia scale. It is possible that different rate controlling processes are occurring for the formation and growth of the internal oxide and the γ′ denuded zone. Oxygen diffusion or diffusion of Al, to the internal oxidation reaction front is likely to be controlling the rate of internal oxidation and further analysis is required to illicit the correct mechanism. It is possible that the diffusion of Al to the internal reaction front induces the dissolution of the γ′ particles and therefore controls the γ′ denuded zone growth.

As expected the parabolic rate constants for the γ′ denuded zone are larger than the corresponding rate constants for the internally oxidised zone. Table 6-XVIII shows the percentage that the γ′ denuded zone is deeper than the internally oxidised zone. This was performed using the square root of the ratio of the rate constants in Table 6-IX and indicates that the γ′ denuded zone is considerably ahead of the internally oxidised zone. This is not unexpected since the dissolution of γ′ particles (nominally Ni_3Al) occurs due to the depletion of aluminium in the near surface region from the formation of internal oxides. The vibro-peened and turned surface conditions show a much larger gap between the penetration depth of the internally oxidised zone and the γ′ denuded zone. This could provide an indication of the volume of the internal oxide that is being produced rather than the penetration depth. The formation of a γ′ denuded zone is driven by depletion of aluminium in the near surface region

which is determined by the formation of the internal oxide. Therefore more internal oxide (not necessarily deeper penetrations) would in theory lead to more dissolution of γ′ particles and a deeper γ′ denuded zone. Additional work measuring the volume of the internal oxide is required to confirm this.

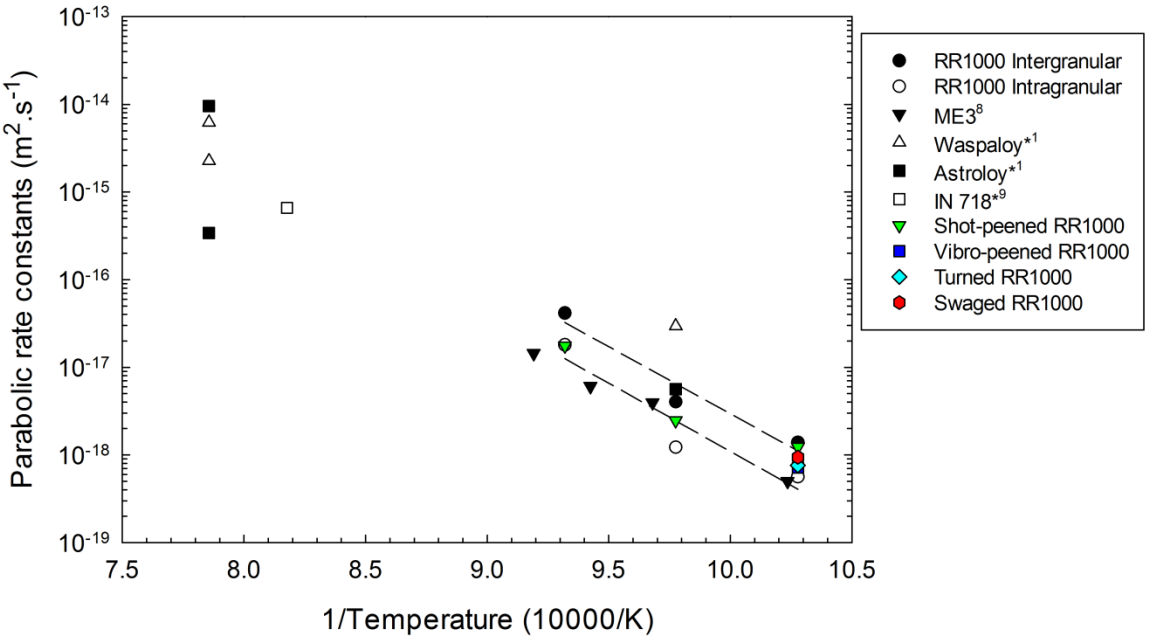

Figure 6-39: Arrhenius plot of internal oxide penetration for all the surface conditions tested here along with several other similar Ni-based superalloys for comparison: some of the values were recorded from single measurements taken from the literature and so are recorded as instantaneous parabolic rate constants [47, 104, 114].

Table 6-XVIII: Percentage the parabolic rate constants for the γ′ denuded zone are larger than the parabolic rate constants for the internal oxidised zone using the parabolic rate constants.

	Percentage γ′ denuded zone is ahead of internal oxidised zone
CG RR1000 – Intragranular	6%
CG RR1000 – Intergranular	23%
Shot-peened CG RR1000	5.5%
Vibro-peened CG RR1000	86%
Turned CG RR1000	79%
Swaged FG RR1000	5.4%

6.2.9 Total oxidation damage kinetics

The kinetics of growth of both the external oxide and the γ′ denuded zone are combined to give the total oxidation damage on all the surface conditions. Figure 6-40 shows that as the exposure temperature and time increases so does the magnitude of the oxidation damage. This is not unexpected as the same was shown in the polished CG RR1000 condition in Chapter 5 and since it is a composition of the damages discussed earlier which show a similar pattern.

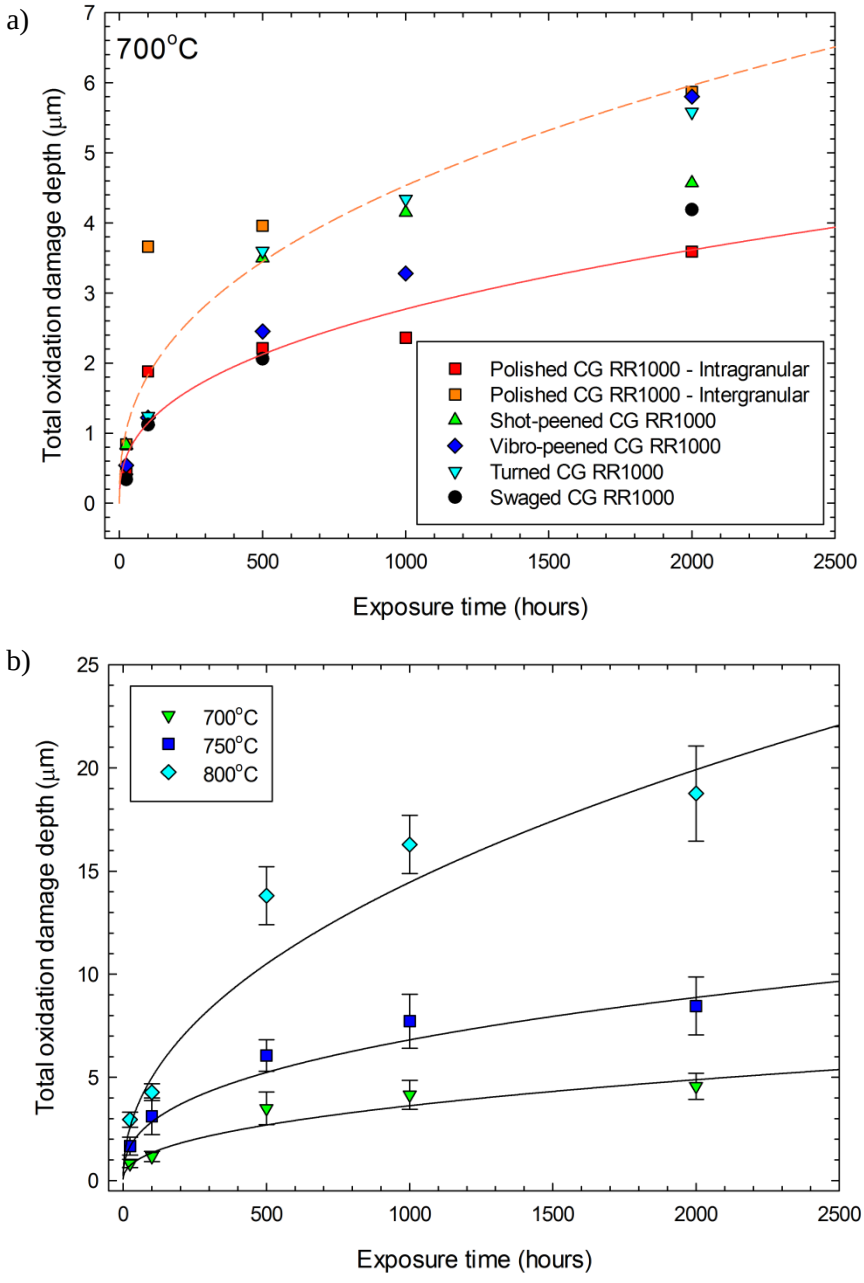

Figure 6-40: Plot of total oxide damage depth against time for each temperature tested for the shot-peened condition and at 700°C for the others (polished, turned, vibro-peened and swaged). Best fit lines were produced using equation 6.14 and the values in Table 6-XIX and Table 6-XX.

The total oxidation damage depth at 700°C for all the surface conditions is shown in Figure 6-40(a) and clearly shows that all the conditions fit within the intragranular and intergranular locations on the polished condition, with the vibro-peened and turned conditions lying near the intergranular polished condition at the longer time periods. This is not surprising since the total oxidation damage is dominated by the γ′ denuded zone, which is much larger than the external oxide thickness in all surface conditions.

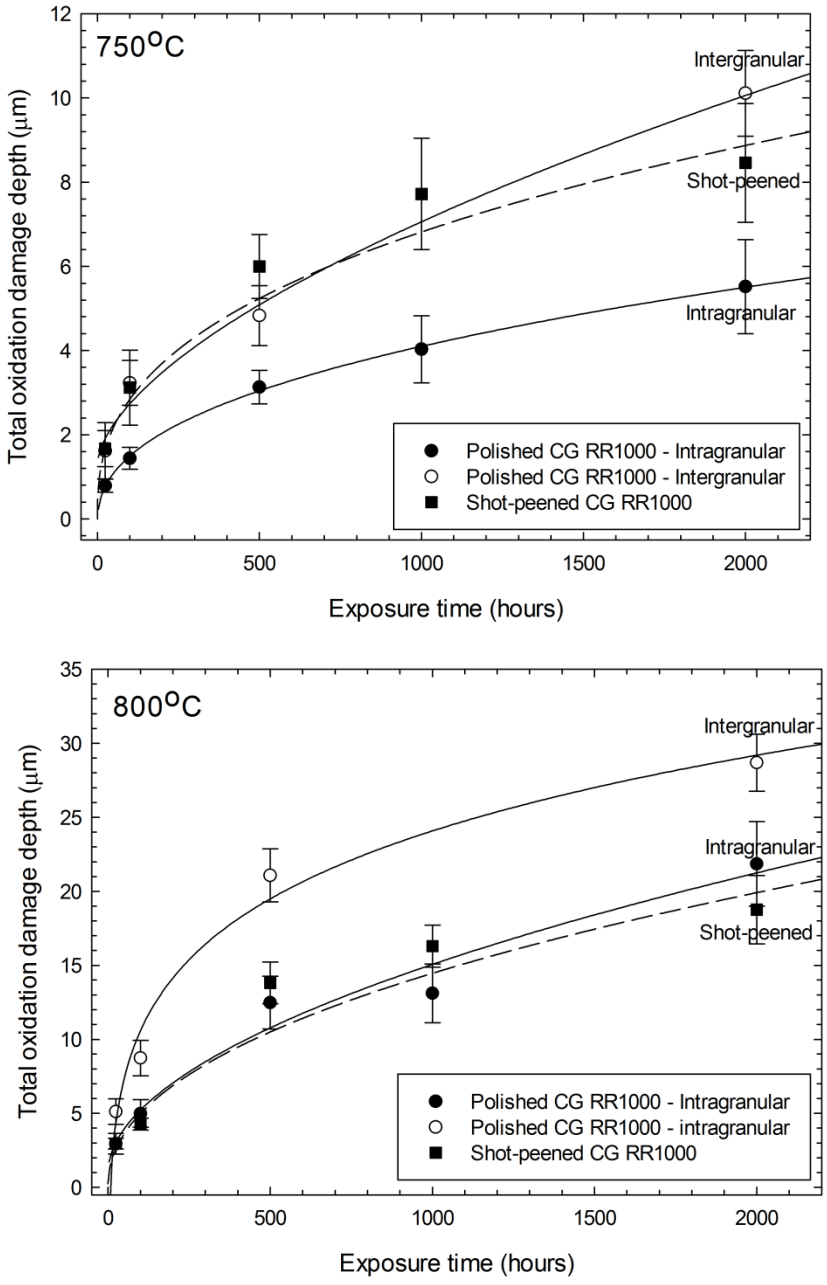

Figure 6-41: Plot of total oxide damage depth at both intragranular and intergranular regions in the polished CG RR1000 condition and in shot-peened CG RR1000 (±1 standard deviation).

Figure 6-41 shows that the total oxidation damage for the shot-peened surface condition falls within the intergranular and intragranular locations in the polished condition. At 750°C the shot-peened condition is almost the same as the intergranular oxidation damage, while at 800°C it overlaps the intragranular oxidation damage. This illustrates that as the temperature increases the depth of the oxidation damage increases at a lower rate relative to the polished condition. This is not unexpected as a similar effect is seen in both the external chromia oxide and the γ′ denuded zone of which the total oxidation damage is comprised of. The high temperature kinetics for the total oxidation damage (external oxide + γ′ denuded zone), τ, for all the surface conditions tested can be approximated using the following equations respectively:

$$\tau = [k_{n\tau}\, t]^{1/n_{\tau o}} \tag{6.14}$$

where $k_{n\tau}$ is the appropriate growth rate constant for total oxidation damage, $n_{\tau o}$ is the oxide growth regime and can be determined by plotting log τ against log of time. The values for the determination of the exponent, along with the parabolic growth constants are shown in Table 6-XIX and Table 6-XX. The parabolic rate constants illustrate the same thing as Figure 6-40(a) and Figure 6-41 with at 700°C the polished condition illustrating the largest and smallest growth, for the intergranular and intragranular penetrations respectively. The shot-peened condition at 750°C showing growth kinetics close to those of the intergranular polished condition and at 800°C close to the intragranular polished condition. This mirrors the mass gain results described earlier.

Table 6-XIX: Exponent, $n_{\tau o}$, actual growth rate constants, $k_{n\tau}$, and parabolic growth rate constants for total oxidation damage, $k_{n\tau}$, at 700°C

		Total damage oxidation damage		
		$n_{\tau o}$	$k_{p\tau}$ ($\mu m^2.s^{-1}$)	$k_{n\tau}$ ($\mu m^n.s^{-1}$)
CG RR1000	**Intragranular**	2.60	$1.39x10^{-6}$	$3.95x10^{-6}$
	Intergranular	2.53	$5.09x10^{-6}$	$1.28x10^{-5}$
Shot-Peened CG RR1000		2.33	$3.44x10^{-6}$	$5.56x10^{-6}$
Vibro-peened CG RR1000		1.96	$4.29x10^{-6}$	$1.68x10^{-6}$
Turned CG RR1000		1.83	$4.63x10^{-6}$	$1.48x10^{-6}$
Swaged FG RR1000		1.60	$2.43x10^{-6}$	$1.14x10^{-6}$

Table 6-XX: Both exponent, $n_{\tau o}$, and parabolic growth rate constants, $k_{p\tau}$, for the total oxidation damage depth of shot-peened CG RR1000 oxidised between 700-800°C.

Temperature	Shot-peened CG RR1000			Polished CG RR1000			
				Intragranular		Intergranular	
	$n_{\tau o}$	$k_{p\tau}$ ($\mu m^2.s^{-1}$)	$k_{n\tau}$ ($\mu m^n.s^{-1}$)	$n_{\tau o}$	$k_{p\tau}$ ($\mu m^2.s^{-1}$)	$n_{\tau o}$	$k_{p\tau}$ ($\mu m^2.s^{-1}$)
700°C	2.33	$3.44x10^{-6}$	$5.56x10^{-6}$	2.60	$1.39x10^{-6}$	2.53	$5.09x10^{-6}$
750°C	2.63	$1.17x10^{-5}$	$4.34x10^{-5}$	2.26	$4.35x10^{-6}$	2.53	$1.41x10^{-5}$
800°C	2.16	$5.62x10^{-5}$	$9.01x10^{-5}$	2.23	$6.37x10^{-5}$	2.14	$1.22x10^{-4}$

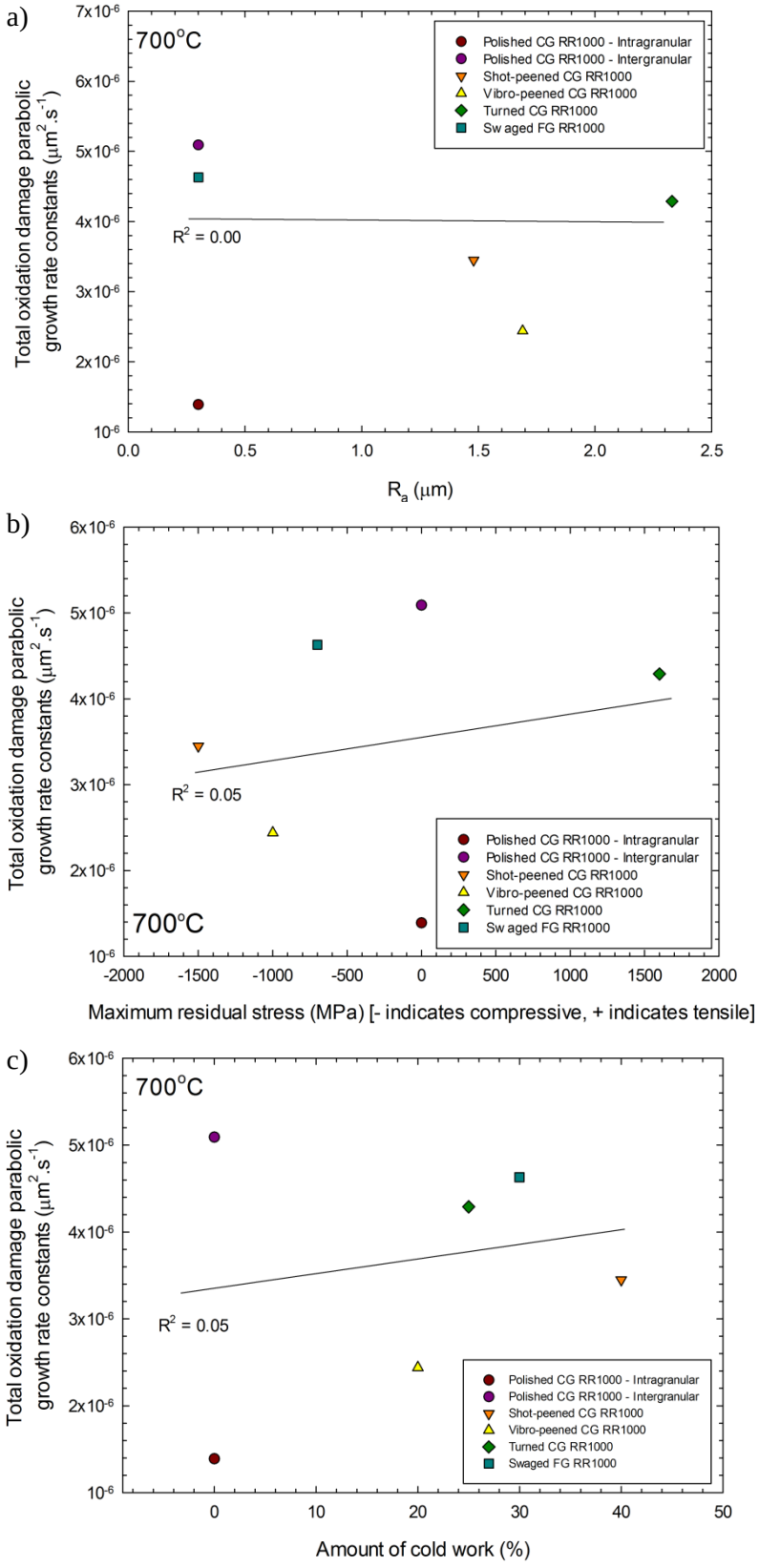

Figure 6-42: Plot of total oxidation damage kinetics against a) surface roughness, b) residual stress and c) cold work for all the surface conditions tested at 700°C.

The parabolic rates constants have been plotted against the amount of surface roughness, cold work and residual stress in each condition and have been used to calculate the effect of surface roughness, cold work and residual stress and are illustrated in Figure 6-42. In all cases no correlation has been found, showing that none of these significantly affect the parabolic rate constants for total oxidation damage.

Table 6-XXI: Activation energies of (kJ.mol^{-1}) of shot-peened CG RR1000, and polished CG RR1000 for the total oxidation damage.

Shot-peened CG RR1000	**Polished CG RR1000**	
	Intragranular	Intergranular
242 kJ.mol^{-1}	329 kJ.mol^{-1}	274 kJ.mol^{-1}

The activation energy for shot-peened CG RR1000 is significantly lower than the polished condition in either the intragranular or intergranular locations (Table 6-XXI). The term activation energy is not strictly accurate as a single activated process is not occurring but it remains a useful means of predicting the temperature dependence of the total oxidation damage. An equation has been produced to describe the total oxidation damage in the shot-peened CG RR1000 condition and is displayed below:

$$k_{p\tau} = 3.07x10^{7} \exp\left[-\frac{241830}{8.314\,T}\right] \quad \mu m^{2}\,.\,s^{-1} \tag{6.15}$$

This can be used to predict the kinetics of the total oxidation damage at any temperature within the temperature range tested (700^{o}C-800^{o}C), allowing the quantification of the depth of oxide damage produced by a high temperature exposure.

The activation energies for oxidation in RR1000 with and without shot-peening can be related to the rate-controlling processes for oxidation. The rate controlling process is complex and is described in more detail in Chapter 5, as similar rate controlling processes are expected for each component of oxidation damage here. Slightly lower activation energies might be expected in the shot-peened condition, because this surface treatment increases dislocation density in the near surface region and induces recrystallisation during oxidation. This would enhance diffusion sub-surface through creating more short circuit diffusion pathways.

6.2.10 Grain boundary phase dissolution zone

As described in Chapter 5, with the polished CG RR1000 condition, the deepest form of oxidation damage can be considered to be the dissolution of grain boundary phases. This is the case here with all the surface conditions. MC carbides reside on the grain boundaries of all the surface conditions (Figure 6-4) and these decompose (Equation 5.20 and 5.21) to form Cr-Mo rich phases, either sigma phase $(Ni\text{-}Co)_x(Cr,Mo)_y$ or $(Cr,Mo)_{23}C_6$ carbides. At 700°C these phases are most likely $(Cr, Mo)_{23}C_6$ carbides, as sigma phase would not be expected to form in large quantities below 800°C in Ni-based superalloys with similar compositions to CG RR1000 [172]. The dissolution of these carbides is likely to be caused by the depletion of chromium underneath the external chromia scale. It is also important to note that the comparison with ME3 is performed at a slightly different time and temperature with ME3 being oxidised for 2020 hours at 704°C instead of 2000 hours at 700°C used in this study.

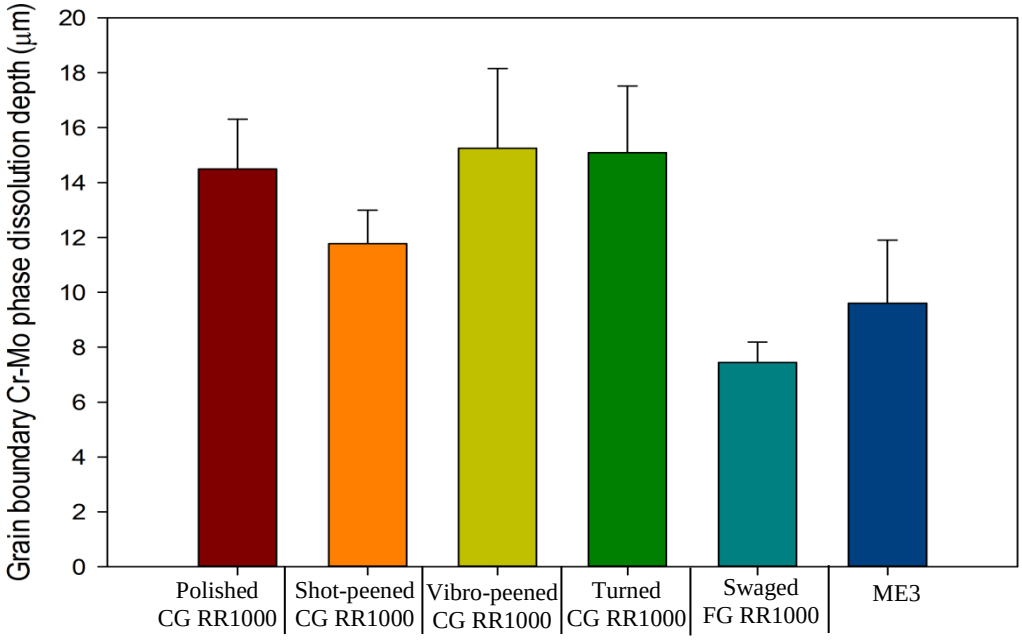

Figure 6-43: Comparison of the carbide dissolution depth for each of the surface conditions tested when oxidised at 700°C for 2000 hours. The ME3 data were taken from [47].

Significant differences in the depth of dissolution zone between the individual surface conditions were checked for, using a one-way ANOVA with Tukey analysis. It was found that at 2000 hours the measurements for polished, vibro-peened and turned conditions are significantly larger ($p<0.05$) than the shot-peened and swaged condition, with the swaged condition also being significantly smaller than the shot-peened condition. This is of no great surprise because Figure 6-43 and Figure 6-44 show that those conditions with smaller grain sizes have considerably smaller carbide dissolution depths. Figure 6-43 compares the depth of the carbide dissolution region in all surface conditions when oxidised at 700°C for 2000 hours, with the vibro-peened condition displaying the largest depth of dissolution region and the swaged FG RR1000 condition the smallest (Figure 6-43). The dissolution

region in all these coarse-grained alloys with and without surface modification is significantly larger than that found in ME3 with a finer grain size 27-30 μm [47]. In the swaged FG RR1000 condition (4-6 μm) the grain boundary phase dissolution depth is smaller than ME3 and follows the trend that the finer the grain size the smaller the dissolution depth (Figure 6-44). Surprisingly the amount of residual stress, surface roughness or cold work has little effect on the depth of grain boundary phase dissolution, with the largest effect coming from the change in grain size. This is not entirely to be unexpected since the frequency of the grain boundaries and number of grain boundary phases is likely to be larger with a fine grain structure, leading to a larger reservoir of chromium on the grain boundaries in the near surface region. Thus, as chromium depletion in the formation of chromia external oxide is the driving force for dissolution of these phases, a greater number of grain boundary phases have to dissolve to achieve the same overall dissolution depth [191].

The following equation can be used to calculate the expected carbide dissolution depth at 700°C for an exposure time of 2000 hours depending on the average grain size of the chromia forming Ni-based superalloy:

$$C_{dr} = 0.201(g) + 5.80 \quad \mu m \tag{6.16}$$

where C_{dr} is the carbide dissolution depth and g is the average grain size of the alloy.

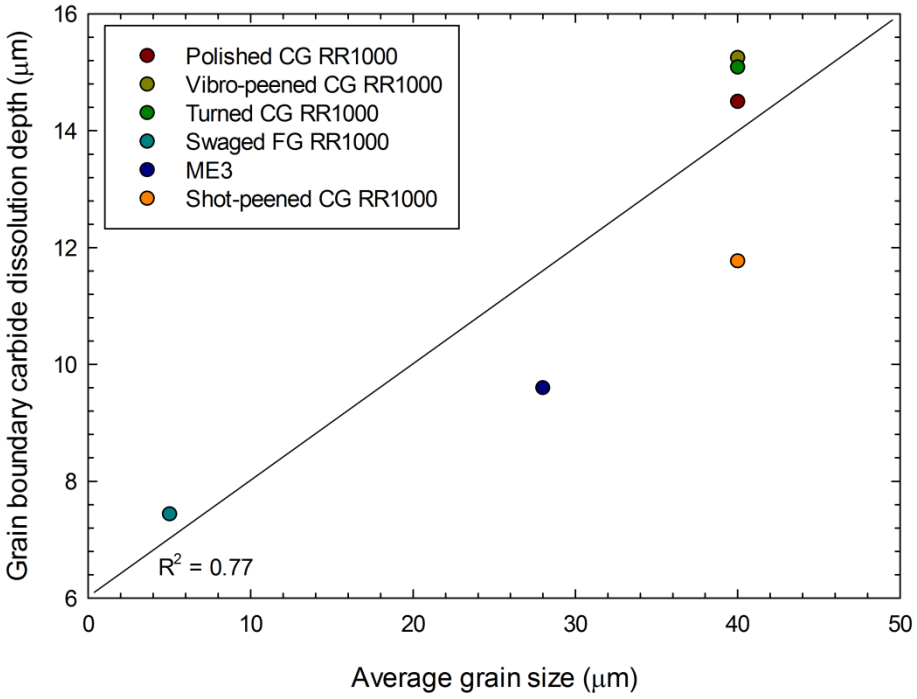

Figure 6-44: Graph illustrating the effect of grain size on the depth of carbide dissolution when oxidised at 700°C for 2000 hours in the conditions used here and 704°C and 2020 hours in ME3 [47].

While the degree of cold work or residual stress does not affect the depth of the carbide dissolution region the morphology of the carbides does change in the swaged and shot-peened condition, with $M_{23}C_6$ carbides found on the grain boundaries as well as within the grains, along slip bands. The dissolution of carbides due to the depletion of chromium in the near surface region leads to a large amount of carbon being released into solution. A diffusion gradient into the centre of the alloy is produced and the slip bands act as nucleation sites for $M_{23}C_6$ formation below the dissolution region. These conditions display the largest amount of deformation in the microstructure giving a potential reason why it only occurs in the swaged and shot-peened conditions. The formation of a higher percentage of carbides underneath a carbide dissolution region has been described previously in the literature [62, 63]. This is one reason why the shot-peened condition shows a significantly lower carbide dissolution region than the other CG RR1000 surface conditions. The fit of the linear regression between the carbide dissolution depth and the alloy grain size can be improved with the removal of the shot-peened condition (R^2 = 0.94 compared with 0.77).

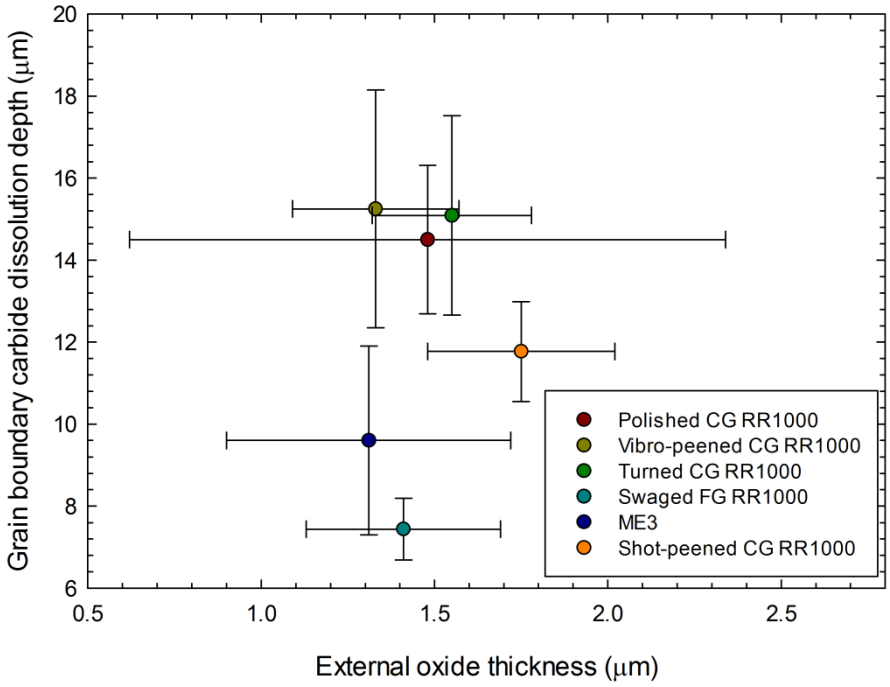

Figure 6-45: Graph displaying how the carbide dissolution depth is affected by the external chromia oxide thickness when oxidised at 700°C for 2000 hours in the conditions used here and 704°C and 2020 hours in ME3 [47].

Figure 6-45 illustrates that the depth of dissolution is not related to the thickness of the external chromia scale, which in itself might be surprising as with a thicker chromia oxide scale it might be expected to see a larger depletion in chromium and therefore a deeper region of carbide dissolution. In this case, it is not surprising as we are sampling several surface conditions which when oxidised

produce external oxide thicknesses which are very similar (1.3-1.7 μm) and therefore the change in chromium depletion would be negligible.

A more detailed analysis is required at several temperatures and exposure times to allow detailed analysis of the kinetics of formation and dissolution of these grain boundary phases. Additionally TEM analysis is required to confirm whether the exact structure of the grain boundary phase dissolving is a carbide or sigma phase, while $M_{23}C_6$ carbides are expected, WDS analysis on an SEM in Chapter 5 was not conclusive.

6.3 Summary and Conclusions

Microstructural characterisation, oxidation kinetics and oxidation damage of the Ni-based superalloy, RR1000 with different surface modifications: Shot-peening, Vibro-peening, Turning and Swaging, has been comprehensively studied through the use of mass gain (shot-peened only) and metallographic measurements (all conditions). This was performed for an exposure time of up to 2000 hours at 700^{o}C in all surface conditions and 700-800^{o}C in the shot-peened condition. The following conclusions can be made:

- A comparison between the different as-received surface modifications has been performed, with respect to surface roughness, microhardness, microstructure and amount of residual stress and cold work. Most surface modifications significantly increase the surface roughness of the alloy although vibro-peening seems not to affect the roughness of the underlying surface and so the pre-vibro-peening surface is important. This is not the case in the other conditions. All the surface treatments also induce significant but different amounts of residual stress and cold work into the near surface region. The swaged condition is the most aggressive approach with the specimen demonstrating a uniform increase in residual stress and cold work throughout the whole cross-section of the specimen. Shot-peening, turning and swaging cause a shallow region of distorted secondary γ′ particles directly beneath the surface. Furthermore a number of slip bands are found within the grains throughout the swaged specimen, but otherwise the microstructure is unaffected, with the grain size being maintained. The grain size is also maintained in the other surface treatments.

- The oxidation kinetics of shot-peened and polished CG RR1000 are similar, with shot-peening having an adverse effect on mass gain kinetics at both 700^{o}C and 750^{o}C but having no significant effect at 800^{o}C. Shot-peening provides short circuit diffusion pathways for diffusion of not only chromium but also titanium and aluminium accounting for higher mass gains than the polished condition. An activation energy of 302 kJ.mol^{-1} was recorded over a

temperature range of 700-800^{o}C and this compares well with the polished condition (301 kJ.mol^{-1}) and a similar Ni-based superalloy, ME3.

- In all conditions, the composition of the oxide formed is similar and in all cases exhibits an external oxide scale of TiO_2 and Cr_2O_3, as well as an extensive internal oxidation zone of alumina. Each surface condition causes the internal oxide to precipitate in a different morphology. Beneath this the formation of TiN occurs in the shot-peened condition at prolonged exposure times (>1000 hours) at 750^{o}C or at 800^{o}C. A significant γ′ denuded zone is present beneath the internal oxides. This follows the contours of the internal oxides. Within the γ′ denuded zone in the shot-peened condition recrystallised grains (0.6 - 2.5 μm) are formed. This is caused by a combination of deformation and elemental depletion in the near surface region along with elevated temperature. The grain boundaries of the small recrystallised grains form shot-circuit diffusion pathways within this region. Forming the deepest aspect of the oxidation damage is a region depleted of grain boundary Cr-Mo rich phases, assumed to be $M_{23}C_6$ carbides. Finally, at 800^{o}C in the shot-peened condition the formation of (Ta, Ti)O_2 occurs on the external oxide/alloy interface. This precipitates in smaller amounts than in the polished condition.

- The growth of the external oxide scale was found to be the lowest in the vibro-peened surface condition with the shot-peened condition forming the upper bound and all the other surface conditions tested falling in between. The external oxide growth in the shot-peened condition is significantly larger than the polished condition at 700 and 750^{o}C, while at 800^{o}C it switches to being significantly lower ($p<0.05$). In all surface conditions the oxide growth was larger than pure chromia formation and a mechanism by which the chromia scale is doped with Ti is provided. Additionally an equation has been produced to describe the temperature dependence of the external oxide growth for the shot-peened condition. The amount of cold work present shows a small correlation ($R^2=0.36$) with the external oxidation kinetics. Further work is required to expand on this to investigate whether this weak trend is correct and the amount of cold work may be the driving force of the change in growth kinetics.

- The growth of the internal oxidised zone and the γ′ denuded zone has been extensively studied and can be approximated to parabolic behaviour. In the internally oxidised zone the same trend is seen as the external oxide, with shot-peened and the intergranular polished condition being the upper bounds and the intragranular polished condition being the lower bound. This changes with the γ′ denuded zone, with the vibro-peened and turned surface conditions having the deepest penetration. The vibro-peened and turned surface conditions

show a much larger gap between the internally oxidised zone and the γ′ denuded zone, than the other conditions. The volume of the internal oxide rather than the penetration depth could be driving the γ′ denuded zone depth. The effect of cold work, residual stress and surface roughness was investigated without finding any strong correlations. Equations to describe the development of the internally oxidised zone and γ′ denuded zone in the shot-peened condition have been produced.

- The grain size of the alloy seems to affect the carbide dissolution depth, as the frequency of the grain boundaries and number of grain boundary phases is likely to be larger with a fine grain structure, leading to a larger reservoir of chromium on the grain boundaries in the near surface region. Thus, as chromium depletion in the formation of the chromia external oxide is the driving force for dissolution of these phases, a greater number of grain boundary phases have to dissolve to achieve the same overall dissolution depth. An equation has been produced to describe the effect at 700^{o}C for an exposure time of 2000 hours. The degree of cold work does not have an effect on the dissolution depth, although it does affect the morphology of the carbides beneath the region of dissolution, with carbides forming on both the grain boundaries and slip bands in the shot-peened and swaged conditions.

Chapter 7 – Use of Focussed Ion Beam Microscopy as a Technique for Characterising Oxidation Damage

7.1 Introduction

FIB sample preparation is now commonly used to examine cross-sections to establish the near-surface microstructure, without time-consuming metallographic procedures, and is particularly advantageous for samples with brittle surface layers such as oxides. Recently, this technique has been used to claim [6-8] that sub-surface voids occur as a consequence of high temperature oxidation, which may or may not be associated with alumina intrusions on an advanced Ni-based superalloy (Figure 7-1). It has been previously well established that chromia-forming Ni-Cr-Al alloys [86] and advanced Ni-based superalloys [104, 114, 115, 193] can form sub-surface alumina intrusions during high temperature exposure. These observations were obtained using conventional metallographic preparation [104, 115, 193] and conflict with the observations of sub-surface void formation obtained when prepared using single-beam focussed ion beam (FIB) techniques [106, 107, 147].

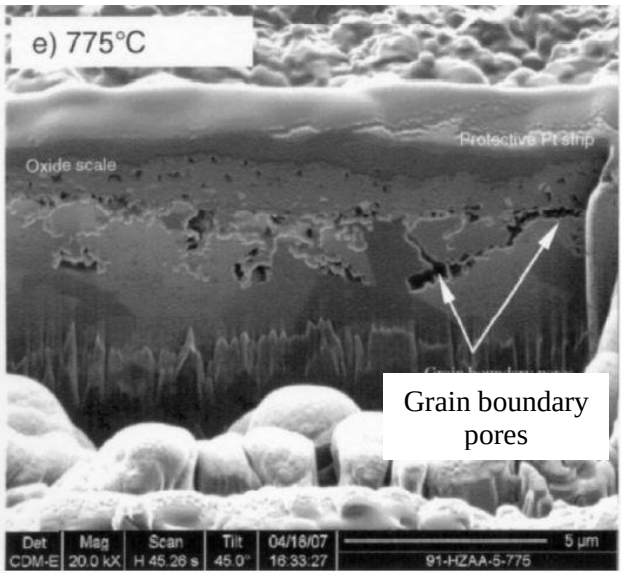

Figure 7-1: Image taken from Encinas-Oropesa et al. showing possible grain boundary voids underneath the oxide scale from FIB analysis, on a sample of Ni-based superalloy, RR1000, following an isothermal oxidation exposure at 775°C for 200 hours [107].

In metallic alloys, vacancy injection [194], dissociation of Cr-rich carbides [195], differing diffusion rates of elements within the alloy [196] or the internal oxidation of carbides or carbon in solution to form CO_2/CO gas bubbles [197] have all been attributed as causes of void formation underneath a growing external oxide scale. The first two mechanisms, of vacancy injection and particle dissociation, are in principle feasible, but the last mechanism is not in highly alloyed material, since thermodynamic calculations [198, 199] show that this cannot occur under a chromia or alumina external scale. This mechanism of void formation would therefore not be expected for most high-

temperature alloys and particularly for the chromia-forming Ni-based superalloy (RR1000) considered here. In addition the use of a beam of highly energetic ions to section a material can cause a number of artefacts to be introduced; these include ion damage, curtaining and differential sputtering rates. These can be reduced with careful well controlled milling and are described in detail in a review article [200].

The aim of this chapter is to evaluate the merits of using FIB techniques to examine oxidation damage. This includes re-examining previous observations of sub-surface void formation in this alloy through a comparison of FIB and conventional metallographic preparation techniques, to assess whether sub-surface voids can be produced as an artefact of sample preparation, sample oxidation and image interpretation.

7.2 Results & Discussion

A comparison between conventional metallographic preparation and FIB techniques has been made in Ni-based superalloy, RR1000, with different microstructural variants oxidised at 800°C for 200 hours. This includes a comparison with the different imaging signals available in a dual-beam FIB: secondary electrons produced using an electron beam ($SE_{electron}$) and secondary electrons produced using an ion beam (SE_{ion}). This study includes a brief appraisal of secondary ions (SI) and secondary ion mass spectroscopy (SIMS) from work conducted in collaboration with Cranfield University and Imperial College.

Starting with the samples prepared by conventional metallographic methods, Figure 7-2 (left-hand side) shows back-scattered electron (BSE) images of three microstructural variants (FG RR1000, CG RR1000 and shot-peened CG RR1000). These images are consistent with previous reports [104, 114, 115, 193] of sub-surface alumina intrusions underneath the external oxide scale. Thus illustrating the absence of the large voids that were previously reported in this alloy [106, 107, 147], when prepared on sections produced and examined using a single-beam FIB (Figure 7-1).

The complex oxide scale of RR1000 has been described previously in Chapter 5 but EDX analysis (Figure 7-3) was performed on the conventionally prepared samples to confirm that the external layer was duplex and rich in Ti, Cr and O with a sub-surface internal network rich in Al and O. These observations correspond well with previous observations, in both the literature and in Chapter 5, that the external oxide is TiO_2 and Cr_2O_3 with an Al_2O_3 internal oxide [104, 115]. It is important to note that no polishing media contamination was observed in any of these samples and that at no stage during the preparation method was any colloidal alumina solution used which may have in-filled voids. So the presence of an internal network of sub-surface features rich in aluminium provides further evidence for the absence of significant quantities of internal voids in this alloy.

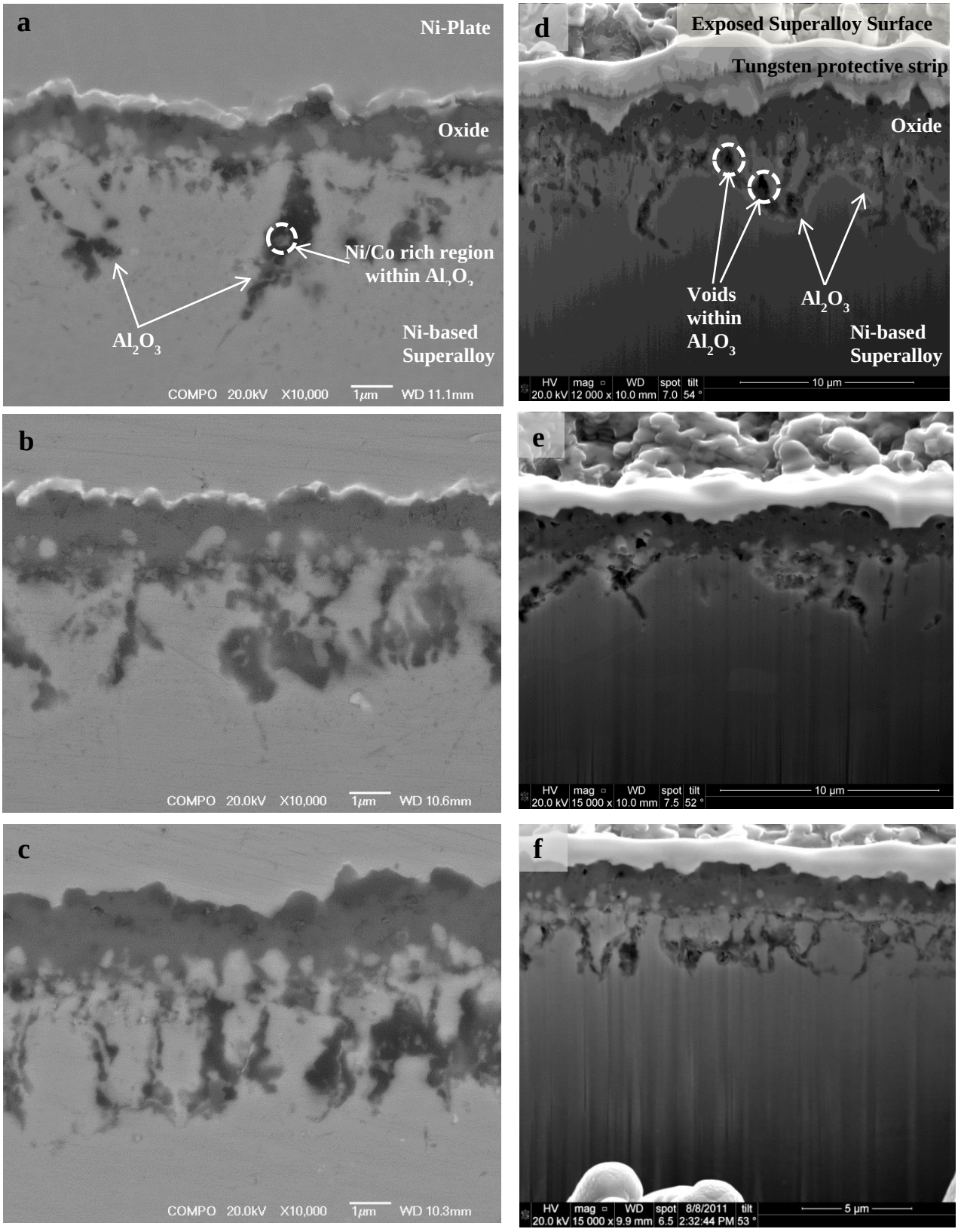

Figure 7-2: A comparison between a backscattered electron image of cross-sections prepared using conventional techniques (images of left-hand side) and SE images, produced using an electron beam during FIB sectioning (Images on right-hand side) on a) and d) CG RR1000, b) and e) FG RR1000, c) and f) shot-peened CG RR1000.

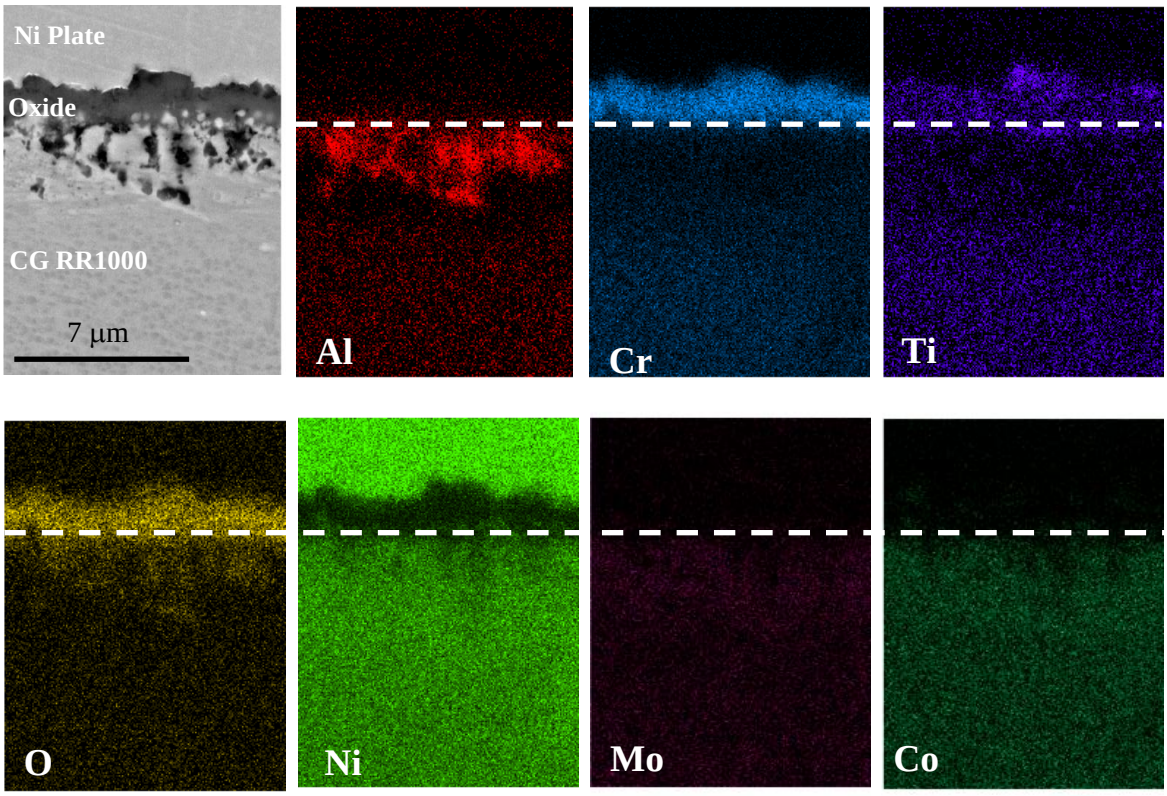

Figure 7-3: A secondary electron image produced using an electron beam, of a section through a CG RR1000 sample oxidised in laboratory air at 800°C for 200 hours with energy dispersive X-ray analysis maps. White dashed lines indicate the interface between the external oxide scale and the alloy.

Analysis of the FIB section was performed using both $SE_{electron}$[1] and SE_{ion}[2]. The $SE_{electron}$ images of the FIB sections (right-hard side, Figure 7-2), clearly show similar sub-surface structures found in conventional preparation. The sub-surface structures shown in $SE_{electron}$ images of the FIB sections are essentially identical to those prepared by conventional metallographic preparation. It should also be noted that these sub-surface structures, Al_2O_3 internal oxides, are remarkably similar to those reported in the literature previously and shown in Figure 7-1. The only difference is that in that case they were incorrectly interpreted as voids [106, 107, 147].

Further evidence for the misinterpretation of these features is shown Figure 7-4, where the effect of tilt angle was investigated with SE_{ion} imaging. Under initial imaging conditions (52° sample tilt) a network of features is found that looks remarkably like those which have previously been attributed as voids, one of which is illustrated by a white arrow in Figure 7-4(a). Each one of these features is surrounded by a bright ring, which could be attributed to edge effects from enhanced secondary electron emission.

[1] $SE_{electron}$ – Secondary electrons produced by the impact of electrons from a field emission gun.
[2] SE_{ion} – Secondary electrons produced by the impact of gallium ions from an ion beam.

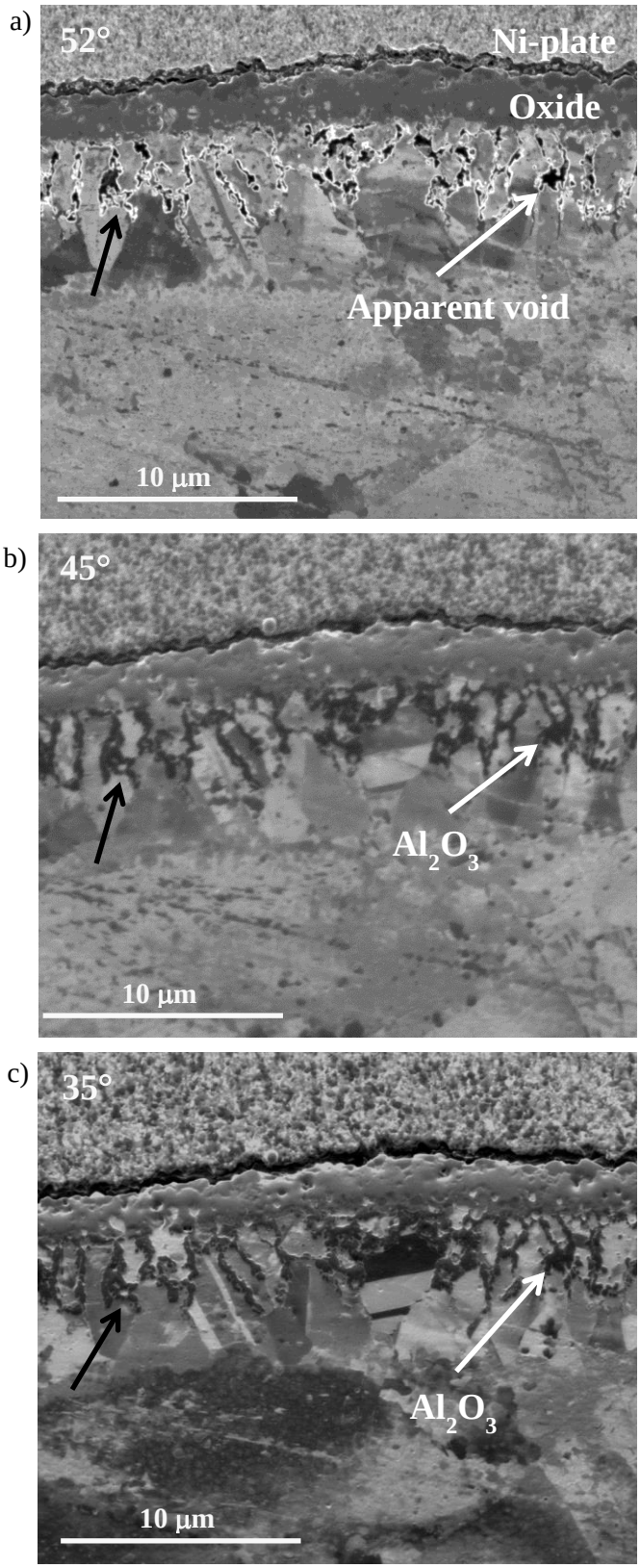

Figure 7-4: Secondary electron (SE_{ion}) images, produced using the gallium ion beam, of a cross-section of a shot-peened CG RR1000 sample oxidised for 200 hours at 800°C. Images were produced at different sample surface tilt angles of a) 52°, b) 45° and c) 35°. Note the change in SE contrast tilt angle shown by the white arrow.

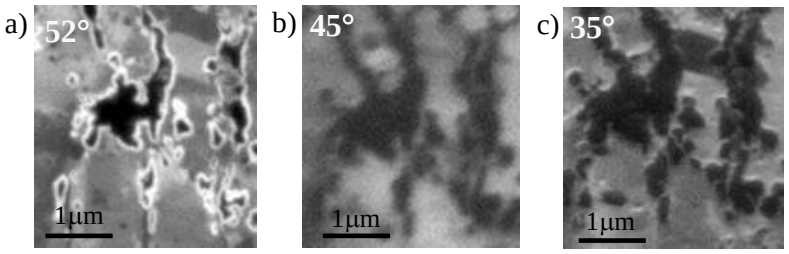

Figure 7-5: Expanded section of Figure 7-4, illustrating more clearly the area highlighted by the white arrow showing the contrast changes with tilt angle. SE_{ion} images produced using the FIB ion beam with the sample surface tilted at 52°, 45° and 35°.

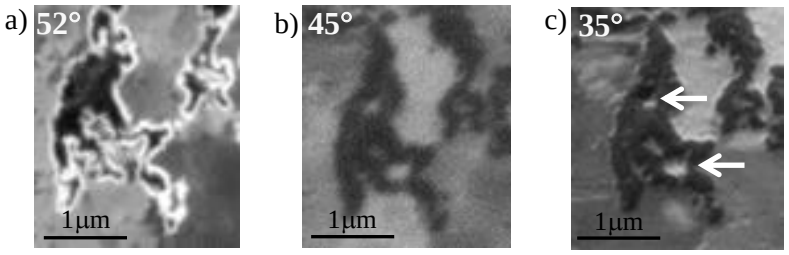

Figure 7-6: Expanded section of Figure 7-4, illustrating more clearly the area highlighted by black arrow showing the small metallic features trapped (white arrow) within the alumina intrusions. SE_{ion} images with the sample tilted at 52°, 45° and 35°.

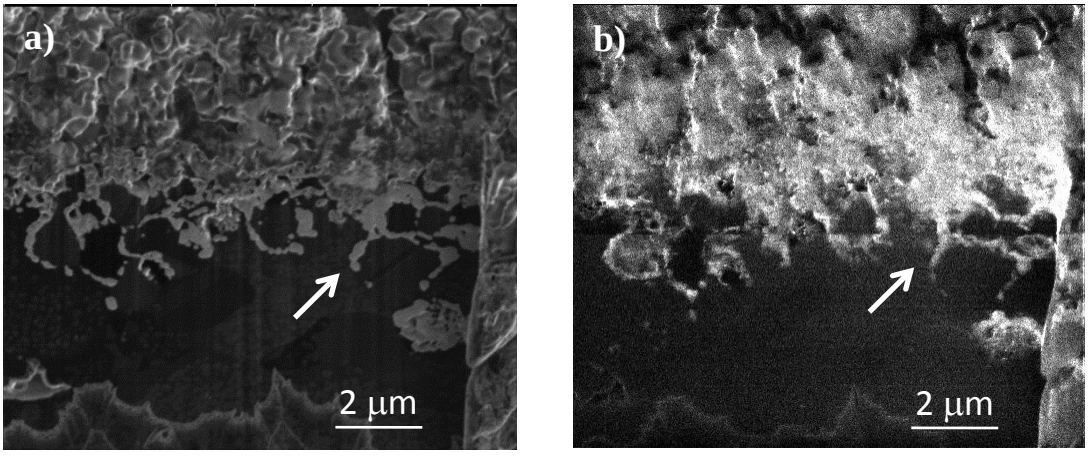

Figure 7-7: FG RR1000 + 0.5% wt.% Si sample oxidised for 1000 hours at 700°C in laboratory air. Ramp milled at ca. 30° to the sample surface, therefore scale is not representative perpendicular to the micron bar. a) Positive SI image with sample tilted at +5°, produced using the total positive unfiltered secondary ion yield collected using a channeltron detector. b) ^{16}O negative SIMS data. Courtesy of B. Foss at Imperial College London.

However once looking at the two other tilt angles (45° and 35°), so that the sample has been tilted relative to the ion beam, these features change contrast, thus proving that these features are in fact filled with solid matter, in this case oxide. This supports the previous images taken using $SE_{electron}$ and the notion that these features are not in fact voids. This is shown more clearly in which one of the features (illustrated by the white arrow) in Figure 7-4 is expanded in Figure 7-5. The use of different tilt angles when examining samples produced and imaged in this way is highly recommended as a key technique in identifying features. It has been demonstrated clearly that what was previously termed a network of voids is in fact a network of internal oxides.

Under these imaging conditions a clear ion channelling contrast is found between different materials and different grains as well as within grains. This allows the illustration of the grain structure and of twinning within a grain. In some grains and at certain tilt angles, γ′ precipitates are visible (35° sample tilt, Figure 7-4(c)). This effect has been used and described previously to show re-crystallisation underneath the oxide layer, within the γ′ denuded zone (Chapter 6) and shows how important information can be gained from this imaging method.

It is also worth noting that in all preparation and imaging conditions the interface between the external oxide scale and the underlying alloy is similar and shows no evidence of cracking. In both preparation techniques small voids were present in the outer oxide scale. The only significant difference between samples produced by the two sectioning techniques is the presence of small void-like features associated within the alumina internal oxide in the FIB prepared specimens (Figure 7-2(d)). These voids are not the features discussed above, since they are associated with alumina internal oxide and do not change contrast with sample tilt angle.

Returning to Figure 7-2(a) it was found using EDX that small regions (circled), rich in Co and Ni, existed within some of the alumina regions. These had probably formed from small volumes of alloy that had been selectively oxidised to form alumina and had then become entrapped within the alumina intrusion. It appears that the small voids observed after dual-beam FIB sectioning were associated with these metallic regions. The origin of these voids is unclear but may be associated with differential sputtering rates between the metallic and adjacent oxide phases, since strongly bonded materials, such as ceramics, typically mill more slowly than metallic specimens. In Figure 7-6(c), these metallic regions appear to be slightly recessed within the alumina intrusions.

SI imaging and SIMS are useful techniques which, in this case, can again show whether the apparent voids are filled with oxide. Figure 7-7 shows images taken using these signals in work performed in collaboration with Cranfield University and Imperial College. In this case analysis was performed on

a FG RR1000 specimen with 0.5 wt. % Si addition, which had been oxidised at 700°C for 1000 hours. Positive SI have a significantly enhanced yield in the presence of oxygen [200] by a factor of approximately 100 and therefore confirms the presence of internal oxide within the specimen, by showing that these features are bright, with one being illustrated by the white arrow (Figure 7-7). SIMS is primarily used for elemental analysis and if set up for ^{16}O negative ions provides final confirmation that no large voids are present in the sub-surface microstructure Figure 7-7(b).

7.3 Concluding Summary

It has been shown using a number of techniques in the present RR1000 alloys that a solid internal network of alumina is present underneath the external oxide scale rather than a network of voids as suggested elsewhere [6-8]. Conventional metallographic preparation and $SE_{electron}$ imaging show a solid network of Al_2O_3 throughout and SE_{ion} imaging has established that void-like features in fact contain solid matter when a range of sample tilt angles is used. If only one tilt angle is used these features can be open to misinterpretation as voids. The reason for this is that when the incident angle of the ion beam is changed relative to the sample a corresponding change in the secondary electron yield and therefore the contrast of the image occurs. This contrast change also occurs depending on the grain orientation and can be useful in revealing the grain structure of the material. Review articles [200, 201] and standard texts [202, 203] provide detailed explanations as to the mechanisms of ion channelling contrast.

Occasional sub-surface void-type damage can still arise only in the FIB sectioned specimens. Sub-surface voids of similar morphology and size were absent from the specimen prepared by conventional sectioning methods. These voids have been attributed to small trapped metallic regions within alumina intrusions that are preferentially milled away and so the inference is that even well-controlled FIB milling can produce void-like artefacts. In addition, small voids were found in the surface oxide scale in samples produced by both FIB and conventional preparation techniques.

In spite of this, significant advantages over conventional metallographic techniques are offered by FIB sectioning. These include the ability to section specific surface features or locations, e.g. oxides/grain boundaries, as well as its usefulness in examining samples from interrupted testing where a surface feature can be sectioned before the sample is returned for further testing. This work illustrates the need to use all the available signals when imaging complex samples. It should be stressed, however, that like all techniques careful preparation and expertise will always be required regardless of the preparation and imaging method, as is the need for a good understanding of the technique being used.

Chapter 8 - Influence of Prior Oxidation on High Cycle Fatigue performance of RR1000 and the Role of Oxidation in Fatigue Crack Initiation

8.1 Introduction

The role of environmental degradation in the mechanical performance of a component is important, since rotor discs operate in high temperature oxidising environments under significant external loads. When these components oxidise, a protective chromia external scale is formed along with significant damage in the form of internal oxides of alumina both intergranularly and intragranularly [115]. Beyond these is a weaker region depleted in γ′ particles and grain boundary carbides. The formation of this sub-surface damage and, in particular, the internal oxides are undesirable and may have a significant detrimental effect on the alloy [84, 152]. It has been postulated that the internal oxides that form at the grain boundaries have the potential to crack and introduce local stress concentrations which promote early crack initiation and therefore reduce component lives [84]. Oxides are inherently brittle materials with tensile failure strains of <1% and K_{1c} values for chromia and alumina in the range of 0.4-2.0 MPa.$m^{1/2}$ [91]. These are typically much lower than the underlying alloy, so it should be no surprise that it is possible for these oxides to fail under tensile loading.

Several studies on the Ni-based superalloys ME3, and Udimet 720 have found that prior oxidation reduces fatigue life and, in IN100, that the crack initiation life was similar to the number of cycles to cause the oxide to fracture [47, 150, 151]. The tests performed on the Ni-based superalloy, ME3, have shown that prior high temperature exposure in an oxidative environment (>700^{o}C) for prolonged periods of time (100-2020 hours) have a detrimental effect on the high temperature (704^{o}C) notched fatigue life [47]. The thicker the external scale and the deeper the internal damage the more pronounced the reduction in life [47]. The reduction in life in this case was driven by $M_{23}C_6$ carbide dissolution. Removal of the internally oxidised region did not lead to a complete recovery in high temperature fatigue life but the removal of the carbide dissolution zone did. This indicated that grain boundary strengthening from the $M_{23}C_6$ carbides is important to crack initiation for these tests. Another study using extensive prior exposures on the Ni-based superalloy, ME3 (704^{o}C for 439 hours) and Udimet 720 (650^{o}C and 704^{o}C for 100 or 1029 hours) found that the mean lives of pre-oxidised specimens had up to a 70% reduction in high temperature LCF life. A change of crack initiation was also seen from sub-surface (as-received) to surface (pre-oxidised). Performing the prior exposures in vacuum led to no reduction in fatigue life, illustrating that oxidation damage is driving the reduction in life [151].

The aim of the present work was to extend the previous research and examine the potential for intergranular internal oxides to act as preferential crack initiation sites and therefore affect the overall life of a component. This work concentrates on the fundamental understanding of the initiation between oxidation and fatigue. The use of pre-oxidised samples undergoing fatigue at room temperature was performed to isolate the effect of oxidation on the fatigue life. This allows the exclusion of any high temperature processes by removing the influence of creep deformation or oxidation ahead of the crack tip that would affect the fatigue crack growth. Bend samples have been used to restrict fatigue failures to the top surface region where the oxide resides.

8.2 Results and Discussion

8.2.1 Oxidation damage caused by pre-oxidation

Previous studies on the Ni-based superalloys Udimet 720, ME3 and RR1000 under cyclic fatigue or dwell fatigue conditions found no change in oxide composition compared with the unstressed condition but did record an enhancement of the oxidation damage [147, 151]. This illustrates that using pre-oxidation as a method of isolating the effect of environmental damage on fatigue performance is a reasonable approach. The typical oxide morphology of the pre-oxidised RR1000 is shown in the cross-sections in Figure 8-1 and is complex. A more detailed description of the oxidation damage and confirmation of the composition are provided in Chapter 5 and in previous studies on this alloy [44, 115, 204]. The oxide is comprised of a continuous external layer of chromia with extensive sub-surface internal oxidation of alumina. This internal oxide occurs in two distinct locations in this alloy: intergranular and intragranular. The intergranular penetrations are deeper and often continuous whereas the intragranular penetrations consist of smaller isolated particles within the grains. A significant γ′ denuded zone encompasses and exists ahead of this internal oxide.

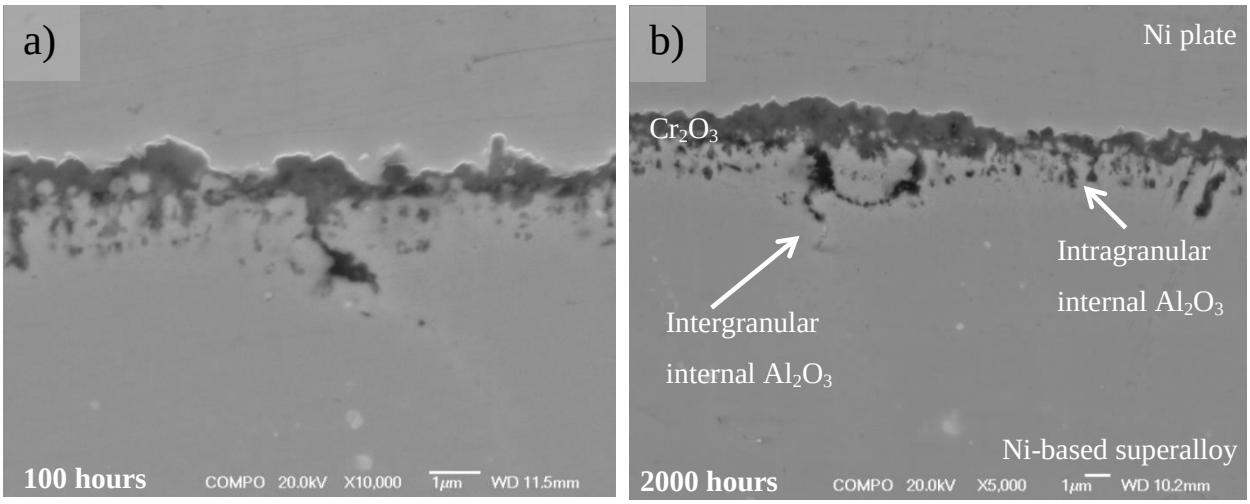

Figure 8-1: BSE image of the cross-section through the typical oxidation damage produced by high temperature exposures at 700°C for a) 2000 hours and b) 100 hours at different magnifications.

Ahead of this zone is a region within which the Cr-Mo rich grain boundary phase has dissociated (Chapter 5). This phase is often assumed to be $M_{23}C_6$ carbides, but equally could be sigma phase [172]. The oxidation damage increases in thickness and depth with increasing time and temperature, the kinetics of which are described elsewhere in the following papers [115, 204] and in Chapter 5.

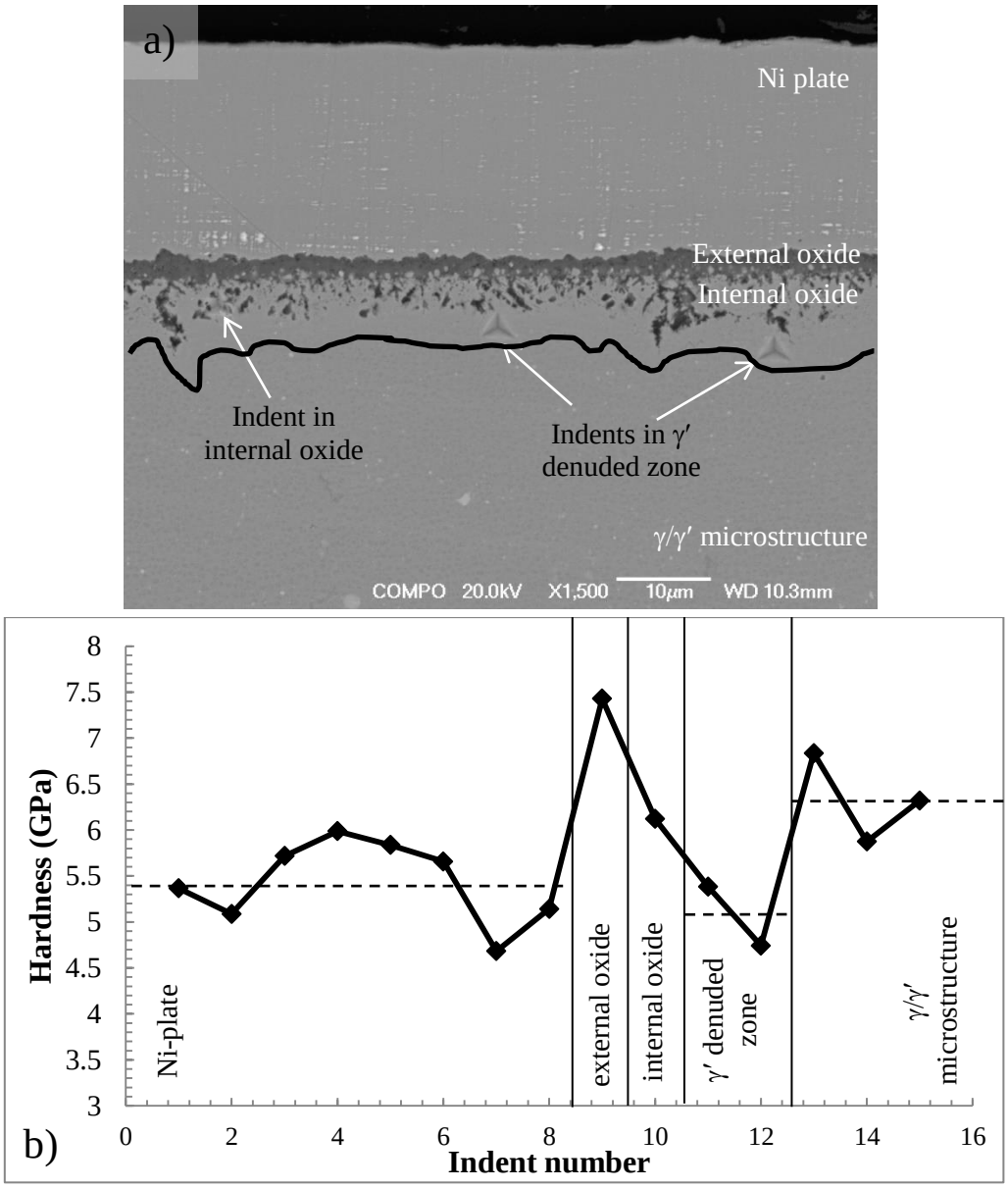

Figure 8-2: a) BSE images of three of the nano-indentations performed, one in the internal oxide and two in the γ′ denuded region. b) Hardness (GPa) for each nano-indentation, with the dotted line showing the average for that region and illustrating that the γ′ denuded region is softer than the base alloy and similar to pure Ni.

Nano-indentation was used to evaluate whether the γ′ denuded zone is weaker/softer than the surrounding alloy. Figure 8-2 shows the hardness for every nano-indent performed on an oxidised sample (800°C for 500 hours) and illustrates that the γ′ denuded zone is considerably weaker than the external oxide scale and the internally oxidised region, as well as the bulk alloy. Interestingly it has a similar average hardness to pure Ni, which was deposited on the surface during specimen preparation

to protect the oxide scale. This is not unexpected seeing as most of the strengthening elements, i.e. Ti and Al, have been consumed in this region during oxidation and therefore only the matrix is left. This weaker region has been shown before [44, 47, 204] and is thought to be part of the cause for the formation of metallic protrusions within the external oxide scale described in Chapter 5 and in previous studies [44, 47, 204].

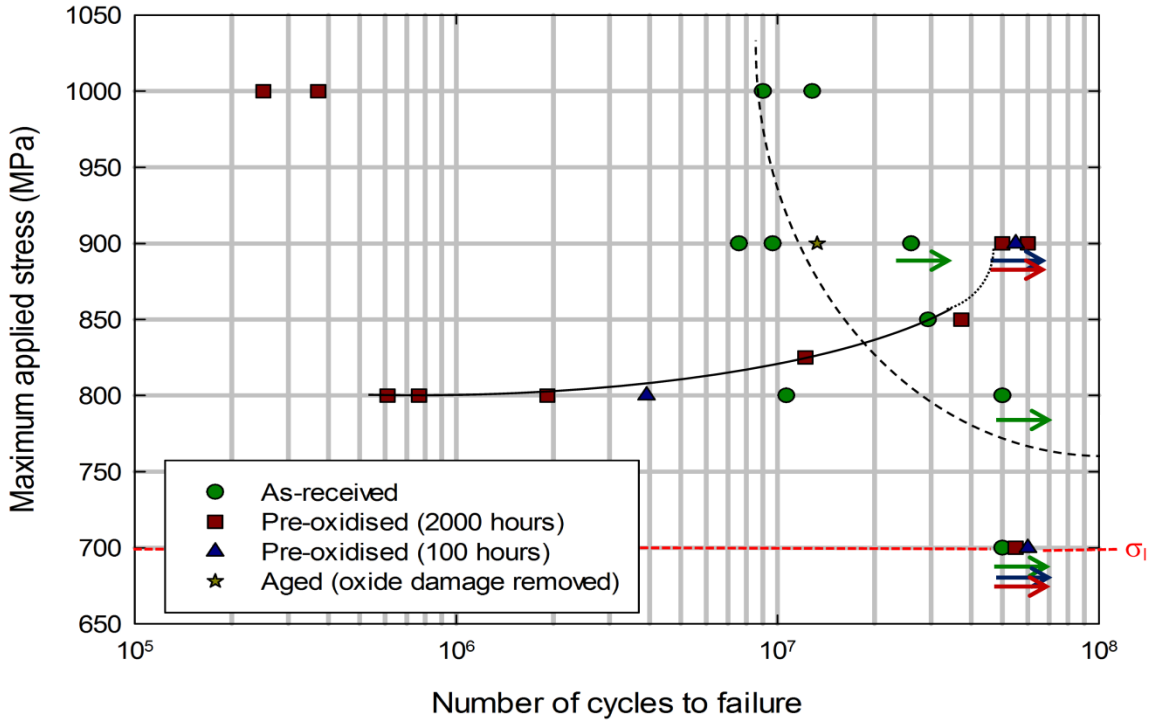

Figure 8-3: A graph depicting the four conditions (as-machined, aged, 100h pre-oxidation and 2000h pre-oxidation) tested showing maximum applied stress against number of cycles to failure. An arrow underneath the symbol demonstrates a runout test at 5 x 10^7 cycles.

8.2.2 Comparison of fatigue lives

The results of room temperature high cycle fatigue (HCF) tests obtained using pre-oxidised and as-machined four-point bend specimens are shown in Figure 8-3. At a stress level of 700 MPa, all testpieces runout at 5 x 10^7 cycles, indicating that this stress level is close to the fatigue endurance. Apparently under such a stress level, no influence of pre-oxidation can be detected. At a maximum applied stress of 800 MPa, failure is not guaranteed in the as-machined condition, as a runout was recorded. Contrastingly, a sharp reduction in fatigue life of up to 2 orders of magnitude, compared to the as-machined testpieces when the stress level is increased to 800 MPa (Figure 8-3). A further reduction in life is seen between the two pre-oxidation conditions, with the longer prior-exposure, and therefore increased depth of oxidation damage, causing a larger reduction in life. This suggests that the environmental damage is the cause of the reduction in life at this stress. With a further increase in applied stress, the fatigue life of the pre-oxidised testpieces increases significantly, with the life

increasing with increasing stress until failure no longer occurs at a maximum applied load of 900 MPa. At the highest stress level investigated here, 1000 MPa, a significant deficit in fatigue life of the pre-oxidised testpieces is again evident.

The fatigue behaviour of the as-machined testpieces is broadly as expected. The fatigue life is generally reduced as the stress increases, as shown by the dashed curve on Figure 8-3. There is some scatter as expected from these type of tests. As the maximum applied stress approaches the room temperature yield stress of RR1000 the fatigue life seems to improve slightly. The slightly larger life at a maximum applied stress of 1000 MPa is attributed to inherent scatter in the initiation life that occurs throughout and is enhanced as yielding is approached. It is worth mentioning that the maximum applied stress is experienced only in a small volume of material in the top surface layer associated with the bend loading configuration. As the maximum stress increases towards the yield stress of the material, localised yielding and strain hardening may occur which is presumably attributed to the slightly increased fatigue life at 1000 MPa.

To assess whether microstructural aging, rather than oxidation, contributed to the fatigue behaviour of the specimen exposed to 700^{o}C, a further test was undertaken. For this the oxidation damage on a pre-oxidised specimen (700^{o}C for 2000 hours) was removed by low stress grinding, and the remaining core of the specimen was fatigued at 900 MPa. The specimen failed at ~1.3x10^{7} cycles, substantially less than the corresponding pre-oxidised samples which remained un-failed at 5x10^{7} cycles (Figure 8-3). The results, although limited, indicate that it is the oxidation process rather than aging that causes an increase in life at this relatively high stress level (900 MPa). It is, perhaps, debateable whether significant microstructural changes had occurred during the pre-oxidised period since the microhardness of both as-machined and the aged specimen was identical at 459 Hv (± 1 standard deviation = 6.1 [aged] and 7.6 [as-machined]). Note that some coarsening of the tertiary and secondary γ′would be expected after a prolonged high temperature exposure [205], through Ostwald ripening and this coarsening has been shown to reduce high temperature fatigue resistance [206].

8.2.3 Fractography

The initiation location of the as-machined specimen and pre-oxidised specimens are compared in Figure 8-4 and Figure 8-5 respectively. At room temperature and in the high cycle fatigue regime, it is generally observed that slip bands tend to form in the larger grains and lead to the initiation of fatigue cracks although the contribution of neighbouring grains, by having nearly-similar Schmid factors, cannot be disregarded [207]. It is not surprising that the initiation site observed in the current study for the as-machined specimens at 800 MPa was beneath the surface because the large grains are distributed randomly and may not appear exactly on the top surface. This can be seen from the particular large facet (~60 μm) upon which initiation occurred (Figure 8-4(a)). The chance to sample

large grains within the shallow top surface high stress layer can vary and is a possible reason for the large discrepancy in life at a maximum applied stress of 800 MPa in the as-machined condition. As one specimen recorded a runout and the other failing at $1.1x10^7$ cycles, with the failure occurring from a particularly large grain and so could be an anomalous result. In all cases around the initiation site, fatigue crack growth demonstrates a faceted manner, which dictates the characteristics of the near threshold crack growth at room temperature. With further crack extension, such faceted crystallographic appearance is replaced with flat transgranular growth, which is typical for crack growth at higher stress intensity factor ranges, within the Paris regime (Figure 8-6). It is understood that the majority of total fatigue life is spent on initiating fatigue cracks and early propagation for such smooth and small laboratory testpieces [208]. At high stresses 900 MPa and 1000 MPa the initiation site in the as-machined specimens shifts from sub-surface to the surface and even at these stresses only a single initiation site was recorded. However, several surface-breaking cracks in the region of highest stress illustrate the potential that more initiation sites are occurring, with one dominating fatigue life. Similarly the aged specimen showed a similar surface initiation at a maximum applied load of 900 MPa.

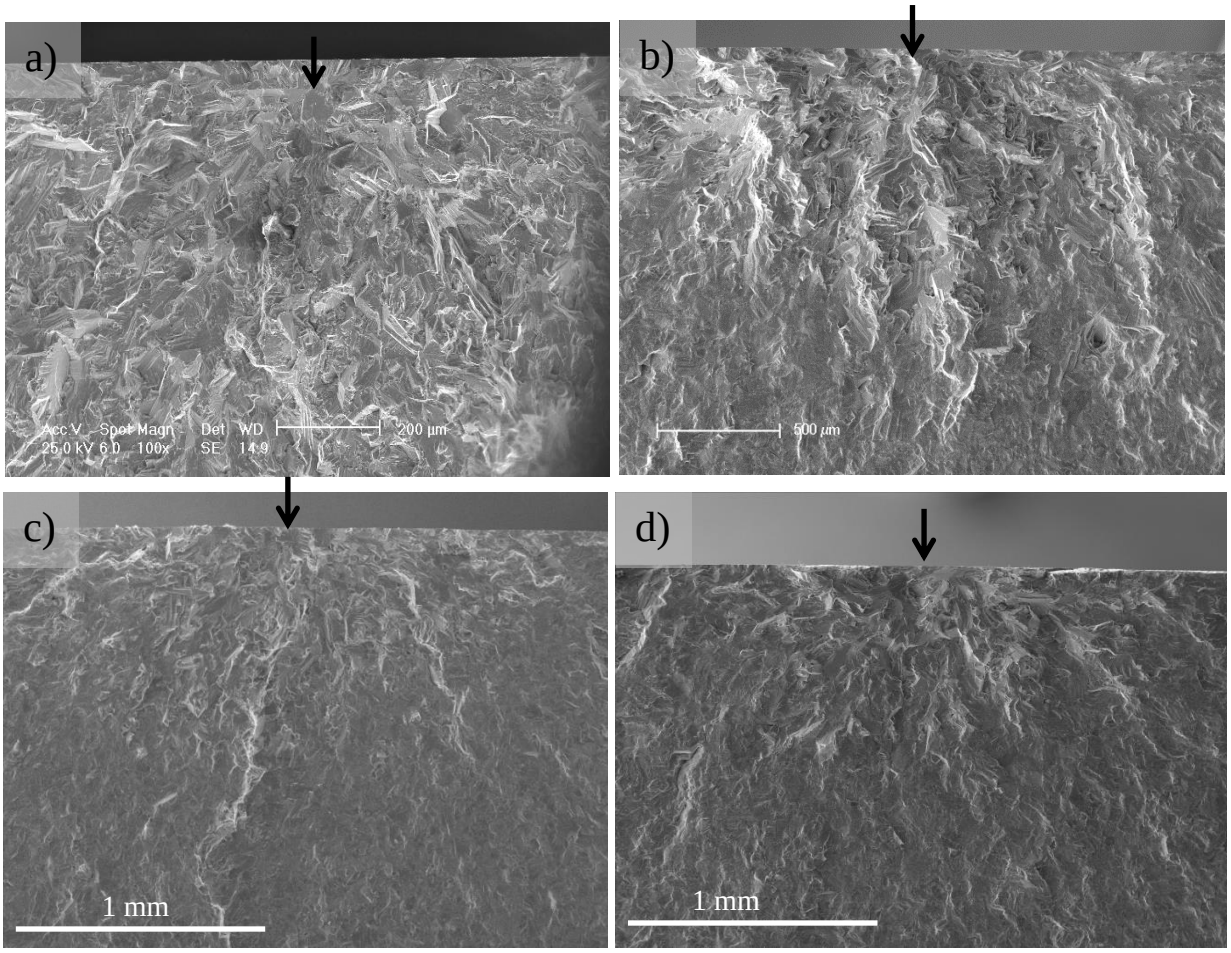

Figure 8-4: Secondary electron images of the fracture surfaces of as-machined specimens, a) failed at $1.1x10^7$ cycles at 800 MPa showing a sub-surface initiation, b) failed at $2.9x10^7$ cycles at 850 MPa, c) failed at $7.5x10^6$ cycles at 900 MPa and d) failed at $1.3x10^7$ cycles at 1000 MPa. An arrow on each image indicates the crack initiation point.

The fatigue crack initiation sites of the pre-oxidised specimens occurred at the surface in all cases of specimen failure (Figure 8-5), with multiple surface initiation sites occurring on the fracture plane at a maximum applied stress of 1000 MPa (Figure 8-7(a&b)) and a single initiation site occurring on the fracture plane at all other stresses. Apart from the surface initiation the morphology is very similar. This indicates that the oxides are the source of crack initiation, while having no effect on room temperature fatigue crack growth. It is expected, as the current investigation was deliberately carried out at room temperature to avoid potential influences of interactions between environment and crack tip, which was found to reduce the crack propagation life by changing the crack growth mechanism from transgranular to intergranular crack growth [163, 164, 166]. Hence the current study purely reflects the input of pre-oxidation on the initiation phase of the fatigue process.

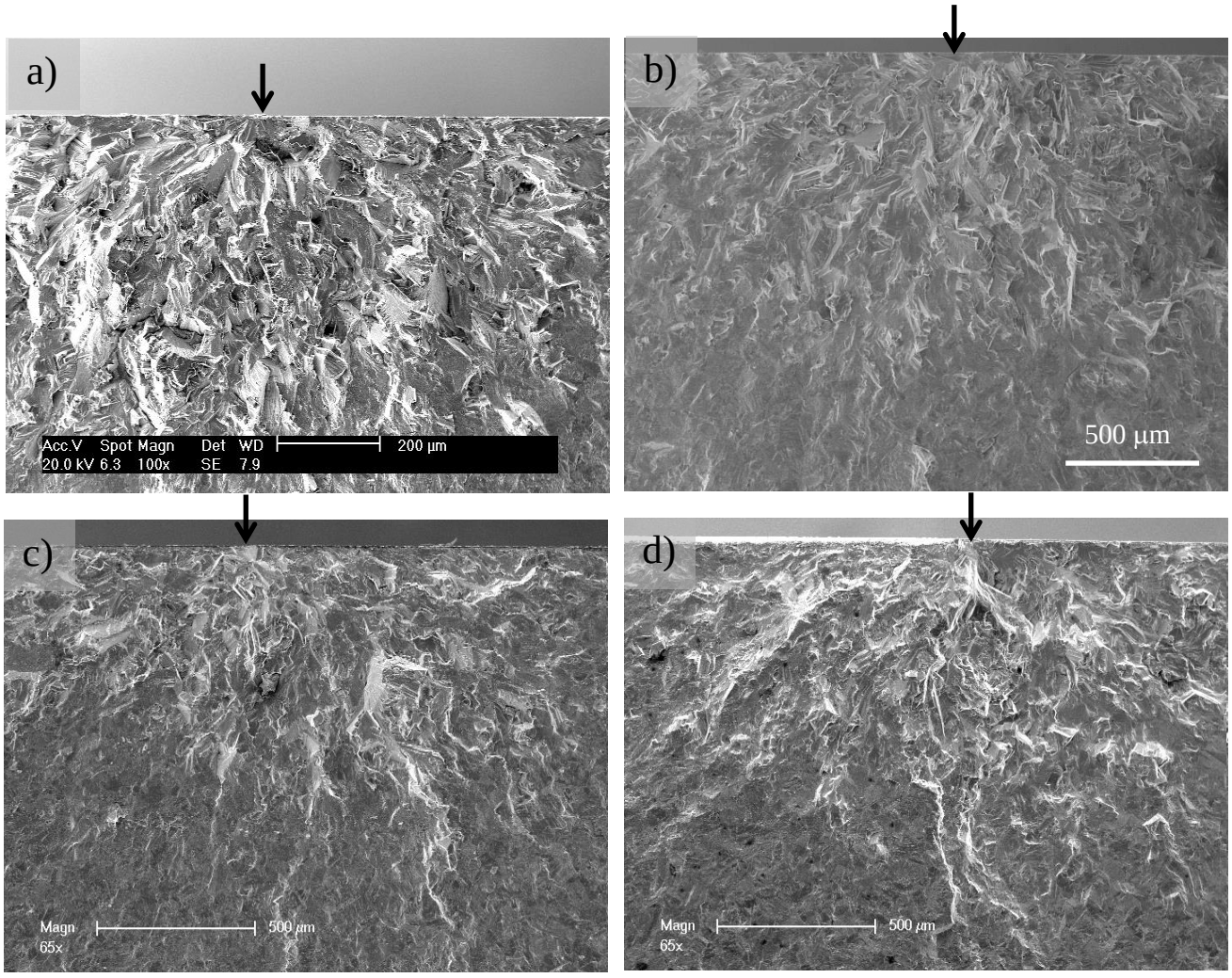

Figure 8-5: Secondary electron images of the fracture surfaces of a) a 2000 hour pre-oxidised specimen that failed after $6x10^5$ cycles at 800 MPa, b) a 100 hour pre-oxidised specimen that failed after $3.9x10^6$ cycles at 800 MPa, c) a 2000 hour pre-oxidised specimen that failed after $1.2x10^7$ cycles at 825 MPa and d) a 2000 hour pre-oxidised specimen that failed after $3.7x10^7$ cycles at 850 MPa. An arrow indicates crack initiation point.

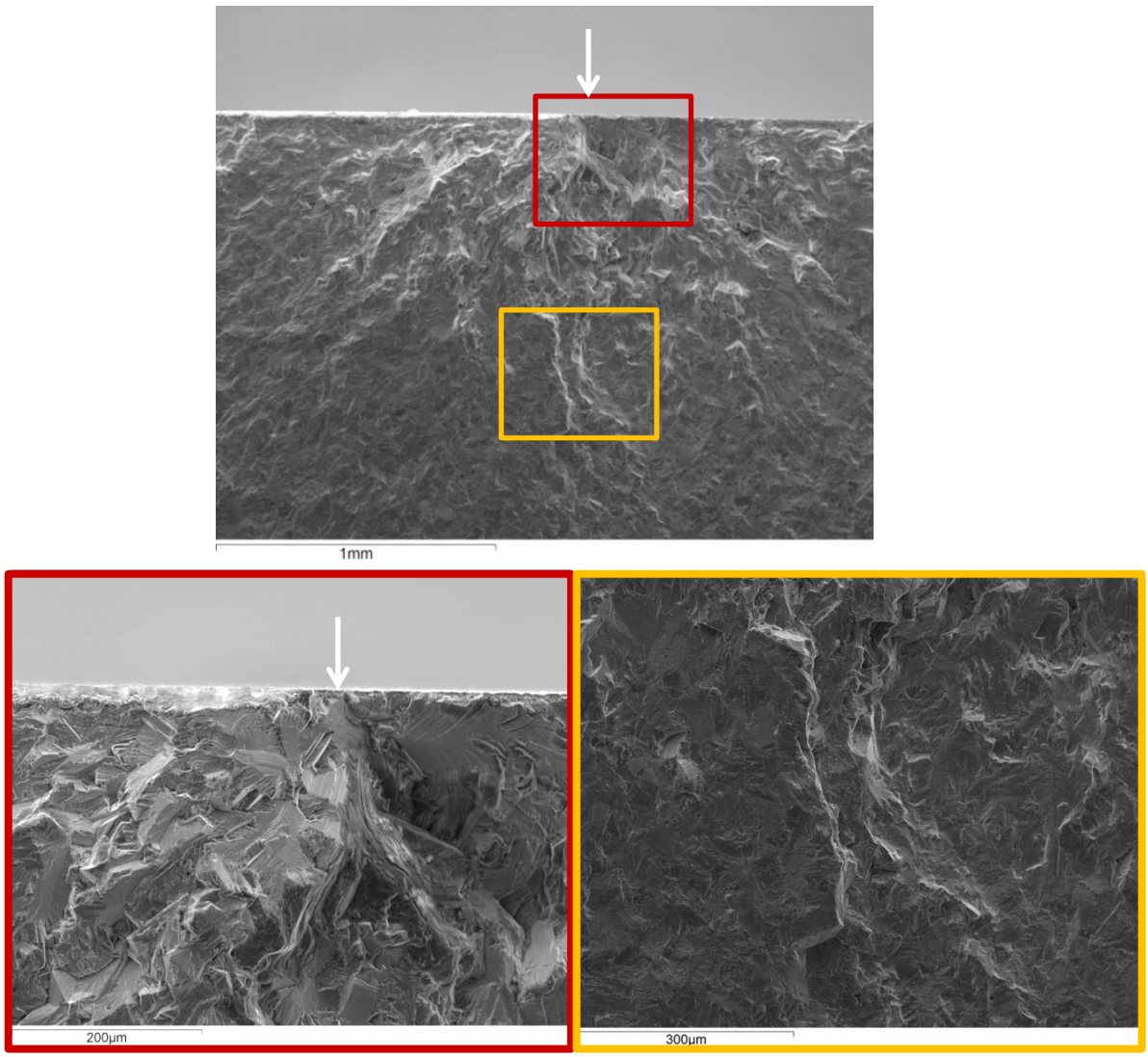

Figure 8-6: A secondary electron image of a fracture surface of a pre-oxidised (2000 hours) specimen that failed at 825 MPa. Highlighted in the red box is the initiation point at a higher magnification to illustrate the highly facetted crystallographic growth in this region. Highlighted in yellow is a region away from the surface showing flat transgranular growth. An arrow indicates the crack initiation point.

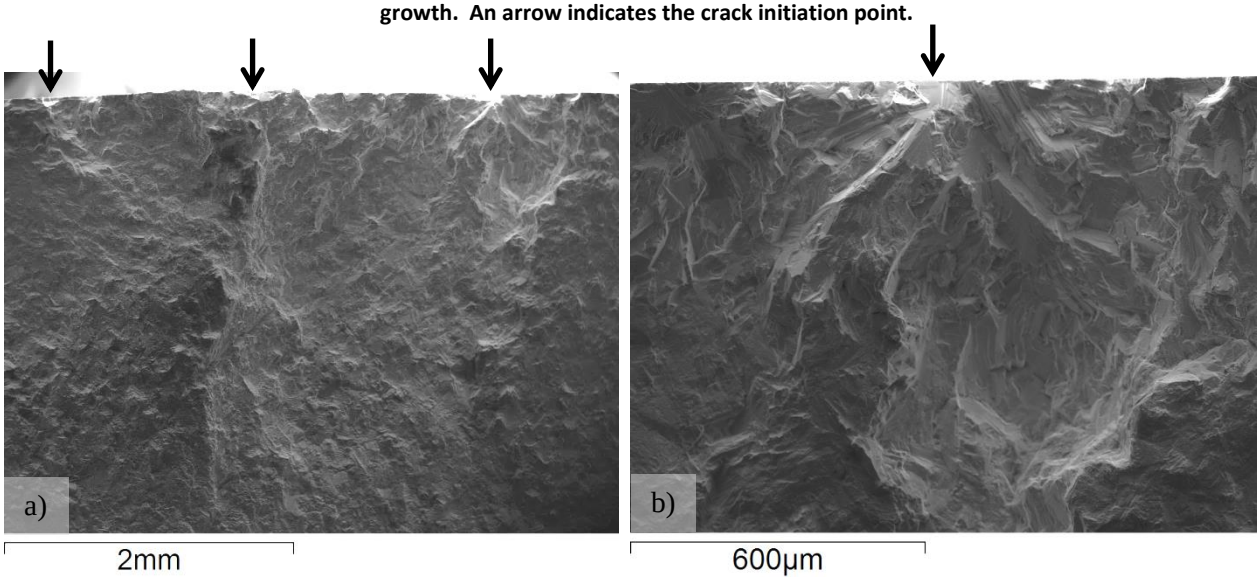

Figure 8-7: Secondary electron images of the fracture surface of a 2000 hour pre-oxidised specimen that failed after $2x10^5$ cycles at 1000 MPa showing, a) multiple initiation sites and b) fatigue crack morphology at one initiation site.

Other studies using cylindrical test specimens, where the surface region is not the region of highest stress, have similarly found surface initiations, however, with pre-oxidised specimens whereas sub-surface initiation occurred in the as-machined condition [151]. The present observations are consistent with these findings and add support to the notion that oxidation damage is the source of fatigue crack initiation.

8.2.4 Cross-sectional analysis

Before metallographic sections were performed the top surface of the tested specimens were firstly examined under the SEM, to check whether there are any other surface cracks present within the gauge section. Multiple cracks were observed on all pre-oxidised specimens except those tested at 700 and 900 MPa. Note that the cracking of external oxide scale was always perpendicular to the stressing direction, whereas it is around a 45^{o} angle to the stressing direction in the as-machined testpieces. This suggests a different mode of failure, with crystallographic slip dominating in the as-machined testpieces and oxide cracking dominating in the pre-oxidised testpieces.

A number of surface-breaking cracks were seen near the fracture surfaces on the area of maximum tensile stress. A schematic diagram of the location of these cracks is shown in Figure 8-8. These cracks have been seen in both the pre-oxidised condition (Figure 8-9(a) and Figure 8-10(a)) and only in the as-received condition at 900 MPa (Figure 8-9(b)) and 1000 MPa. Additionally no cracking of the external oxide was seen in the un-failed pre-oxidised samples (700 MPa and 900 MPa).

The reason for sectioning these surface-breaking cracks is that they provide insight into the initiation process and how the main crack that caused failure initiated. In order to indicate whether these cracks originate from sub-surface environmental damage features, such as internal oxides, cross-sections were taken through the specimens using both conventional and focussed ion beam sectioning. Figure 8-10(a) clearly shows a surface-breaking crack cutting through the external chromia scale, penetrating down an intergranular internal oxide and proceeding into the alloy in a pre-oxidised specimen (2000 hours) at a maximum applied stress of 800 MPa. EDX analysis in Figure 8-11 confirms that these cracks are penetrating through the chromium rich surface oxide and down aluminium rich internal oxides. A large number of similar cracks at 30-50 μm intervals occurred within the area of maximum stress, with each one being associated with an intergranular internal oxide. In all cases, these cut through the external chromia scale, penetrate down an intergranular internal oxide and proceed into the alloy (Figure 8-12). Electron channelling contrast imaging and chemical etching were used to reveal the microstructure around these cracks and found that they penetrated through the base alloy either by following a crystallographic facet (Figure 8-12 (b)) or the grain boundary (Figure 8-13).

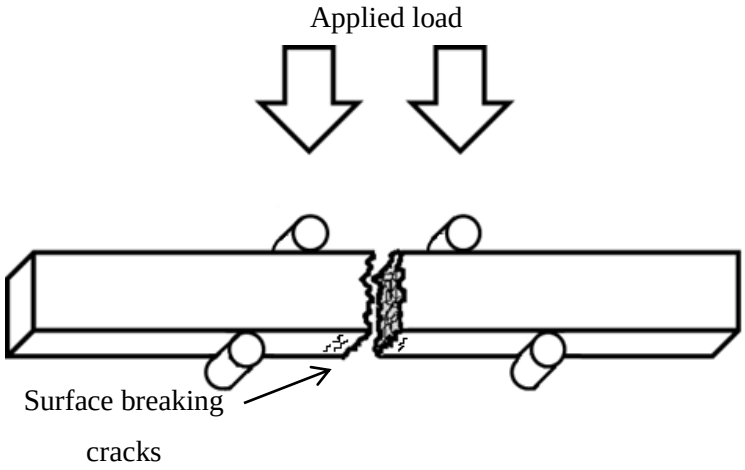

Figure 8-8: Schematic diagram of a fractured four-point test piece illustrating the location of any surface breaking cracks that were subsequently sectioned. The maximum tensile stress is experienced on the bottom surface between the two wider rollers.

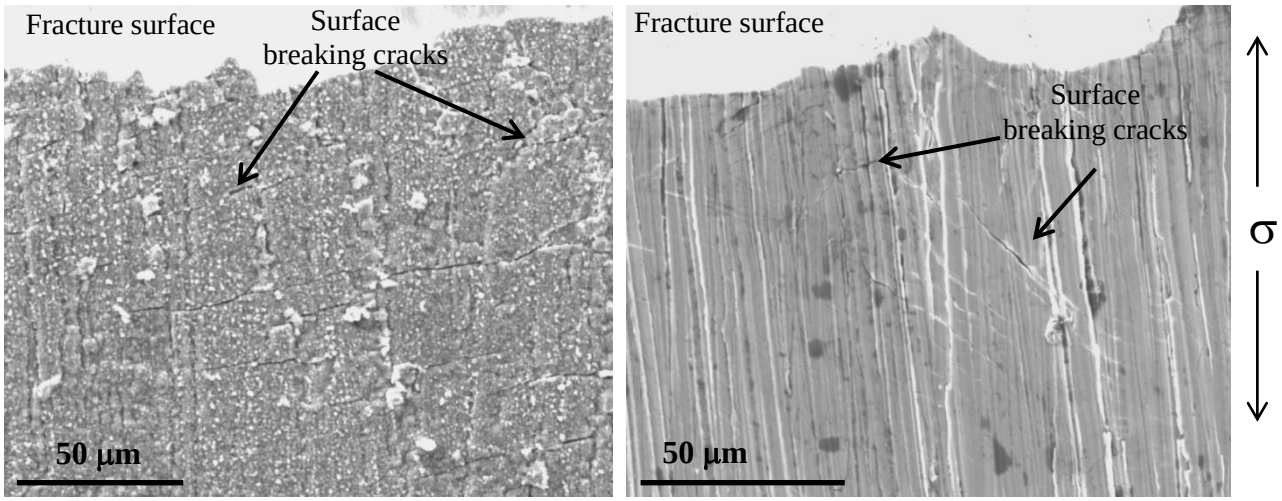

Figure 8-9: Secondary electron images of surface breaking cracks as illustrated in Figure 8-8. a) A pre-oxidised (2000h at 700°C) that failed at 3.7x10^7 cycles at a maximum applied stress of 850 MPa and b) an as-machined specimen that failed after 9.6x10^6 cycles at 900 MPa. The direction of the applied stress is parallel to the machining marks and is indicated.

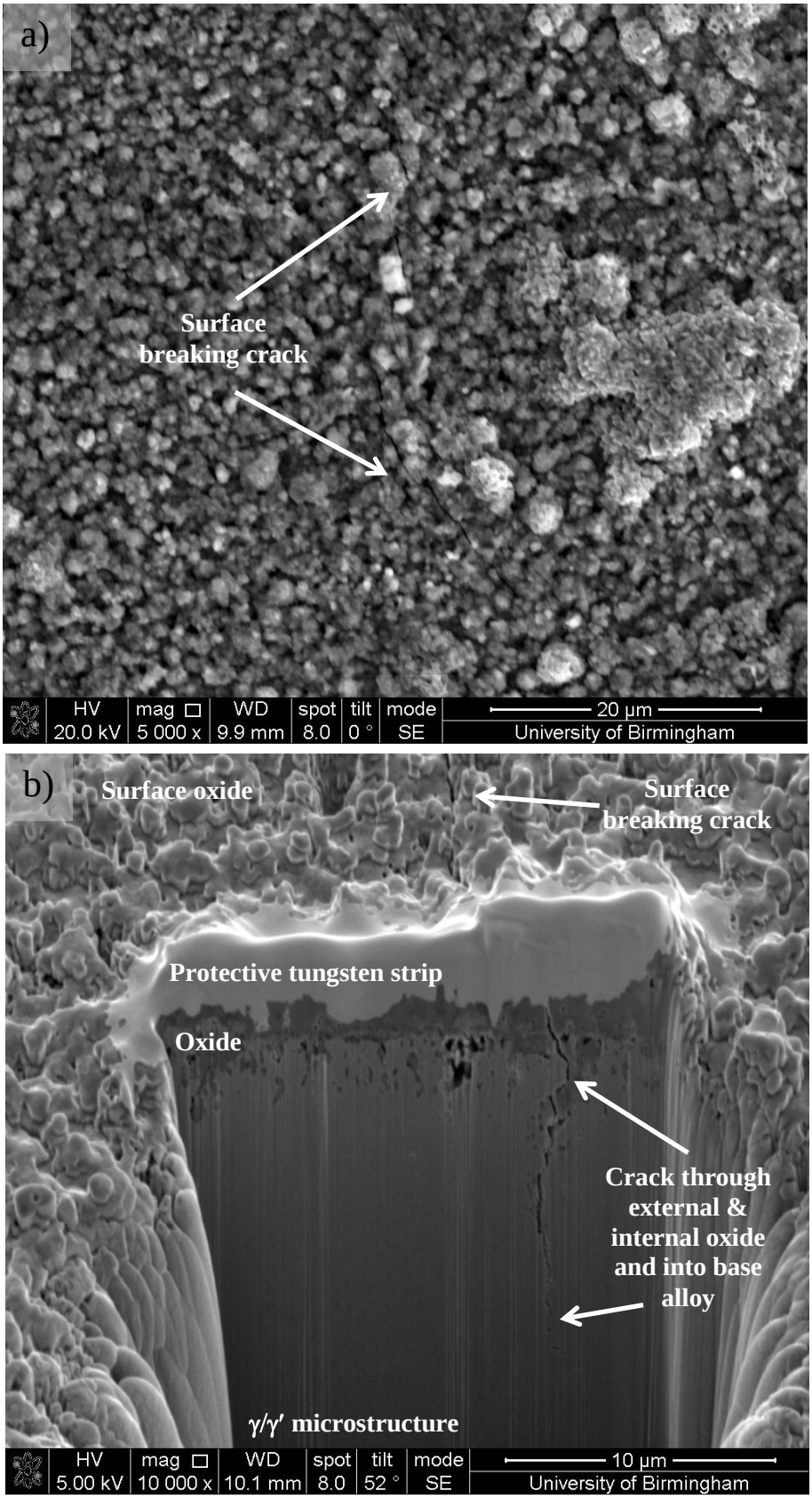

Figure 8-10: SE images taken using the electron beam on the FIB section of a pre-oxidised (2000 h) specimen that failed after $6x10^5$ cycles at 800 MPa with a) surface-breaking cracks in the external oxide and b) section through surface-breaking crack in a) showing a crack progressing through the external oxide and intergranular internal oxide before penetrating into the base alloy.

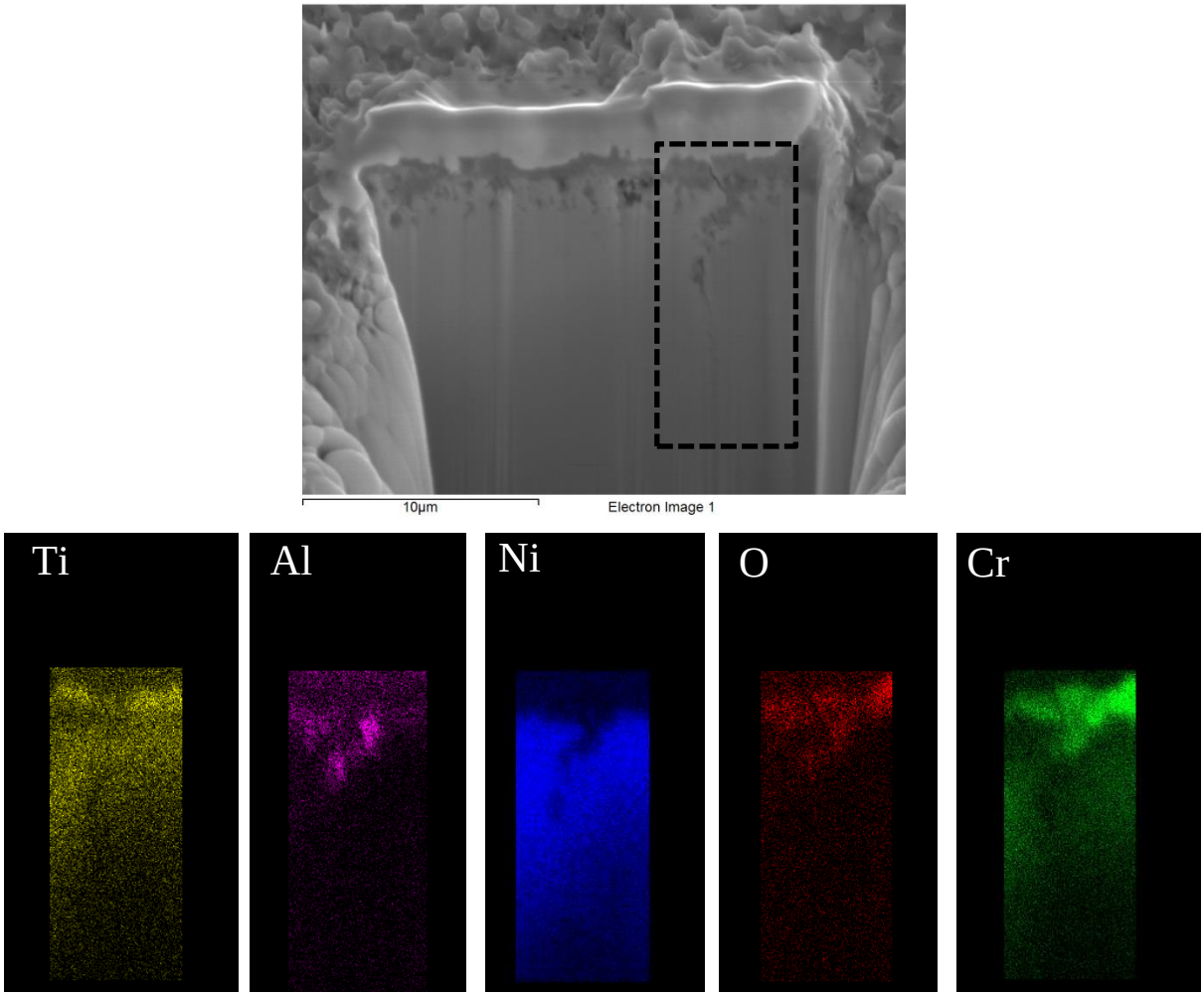

Figure 8-11: EDX image of the highlighted region of Figure 8-10, showing the oxide composition around the crack.

A large singular crack was found in the shorter pre-oxidised condition (100 hours at 700^{o}C) at a maximum applied stress of 800 MPa (Figure 8-12 (c)). This crack seems to originate in a similar manner as those in the longer pre-oxidation specimens, with it cutting through the external and intergranular internal oxide before progressing into the alloy by following crystallographic facets. This is not unexpected since the surface region is the area of highest tensile stress and these intergranular internal oxides are inherently sharp brittle structures with low fracture toughness. The tensile failure strains (<1%) and fracture toughness of both chromia (K_{1c} ~ 2.0 MPa.m$^{1/2}$)[91] and alumina (K_{1c} ~ 0.4-1.0 MPa.m$^{1/2}$) [91] are significantly lower than the bulk alloy for which the fatigue crack growth threshold is around 10 MPa.m$^{1/2}$. It is therefore feasible that these oxides crack preferentially leading to early fatigue crack initiation at a maximum applied stress of 800 MPa and therefore a deficit in fatigue life, since initiation is known to constitute the majority of the fatigue life.

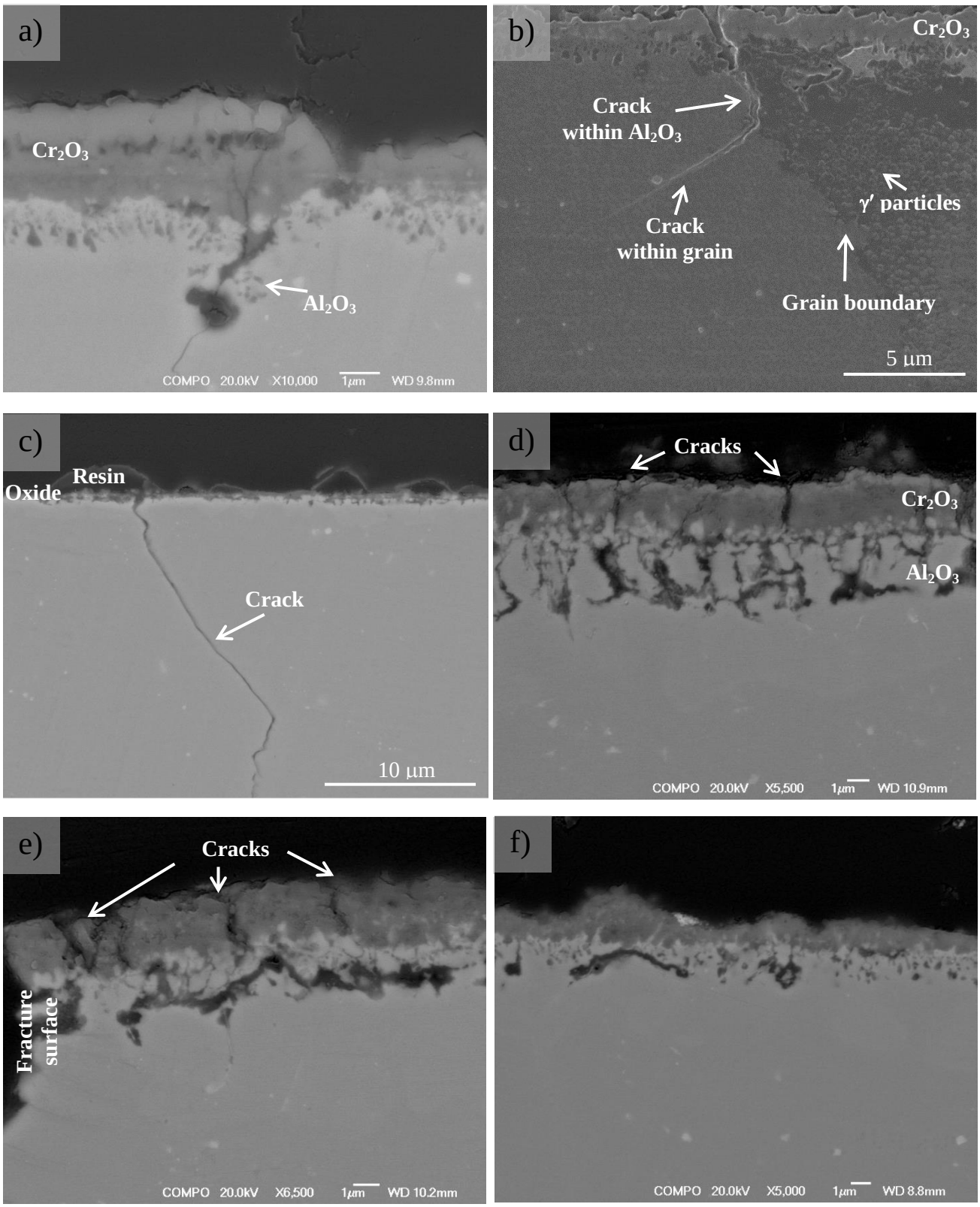

Figure 8-12: Images (BSE unless stated otherwise) of cross-sections through the area of maximum tensile stress showing: a) a crack through an intergranular alumina penetration of a pre-oxidised specimen (2000 hours) that failed after $1.9x10^6$ cycles at 800 MPa, b) a crack through an intergranular alumina penetration of the same sample as a) taken using electron channelling contrast imaging (ECCI), c) a pre-oxidised specimen (100 hours) that failed after $3.9x10^6$ cycles at 800 MPa, d) a pre-oxidised specimen (2000 hours) that failed after $1.1x10^7$ cycles at 825 MPa showing cracks only in the external chromia oxide, e) a pre-oxidised specimen (2000 hours) that failed after $3.7x10^7$ million cycles at 850 MPa again showing cracks only in the external chromia oxide and f) a pre-oxidised specimen (2000 hours) that did not fail at 900 MPa.

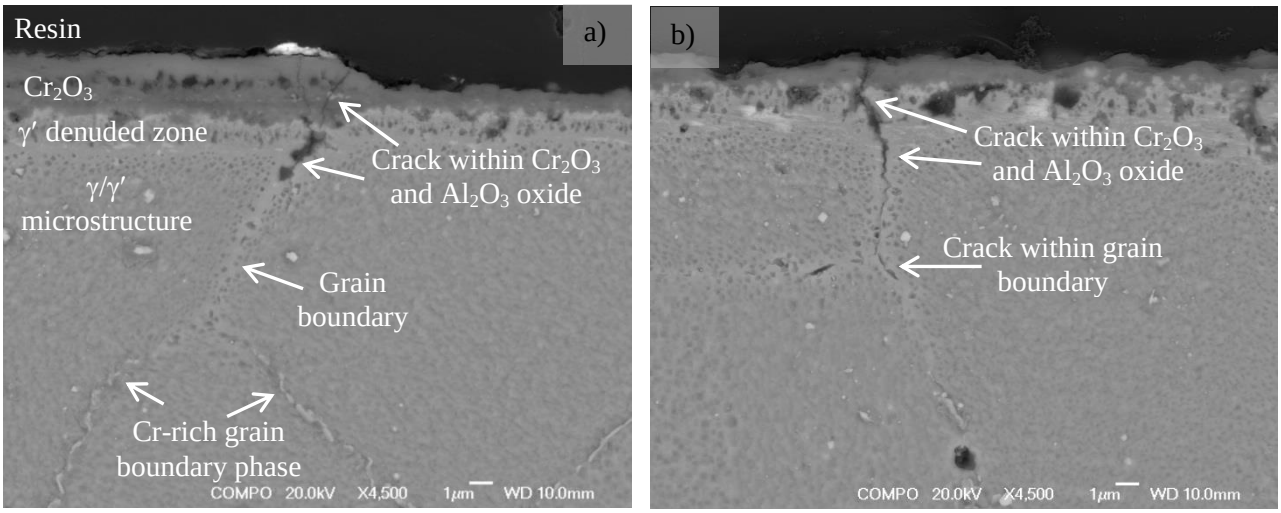

Figure 8-13: BSE images of an etched pre-oxidised (2000h) specimens that failed after 1.9x10^6 cycles at a maximum applied stress of 800 MPa, showing cracking of the external and intergranular internal oxide along with the presence of both a γ′ denuded zone and carbide dissolution zone.

This method of initiation is supported by a previous study which found that surface oxide cracking and crack initiation are closely correlated [150]. It is currently unclear which oxide is cracking initially and causing initiation. No cracking of the external oxide occurred above an intragranular internal oxide at this stress (800 MPa), nor was any cracking of the intragranular oxides recorded at any stresses. One possible reason that only the internal intergranular oxides crack is due to the intrusions being longer and thicker than intragranular ones. More importantly, perhaps, is the anisotropic nature of deformation between neighbouring grains, which can impose strain concentrations at the grain boundaries and promote cracking of the brittle intergranular oxide. Additionally they can act as a small notch, which creates a stress concentration which facilitates initiation and propagation more readily.

Above 800 MPa, an increase in fatigue life is found in the pre-oxidised specimens, with specimens at 825 and 850 MPa exhibiting longer lives and specimens at 900 MPa running out. This occurred in both pre-oxidised conditions (100 and 2000 hours at 700^{o}C). No cracks were visible in the sectioned 900 MPa specimens with cracks in the external oxide scale seen in both sectioned 825 and 850 MPa specimens. No cracks occurred sub-surface in the intragranular or intergranular internal oxides, at a maximum applied stress between 825-900 MPa. Above this stress range at a maximum outer fibre stress of 1000 MPa, failure occurs quickly displaying very short lives (2-4x10^5 cycles), in this case multiple cracks were found in the area of maximum stress in the external oxide scale and the intergranular alumina intrusions, often then penetrating further into the alloy (Figure 8-14). This indicates the stress above which catastrophic failure (σ_f) occurs.

Sudbrack et al (2012) [47] suggested that failure within the carbide dissolution zone was the main cause of the high temperature notched fatigue life deficit in the Ni-based superalloy, ME3, where weakened grain boundaries were thought to be the sites of initiation at high temperature [47]. In the present case, the Cr-Mo rich grain boundary phase dissolution zone is present appreciably beyond the crack and internal oxides (Table 8-I) with the crack penetrating into this zone, either being fully contained within the oxide (Figure 8-13(a)) or penetrating down the weaken grain boundary (Figure 8-13(b)). It is thought that these Cr-Mo rich grain boundary phases are $M_{23}C_6$. It seems these carbide-free grain boundaries could provide a weak path for the crack to propagate once it has initiated, although they could equally inhibit crack growth as a result of stress relaxation. It is likely that this region is more significant in the high temperature regime, where creep damage is significant. Supplementary work is required to clarify this further and investigate whether a similar method of initiation is seen at high temperature. The initiation mechanism at high temperature would be expected to differ to that at room temperature due to a significant increase in cross-slip, while the crack growth mechanism might change from transgranular morphology to an intergranular crack path, especially with the introduction of a dwell cycle. This occurs due to the subsequent cracking and reforming of grain boundary oxides ahead of the crack tip, leading to an intergranular crack morphology [163, 164, 166].

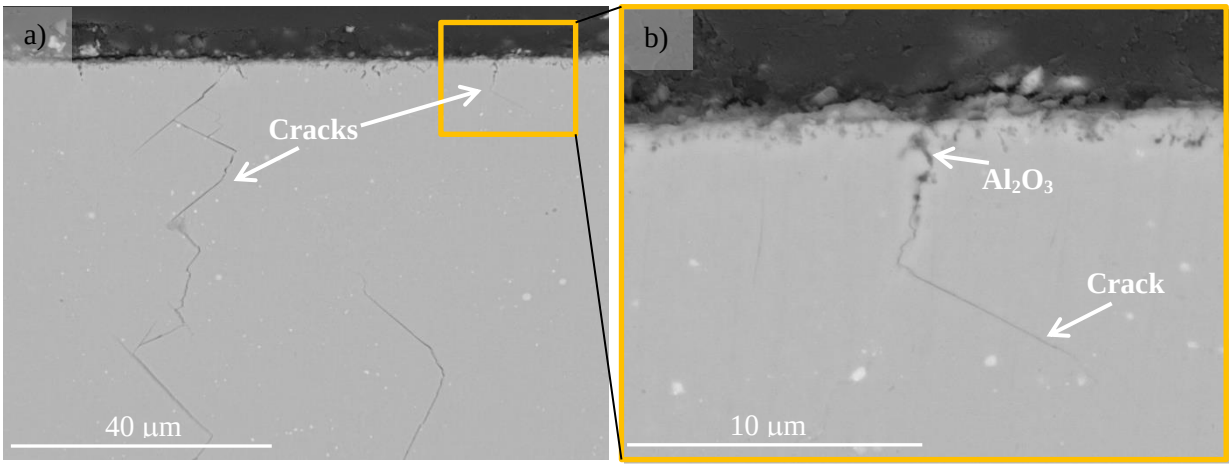

Figure 8-14: BSE images of a cross-section through the area of maximum tensile stress of a pre-oxidised specimen (2000 hours) that failed after 2x10^5 cycles, showing a) an overview of a small crack and a large crack both emanating from the surface and b) a higher magnification image of the highlighted region showing the crack progressing through internal alumina and into the alloy.

Table 8-I: Oxidation damage measurements, in microns, of both pre-oxidation conditions, 700°C for 100 and 2000 hours (±1 standard deviation).

Units in μm	External oxide scale	Internal oxide		γ′ denuded zone		Carbide dissolution
		Intragranular	Intergranular	Intragranular	Intergranular	
100 hours	0.84 (±0.21)	0.80 (±0.27)	1.55 (±0.26)	1.04 (±0.29)	2.52 (±0.56)	-
2000 hours	1.48 (±0.86)	2.06 (±0.46)	2.92 (±0.48)	2.11 (±0.32)	3.72 (±0.72)	14.50 (±1.81)

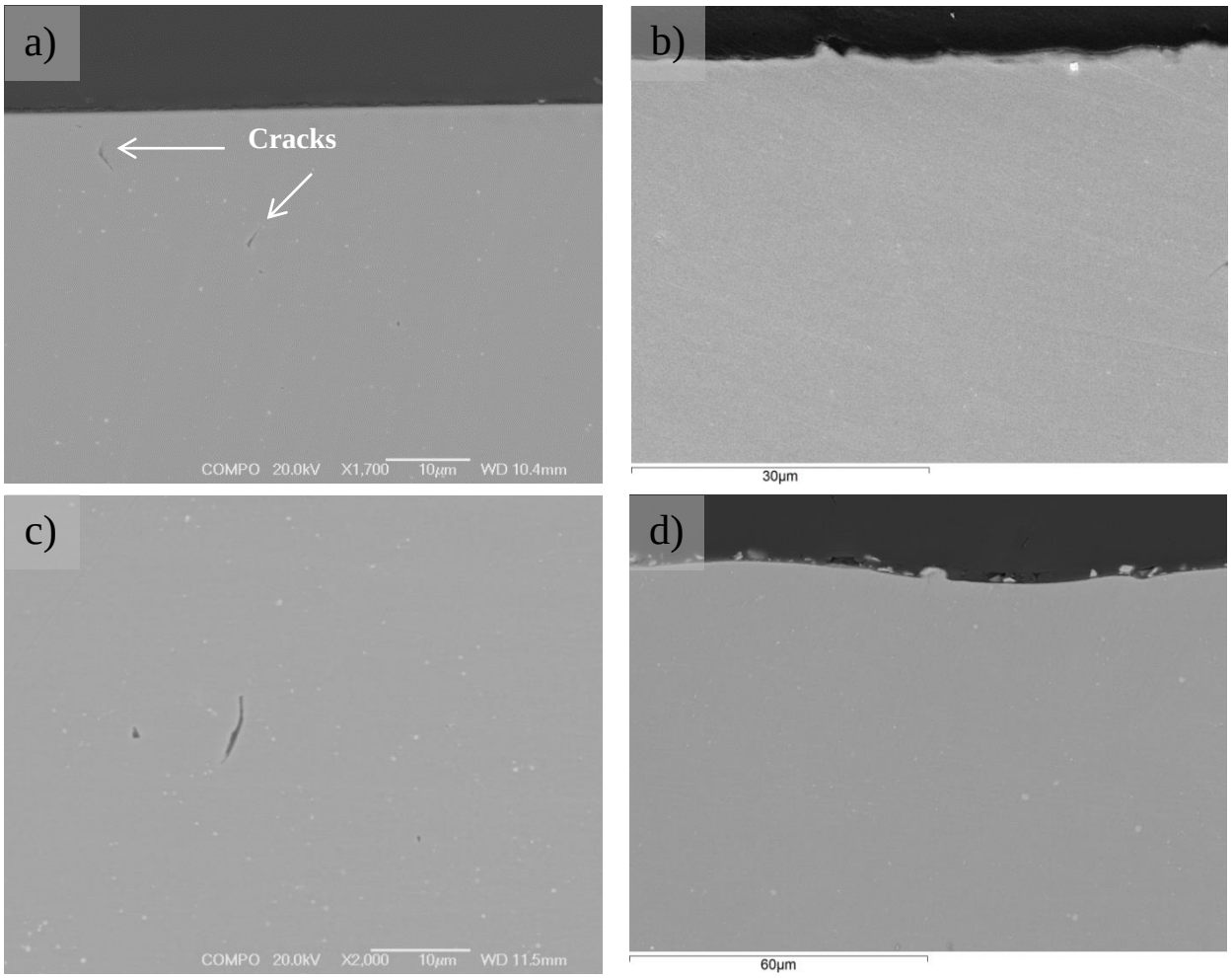

Figure 8-15: Images of cross-sections through the area of maximum applied stress of an as-machined specimen that failed after a) $1.1x10^7$ cycles at 800 MPa, b) $2.9x10^7$ cycles at 850 MPa and c) $9.6x10^6$ cycles at900 MPa and d) $1.3x10^7$ cycles at 1000 MPa. Some of them illustrate a number of small cracks both in sub-surface and surface regions.

In the as-machined condition some small cracks are recorded at most stresses (Figure 8-15) illustrating that these are likely to be forming sub-surface and likely to be from crystallographic facets that develop into large cracks which eventually bring about fracture.

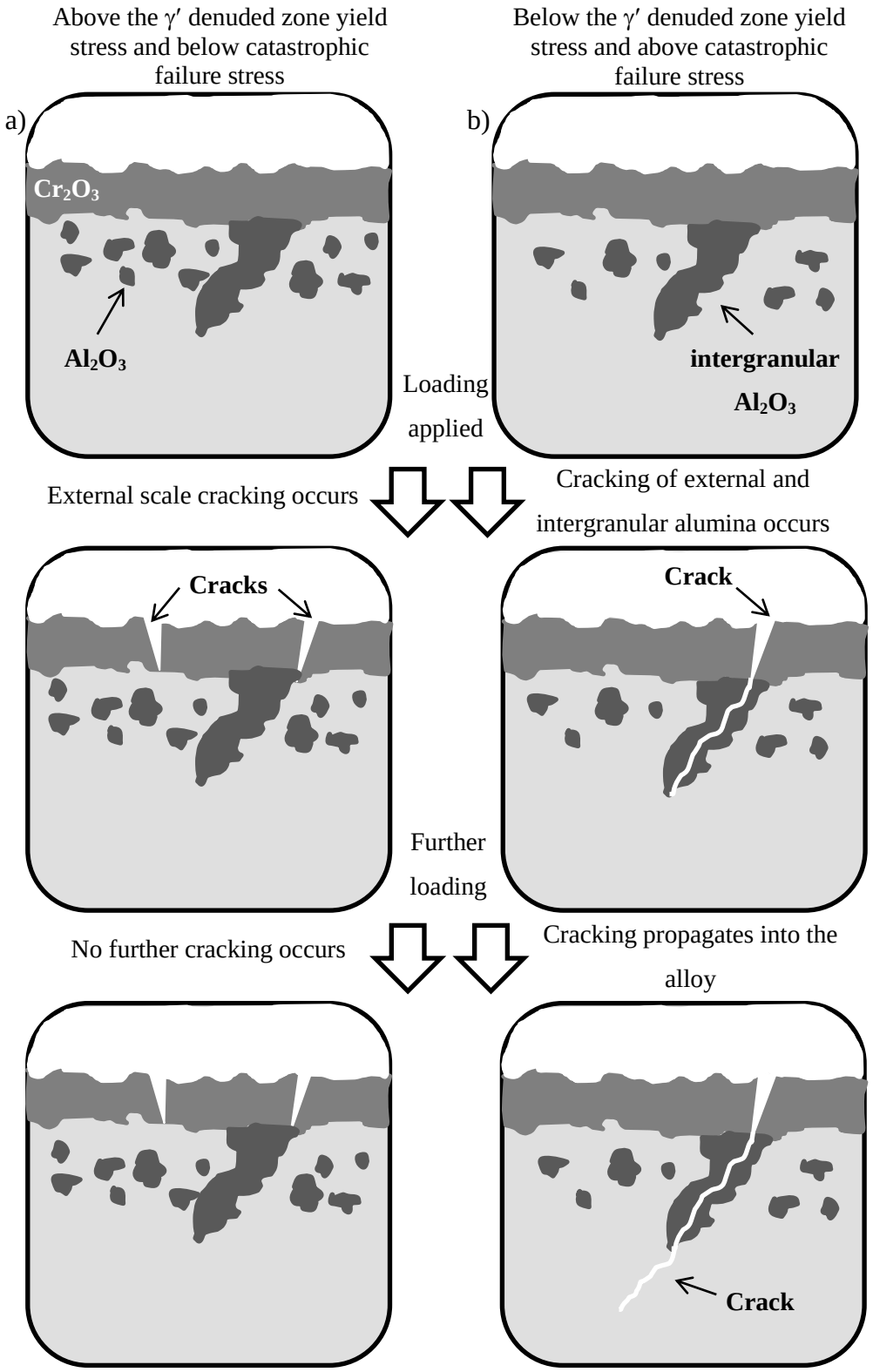

Figure 8-16: Schematic diagram of the mechanism of crack initiation in a pre-oxidised sample occurring a) above the predicted γ′ denuded zone yield stress, with no crack initiation occurring just cracking of the external oxide scale and b) below the predicted γ′ denuded zone yield stress where cracking of the external oxide scale, intergranular internal oxide and the alloy have occurred.

8.2.5 Mechanisms

A schematic diagram for the mechanism of fatigue crack initiation in pre-oxidised specimens is shown in Figure 8-16. This illustrates that at an applied stress of 800 MPa and 1000 MPa cracking of the external oxide scale and intergranular internal oxides occurs, thus causing early crack initiation and a significant reduction in fatigue life over the as-machined condition.

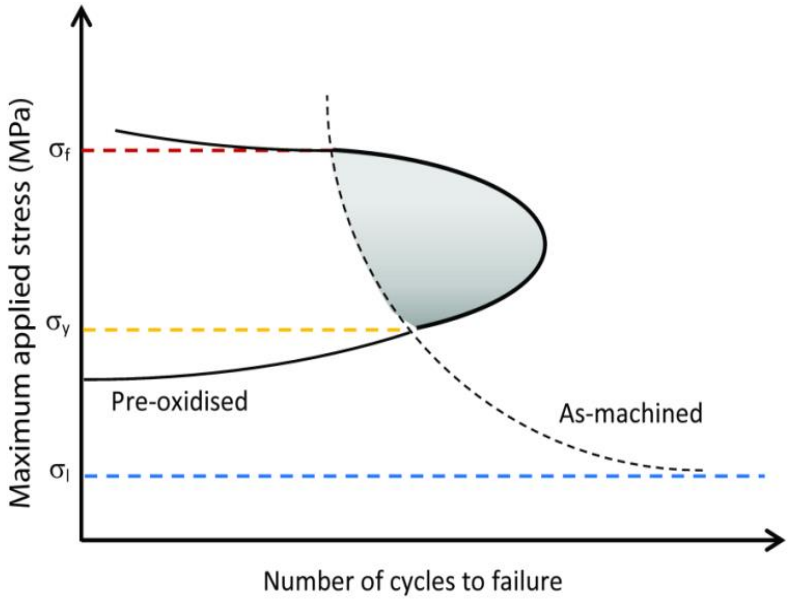

Figure 8-17: Schematic diagram of the room temperature high cycle fatigue performance of RR1000, in both the as-received and pre-oxidised conditions. The highlighted grey area is where the pre-oxidised condition exhibits a larger life than the as-received. σ_y indicates the yield stress of the γ′ denuded zone, σ_f indicates where above this catastrophic failure occurs and σ_l indicates the endurance limit.

At a stress level between 825 and 900 MPa a different mechanism is proposed to accommodate the increase in life found in the pre-oxidised samples. It has been established that the γ′ denuded zone has a significantly lower hardness that the bulk alloy. This weaker region could yield at a much lower stress (σ_y) than the bulk alloy and could therefore act as a barrier to blunt the crack by deforming to accommodate the stress, or to prevent the cracking of the intergranular alumina intrusions. This crack tip blunting mechanism could hinder the propagation of cracks both within the intergranular internal alumina intrusions and through the γ′ denuded region. It could also be possible that in the act of yielding to accommodate the stress that it stops cracks from forming internally hindering initiation (Figure 8-16). It is postulated that this γ′ denuded region yields at between 825 and 850 MPa, as the mechanism seems to start occurring at 825 MPa, with the enhancement in fatigue life becoming more pronounced as the applied load increases. This only occurs up to a point (σ_f) after which catastrophic failure of the alloy occurs. At 1000 MPa pre-oxidised specimens (2000 hours) fail much earlier than the as-machined specimens. It is suggested that early initiation occurs due to cracking of both the external and intergranular oxides and that the γ′ denuded zone is unable to accommodate the stress

concentration induced by this cracking through yielding. Therefore no crack blunting can occur and the weakened grain boundaries then act as low resistance crack pathways promoting quick crack growth and catastrophic failure.

This complex influence of pre-oxidation is summarised schematically in Figure 8-17. From this it can be approximated that a benefit exists at stresses between 825 MPa to ~950 MPa for the reasons discussed above. While either side of these stresses the pre-oxidised specimens display a significantly shorter fatigue life, illustrating that the oxides can have both a beneficial and detrimental effect on the fatigue life depending on the maximum applied stress of the fatigue cycle.

One uncertainty in this discussion is the actual level of stress present in the outer region of the testpiece. Here, there is a complex interaction occurring, as significant compressive stresses would be expected to develop in the external scale upon cooling to room temperature after a prolonged pre-oxidation exposure at 700^{o}C. The in-plane stress can be calculated for thin oxides on a thick substrate using the following equation stated in the literature review:

$$\sigma_{ox} = \frac{-E_{ox}\ \Delta T\ (\alpha_{met} - \alpha_{ox})}{1 - v_{ox}} \tag{8.1}$$

where, σ_{ox} is the in-plane stress in the oxide layer, E_{ox} is the Young's modulus of the oxide, α_{met} and α_{ox} are the thermal coefficient of expansion of the metal and oxide respectively, ΔT is the temperature change (initial temperature minus final temperature) and v_{ox} is the Poisson's ratio of the oxide. In the case here parameters for the thermal co-efficient of thermal expansion are shown in Table 8-II. Assuming a room temperature of 20^{o}C (293 K) a temperature drop of 680 K would occur. The Young's modulus of chromia is 275 GPa [94] and has a Poisson's ratio of 0.29 [95]. The total compressive stress developed during cooling would be 1.8 GPa. Now this cannot be the case here as we have amply demonstrated that the chromia oxide cracks in a tensile manner on the application of a tensile load of just 800 MPa. This would mean that tensile cracks were developing in an oxide scale that is experiencing a compressive stress of 1000 MPa, which is not plausible. A possible reason for the oxide scale to be experiencing a much lower compressive stress after cooling is that significantly internal compressive stresses develop in the near surface region because of the volume expansion associated with a significant precipitation of internal alumina. This would cause the external oxide scale to experience significant tensile stresses during oxidation. These would reduce the magnitude of the compressive stresses the chromia scale experiences once cooled.

That said the stress state underneath the external oxide scale is not known since there is a complex interaction between compressive stresses induced by the volume expansion of the internal oxides,

dissolution of both the γ′ strengthening phase and grain boundary carbides as well as the formation of metallic protuberances in the surface oxide attributed to creep relaxation of the underlying metallic region to accommodate some of the stresses induced by internal oxidation. This needs further investigation as it will affect the stress experienced by the internal oxides and consequently affect crack initiation.

Table 8-II: Coefficients of thermal expansion [92, 95].

Material	Coefficient of thermal expansion ($10^6 K^{-1}$)	T (^oC)
Cr_2O_3	8.5	400-800
Al_2O_3	8.1	400-800
Nimonic 75	15.4	20-700
CMSX 6	15.8	-

8.3 Concluding Summary

The effects of prior oxidation on the fatigue performance of a coarse-grained RR1000 have been studied at room temperature using four-point bend of rectangular bar testpieces. The following conclusions can be drawn:

- Pre-oxidation at 700^{o}C in air produces a continuous surface oxide scale mainly composed of a protective chromia scale. Sub-surface damage consisted of intergranular and intragranular intrusions of internal alumina. This is followed by a softer γ′ denuded region. This is found in both pre-oxidation time periods, with the longer time period having a deeper penetration of oxidation damage.

- Pre-oxidation significantly affects the fatigue life above the fatigue limit. While pre-oxidised testpieces failed predominantly with shorter fatigue lives than those obtained from the as-machined testpieces, they were also observed to outperform the as-machined testpieces at stress levels around 825-900 MPa. Around and below the fatigue limit (<700 MPa), the oxide scale remains un-cracked and no fatigue deficit is observed.

- At low stresses ~800 MPa a change in initiation location from that in the as-machined specimens was seen after pre-oxidation, from sub-surface to surface locations. This indicated that oxidation and not crystallographic facets were the cause of early crack nucleation in the

pre-oxidised samples. Above 850 MPa the as-machined specimens exhibited surface initiations.

- Above the fatigue limit, the chromia oxide scale and intergranular alumina intrusions are prone to crack which introduces a local stress concentration and therefore promotes earlier fatigue crack initiation. This has been confirmed to be the case both below and above a stress level of 900 MPa. It is anticipated that such an effect could also be achieved through localised creep deformation around crack tips at high temperature. A schematic diagram has been produced to describe the fatigue crack initiation mechanisms (Figure 8-16).

- The better fatigue performance of the pre-oxidised specimens at 900 MPa is attributed to plastic yielding of the weaker γ' denuded zone, which either effectively eases the stress concentration introduced by the cracking of the chromia scale and intergranular internal oxides or by preventing the cracking of the external oxide/intergranular internal oxides. This hinders further crack penetration into the matrix, thus, improving fatigue life. It is anticipated that such an effect could also be achieved through localised creep deformation around crack tips at high temperatures.

- Similar trends on the impact on fatigue life are found for two pre-oxidation periods despite the different depths of oxidation damage.

- Additional work is needed to try and provide further clarification of both the stress state in the external oxide upon cooling and in the sub-surface internally oxidised region as this will have a dramatic effect on the applied load and the mechanisms for the fatigue life enhancement/deterioration in life of the pre-oxidised specimens.

Chapter 9 - Summary and Conclusions

A summary of the main finding of this doctoral research are described below:

- In Chapter 1 a comprehensive review of the relevant literature was performed. This includes a description of the engine environment and architecture. In particular the drive for improved fuel economy and reduced CO_2 emissions driving operating temperatures upwards. The materials used for turbine discs, chromia forming Ni-based superalloys, have been extensively described. The fundamentals of oxidation were addressed, including the thermodynamics, kinetics, types of oxidation damage and response to stress. More specifically the oxidation of Ni-based superalloys and the effect of surface modifications, effect of an applied external load and effect of mechanical performance on oxidation performance was reviewed and summarised. This highlighted several gaps in current research, which will be addressed in the following chapters, these include the need to investigate: the effect of shot-peening and other surface conditions/amounts of cold work on the oxidation performance of Ni-based superalloys, and the role oxidation plays in fatigue crack initiation. Chapters 2, 3 and 4 deal with the aims, materials used and the experimental procedures and equipment used.

- In Chapters 5 and 6 the oxidation kinetics and oxidation damage of the Ni-based superalloy, RR1000, with several different surface conditions (polished, shot-peened, vibro-peened, turned and swaged), exposure times and temperatures (650^{o}C - 800^{o}C) has been comprehensively studied. The mass gain kinetics of polished CG RR1000 display parabolic growth across all temperatures tested and compare well with other similar Ni-based superalloys. Shot-peening had an adverse effect on the mass gain kinetics at 700^{o}C and 750^{o}C, but had no significant effect at 800^{o}C. The enhanced kinetics are because while shot-peening forms a protective oxide layer of chromia, as does the polished condition, it also provides shot-circuit diffusion pathways that enhance diffusion of chromium, titanium and aluminium. This accounts for the higher mass gain. In both cases kinetics were considerably higher than pure chromia formation, which was not unexpected since Ni-based superalloys have been shown to oxidise more than one element.

- In all cases the oxide composition comprised of an external scale of Cr_2O_3 with isolated grains of TiO_2 on the outer surface. Sub-surface alumina is present in several different morphologies depending on the surface conditions and level of residual stress/cold work prior to high temperature exposure. Beneath the alumina precipitates at temperatures at or above 800^{o}C is the presence of small TiN particles. All this sub-surface damage is contained within a γ' denuded zone which penetrates ahead of these internal precipitates. Penetrating further into the alloy is a grain boundary carbide dissolution region, which forms the deepest bounds of the oxidation

damage. At the external oxide/alloy interface an additional oxide of (Ti, Ta)O_2 forms at 800^{o}C in the shot-peened and polished conditions. Finally protuberances of base alloy were recorded within the external chromia scale and are postulated to form from the outward creep of the weaker depleted γ′ denuded zone to accommodate the increased volume resulting from the formation of internal oxides.

- Recrystallisation occurs, in the shot-peened condition, within this γ′ denuded zone, with a large number of micron sized grains (0.6 – 2.5 μm) formed. It is thought that in this case a combination of cold work, high temperature and elemental depletion is required in order for this to occur and therefore it would be expected in other surface modifications. The grain boundary carbide dissolution region depth is independent of cold work, residual stress and surface roughness. It is however affected significantly by the grain size of the alloy with a fine grain structure, leading to a larger reservoir of chromium on the grain boundaries in the near surface region. Thus, as chromium depletion in the formation of chromia external scale is the driving force for dissolution of these phases, a greater number of grain boundary phases have to dissolve to achieve the same overall dissolution depth.

- The external oxide scale grows significantly faster than pure chromia formation on chromium or high chromium containing austenitic steel, in all surface conditions. This increased oxidation rate is attributed to increased ionic transport caused by doping of the chromia external layer by titanium and the consequent creation of vacancies on the chromium sub-lattice. This enhancement decreases with oxide thickness in all conditions and temperatures apart from 800^{o}C for the polished condition and 700^{o}C for the turned condition. The enhancement can be as much as 2 orders of magnitude for thin scales although this decreases to a value of >10 at oxide thicknesses of 2 μm. At 800^{o}C in the polished condition the enhancement occurs but rather than decreasing with thickness it stays constant at a relatively low level ~14 and in the turned condition the enhancement occurs but increases slightly with oxide thickness.

- The internally oxidised zone and γ′ denuded zone were extensively studied in all conditions, with the vibro-peened and turned surface conditions showing a much larger distance, than the other surface conditions, between the internally oxidised zone and the γ′ denuded zone. The volume of the internal oxide rather than the penetration depth could be driving the γ′ denuded zone depth. The effect of cold work, residual stress and surface roughness was investigated without finding any strong correlations. Equations to describe the development of the internally oxidised zone and γ′ denuded zone of shot-peened condition have been produced.

- In Chapter 7 the use of focussed ion beam (FIB) as a sectioning and imaging technique has been evaluated to investigate the reported presence of a network of voids in the Ni-based superalloy, RR1000, after a high temperature exposure. The positive identification of voids and oxides using FIB techniques can be complex and prone to misinterpretation. The use of both conventional metallographic preparation and $SE_{electron}$ imaging showed a solid network of alumina throughout. SE_{ion} imaging has established that void-like features in fact contain solid matter when a range of sample tilts is used. This is a well-known phenomenon called ion channelling contrast, where feature contrast changes dependent on the incident angle of the ion beam. A number of different imaging conditions and tilt angles must be used, along with conventional preparation methods, to confidently and accurately confirm or refute the presence of 'voids' underneath oxides. In addition, like all techniques careful preparation, expertise and a good understanding of the technique being used will always be required.

- In Chapter 8 the room temperature four-point bend fatigue performance of RR1000 with and without pre-oxidation at 700^{o}C for 2000 or 100 hours, was investigated. This was done to investigate the role oxidation plays in fatigue crack initiation. Pre-oxidised testpieces failed predominantly with shorter fatigue lives than those obtained from the as-machined testpieces, although they were also observed to outperform the as-machined testpieces at stress levels around 825-900 MPa. Around and below the fatigue limit (<700 MPa), the oxide scale remains un-cracked and no fatigue deficit is observed. In all cases a surface initiation was found in the pre-oxidised condition, instead of the sub-surface initiations seen at low stresses in the as-received specimens, indicating that the oxides are the source of initiation.

- Above the fatigue limit oxides, especially internal intergranular oxides, have been shown to crack under fatigue conditions. This, combined with the fatigue life deficit found in the pre-oxidised conditions, indicates that it is feasible in principle that these external and internal oxides are the source of early fatigue crack initiation. Between 825-900 MPa plastic yielding of the weaker γ' denuded zone, effectively eases the stress concentration introduced by the cracking of the chromia scale and intergranular internal oxides. This hinders further crack penetration into the matrix, thus, improving fatigue life.

Chapter 10 - Future Work

Further work that has been highlighted by this doctoral research and which would complement this research is described in detail below:

- Detailed analysis of the oxidation damage is required of all the surface modifications (Vibro-peened, Turned and swaged) at a range of temperatures (600-900^{o}C) to complement those performed on the polished and shot-peened surface conditions. In addition the mass gain kinetics of all the oxidised surface conditions would be useful and would allow an accurate comparison with a number of superalloys in the literature. This would allow the more accurate determination of the activation energy for each type of oxidation damage in the shot-peened and polished conditions and illustrate whether two different activated processes are occurring at lower and higher temperatures as has been found in the mass gain results from the polished condition. It would also allow the activation energy for oxide formation to be calculated for the other surface modifications.

- There is the need to understand the reason why a constant enhancement occurs in the chromia growth rates of the polished surface condition at 800^{o}C whereas at 700^{o}C and 750^{o}C a decreasing rate-enhancement occurs. This constant rate-enhancement is not found in the shot-peened condition at any temperature or in any of the other surface conditions when oxidised at 700^{o}C, where a decreasing chromia growth rate-enhancement is found. There are several possible reasons that require further research, as recrystallisation of the sub-surface region is recorded in the oxidised shot-peened condition at 800^{o}C and not in the oxidised polished condition. Furthermore, in both conditions at 800^{o}C (Ti, Ta)O_2 is formed at the chromia/alloy interface, with a much smaller amount being found in the shot-peened condition. It is possible that this phase buffers Ti into the oxide scale at the longer time periods, but further work is required to clarify this. The investigation of whether recrystallisation occurs in the near surface region of the oxidised shot-peened condition at 700^{o}C and 750^{o}C as well as in all the oxidised surface modifications of RR1000 at 700^{o}C is required. In the oxidised turned surface condition a slight increase in the chromia rate-enhancement was found and this requires further investigation, as this is not understood.

- The rate controlling process for the sub-surface damage requires further effort using high resolution (STEM) elemental analysis to elucidate the diffusion of which oxidising species is controlling the formation of internal oxide. Additionally measuring the volume of internal alumina in the internally oxidised zone would produce some meaningful results and could allow

the prediction of the depth of the γ′ denuded zone. It might also help in the calculation of a conversion between the mass gain measurements recorded and the oxide depth produced as well as possibly eluding further correlations between the internal oxide and the amount of cold work or residual stress. TEM analysis is also required to confirm that the Cr-Mo rich grain boundary phases seen are $M_{23}C_6$ carbides and not sigma phase, as expected. Furthermore, detailed cross-sectional measurements need to be taken at a range of times and temperatures in order to calculate the kinetics of the dissolution of this phase. As the dissolution of these grain boundary phases are the deepest form of oxidation damage seen in RR1000. This would similarly require the use of additional grain sizes to further refine the strong correlation grain size has on Cr-Mo rich grain boundary phase dissolution depth.

- Moreover, more analysis and testing are required to isolate whether cold work, residual stress, surface roughness or recrystallisation (very fine grain size) is the driving force for the change in morphology and kinetics of the internal oxidation damage.

- Additional research is needed to try and provide further clarification of both the stress state in the external oxide upon cooling and in the sub-surface internally oxidised region. This is required as it will have a dramatic effect on the applied load the oxide experiences as well as the mechanisms for the fatigue life enhancement/deterioration in life seen in the pre-oxidised HCF specimens. The stress state in the external oxide once cooled could be performed using XRD analysis. Furthermore, it is important to clarify how the deficit in fatigue life at low stresses and the enhancement at high stresses occurs in both tension-tension specimens where the near surface region is no-longer the region of highest stress. The effect that elevated temperature has also requires further study as the fatigue mechanism changes with increasing temperature. Previous research has shown that the deficit occurs in pre-oxidised tension-tension specimens and attributes this to oxide cracking causing early fatigue crack initiation [150] but whether the mechanism of enhanced life occurs at elevated temperatures (>700^{o}C) is unclear. The use of an additional surface condition, i.e. shot-peening, would further knowledge in the area. As this is the surface condition the component goes into service. Additionally, the oxidation damage present on this surface condition does not contain the deep grain boundary internal oxides that crack during fatigue cycling.

- The effect of both a tensile and compressive static stress on the oxidation kinetics needs investigating at a range of stresses and temperatures, as like in the present study, high temperature oxidation of metals have primarily focussed on the study of oxidation in the unstressed condition. This is an important omission as in service components will experience significant external loads. This needs to be performed using detailed metallographic

measurements to characterise the composition and kinetics for each type of oxide growth, allowing the quantification of any enhancement that occurs in the oxide. It could also provide support for the growth enhancement that occurs on the growth of the oxides at the highly stressed crack tip. Again clarification of the stress state sub-surface and in the surface oxide would be required to elucidate the actual applied stress under which the oxide experienced during growth.

References

1. Rolls-Royce plc., *The Jet engine*. 5th ed. 2005: Rolls-Royce.

2. Cumpsty, N., *Jet Propulsion: A simple guide to the aerodynamic and thermodynamic design and performance of jet engines*. 2003: Cambridge University Press.

3. ACARE *European Aeronautics: A vision for 2020*. 2001.

4. Salomon, K.A., *Selection and development of alloys for turbine disc applications* in *Department of Metallurgy and Materials*. 2006, University of Birmingham: Birmingham. p. 71.

5. Claudio, R.A., C.M. Branco, E.C. Gomes, G.F. Harrison, and M.R. Winstone, *Fatigue life prediction and failure analysis of a gas turbine disc using the finite-element method.* Fatigue & Fracture of Engineering Materials & Structures, 2004. **27**(9): p. 849-860.

6. Knott, J.F., *The durability of rotating components in gas turbines*, in *PARSONS 2000: Fifth International Charles Parsons Turbine Conference*. 2000: Cambridge, UK. p. 950-960.

7. Reed, R., ed. *The Superalloys: Fundamentals and applications*. 2006, Cambridge university press: Cambridge.

8. Geddes, B., H. Leon, and X. Huang, *Introduction*, in *Superalloys: Alloying and performance* 2010, ASM International. p. 1-8.

9. Durand-Charre, M., *The microstructure of superalloys*. 1997: Gordon and Breach Science Publishers.

10. Holt, R.T. and W. Wallace, *Impurities and trace elements in nickel-base superalloys.* International Metals Reviews, 1976. **21**(1): p. 1-24.

11. Sinha, O.P., M. Chatterjee, V.V.R.S. Sarma, and S.N. Jha, *Effect of residual elements on high performance nickel base superalloys for gas turbines and strategies for manufacture.* Bulletin of Materials Science, 2005. **28**(4): p. 379-382.

12. Geddes, B., H. Leon, and X. Huang, *Compositional effects*, in *Superalloys: Alloying and performance*. 2010, ASM international.

13. Ross, E.W. and C.T. Sims, *Nickel-base alloys*, in *Superalloys II*, C.T. Sims, N.S. Stoloff, and W.C. Hagel, Editors. 1987, John Wiley and Sons, Inc. : New York. p. 97-133.

14. Sims, C.T., *Superalloys: Genesis and character*, in *Superalloys II*, C.T. Sims, N.S. Stoloff, and W.C. Hagel, Editors. 1987, John Wiley and Sons, Inc. : New York. p. 3-26.

15. Gabb, T.P., J. Telesman, P.T. Kantzos, J.W. Smith, and P.F. Browning, *Effects of high temperature exposures on fatigue life of disk superalloys.* Superalloys 2004, 2004: p. 269-274.

16. Gayda, J. and R.V. Miner, *Fatigue crack initiation and propagation in several nickel-base superalloys at 650°C.* International Journal of Fatigue, 1983. **5**(3): p. 135-143.

17. Kennedy, R.L., *Allvac 718plus, superalloy for the next forty years*, in *Superalloys 718, 625, 706 and derivatives 2005*, E.A. Loria, Editor. 2005, TMS: USA.

18. Donachie, M.J. and S.J. Donachie, *Understanding superalloy metallurgy,* in *Superalloys: A technical guide*. 2002, ASM International. p. 26-39.

19. Ricks, R.A., A.J. Porter, and R.C. Ecob, *The growth of γ′ precipitates in nickel-base superalloys.* Acta Metallurgica, 1983. **31**(1): p. 43-53.

20. Geddes, B., H. Leon, and X. huang, *Compositional Effects*, in *Superalloys: Alloying and Performance*. 2010, ASM International.

21. Song, K. and M. Aindow, *Grain growth and particle pinning in a model Ni-based superalloy.* Materials Science and Engineering: A, 2008. **479**(1–2): p. 365-372.

22. Reed, R.C., M.P. Jackson, and Y.S. Na, *Characterization and modeling of the precipitation of the sigma phase in UDIMET 720 and UDIMET 720Li.* Metallurgical and Materials Transactions A, 1999. **30**(3): p. 521-533.

23. Geddes, B., H. Leon, and X. Huang, *Strengthening mechanisms*, in *Superalloys: Alloying and performance*. 2010, ASM International.

24. Stoloff, N.S., *Fundamentals of strengthening,* in *Superalloys II*, C.T. Sims, N.S. Stoloff, and W.C. Hagel, Editors. 1987, John Wiley and Sons, Inc. : New York. p. 61-95.

25. Donachie, M.J. and S.J. Donachie, *Structure/property relationships*, in *Superalloys: A technical guide*. 2002, ASM International. p. 212-286.

26. Soboyejo, W., *Dislocation strengthening mechanisms*, in *Mechanical Properties of Engineering Materials* 2002, Marcel Dekker, Inc: New York.

27. Dieter, G.E. and D. Bacon, *Mechanical metallurgy*. 1988: McGraw-Hill.

28. Davies, R.G. and N.S. Stoloff, *On the yield stress of aged Ni-Al alloys.* Transactions of the Metallurgical Society of AIME, 1965. **233**: p. 714-719.

29. Beardmore, P., R.G. Davies, and T.L. Johnston, *On the temperature dependence of the flow stress of nickel-base alloys.* Transactions of the Metallurgical Society of AIME, 1969. **245**: p. 1537-1545.

30. Thornton, P.H., R.G. Davies, and T.L. Johnston, *The temperature dependence of the flow stress of the γ' phase based upon Ni3Al.* Metallurgical Transactions, 1970. **1**(1): p. 207-218.

31. Reed, R.C., *Superalloys for turbine disc applications*, in *The Superalloys: Fundamentals and applications*. 2006, Cambridge University Press: Cambridge. p. 217-282.

32. Campbell, F.C., *Superalloys*, in *Manufacturing technology for aerospace structural materials*. 2006, Elsevier Science: Oxford. p. 211-272.

33. Silva, J.M., R.A. Cláudio, C.M. Branco, and J.M. Ferreira, *Creep-fatigue behavior of a new generation Ni-base superalloy for aeroengine usage*. Procedia Engineering, 2010. **2**(1): p. 1865-1875.

34. Pint, B.A., J.R. DiStefano, and I.G. Wright, *Oxidation resistance: One barrier to moving beyond Ni-base superalloys.* Materials Science and Engineering: A, 2006. **415**(1-2): p. 255-263.

35. Pieraggi, B., *Defects and transport in oxides and oxide scales*, in *Shreir's corrosion: Basic concepts, high temperature corrosion*, T.J.A. Richardson, Editor. 2010. p. 101-131.

36. Birks, N., G.H. Meier, and F.S. Pettit, *Introduction to the high temperature oxidation of metals*. 2nd ed. 2006: Cambridge university press.

37. Chevalier, S., *Mechanisms and kinetics of oxidation*, in *Shreir's corrosion: Basic concepts, high temperature corrosion*, T.J.A. Richardson, Editor. 2010. p. 132-152.

38. Gleeson, B., *Thermodynamics and theory of external and internal oxidation of alloys*, in *Shreir's corrosion: Basic concepts, high temperature corrosion*, T.J.A. Richardson, Editor. 2010. p. 180-194.

39. Kofstad, P., *High-temperature oxidation of metals*. 1966: Wiley.

40. Kofstad, P., *Defects and transport properties of metal oxides.* Oxidation of Metals, 1995. **44**(1-2): p. 3-27.

41. Naoumidis, A., H.A. Schulze, W. Jungen, and P. Lersch, *Phase studies in the chromium-manganese-titanium oxide system at different oxygen partial pressures.* Journal of the European Ceramic Society, 1991. **7**(1): p. 55-63.

42. Blacklocks, A.N., A. Atkinson, R.J. Packer, S.L.P. Savin, and A.V. Chadwick, *An XAS study of the defect structure of Ti-doped α-Cr_2O_3.* Solid State Ionics, 2006. **177**(33–34): p. 2939-2944.

43. Atkinson, A., M.R. Levy, S. Roche, and R.A. Rudkin, *Defect properties of Ti-doped Cr_2O_3.* Solid State Ionics, 2006. **177**(19–25): p. 1767-1770.

44. Cruchley, S., H.E. Evans, M.P. Taylor, M.C. Hardy, and S. Stekovic, *Chromia layer growth on a Ni-based superalloy: Sub-parabolic kinetics and the role of titanium.* Corrosion Science, 2013. **75**: p. 58-66.

45. Wagner, C., *Reaktionstypen bei der Oxydation von Legierungen.* Zeitschrift für Elektrochemie, Berichte der Bunsengesellschaft für physikalische Chemie, 1959. **63**(7): p. 772-782.

46. Pieraggi, B., *Calculations of parabolic reaction rate constants.* Oxidation of Metals, 1987. **27**(3-4): p. 177-185.

47. Sudbrack, C.K., S.L. Draper, T.T. Gorman, J. Telesman, T.P. Gabb, and D.R. Hull, *Oxidation and the effects of high temperature exposures on notched fatigue life of an advanced powder metallurgy disk superalloy*, in *Superalloys 2012: 12th International Symposium on Superalloys*, E.S. Huron, et al., Editors. 2012, TMS: Seven Springs, PA. p. 863-872.

48. Brady, M.P., I.G. Wright, and B. Gleeson, *Alloy design strategies for promoting protective oxide-scale formation.* JOM, 2000. **52**(1): p. 16-21.

49. Tedmon, C.S., *The effect of oxide volatilization on the oxidation kinetics of Cr and Fe-Cr Alloys.* Journal of The Electrochemical Society, 1966. **113**(8): p. 766-768.

50. Wood, G.C., *High-temperature oxidation of alloys.* Oxidation of Metals, 1970. **2**(1): p. 11-57.

51. Stott, F.H., *Influence of alloy additions on oxidation.* Materials Science and Technology, 1989. **5**(8): p. 734-740.

52. Stott, F.H., *The protective action of oxide scales in gaseous environments at high temperature* Reports on Progress in Physics, 1987. **50**(7): p. 861-913.

53. Hussey, R.J., D.F. Mitchell, and M.J. Graham, *The growth and structure of oxide films formed on single crystal (100) and polycrystalline Cr between 550 and 900 °C.* Materials and Corrosion, 1987. **38**(10): p. 575-583.

54. Lillerud, K.P. and P. Kofstad, *On high temperature oxidation of chromium: I . Oxidation of annealed, thermally etched chromium at 800°–1100°C.* Journal of The Electrochemical Society, 1980. **127**(11): p. 2397-2410.

55. Pieraggi, B. and R.A. Rapp, *Chromia scale growth in alloy oxidation and the reactive element effect.* Journal of the Electrochemical Society, 1993. **140**(10): p. 2844-2850.

56. Hou, P.Y., *Oxidation of metals and alloys*, in *Shreir's Corrosion*, B. Cottis, et al., Editors. 2010, Elsevier: Oxford. p. 195-239.

57. Hou, P.Y., *Segregation phenomena at thermally grown Al_2O_3/alloy interfaces.* Annual Review of Materials Research, 2008. **38**(1): p. 275-298.

58. Stott, F.H., G.C. Wood, and M.G. Hobby, *A comparison of the oxidation behavior of Fe-Cr-Al, Ni-Cr-Al, and Co-Cr-Al alloys.* Oxidation of Metals, 1971. **3**(2): p. 103-113.

59. Lobb, R.C., J.A. Sasse, and H.E. Evans, *Dependence of oxidation behaviour on silicon content of 20%Cr austenitic steels.* Materials Science and Technology, 1989. **5**(8): p. 828-834.

60. Issartel, J., S. Martoia, F. Charlot, V. Parry, G. Parry, R. Estevez, and Y. Wouters, *High temperature behavior of the metal/oxide interface of ferritic stainless steels.* Corrosion Science, 2012. **59**(0): p. 148-156.

61. Stott, F.H., G.C. Wood, and J. Stringer, *The influence of alloying elements on the development and maintenance of protective scales.* Oxidation of Metals, 1995. **44**(1-2): p. 113-145.

62. Ennis, P.J., W.J. Quadakkers, and H. Schuster, *The effect of selective oxidation of chromium on the creep strenght of Alloy 617* Journal De Physique Iv, 1993. **3**(C9): p. 979-986.

63. Durham, R.N., B. Gleeson, and D.J. Young, *Factors affecting chromium carbide precipitate dissolution during alloy oxidation.* Oxidation of Metals, 1998. **50**(1-2): p. 139-165.

64. Pillai, S.R., N.S. Barasi, H.S. Khatak, and J.B. Gnanamoorthy, *Effect of external stress on the behavior of oxide scales on 9Cr-1Mo steel.* Oxidation of Metals, 1998. **49**(5-6): p. 509-530.

65. Chyrkin, A., P. Huczkowski, V. Shemet, L. Singheiser, and W.J. Quadakkers, *Sub-scale depletion and enrichment processes during high temperature oxidation of the nickel-base alloy 625 in the temperature range 900–1000 °C.* Oxidation of Metals, 2011. **75**(3-4): p. 143-166.

66. Pillai, R., H. Ackermann, H. Hattendorf, and S. Richter, *Evolution of carbides and chromium depletion profiles during oxidation of Alloy 602 CA.* Corrosion Science, 2013. **75**(0): p. 28-37.

67. Edmonds, I.M., H.E. Evans, C.N. Jones, and R.W. Broomfield, *Intermediate temperature internal oxidation in fourth generation Ru-bearing single-crystal nickel-base superalloys.* Oxidation of Metals, 2008. **69**(1-2): p. 95-108.

68. Young, D.J., *High Temperature Oxidation and Corrosion of Metals*. 2008: Elsevier.

69. Wood, G.C., T. Hodgkiess, and D.P. Whittle, *A comparison of the scaling behaviour of pure iron-chromium and nickel-chromium alloys in oxygen.* Corrosion Science, 1966. **6**(3–4): p. 129-147.

70. Young, D.J., *Predicting internal oxidation: Building on the wagner model.* . Materials Science Forum, 2011. **969**: p. 1-11.

71. Admed, O. and D.J. Young, *Precipitate distributions in internally carburised and oxidised Fe-Cr alloys*, in *High temperature corrosion and materials chemisty II*, M.J. McNallan, et al., Editors. 2000, The Electrochemical society.

72. Chang, S.Y., U. Krupp, and H.J. Christ, *Formation and compensation of internal stresses during internal nitridation of nickel-base alloys.* Materials Science and Engineering: A, 2001. **301**(2): p. 196-206.

73. Ackermann, H., G. Teneva-Kosseva, K. Lucka, H. Koehne, S. Richter, and J. Mayer, *Oxidation behaviour of selected wrought Ni-base high temperature alloys when used as flame tube material in modern blue flame oil burners.* Corrosion Science, 2007. **49**(10): p. 3866-3879.

74. Mackert, J.R., R.D. Ringle, and C.W. Fairhurst, *High-temperature behavior of a PD-AG alloy for porcelain* Journal of Dental Research, 1983. **62**(12): p. 1229-1235.

75. Edmonds, I.M., H.E. Evans, and C.N. Jones, *The role of γ′ precipitate dispersion in forming a protective scale on Ni-based superalloy at 750°C.* Oxidation of Metals, 2012. **73**: p. 193-206.

76. Issartel, J., R. Estevez, G. Parry, V. Parry, S. Martoia, and Y. Wouters, *A possible mechanism for protrusions formation at the metal/oxide interface during short time oxidation of ferritic stainless steel.* Oxidation of Metals, 2013. **79**(1-2): p. 65-72.

77. Huszkowski, P., S. Ertl, J. Piron-Abellan, N. Christiansen, T. fler, V. Shemet, L. Singheiser, and W.J. Quadakkers, *Effect of component thickness on lifetime and oxidation rate of chromia forming ferritic steels in low and high pO_2 environments.* Materials at High Temperatures, 2005. **22**(3-4): p. 253-262.

78. Rubly, R.P. and D.L. Douglass, *Internal nitridation of nickel-chromium alloys.* Oxidation of Metals, 1991. **35**(3-4): p. 259-278.

79. Yi, H.C., S.W. Guan, W.W. Smeltzer, and A. Petric, *Internal oxidation of Ni-Al and Ni-Al-Si alloys at the dissociation pressure of NiO.* Acta Metallurgica et Materialia, 1994. **42**(3): p. 981-990.

80. Shida, Y., F.H. Stott, B.D. Bastow, D.P. Whittle, and G.C. Wood, *Development of preferential intergranular oxides in nickel-aluminum alloys at high temperatures.* Oxidation of Metals, 1982. **18**(3-4): p. 93-113.

81. Rhines, F.N., W.A. Johnson, and W.A. Anderson, *Rates of high-temperature oxidation of dilute copper alloys.* Transactions of the American Institute of Mining and Metallurgical Engineers, 1942. **147**: p. 205-220.

82. Maak, F., *Zur Auswertung Von Messungen Der Schichtdicken Binarer Legierungen Mit Innerer Oxydation Dei Gleichzeitiger Ausserer Oxydation* Zeitschrift Fur Metallkunde, 1961. **52**(8): p. 545-546.

83. Rapp, R.A., *Kinetics, Microstructures and Mechanism of Internal Oxidation - Its Effect and Prevention in High Temperature Alloy Oxidation.* Corrosion, 1965. **21**: p. 382-401.

84. Stott, F.H. and G.C. Wood, *Internal oxidation.* Materials Science and Technology, 1988. **4**: p. 1072-1078.

85. Douglass, D.L., *A critique of internal oxidation in alloys during the post-wagner era.* Oxidation of Metals, 1995. **44**(1-2): p. 81-111.

86. Giggins, C.S. and F.S. Pettit, *Oxidation of Ni-Cr-Al Alloys Between 1000^{o} and 1200^{o}C.* Journal of the Electrochemical Society, 1971. **118**(11): p. 1782-1790.

87. Evans, H. and M. Taylor, *Oxidation of high-temperature coatings.* Proceedings of the Institution of Mechanical Engineers, Part G: Journal of Aerospace Engineering, 2006. **220**(1): p. 1-10.

88. Evans, H.E., A.T. Donaldson, and T.C. Gilmour, *Mechanisms of breakaway oxidation and application to a chromia-forming steel.* Oxidation of Metals, 1999. **52**(5-6): p. 379-402.

89. Evans, H.E. and M.P. Taylor, *Diffusion cells and chemical failure of MCrAlY bond coats in thermal-barrier coating systems.* Oxidation of Metals, 2001. **55**(1-2): p. 17-34.

90. Schütze, M., *Stress effects in high temperature oxidation*, in *Shreir's Corrosion*, B. Cottis, et al., Editors. 2010, Elsevier: Oxford. p. 153-179.

91. Evans, H.E., *Stress effects in high temperature oxidation of metals.* International Materials Reviews, 1995. **40**(1): p. 1-40.

92. Schütze, M., D.R. Holmes, and I.o. Corrosion, *Protective oxide scales and their breakdown*. 1997: Wiley.

93. Wood, G.C., F.H. Stott, D.P. Whittle, Y. Shida, and B.D. Bastow, *The high-temperature internal oxidation and intergranular oxidation of nickel-chromium alloys.* Corrosion Science, 1983. **23**(1): p. 9-25.

94. Saeki, I., T. Ohno, D. Seto, O. Sakai, Y. Sugiyama, T. Sato, A. Yamauchi, K. Kurokawa, M. Takeda, and T. Onishi, *Measurement of Young's modulus of oxides at high temperature related to the oxidation study.* Materials at High Temperatures, 2011. **28**(4): p. 264-268.

95. Robertson, J. and M.I. Manning, *Limits to adherence of oxide scales.* Materials Science and Technology, 1990. **6**(1): p. 81-92.

96. Schütze, M., M. Malessa, V. Rohr, and T. Weber, *Development of coatings for protection in specific high temperature environments.* Surface and Coatings Technology, 2006. **201**(7): p. 3872-3879.

97. Hancock, P. and J.R. Nicholls, *Application of fracture mechanics to failure of surface oxide scales.* Materials Science and Technology, 1988. **4**(5): p. 398-406.

98. Schütze, M., *Deformation and cracking behavior of protective oxide scales on heat-resistant steels under tensile strain.* Oxidation of Metals, 1985. **24**(3-4): p. 199-232.

99. Schütze, M., *Assessment of the limits to the protective effect of oxide scales in high temperature technology, set by deformation of the substrate material.* International Journal of Pressure Vessels and Piping, 1991. **47**(3): p. 293-315.

100. Evans, H.E. and R.C. Lobb, *Conditions for the initiation of oxide-scale cracking and spallation.* Corrosion Science, 1984. **24**(3): p. 209-222.

101. Evans, H.E., *Cracking and spalling of protective oxide layers.* Materials Science and Engineering: A, 1989. **120–121, Part 1**(0): p. 139-146.

102. Schütze, M., *Plasticity of protective oxide scales.* Materials Science and Technology, 1990. **6**(1): p. 32-38.

103. Schütze, M., *The healing behavior of protective oxide scales on heat-resistant steels after cracking under tensile strain.* Oxidation of Metals, 1986. **25**(5-6): p. 409-421.

104. Chen, J., P. Rogers, and J.A. Little, *Oxidation behavior of several chromia-forming commercial nickel-base superalloys.* Oxidation of Metals, 1997. **47**(5): p. 381-410.

105. Taylor, M.P., H.E. Evans, S. Stekovic, and M.C. Hardy, *The Oxidation Characteristics of the Ni-base Superalloy, RR1000, at Temperatures 700-900^{o}C,* in *Microscopy of Oxidation 8,* G.J. Tatlock and H.E. Evans, Editors. 2011: Liverpool.

106. Encinas-Oropesa, A., G.L. Drew, M.C. Hardy, A.J. Leggett, J.R. Nicholls, and N.J. Simms, *Effects of oxidation and hot corrosion in a nickel disc alloy*, in *Superalloys 2008: 11th International Symposium on Superalloys* 2008, TMS. p. 609-618.

107. Encinas-Oropesa, A., N.J. Simms, J.R. Nicholls, G.L. Drew, J. Leggett, and M.C. Hardy, *Evaluation of oxidation related damage caused to a gas turbine disc alloy between 700 and 800°C.* Materials at High Temperatures, 2009. **26**(3): p. 241-249.

108. Evans, J.L., *Effect of surface roughness on the oxidation behavior of the Ni-base superalloy ME3.* Journal of Materials Engineering and Performance, 2010. **19**(7): p. 1001-1004.

109. Sudbrack, C.K., S.L. Draper, T.T. Gorman, J. Telesman, T.P. Gabb, and D.R. Hull, *Oxidation and the Effects of High Temperature Exposures on Notched Fatigue Life of an Advanced Powder Metallurgy Disk Superalloy*, in *Superalloys 2012: 12th International Symposium on Superalloys* 2012, TMS. p. 862.

110. Kim, D., C. Jang, and W. Ryu, *Oxidation characteristics and oxide layer evolution of Alloy 617 and Haynes 230 at 900 °C and 1100 °C.* Oxidation of Metals, 2009. **71**(5): p. 271-293.

111. Khalid, F.A., N. Hussain, and K.A. Shahid, *Microstructure and morphology of high temperature oxidation in superalloys.* Materials Science and Engineering: A, 1999. **265**(1–2): p. 87-94.

112. Greene, G.A. and C.C. Finfrock, *Oxidation of Inconel 718 in Air at High Temperatures.* Oxidation of Metals, 2001. **55**(5): p. 505-521.

113. Zheng, L., M. Zhang, and J. Dong, *Oxidation behavior and mechanism of powder metallurgy Rene95 nickel based superalloy between 800 and 1000 °C.* Applied Surface Science, 2010. **256**(24): p. 7510-7515.

114. Al-Hatab, K., M. Al-Bukhaiti, U. Krupp, and M. Kantehm, *Cyclic oxidation behavior of IN 718 Superalloy in air at high temperatures.* Oxidation of Metals, 2011. **75**(3): p. 209-228.

115. Taylor, M.P., H.E. Evans, S. Stekovic, and M.C. Hardy, *The oxidation characteristics of the Ni-base superalloy, RR1000, at temperatures 700-900^{o}C.* Materials at High Temperatures, 2012. **29**(2): p. 145-150.

116. Child, D.J., G.D. West, and R.C. Thomson, *Assessment of surface hardening effects from shot peening on a Ni-based alloy using electron backscatter diffraction techniques.* Acta Materialia, 2011. **59**(12): p. 4825-4834.

117. Foss, B.J., S. Gray, M.C. Hardy, S. Stekovic, D.S. McPhail, and B.A. Shollock, *Analysis of shot-peening and residual stress relaxation in the nickel-based superalloy RR1000.* Acta Materialia, 2013. **61**(7): p. 2548-2559.

118. Raceanu, L., V. Optasanu, T. Montesin, G. Montay, and M. François, *Shot-peening of pre-oxidized plates of zirconium: Influence of residual stress on oxidation.* Oxidation of Metals, 2013. **79**(1-2): p. 135-145.

119. Naraparaju, R., H.J. Christ, F. Renner, and A. Kostka, *Effect of shot-peening on the oxidation behaviour of boiler steels.* Oxidation of Metals, 2011: p. 1-13.

120. Naraparaju, R., H.J. Christ, F.U. Renner, and A. Kostka, *Dislocation engineering and its effect on the oxidation behaviour.* Materials at High Temperatures, 2012. **29**(2): p. 116-122.

121. Rosser, J.C., M.I. Bass, C. Cooper, T. Lant, P.D. Brown, B.J. Connolly, and H.E. Evans, *Steam oxidation of Super 304H and shot-peened Super 304H.* Materials at High Temperatures, 2012. **29**(2): p. 95-106.

122. Zengwu, Y., F. Min, W. Xuegang, and L. Xingeng, *Effect of shot-peening on the oxidation resistance of TP304H and HR3C steels in water vapor.* Oxidation of Metals, 2011: p. 1-10.

123. Tan, L., X. Ren, K. Sridharan, and T.R. Allen, *Effect of shot-peening on the oxidation of alloy 800H exposed to supercritical water and cyclic oxidation.* Corrosion Science, 2008. **50**(7): p. 2040-2046.

124. Khanna, A.S. and J.B. Gnanamoorthy, *Effect of cold work on the oxidation resistance of 2.25Cr-1 Mo steel.* Oxidation of Metals, 1985. **23**(1-2): p. 17-33.

125. Warzee, M., J. Hennaut, M. Maurice, C. Sonnen, J. Waty, and P. Berge, *Effect of surface treatment on the corrosion of stainless steels in high-temperature water and steam.* Journal of The Electrochemical Society, 1965. **112**(7): p. 670-674.

126. Langevoort, J.C., T. Fransen, and P.J. Geilings, *On the influence of cold work on the oxidation behavior of some austenitic stainless steels: High temperature oxidation.* Oxidation of Metals, 1984. **21**(5-6): p. 271-284.

127. Tomlinson, W.J. and K. Blick, *Substrate roughness, cold work and the oxidation of pure iron at 200 to 600° C.* Journal of Materials Science Letters, 1990. **9**(9): p. 1005-1010.

128. Caplan, D. and M. Cohen, *Effect of cold work on the oxidation of iron from 400–650 °C.* Corrosion Science, 1966. **6**(7): p. 321-335.

129. Caplan, D., G.I. Sproule, and R.J. Hussey, *Comparison of the kinetics of high-temperature oxidation of Fe as influenced by metal purity and cold work.* Corrosion Science, 1970. **10**(1): p. 9-17.

130. Huntz, A.M., B. Lefevre, and F. Cassino, *Roughness and oxidation: application to NiO growth on Ni at 800°C.* Materials Science and Engineering: A, 2000. **290**(1–2): p. 190-197.

131. Eubanks, A.G., D.G. Moore, and W.A. Pennington, *Effect of surface roughness on the oxidation rate of iron.* Journal of The Electrochemical Society, 1962. **109**(5): p. 382-389.

132. Uran, S., B. Veal, M. Grimsditch, J. Pearson, and A. Berger, *Effect of surface roughness on oxidation: Changes in scale thickness, composition, and residual stress.* Oxidation of Metals, 2000. **54**(1-2): p. 73-85.

133. Zhang, Z.G., P.Y. Hou, F. Gesmundo, and Y. Niu, *Effect of surface roughness on the development of protective Al_2O_3 on Fe–10Al (at.%) alloys containing 0–10 at.% Cr.* Applied Surface Science, 2006. **253**(2): p. 881-888.

134. Tang, J.E., M. Halvarsson, H. Asteman, and J.E. Svensson, *Microstructure of oxidised 304L steel and the effects of surface roughness on oxidation behaviour.* Materials Science Forum, 2001. **369-372**: p. 205-214.

135. Taylor, M.P., W.M. Pragnell, and H.E. Evans, *Influence of bond coat surface roughness on chemical failure and delamination in thermal barrier coating systems.* Materials and Corrosion, 2008. **59**: p. 508.

136. Zhou, C.H., H.T. Ma, and L. Wang, *Comparative study of oxidation kinetics for pure nickel oxidized under tensile and compressive stress.* Corrosion Science, 2010. **52**(1): p. 210-215.

137. Zhou, C., H. Ma, and L. Wang, *Effect of mechanical loading on the oxidation kinetics and oxide-scale failure of pure Ni.* Oxidation of Metals, 2008. **70**(5): p. 287-294.

138. Moulin, G., P. Arevalo, and A. Salleo, *Influence of external mechanical loadings (creep, fatigue) on oxygen diffusion during nickel oxidation.* Oxidation of Metals, 1996. **45**(1-2): p. 153-181.

139. Rolls, R. and M.H. Shahhosseini, *Effect of creep on the oxidation characteristics of Fe-Si alloys at 973–1073 K.* Oxidation of Metals, 1982. **18**(3-4): p. 115-126.

140. Rolls, R. and M.H. Shahhosseini, *Simultaneous creep and oxidation of Fe-Si alloys at 973–1073 K.* Acta Metallurgica, 1982. **30**(8): p. 1503-1510.

141. Calvarin-Amiri, G., A.M. Huntz, and R. Molins, *Effect of an applied stress on the growth kinetics of oxide scales formed on Ni20Cr alloys.* Materials at High Temperatures, 2001. **18**(2): p. 91-99.

142. Calvarin-Amiri, G., R. Molins, and A.M. Huntz, *Effect of the application of a mechanical load on the oxide-layer microstructure and on the oxidation mechanism of Ni-20Cr foils.* Oxidation of Metals, 2000. **53**(3-4): p. 399-426.

143. Takei, A. and K. Nii, *Effects of tensile stress on high temperature oxidation of a Ni-20Cr-4Al Alloy* Transactions of the Japan Institute of Metals, 1984. **25**(8): p. 561-568.

144. Zhou, C.H., H. Ma, and L. Wang, *A critical compressive stress for increasing the oxidation kinetics of Fe–20Cr alloy oxidized at 900 °C.* Oxidation of Metals, 2009. **71**(5-6): p. 335-341.

145. Azari, Z., M. Abbadi, H. Moustabchir, and M. Lebienvenu, *The influence of fatigue cycling on the oxidation kinetics and crack initiation of a Cr–Mo steel.* International Journal of Fatigue, 2008. **30**(3): p. 517-527.

146. Kusabiraki, K., H. Tsujino, and S. Saji, *Effects of tensile stress on the high-temperature oxidation of an Fe-38Ni-13Co-4.7Nb-1.5Ti-0.4Si superalloy in air.* Isij International, 1998. **38**(9): p. 1015-1021.

147. Karabela, A., L.G. Zhao, J. Tong, N.J. Simms, J.R. Nicholls, and M.C. Hardy, *Effects of cyclic stress and temperature on oxidation damage of a nickel-based superalloy.* Materials Science and Engineering: A, 2011. **528**(19-20).

148. Cruchley, S., J.F. Sun, M.P. Taylor, H.E. Evans, P. Bowen, J. Sumner, J.R. Nicholls, N.J. Simms, B.A. Shollock, R.J. Chater, B.J. Foss, M.C. Hardy, and S. Stekovic, *Cautionary note on use of focused ion beam sectioning as technique for characterising oxidation damage in Ni based superalloys.* Materials at High Temperatures, 2014. **31**(1): p. 27-33.

149. Barnard, B.R., P.K. Liaw, R.A. Buchanan, and D.L. Klarstrom, *Affects of applied stresses on the isothermal and cyclic high-temperature oxidation behavior of superalloys.* Materials Science and Engineering: A, 2010. **527**(16-17): p. 3813-3821.

150. Reger, M. and L. Remy, *Fatigue oxidation interaction in IN-100 superalloy* Metallurgical Transactions A - Physical Metallurgy and Materials Science, 1988. **19**(9): p. 2259-2268.

151. Gabb, T.P., J. Telesman, P.T. Kantzos, J.W. Smith, and P.F. Browning. *Effects of high temperature exposures on fatigue life of disk superalloys*. in *Superalloys 2004: 10th international symposium on superalloys*. 2004. Seven Springs, PA: TMS.

152. Rapp, R.A., *Kinetics, microstructures and mechanism of internal oxidation - its effect and prevention in high temperature alloy oxidation.* Corrosion 1965. **21**(12): p. 382-401.

153. Antolovich, S.D., P. Domas, and J.L. Strudel, *Low cycle fatigue of René 80 as affected by prior exposure.* Metallurgical Transactions A - Physical Metallurgy and Materials Science, 1979. **10**(12): p. 1859-1868.

154. Woodford, D.A., *Gas phase embrittlement and time dependent cracking of nickel based superalloys.* Energy Materials: Materials Science and Engineering for Energy Systems, 2006. **1**: p. 59-79.

155. Onofrio, G., G.A. Osinkolu, and M. Marchionni, *Fatigue crack growth of UDIMET 720 Li superalloy at elevated temperature*. International Journal of Fatigue, 2001. **23**(10): p. 887-895.

156. Marchionni, M., G.A. Osinkolu, and G. Onofrio, *High temperature low cycle fatigue behaviour of UDIMET 720 Li superalloy.* International Journal of Fatigue, 2002. **24**(12): p. 1261-1267.

157. Coffin Jr, L., *Fatigue at high temperature*, in *Fatigue at Elevated Temperatures*. 1973, ASTM STP. p. 5-34.

158. Krupp, U., W.M. Kane, C. Laird, and C.J. McMahon, *Brittle intergranular fracture of a Ni-base superalloy at high temperatures by dynamic embrittlement.* Materials Science and Engineering A, 2004. **387-389**: p. 409-413.

159. Pfaendtner, J.A. and C.J. McMahon Jr, *Oxygen-induced intergranular cracking of a Ni-base alloy at elevated temperatures—an example of dynamic embrittlement.* Acta Materialia, 2001. **49**(16): p. 3369-3377.

160. Ma, L. and K. Chang, *Identification of SAGBO-induced damage zone ahead of crack tip to characterize sustained loading crack growth in alloy 783.* Scripta Materialia, 2003. **48**(9): p. 1271-1276.

161. McMahon Jr, C.J., *Comments on "Identification of SAGBO-induced damage zone ahead of crack tip to characterize sustained loading crack growth in alloy 783".* Scripta Materialia, 2006. **54**(2): p. 305-307.

162. Krupp, U., *Dynamic embrittlement — Time–dependent quasi–brittle intergranular fracture at high temperatures.* International Materials Reviews, 2005. **50**(2): p. 83-97.

163. Andrieu, E., R. Molins, H. Ghonem, and A. Pineau, *Intergranular crack tip oxidation mechanism in a nickel-based superalloy.* Materials Science and Engineering: A, 1992. **154**(1): p. 21-28.

164. Liu, H.W. and Y. Oshida, *Grain boundary oxidation and fatigue crack growth at elevated temperatures.* Theoretical and Applied Fracture Mechanics, 1986. **6**(2): p. 85-94.

165. Evans, H.E., H.Y. Li, and P. Bowen, *A mechanism for stress-aided grain boundary oxidation ahead of cracks.* Scripta Materialia, 2013. **69**(2): p. 179-182.

166. Kitaguchi, H.S., H.Y. Li, H.E. Evans, R.G. Ding, I.P. Jones, G. Baxter, and P. Bowen, *Oxidation ahead of a crack tip in an advanced Ni-based superalloy.* Acta Materialia, 2013. **61**(6): p. 1968-1981.

167. Viskari, L., M. Hörnqvist, K.L. Moore, Y. Cao, and K. Stiller, *Intergranular crack tip oxidation in a Ni-base superalloy.* Acta Materialia, 2013. **61**(10): p. 3630-3639.

168. Petzow, G., *Metallographic Etching*. Second ed. 2001, Materials Park, OH: ASM International.

169. Huang, Z.W., H.Y. Li, M. Preuss, M. Karadge, P. Bowen, S. Bray, and G. Baxter, *Inertia friction welding dissimilar nickel-based superalloys alloy 720Li to IN718.* Metallurgical and Materials Transactions A, 2007. **38A**: p. 1608-1620.

170. Fischer-Cripps, A.C., *The IBIS handbook of nanoindentation*. 2005: Fischer-Cripps Laboratories.

171. Evans, H.E., D.A. Hilton, R.A. Holm, and S.J. Webster, *Influence of a titanium nitride dispersion on the oxidation behaviur of 20%Cr 25%Ni stainless steel.* Oxidation of Metals, 1978. **12**(6): p. 473-485.

172. Mitchell, R.J., C.M. Rae, and S. Tin, *Grain boundary transformations during isothermal exposure of powder metallurgy nickel base superalloys for turbine disc applications.* Materials Science and Technology, 2005. **21**: p. 125-132.

173. Geddes, B., H. Leon, and X. Huang, *Phases and microstructure*, in *Superalloys: Alloying and performance*. 2010, ASM International. p. 25-57.

174. El-Menshawy, K., H.P. Buchkremer, F. Tietz, and D. Stoever, *Electrical conductivity of sintered chromia mixed with TiO_2, CuO and Mn-oxides.* Journal of Materials Science and Technology, 2006. **22**(2): p. 245-251.

175. Du, Y., H. Xu, Y. Zhou, Y. Ouyang, and Z. Jin, *Phase equilibria of the Ni–Ti–Ta system at 927°C.* Materials Science and Engineering: A, 2007. **448**(1–2): p. 210-215.

176. Samsonov, G.V., *The oxide handbook*. 2nd Edition ed. 1982, New York and London: IFI/Plenum.

177. Ennis, P.J. and W.J. Quadakkers, *Corrosion and creep of nickel-base alloys in steam reforming gas*, in *High Temperature Alloys*, J.B. Marriott, et al., Editors. 1988, Springer Netherlands. p. 465-474.

178. Buscail, H., S. Perrier, and C. Josse, *Oxidation mechanism of the Inconel 601 alloy at high temperatures.* Materials and Corrosion, 2011. **62**(5): p. 416-422.

179. Nagai, H., M. Okabayashi, and H. Mitani, *The effects of rare earths and reactive elements on the oxidation resistance of Ni-20Cr alloy.* Transactions of the Japan Institute of Metals, 1980. **21**(6): p. 341-348.

180. Stott, F.H., S. Berg, M. Sang, and N. Karim, *The oxidation performance of superalloys in gaseous environments at very high temperatures*, in *High temperature materials for power engineering*, E. Bachelet, et al., Editors. 1990, Kluwer Academic Publishers. p. 213-226.

181. Strawbridge, A., H.E. Evans, and C.B. Ponton, *Spallation of oxide scales from NICrAlY overlay coatings*, in *High temperature corrosion and protection of materials 4*, R. Streiff, et al., Editors. 1997, Trans Tech Publications. p. 365-372.

182. Gleeson, B. and M.A. Harper, *Effects of minor alloying additions on oxidation behaviour of chromia forming alloys*, in *Lifetime modelling of high temperature corrosion processes: (EFC 34)*, M. Schutze, W.J. Quadakkers, and J.R. Nicholls, Editors. 2001, Maney Publishing. p. 167-177.

183. Holt, A. and P. Kofstad, *Electrical conductivity of Cr_2O_3 doped with TiO_2.* Solid State Ionics, 1999. **117**(1–2): p. 21-25.

184. Sabioni, A.C.S., A.M. Huntz, F. Millot, and C. Monty, *Self-diffusion in Cr_2O_3 III. Chromium and oxygen grain-boundary diffusion in polycrystals.* Philosophical Magazine A, 1992. **66**(3): p. 361-374.

185. Nam, H.O., I.S. Hwang, K.H. Lee, and J.H. Kim, *A first-principles study of the diffusion of atomic oxygen in nickel.* Corrosion Science, 2013. **75**(0): p. 248-255.

186. Park, J.-W. and C. Altstetter, *The diffusion and solubility of oxygen in solid nickel.* Metallurgical Transactions A, 1987. **18**(1): p. 43-50.

187. Karunaratne, M.S.A., P. Carter, and R.C. Reed, *On the diffusion of aluminium and titanium in the Ni-rich Ni–Al–Ti system between 900 and 1200°C.* Acta Materialia, 2001. **49**(5): p. 861-875.

188. Smith, A.F. and G.B. Gibbs, *Volume and grain-boundary diffusion in 20 Cr/25 Ni/Nb stainless steel.* Metal Science, 1969. **3**(1): p. 93-94.

189. Chen, T.-F., Y. Iijima, K.-i. Hirano, and K. Yamauchi, *Diffusion of chromium in nickel-Base Ni-Cr-Fe Alloys.* Journal of Nuclear Materials, 1989. **169**(0): p. 285-290.

190. Sabioni, A.C.S., B. Lesage, A.M. Huntz, J.C. Pivin, and C. Monty, *Self-diffusion in Cr_2O_3 I. Chromium diffusion in single crystals.* Philosophical Magazine A, 1992. **66**(3): p. 333-350.

191. Berthod, P., *Influence of Chromium Carbides on the High Temperature Oxidation Behavior and on Chromium Diffusion in Nickel-Base Alloys.* Oxidation of Metals, 2007. **68**(1-2): p. 77-96.

192. Rollett, A., F.J. Humphreys, and G.S. Rohrer, *Recrystallization and Related Annealing Phenomena*. 2004: Elsevier Science.

193. Cruchley, S., M.P. Taylor, H.E. Evans, P. Bowen, M.C. Hardy, and S. Stekovic, *Microstructural Characterisation of High Temperature Oxidation of Nickel Base Superalloy RR1000 and the Effect of Shot-Peening*, in *Superalloys 2012: 12th International Symposium on Superalloys*, E.S. Huron, et al., Editors. 2012, TMS: Seven Springs, PA. p. 751-758.

194. Engell, H. and F. Wever, *Über einige grundfragen der bildung und der haftung von zunder auf eisen.* Acta Metallurgica, 1957. **5**(12): p. 695-702.

195. Evans, H.E., D.A. Hilton, and R.A. Holm, *Internal attack during the oxidation of nitrided stainless steels.* Oxidation of Metals, 1977. **11**(1): p. 1-21.

196. Gorman, A., R.L. Higginson, H. Du, G. McClovin, A.T. Fry, and R.C. Thomson, *Microstructural Analysis of IN617 and IN625 Oxidised in the Presence of Steam for use in Ultra-Supercritical Power Plant*, in *8th International Symposium on High-Temperature Corrosion and Protection of Materials* 2012: Les Embiez, France.

197. Bricknell, R.H. and D.A. Woodford, *The mechanism of cavity formation during high temperature oxidation of nickel.* Acta Metallurgica, 1982. **30**(1): p. 257-264.

198. Dyson, B.F., *An analysis of carbon/oxygen gas bubble formation in some nickel alloys.* Acta Metallurgica, 1982. **30**(8): p. 1639-1646.

199. Evans, H.E., *Spallation of oxide from stainless steel AGR nuclear fuel cladding: mechanisms and consequences.* Materials Science and Technology, 1988. **4**(5): p. 414-420.

200. Munroe, P.R., *The application of focused ion beam microscopy in the material sciences.* Materials Characterization, 2009. **60**(1): p. 2-13.

201. Phaneuf, M.W., *Applications of focused ion beam microscopy to materials science specimens.* Micron, 1999. **30**(3): p. 277-288.

202. Giannuzzi, L.A. and S.F. A., *Introduction to focused ion beams: Instrumentation, theory, techniques and practice*. 2005: Springer.

203. Orloff, J., *Handbook of charged particle optics*. 2008: CRC Press.

204. Cruchley, S., M.P. Taylor, H.E. Evans, D.J. Child, and M.C. Hardy, *Characterisation of the sub-surface oxidation damage in the Ni-based superalloy, RR1000* Materials Science and Technology - Accepted in Press, 2014.

205. Zhao, S., X. Xie, G.D. Smith, and S.J. Patel, *Gamma prime coarsening and age-hardening behaviors in a new nickel base superalloy.* Materials Letters, 2004. **58**(11): p. 1784-1787.

206. King, J.E., *Fatigue crack propagation in nickel-base superalloys – effects of microstructure, load ratio, and temperature.* Materials Science and Technology, 1987. **3**(9): p. 750-764.

207. Kobayashi, K., K. Yamaguchi, M. Hayakawa, and M. Kimura, *High-temperature fatigue properties of austenitic superalloys 718, A286 and 304L.* International Journal of Fatigue, 2008. **30**(10–11): p. 1978-1984.

208. Suresh, S., *Fatigue of Materials*. 1998: Cambridge University Press.

Appendix

A.1 Glossary of Terms

The following abbreviations are used throughout and appear in the order that they are first described:

HP = High pressure
IP = Intermediate pressure
LP = Low pressure
TET = Turbine entry temperature
OPR = Overall pressure ratio
PPM = Parts per million
FCC = Face centred cubic
BCT = Body centred tetragonal
APB = Anti-phase boundary
VIM = Vacuum induction melting
HIP = Hot isostatic pressure
NDE = Non-destructive testing
M = Metal atom
O = Oxygen atom
T = Temperature
t = Time
R = Molar gas constant
Po_2 = Partial pressure of oxygen
MICF = Mechanically induced chemical failure
InCF = Intrinsic chemical failure
Sagbo = Stress assisted grain boundary oxidation
CG = Coarse-grained
FG = Fine-grained
PO = Polished
SP = Shot-peened
VP = Vibro-peened
TU = Turned
SW = Swaged
XRD = X-ray diffraction
SEM = Scanning electron microscopy
HCF = High cycle fatigue
R ratio = $\sigma_{min}/\sigma_{max}$

RT = Room temperature

EDX = Elemental dispersive c-ray spectroscopy

FIB = Focussed ion beam

FEG = Field emission gun

WDS = Wave dispersive x-ray spectroscopy

$SE_{electron}$= Secondary electrons produced by the impact of electrons from a FEG

SE_{ion} = Secondary electrons produces by the impact of gallium ions from an ion beam

FWHM = Full width at half maximum

The following symbols are used throughout and appear in the order that they are first described:

γ = Gamma phase

γ' = Gamma prime phase

σ = TCP phase sigma

μ = TCP phase mu

δ = Orthorhombic delta phase

γ'' = Gamma double prime phase

ΔG^o = Gibbs free energy change

ΔH^o = Enthaply change under standard conditions

ΔS^o = Entropy change under standard conditions

V_m^n = Metal cation vacancies

O^{2-} = Oxygen interstitials

V_o^{2+} = Oxygen vacancies

M^{n+} = Self-interstitial cation

I_m = Cation interstitial

I_o = Anion interstitial

$\left(\frac{\Delta m}{A}\right)$ = Mass change/Surface area

ξ = Oxide thickness

k_n = Rate constant for mass gain data

k_n' = Rate constant for thickness data

n = Oxide growth regime

k_o = Pre-exponential constant

Q = Activation energy for oxide formation

ξ_I = Internal oxidised zone

D_o = Self-diffusion coefficient of oxygen

$N_o^{(s)}$ = Oxygen solubility in the substrate

$N_m^{(0)}$ = Mole fraction of oxidising element (M)

υ = Number of oxygen atoms per M atom in precipitated oxide

X = Position of metal/oxide interface

k_p' = Parabolic rate constant for external oxide

D_m = Diffusivity of oxygen

v_{ox} = Molar volume of oxide

v_m = Molar volume of solute metal

v_{alloy} = Molar volume of the alloy

N_{ox}^{o} = Volume of oxide formed from one mole of solute atoms

N_m^{o} = Molar fraction of metal solute atoms in the alloy

σ_{ox} = In-plane stress in the oxide

E_{ox} = Young's modules of oxide

α_{met} = Thermal coefficient of expansion of metal

α_{ox} = Thermal coefficient of expansion of oxide

υ_{ox} = Poissons ratio

ΔT = Temperature change

K_{1c} = Fracture toughness

σ_c = Critical stress to failure

f = Defect geometry

ε_c = Critical strain to failure

t_h = Time to scale healing

ξ_c = Crack thickness

w = Crack width

$\dot{\varepsilon}_c$ = Critical strain for crack healing

λ_1 = Spacing between cracks measured at $\dot{\varepsilon}_1$ strain rate

$\dot{\varepsilon}_1$ = Strain rate

m = exponent describing dependence of λ on

σ_{min} = Minimum applied stress

σ_{max} = Maximum applied stress

S_a = Arithmetic mean surface roughness of an area

R_a = Arithmetic mean surface roughness of a line

R_c = Mean height of the surface roughness profile peaks

H_n = Hardness from nano-indentation

P_{max} = Maximum applied load

A_r = Residual indentation area

h_c = Depth of indenter after elastic relaxation

ε = Geometric constant for indenter

k_p = Parabolic rate constant for oxide mass gain

n_{ox} = Oxide growth regime for external oxide scale growth

r = Ratio of the rate of external oxide growth for RR1000 to the rate of external oxide growth of pure chromium at a given oxide thickness

$(d\xi/dt)_s$ = Oxide growth rate of RR1000 at a given oxide thickness

$(d\xi/dt)_{cr}$ = Oxide growth rate of pure chromium at a given oxide thickness

Q_{ox} = Activation energy for external chromia formation

$(k_n')_{gb}$ = Growth rate constant for growth of the external oxide scale at the grain boundaries

$(n_{ox})_{gb}$ = Oxide growth regime for enhanced grain boundary external oxidation

$(k_p')_{gb}$ = Parabolic rate constant for the growth of the external oxide scale at the grain boundaries

ℓ_{gb} = Internal oxide depth for intergranular penetrations

ℓ_{tr} = Internal oxide depth for intragranular penetrations

$(k_{n\ell})_{gb}$ = Growth rate constant for internal oxidation at the grain boundaries

$(k_{n\ell})_{tr}$ = Growth rate constant for intragranular internal oxidation

$(n_{ioz})_{gb}$ = Oxide growth regime for internal oxidation at the grain boundaries

$(n_{ioz})_{tr}$ = Oxide growth regime for intragranular internal oxidation

$(k_{ny})_{gb}$ = Growth rate constant for the γ' denuded zone growth at the grain boundaries

$(k_{ny})_{tr}$ = Growth rate constant for the intragranular γ' denuded zone growth

$(n_{dz})_{gb}$ = Oxide growth regime for the γ' denuded zone growth at the grain boundaries

$(n_{dz})_{tr}$ = Oxide growth regime for intragranular γ' denuded zone growth

τ_{gb} = Total oxidation damage at the grain boundaries

τ_{tr} = Total oxidation damage intragranularly

$(k_{n\tau})_{gb}$ = Growth rate constant for the total oxidation damage at the grain boundaries

$(k_{n\tau})_{tr}$ = Growth rate constant for the total oxidation damage intragranularly

$(n_{\tau d})_{gb}$ = Oxide growth regime for the total oxidation damage at the grain boundaries

$(n_{\tau d})_{tr}$ = Oxide growth regime for the total oxidation damage intragranularly

A.2 List of Figures

A.3 List of Tables